Universität Potsdam

Mathematisch-Naturwissenschaftliche Fakultät
Institut für Physik und Astronomie

Ultraschnelle Dynamik in Kondensierter Materie

Magnetoacoustics observed with Ultrafast X-ray Diffraction

Publikationsbasierte Dissertation

zur Erlangung des akademischen Grades
doctor rerum naturalium (Dr. rer. nat.)
in der Wissenschaftsdisziplin: Experimentalphysik

Autor:	Steffen Peer Zeuschner Universität Potsdam & Helmholtz-Zentrum Berlin
Disputation:	01. September 2022

Betreuer: Prof. Dr. Matias Bargheer
Universität Potsdam & Helmholtz-Zentrum Berlin

Gutachter: Prof. Dr. Klaus Sokolowski-Tinten
Universität Duisburg Essen

PD Dr. Klaus Habicht
Universität Potsdam & Helmholtz-Zentrum Berlin

Published online on the
Publication Server of the University of Potsdam:
https://doi.org/10.25932/publishup-56109
https://nbn-resolving.org/urn:nbn:de:kobv:517-opus4-561098

to my loved ones

Abstract

In the present thesis I investigate the lattice dynamics of thin film hetero structures of magnetically ordered materials upon femtosecond laser excitation as a probing and manipulation scheme for the spin system. The quantitative assessment of laser induced thermal dynamics as well as generated picosecond acoustic pulses and their respective impact on the magnetization dynamics of thin films is a challenging endeavor. All the more, the development and implementation of effective experimental tools and comprehensive models are paramount to propel future academic and technological progress.

In all experiments in the scope of this cumulative dissertation, I examine the crystal lattice of nanoscale thin films upon the excitation with femtosecond laser pulses. The relative change of the lattice constant due to thermal expansion or picosecond strain pulses is directly monitored by an ultrafast X-ray diffraction (UXRD) setup with a femtosecond laser-driven plasma X-ray source (PXS). Phonons and spins alike exert stress on the lattice, which responds according to the elastic properties of the material, rendering the lattice a versatile sensor for all sorts of ultrafast interactions. On the one hand, I investigate materials with strong magneto-elastic properties; The highly magnetostrictive rare-earth compound Terbium Iron ($TbFe_2$), elemental Dysprosium or the technological relevant Invar material Iron Platinum (FePt). On the other hand I conduct a comprehensive study on the lattice dynamics of $Bi_1Y_2Fe_5O_{12}$ - Bismuth-substituted Yttrium Iron-Garnet (Bi:YIG), which exhibits high-frequency coherent spin dynamics upon femtosecond laser excitation according to the literature. Higher order standing spin waves (SSWs) are triggered by coherent and incoherent motion of atoms, in other words phonons, which I quantified with UXRD. We are able to unite the experimental observations of the lattice and magnetization dynamics qualitatively and quantitatively. This is done with a combination of multi-temperature, elastic, magneto-elastic, anisotropy and micro-magnetic modeling.

The collective data from UXRD, to probe the lattice, and time-resolved magneto-optical Kerr effect (tr-MOKE) measurements, to monitor the magnetization, were previously collected at different experimental setups. To improve the precision of the quantitative assessment of lattice and magnetization dynamics alike, our group implemented a combination of UXRD and tr-MOKE in a singular experimental setup, which is to my knowledge, the first of its kind. I helped with the conception and commissioning of this novel experimental station, which allows the simultaneous observation of lattice and magnetization dynamics on an ultrafast timescale under identical excitation conditions. Furthermore, I developed a new X-ray diffraction measurement routine which significantly reduces the measurement time of UXRD experiments by up to an order of magnitude. It is called reciprocal space slicing (RSS) and utilizes an area detector to monitor the angular motion of X-ray diffraction peaks, which is associated with lattice constant changes, without a time-consuming scan of the diffraction angles with the goniometer. RSS is particularly useful for ultrafast diffraction experiments, since measurement time at large scale facilities like synchrotrons and free electron lasers is a scarce and expensive resource. However, RSS is not limited to ultrafast experiments and can even be extended to other diffraction techniques with neutrons or electrons.

Kurzdarstellung

In der vorliegenden Arbeit untersuche ich die Gitterdynamik von magnetisch geordneten und dünnen Filmen, deren Spinsystem mit Femtosekunden-Laserpulsen angeregt und untersucht wird. Die Quantifizierung der laserinduzierten thermischen Dynamik, der erzeugten Pikosekunden-Schallpulse sowie deren jeweiliger Einfluss auf die Magnetisierungsdynamik ist ein schwieriges Unterfangen. Umso mehr ist die Entwicklung und Anwendung von effizienten experimentellen Konzepten und umfangreichen Modellen grundlegend für das Antreiben des zukünftigen wissenschaftlichen und technologischen Fortschritt.

In jedem Experiment dieser kummulativen Dissertation untersuche ich das Kristallgitter von Nanometer dünnen Filmen nach der Anregung mit Femtosekunden-Laserpulsen. Die relative Änderung der Gitterkonstante, hervorgerufen durch thermische Ausdehnung oder Pikosekunden-Schallpulse, wird dabei direkt mittels ultraschneller Röntgenbeugung (UXRD) gemessen. Der Aufbau nutzt zur Bereitstellung von ultrakurzen Röntgenpulsen eine lasergetriebene Plasma-Röntgenquelle (PXS). Phononen und Spins üben gleichermaßen einen Druck auf das Gitter aus, welches entsprechend der elastsischen Eigenschaften des Materials reagiert, was das Gitter zu einem vielseitigen Sensor für ultraschenlle Wechselwirkungen macht. Zum einen untersuche ich Materialien mit starken magnetoelastischen Eigentschaften: die stark magnetostriktive Seltenen-Erden-Verbindung $TbFe_2$, elementares Dysprosium oder das technologisch relavante Invar-Material FePt. Zum anderen habe ich eine umfangreiche Studie der Gitterdynamik von $Bi_1Y_2Fe_5O_{12}$ (Bi:YIG) angestellt, in dem der Literatur zufolge hochfrequente kohärente Spindynamiken durch Femtosekunden-Laseranregung zu beobachten sind. Diese stehenden Spinwellen (SSWs) höherer Ordnung entstehen durch die kohärente und inkohärente Bewegung von Atomen, in anderen Worten Phononen, welche ich durch UXRD vermessen habe. Somit sind wir in der Lage, die experimentellen Beobachtungen der Gitter- und Spindynamik qualitativ und quantitativ zu vereinigen. Dies geschieht durch eine Kombination von Viel-Temperatur- und Anisotropiemodellierung sowie elastische, magnetoelastische, und mikromagnetsiche Modelle.

Die gemeinsamen Daten von UXRD und der zeitaufgelösten magnetooptischen Kerr-Effekt Messungen (tr-MOKE), um jeweils die Gitter- und Spindynamik zu messen, wurden in der Vergangenheit noch an unterschiedlichen experimentellen Aufbauten gemessen. Um die Quantifizierung präziser zu gestalten, haben wir in unserer Arbeitsgruppe UXRD und tr-MOKE in einem einzigen Aufbau kombiniert, welcher somit meines Wissens der erste seiner Art ist. Ich half bei dem Entwurf und der Inbetriebnahme des neuen Aufbaus, welcher die gleichzeitige Messung von Gitter- und Spindynamik auf einer ultraschnellen Zeitskala unter identischen Anregungsbedingungen ermöglicht. Außerdem entwickelte ich eine neue Messroutine für Röntgenbeugung, welche die Messzeit von UXRD-Experimenten um bis zu einer Größenordnungen reduziert. Es nennt sich das Schneiden des reziproken Raumes (reciprocal space slicing, RSS) und nutzt den Vorteil von Flächendetektoren die Bewegung von Beugungsreflexen zu detektieren, was von einer Änderung der Gitterkonstante einhergeht, ohne zeitintensive Scans der Beugungswinkel mit dem Goniometer durchzuführen. RSS ist besonders nützlich für ultraschnelle Beugungsexperimente, weil die Messzeit an Großgeräten wie Synchrotrons oder Freie Elektronen Laser eine seltene und teure Ressource ist. Darüber hinaus ist RSS nicht zwangsläufig auf die Anwendung in ultraschnellen Experimenten beschränkt und kann sogar auf andere Beugungsexperimente, wie die mit Neutronen und Elektronen, ausgeweitet werden.

Abbreviations

Bi:YIG $Bi_1Y_2Fe_5O_{12}$ - Bismuth-substituted Yttrium Iron-Garnet

FePt Iron Platinum

GGG $Gd_3Ga_5O_{12}$ - Gadolinium Gallium-Garnet

HAMR heat assisted magnetic recording

HDD hard disk drive

PXS plasma X-ray source

RSS reciprocal space slicing

SiO_2 Silicium Dioxide

SSWs standing spin waves

$TbFe_2$ Terbium Iron

tr-MOKE time-resolved magneto-optical Kerr effect

UDKM ultrafast dynamics in condensed matter

UXRD ultrafast X-ray diffraction

Contents

Abstract **I**

Kurzdarstellung **III**

Abbreviations **V**

1 Introduction **1**
1.1 The Scope of Ultrafast X-ray diffraction . . . 3
1.2 Technological and academic applications of UXRD . . . 6
1.3 Methods . . . 8
1.3.1 X-ray diffraction and reciprocal space . . . 8
1.3.2 Pump-probe technique and UXRD . . . 9
1.3.3 Temperature and strain modeling . . . 9

2 Results of the PhD **11**
2.1 Advancing Ultrafast X-ray diffraction . . . 12
2.1.1 Reciprocal Space Slicing . . . 12
2.1.2 Combining UXRD and tr-MOKE . . . 14
2.2 Ultrafast Magnetoacoustics in Bi:YIG . . . 17
2.2.1 Direct excitation via one and two photon absorption . . . 17
2.2.2 Transducer mediated indirect excitation via strain waves . . . 19
2.2.3 Generation of standing spin waves with sound and heat . . . 22

3 Articles **25**
I Tracking picosecond strain pulses in heterostructures that exhibit giant magnetostriction . 27
II Unconventional picosecond strain pulses resulting from the saturation of magnetic stress within a photoexcited rare earth layer . . . 39
III Measurement of transient strain induced by two-photon excitation . . . 53
IV Spin stress contribution to the lattice dynamics of FePt . . . 61
V Generation of spin waves via spin-phonon interaction in a buried dielectric thin film . . . 71
VI Reciprocal space slicing: A time-efficient approach to femtosecond x-ray diffraction . . . 81
VII Ultrafast control of lattice strain via magnetic circular dichroism . . . 93
VIII Standing spin wave excitation in Bi:YIG films via temperature induced anisotropy changes and magnetoacoustic coupling . . . 103

4 Conclusion **117**

5 Outlook **119**

Bibliography **121**

Statement of Authorship - Selbstständigkeitserklärung **VII**

Acknowledgements **IX**

Chapter 1

Introduction

Ultrafast X-ray Diffraction (UXRD) is an experimental procedure to quantify the motion of atoms upon excitation in crystalline nanostructures on an ultrashort timescale [1, 2, 3, 4]. This nondestructive technique combines the capability of X-ray diffraction to measure the interatomic distances with a precision of up to 10^{-4} Å with a temporal resolution of hundreds of femtoseconds. This is particularly useful for the ultrafast dynamics in condensed matter research field and, in extend, for emerging technological advancements. This is because the nature of the solid state needs to be thoroughly studied on the scale of femto- to picoseconds and nanometers to make contemporary technologies faster and smaller.

An intriguing example to illustrate the complexity of solids on an ultrafast timescale is the concept of temperature. From a macroscopic point of view, usually a single temperature is assigned locally to solids and can change due to thermal gradients. It is the same for the electrons, phonons and spins which are in equilibrium and are accordingly described by their respective Fermi-Dirac- and Bose-Einstein-statistics [5]. On an ultrafast timescale however, this view is not an appropriate model anymore for two reasons [6]. Firstly, the temperatures of the three subsystems differ, because the absorption of a femtosecond laser pulse primarily heats up the electrons and it takes several femto to picoseconds to increase the phonon and spin temperature. Secondly, it is possible that individual subsystems themselves are not equilibrated and can not be described by the respective quantum statistics, which prevents the attribution of a single distinct temperature even locally.

Besides the concept of temperature, there are many other interesting facets of solids from a equilibrated and macroscopic or ultrafast and nanoscopic point of view. Many of them have something in common; they are directly or indirectly entangled with the solid crystal lattice. Whether it is magnetic ordering, the electronic band structure or occupied phonon states, the lattice can be used to monitor the subsystems via mechanisms such as magnetostriction [7], deformation potential [8] or phonon pressure [5], respectively. This is the reason why UXRD, which quantitatively probes the lattice, has a large potential for many ultrafast research fields, as spintronic, picosecond hypersonics, femtomagnetism, phononics, or thermometry.

In this short introductory Chapter 1 I will elaborate on the nanoscopic ultrafast modeling of solids to clarify the main focus of my studies. In addition, I will expand on the possible applications of UXRD in the ultrafast research community and give a contemporary technological example in heat-assisted magnetic recording, to substantiate why UXRD is a useful and elegant tool. Furthermore, i give insights to the methodology of UXRD experiments and especially how I conduct them during my studies with the plasma X-ray source.

In Chapter 2 I present my work and findings of my PhD-studies at the University of Potsdam in the ultrafast dynamics in condensed matter (UDKM) group in depth. Those are, on a technical note, the improvements to the experimental technique of ultrafast X-ray diffraction. I worked on the conception

of the new reciprocal space slicing (RSS) approach, which drastically reduces the measurement time and developed the combination of UXRD and time-resolved magneto-optical Kerr effect measurements (tr-MOKE) in a single setup to quantitatively assess magnetoelastic coupling phenomena on an ultrafast timescale. On a fundamental note, I discuss my findings about magnetoacoustics on the case example of $B_1Y_2Fe_5O_{12}$ (Bi:YIG) thin films, a ferromagnetic insulator. I show how Bi:YIG can be excited directly by a laserpulse or indirectly via strainwaves and heat transport to trigger coherent magnetic excitations on a picosecond timescale, so called standing spin waves. Modelling the inner mechanics via masses and springs to feed magnetization dynamics simulations reveal the significant role of heat and sound to trigger the SSWs.

In Chapter 3 I present the articles I authored or co-authored during my studies. Before each article, I give a complete overiew about my contributions to the publication as well as comments on the main findings and additional, unpublished, information.

1.1 The Scope of Ultrafast X-ray diffraction

Ultrafast X-ray Diffraction (UXRD) quantifies the lattice dynamics of thin film crystal structures with a femtosecond time resolution [1, 2, 3, 4]. It is able to detect changes of lattice constants c below one permille in real time, combining the structural spatial nanoscopic capabilities of X-ray diffraction with the temporal nanoscopic qualities of the stroboscopic pump-probe technique. The crystal lattice of a solid is a useful indicator for ultrafast dynamics on the nanoscale, since electrons, phonons and spins act on the lattice in many different ways, as illustrated in Fig. 1.1.1.

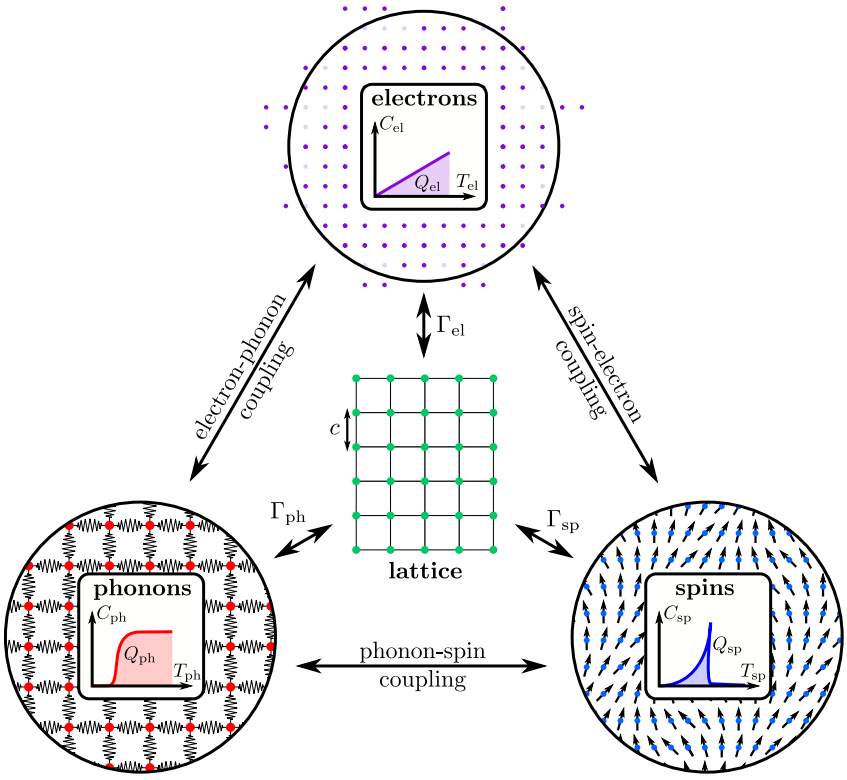

Figure 1.1.1: **Overview of the three subsystems of a solid and their interactions.** The **electrons** in the top are visualized by their reciprocal space with the Fermi surface being the surrounding circle. Dark and light purple dots correspond to occupied and unoccupied states, respectively. The **spin** subsystem on the bottom right is visualized by an arrangement of small arrows representing the microscopic magnetization vectors of atoms in a crystal lattice. The **phonons** are visualized by an arrangement of masses and springs, according to the definition of quantized lattice vibrations in the bottom left. The schematic graphs of the heat capacities C_i depending on their temperature T_i and corresponding amounts of heat Q_i as the integrals are placed in the centers of the circles, respectively. The interactions of the subsystems are named and the stresses on the **lattice** in the center are labeled with the respective proportionality constants, the Grüneisen parameters Γ_i.

Although the topic is complex, the interactions and systems discussed in the research field of ultrafast dynamics exhibit a multitude of similarities and symmetries. First of all, it is commonly accepted to view the electrons and phonons as coupled heat baths with the same temperature in equilibrium [9, 10]. In magnetially ordered materials, such as ferro- ferri- or antiferromagnets, the spins account for an additional degree of freedom where energy can be stored and thus the model is commonly extended to a three-temperature model [11]. Heating a specific system, for example by the absorption of light by electrons, will eventually lead to the increase of temperature of the phonons and the spins as well [6, 11].

However, the amount of thermal energy Q_i stored in the subsystems is determined by the respective heat capacity C_i, which are drastically different, see Fig. 1.1.1. The energy transfer between the subsystems can be thought of as semi-classical scattering processes of the quasiparticles of electrons, phonons and magnons. Following this thermodynamic approach, the effects of the subsystems can be generalized by the Grüneisen approach which allocates an acting stress or pressure on the lattice σ_i to every amount of energy density ρ_i in the subsystems, see Eq. 1.1.1 [12].

$$\sigma_i = \Gamma_i \cdot \rho_i \tag{1.1.1}$$

This stress on the lattice leads to a deformation of the lattice, according to classical elasticity theory of solids [5]. The latter is a generalized version of Hook's law, where the deformation is proportional to the acting force. In the case of solids, the relative change of the lattice constant, i.e. the strain $\epsilon = \frac{\Delta c}{c}$, is proportional to the stress or pressure, i.e. force per area. The proportionality constant in this case is not a scalar spring constant but the elasticity tensor $\overleftrightarrow{C}_{i,j}$, where i and j are now indices according to the Voigt notation of symmetrical tensors [5]:

$$\epsilon_j = \overleftrightarrow{C}_{i,j} \cdot \sigma_i \tag{1.1.2}$$

UXRD offers the possibility to monitor the strain on a femto- to nanosecond timescale, which is why it is a useful research tool for ultrafast dynamics in general. Measuring the strain and correctly attributing certain strain signatures to the driving stresses and furthermore the dynamics in the spin, electron or phonon systems is vital for generating insights about the interactions of nanoscale matter.

Having elaborated the similarities of the subsystems and the generalized approaches to the ultrafast dynamics, it is also important to discuss the specifics and intricacies of the respective subsystems, which I will do in the following paragraphs.

The electrons are usually the fastest subsystem in terms of equilibration and transport of energy. The thermal equilibration, back to a thermal Fermi distribution with larger temperature, takes place in a matter of femtoseconds, succeeding the efficient ultrafast photoexcitation [6]. The electronic temperature can easily exceed thousands of Kelvin since the heat capacity C_{el} of the electrons is small compared to phonons. C_{el} rises linearly with the temperature and in metals, the electrons transport the energy spatially via electronic thermal conduction or ballistic electrons at the Fermi velocity [5, 13]. In contrast, in insulators or semiconductors, this energy transport is inefficient due to a negligible conductivity. In ultrafast pump probe experiments, the initial optical pump laser pulse is often mainly absorbed by the electrons and the energy is subsequently transferred to the phonons on a femto to picosecond timescale, depending on the material [6]. The interaction of the electrons and the lattice exhibits many interesting features. On the one side, it is possible to excite electrons to states with a different bonding distance and strength, described by the deformation potential or even to non-binding orbitals which leads to non-thermal melting [14]. On the other side, the electronic band structure is partially defined by the arrangement of the atoms in the solid. Thus, a distortion of the lattice will change the electronic band structure, which becomes apparent in structural phase transitions accompanied by an electronic metal-insulator phase transition [15].

The phonon subsystem exhibits, compared to electrons, rather slow dynamics on a picosecond to nanosecond time scale. Those dynamics can be divided into coherent and incoherent components. The coherent dynamics are the phonon wave packets which interfere constructively to manifest in strain pulses or sound waves [16, 17]. Those spatio-temporal harmonic distortions of the lattice can be monitored by UXRD and are the main object of research in the field of picosecond acoustics or ultrasonics. The incoherent dynamics are the thermal conduction via diffusion; phonon-phonon scattering processes which can be classically described by the Fourier heat law [5]. Due to the comparably large heat capacity, the largest amount of energy is in fact transported into the phonons due to thermalization of the subsystems. Since the stress on the lattice is proportional to the energy density, thermal expansion is often associated with the excited phonons in solids. This however is not the case for the non-equilibrium at ultrafast timescales on the one

hand, where the amount of energy in the electrons is considerably larger or equally large for femto- to picoseconds, depending on the electron-phonon coupling time [18]. On the other hand, spins exhibit fairly large heat capacities near magnetic phase transitions, where the magnetic stress rivals the phonon stress in amplitude, which we observed in FePt and Dy, see Article II and IV. Only if all relevant subsystems are described by the same Grüneisen parameter, the contribution of spins and electrons can be neglected.

The spin system most notably has a significant effect on the lattice in solids with a magnetic ordering. In those materials, the timescale of spin dynamics ranges from femtosecond demagnetization over picosecond spin waves to up to nanosecond remagnetization [11, 19, 20]. Antiferromagnets, ferri- and ferromagnets alike exhibit magnetostriction, which means that a change of the magnetization state results in a stress on the lattice [7]. This is mainly due to a strong spin-orbit coupling which connects the alignment of spin and orbital angular momentum, i.e. the magnetization and the spatial distribution of electrons and thus the binding properties [21]. Inverse magnetostriction is consequently possible as well. For example, a picosecond strain pulse can trigger a magnetic response, coherent precession [22]. Another relevant quantity of the spin system is the magnetic anisotropy which describes the preferential direction of the magnetization. Empirically, it was shown, that the anisotropy depends on the spin temperature, i.e. the amount of random disorder of the aligned spins [21].

I mainly focus on the interaction of phonons, spins and the lattice, with UXRD as my tool of choice to monitor the lattice on the ultrafast timescale, hence the title of the thesis.

1.2 Technological and academic applications of UXRD

The storage of data with magnetic materials is older than a century and since then tapes are widely used for sound recording or archives, due to it's durability and reusability [23]. The large increase of the areal storage density of magnetic recording media was started with the introduction of the first hard disk drive (HDD) by IBM in 1956 with a capactiy of 5 MB and 2 kb/in.^{2} areal storage density [23]. Since then, contemporary HDDs exhibit an areal density of 600 Gb/in.^{2} exceeding capacities of 1GB. However, the storage densities of conventional HDDs seem to have reached a limit, since the writing and reading areas can not be constructed smaller without the loss of a longterm stability as well as fast and easy writing and reading. Combining all three; the large storage densities, the stability and the easy access, is called the trilemma of magnetic storage technology, as they rule each other out to some degree [24].

The trilemma is a consequence of the storage mechanism itself. To store digital information on a magnetic device, a small unit area is set to a certain magnetization by an external field. This magnetization can be set in two different directions, resembling the states of bits; up and down, 1 and 0. To read information, the magnetic state of the unit area is evaluated by a magnetic field sensor [23]. The anisotropy of magnetically ordered materials is a measure for how strongly the magnetiaztion state is fixed after being set [21]. A large anisotropy has the advantage of being impervious in relation to thermal fluctuations or external fields and thus yield a reliable and long term stability of stored data. However, a much larger amount of energy is required to change the magnetization state when writing new information on a medium with large anisotropy. Additionally, the smaller the unit areas of the magnetization bits become, the stronger their interaction becomes, demanding larger anisotropies to ensure stability and the prevention of data loss.

Conveniently, heat assisted magnetic recording (HAMR) offers a solution to the trilemma and is already made commercially available, for example by Seagate [25]. HAMR employs a storage medium with a large magnetic anisotropy and circumvents the potentially difficult writing process by heating a small area of the storage medium to reduce the anisotropy temporally during the writing process [26]. This results in a large stability with an efficient writing process of future HDDs. A leading example of the used materials is FePt [27], which I examined as part of my studies, see article IV. To additionally achieve a large areal storage density, it is paramount to study the intricacies of the nanoscale thermodynamics of the storage medium. The magnetic and anisotropic dynamics belong to it, as well as the heat transport itself. The heating and cooling of the storage medium needs to be analyzed and modeled to design media with small lateral heat flow, to not disturb neighboring magnetic bits, and a fast heat flow out of the storage area to accelerate the writing process. The observation of ultrafast nanoscaled dynamics on magnetic materials therefore acts as a possible foundation for the future technological advances in HAMR and other storage technologies [28].

The example of HAMR illustrates, how UXRD is essential to build a solid foundation of physical models for new technologies to stand on. In the case of HAMR, UXRD can assist the research about ultrafast de- and remagnetization processes by quantifying the state of the lattice. As the latter is constantly stressed by transient magnetic and phononic contributions, the lattice acts as a proxy for the energy dynamics of and in between the two subsystems. This field of research is called femtomagnetism and was essentially initiated by the observation of the ultrafast demagnetization of Nickel in 1996 by Bearepaire et al., which happens on a timescale of 100 fs [11]. The major contribution of my work regarding the field of femtomagnetism is the quantification of coherent and incoherent phonon dynamics in Article V, VII and VIII, which generate standing spin waves in the ferromagnetic insulator Bi:YIG [29, 19]. In particular I was able to show that the generation process of this insulator is thermally induced via a two-photon absorption process, see Article III.

Emerging from femtomagnetism, spintronics is another research field, which possibly can benefit from UXRD. The goal of spintronics is to manipulate the magnetic order in materials via electrical stimuli or spin currents so that spintronic technology can ultimately complement or even replace contemporary

electronic devices [30]. Since the spins are carried by the electrons and are collectively ordered in ferromagnetic materials, it is possible to generate spin currents by moving spin polarized electrons with an electronic current. This is the reason for the spin Seebeck effect, where a magnetic potential difference is accumulated by a thermal gradient, similar to the electrical voltage in the scope of the regular Seebeck effect [5, 31]. The spin Seebeck effect is also observable on a picosecond timescale [32] and since a temperature gradient is the driving force, UXRD could be employed for a quantitative assessment of the temperature via monitoring the thermal expansion of the lattice.

I have demonstrated in my PhD studies that UXRD is also very useful in the field of picosecond ultrasonics. This field of research is based on the work of Thomsen, Grahn, Maris and Tauc et al. who experimentally and theoretically investigated the generation and detection of picosecond strain pulses in solids, excited by ultrafast laser pulses, beginning in 1984 [16, 17]. Monitoring the coherent phonon wave packets in solids yields insights about the acoustic properties in the GHz to THz range with wavelengths of 4-100 nm [33, 34]. As the sound waves are local spatio-temporal distortions of the lattice, manifested by the coherent superposition of phonons, UXRD is capable of monitoring this transient deformation directly, as I show in articles I to V and VIII. Even more so, UXRD has several upsides compared to conventional optical probing of the sound pulses as I explain in Sec. 2.1.2.

To conclude, UXRD is a useful tool in many research fields of the ultrafast dynamics in condensed matter. Its capability to directly and exclusively monitor lattice dynamics on a femto- to nanosecond timescale introduces an easy and reliable way to determine the lattice temperature and the strain dynamics. It thus facilitates a comprehensive modeling and understanding of the interactions in solids on an ultrafast timescale. Besides the academic purpose of UXRD, technological advances are consequently also propelled by it, as I exemplified with the HAMR technology.

1.3 Methods

In the following subsections I will shortly present the physical models, experimental techniques and modeling tools which I mainly used during my PhD studies.

1.3.1 X-ray diffraction and reciprocal space

X-ray diffraction is a widely used tool in the structure analysis of solids, since it's conception in the early 1900's by Bragg and Laue [35]. It enables measuring the distances of atoms, i.e. the lattice constant c, in crystalline ordered solids. To do so, the diffracted intensity of a parallel X-ray beam is measured as a function of the diffraction angle θ. A maximum of the intensity can be associated with the distance of neighboring scattering centers, which are mainly the core electrons positioned in the vicinity of the lattice points in a crystal structure. This is done by the Bragg equation $n\lambda = 2d\sin(\theta)$, which derives from the condition of constructive interference from the scattered planar light wave of neighboring scattering centers. Knowing the wavelength of the light λ and the diffraction order n, the distance of lattice planes d is calcualted. d is equal to the lattice constant c, if the crystalline structure of the sample is aligned to the sample surface, as shown in Fig. 1.3.1.

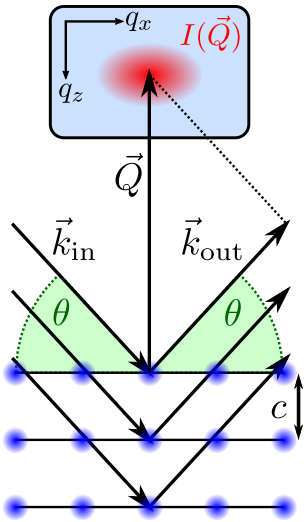

Figure 1.3.1: **Schematic of the Bragg- and Laue diffraction.** The incident X-rays ($\vec{k}_{\text{in}}$) are diffracted by the crystal lattice (blue circles) under the angle 2θ to $\vec{k}_{\text{out}}$. The scattering vector $\vec{Q}$ is perpindular to the diffracting planes and point to a small section of the reciprocal space with an intensity distribution $I(\vec{Q})$ in the inset.

The Bragg equation however is merely a special case of the more universal Laue condition [36]. It is possible to think of other geometric configurations which lead to a constructive interference, without the constraint of equal incident and emergent angles. In fact, in an infinitely large crystal lattice, which is a good approximation for solids, there are infinitely many equal or non-equal pairs of incident and emergent angles with which constructive interference is observed. Thus, Bragg's method was generalized to not measure the intensity as a function of the angle θ but as a function of the so called scattering vector $\vec{Q} = (q_x, q_y, q_z)$ which is defined by the change of the X-ray momentum $\vec{Q} := \Delta\vec{k} = \vec{k}_{\text{out}} - \vec{k}_{\text{in}}$, see Fig. 1.3.1 [36]. This ensuing three dimensional space of possible scattering vectors $\vec{Q}$ is called the reciprocal space. Scanning the reciprocal space with different combinations of $\vec{k}_{\text{in}}$ and $\vec{k}_{\text{out}}$ leads to the observation of many local maxima of diffracted intensity, visualized by the red intensity distribution in the inset of Fig. 1.3.1. Those correspond to a certain set of parallel diffracting planes, to which the respective scattering vector is perpendicular. Moreover, the arrangement of those maxima is a lattice itself, the so called reciprocal lattice, whose lattice spacing is directly linked to the inverse of the spacing of the crystal structure in real space [36]. Ultimately, a theoretical scan of the whole reciprocal space of a solid is comparable to a Fourier transformation of the scattering probability's spatial distribution, and thus the spatial distribution of the electron density and by extend the atomic positions or the actual crystal lattice [36]. Other than the Bragg equation, which associates a certain angle under which constructive interference is observed, to a lattice spacing, the Laue condition does this in all 3 dimensions. It states, that a local maximum of scattered intensity $I(\vec{Q})$ is observed, if the scattering vector equals a reciprocal lattice vector, i.e. $\vec{Q} = \vec{G}$. Besides, the Laue condition offers the possibility to add quantum mechanical momenta to the scattering process, for example from phonons [37]. With that, scattering processes with quasi-particles can be included in the Laue model.

The experimental observable of X-ray diffraction is therefore the intensity distribution in the recip-

rocal space, i.e. the intensity as a function of the scattering vector $I(\vec{Q})$. On a reciprocal lattice vector ($\vec{Q} = \vec{G}$), the intensity reaches a local maximum which is quantified by three variables: the position, the amplitude and the width [1]. The first is directly linked to the lattice constant. The other two are related to the structure factor and the lattice sum, i.e. atomic positions in the unit cell and the coherence length of the scattering lattice. In this work, I mainly focus on the position of the Bragg reflections in the reciprocal space as changes to the position of the diffraction maxima directly correspond to changes of the lattice constants. The main observable is thus the strain $\epsilon := \frac{\Delta c}{c}$, the realtive change of the lattice constant.

1.3.2 Pump-probe technique and UXRD

Now, after discussing how to extract the lattice constant of solids via X-ray diffraction, this experimental method needs an upgrade to measure the change of the lattice constant on an ultrafast timescale. This is done by the so called pump-probe technique, where an intense ultrashort laser pulse excites the sample and a second, usually far less intense ultrashort laser pulse probes the sample at a certain delay [38]. This process is repeated thousands to hundreds of thousands of times per second, depending on the repetition rate of the ultrashort laser system. The pulse duration of the laserpulses usually reaches from 10 to 1000 fs in contemporary research. The delay of the two laser pulses is continuously scanned on a femto- to nanosecond timescale to monitor the change of the probe signal after excitation. In an all-optical setup, the changes of specific parameters of the probe pulse after excitation of the sample are measured, such as the transmission, reflection or polarization. With this, is it possible to observe changes in the electron-, phonon- or spin-subsystem on an ultrafast timescale. It is even possible to detect the lattice response by optical means. However, in ultrafast X-ray diffraction experiments, the probe pulse is a short X-ray pulse, not an optical light pulse. The X-ray pulse is diffracted from the lattice, capturing the current state of the lattice according to X-ray diffraction [1, 2, 4].

As it took many years to realize the generation of intense ultrashort laser pulses in the visible, infrared or ultraviolet regime, the biggest technological hurdle for UXRD is the provision of ultrashort X-ray pulses. Synchrotrons were the first source of nano- and picosecond X-ray pulses but a pulse duration of 10 or even 1 ps is not feasible in state-of-the-art synchrotrons. The only sub-picosecond X-ray sources are slicing beamlines at synchrotrons, free electron lasers or laser driven plasma X-ray sources (PXS). I mainly used the latter for the UXRD measurements in this thesis and a detailed experimental overview of the PXS of the UDKM group at the University of Potsdam is given in Sec. 2.1.2 and the given references. With the PXS, we are able to generate X-ray pulses with a pulse duration below 200 fs. We use those to measure the lattice constant as a function of the delay to the optical pump pulse, yielding a sub-picosecond temporal resolution of the lattice dynamics upon femtosecond photoexcitation in thin films.

1.3.3 Temperature and strain modeling

The modeling to fit the data collected by the UXRD measurements is usually performed with a comprehensive multi-temperature model in combination with a one-dimensional model of masses and springs, provided by the udkm1Dsim-toolbox [39, 40]. This collection of MATLAB or PYTHON routines was programmed and developed by former and current members of the UDKM group of the University of Potsdam, in particular Daniel Schick. With the use of thermophysical parameters (see Tab. 2.2.1) it is possible to simulate a multi-temperature sample system spatio-temporally. Furthermore, the elastic response of the lattice is calculated with a simple but unit-cell resolved basic version of the Grüneisen model which results in a spatio-temporal strain distribution which can be fitted to the measurements. All the modeling is one dimensional, because an in-plane dynamic of the thin films can be neglected, since the probe spot is usually much smaller than the area excited by the pump pulse. The measured data can be thus modeled under the assumption of a homogeneous in-plane excitation, leaving behind one dimension in which dynamics occur; out-of-plane. Additionally, the toolbox offers the possibility to kinetically or dynamically simulate the time-resolved specular X-ray diffraction signal of the sample.

Chapter 2

Results of the PhD

In this chapter I will present the main results and findings of my studies. Those are on one side the technological advancements I propelled by introducing reciprocal space slicing and by the manifold combination of ultrafast X-ray diffraction and time resolved magneto-optical Kerr Effect measuremnts. On the other side, I used my expertise about the latter conjunction to analyze the role of sound and heat in Bi:YIG, which are the origins of the various ultrafast magnetization dynamics of the much investigated ferromagnetic insulator.

2.1 Advancing Ultrafast X-ray diffraction

Ultrafast X-ray diffraction is a tool to monitor the lattice dynamics of crystalline nanostructures upon femtosecond laser excitation [1, 2, 3, 4]. The deposited energy triggers a spatiotemporal distortion of the crystal lattice which is quantified by the strain, the relative change of the lattice constant at any given point in time and space. Analyzing the strain on a femto- to nanosecond timescale yields insights about the energy redistribution and transport phenomena on the nanoscale.

In this section, I will give an overview of my contributions to the field of ultrafast X-ray diffraction during my PhD studies in the UDKM joint research group at the University of Potsdam and the Helmholtz Zentrum Berlin. The first is to speed up experiments by reciprocal space slicing as a time-efficient alternative for conventional reciprocal space mapping on the one hand. The second advancement aims at making UXRD useful in the ultrafast magnetism comunity. To this end, we started the combination of ultrafast X-ray diffraction with time resolved magneto-optical Kerr effect measurements at the same experimental setup, ensuring identical excitation conditions.

2.1.1 Reciprocal Space Slicing

Reciprocal space slicing (RSS) is an experimental technique which allows a significantly faster assessment of strain in quasi-static and ultrafast X-ray diffraction experiments compared to conventional full reciprocal space mapping [41, 42, 43, 44]. Employing line- or area detectors in combination with a fixed angle geometry, RSS reduces the measurement time for time- or temperature resolved strain signatures by up to an order of magnitude. Thus it is essential for diffraction experiments at large scale facilities such as free electron lasers and synchrotrons as measurement time there is a costly and scarce resource. Even more, this applies to the Plasma X-ray Source setup used during my thesis, since the intensity of the X-rays is comparatively low.

To understand the working principle and advantages of RSS which are described in detail in publication VI, it is instructive to compare it to conventional reciprocal space mapping. When using the latter for strain assessment, the reciprocal space in the vicinity of a reciprocal lattice point is scanned by rocking the sample by the angle ω and moving the detector by the angle 2θ with respect to the incident X-ray beam, see green area in Fig. 2.1.1 a) [42, 43]. Doing so before and while the lattice dynamics occur, two reciprocal space maps (RSMs) can be compared to determine the position change Δq_z of the reciprocal lattice point in reciprocal space, which is directly linked to the average strain [45]. This takes a comparably long amount of time since the goniometer of the diffraction setup is moved multiple times for each RSM. However, the necessary ingredient for RSS to work is already utilized in most reciprocal space mapping procedures, which is a line or area detector [44]. As seen in Fig. 2.1.1 a), the green lines indicate the subsets of the reciprocal space for which the diffracted intensity is recorded simultaneously by the position sensitive detector. Moreover, those subsets do always have a certain q_z and q_x range which allows the detection of a moving reciprocal lattice point without moving the detector or the sample.

This idea is illustrated in Fig. 2.1.1 b), where a fixed detection geometry results in a single and one-dimensional subset of the reciprocal space being monitored, the so called reciprocal space slice, indicated by the green detector line. The pixels on the detector measure the diffracted intensity for a fixed range of 2θ angles with a fixed ω angle and cut intensity distribution $I(q_x, q_z)$ (red shaded area) in the center of the reciprocal lattice point. In this configuration, the maximum of the integrated intensity along q_x is at the same q_z value as the maximum of the RSM, as visualized by the inset diagram in Fig. 2.1.1 b). A shift of the reciprocal lattice point by Δq_z also results in a shift of the intensity distribution measured by the fixed detector line $\Delta q_{z,D}$. However, the observed shift in this configuration is always smaller than the actual Δq_z of the reciprocal lattice point. This is due to the fact that the monitored reciprocal space slice is always inclined approximately by the diffraction angle ω and thus cuts the shifted intensity distribution off center [36, 41]. This is shown in Fig. 2.1.1 b), where the green detector line intersects the 4th dashed, red contour line of the shifted intensity distribution at q_x and q_z larger than the center.

The scaling factor S between the observed shift $\Delta q_{z,D}$ and the actual shift Δq_z can be calculated and mainly depends on the Bragg diffraction angle θ_B and the intensity distribution widths σ_x and σ_z of the measured reciprocal lattice point.

I have shown, that S is close to one for small diffraction angles and larger widths along q_x compared to q_z, which makes RSS useful in those cases. Also, Δq_z needs to be smaller than the size of the reciprocal space splice monitored by the detector and the width of the intensity distribution. Otherwise, the reciprocal lattice point moves out of the detection range or the intensity becomes too small to measure. In other words, RSS is especially useful for hard X-ray experiments on thin films, since the scattering angles are small and the widths of the intensity distributions are significantly larger than those of bulk single crystals. During my studies I always worked with hard X-rays and thin film heterostructes and almost never encountered the problem of a shift being too large so that the reciprocal lattice point was moving out of the monitored reciprocal space slice. The strain and the relative shift likewise rarely exceed a few permille which is why every single strain assessment in the published articles I to VI and VIII presented in this thesis was done via the RSS technique, unless stated otherwise. Exceptions for the use of reciprocal space slicing in our group and thus falling back on to reciprocal space mapping are predominantly the recent studies about $SrRuO_3$ and FeRh (unpublished) thin films lead by Maximilian Mattern [46]. There, large diffraction angles and consequently large RSS scaling factors significantly lower the signal-to-noise contrast, which renders RSS suboptimal in those special situations.

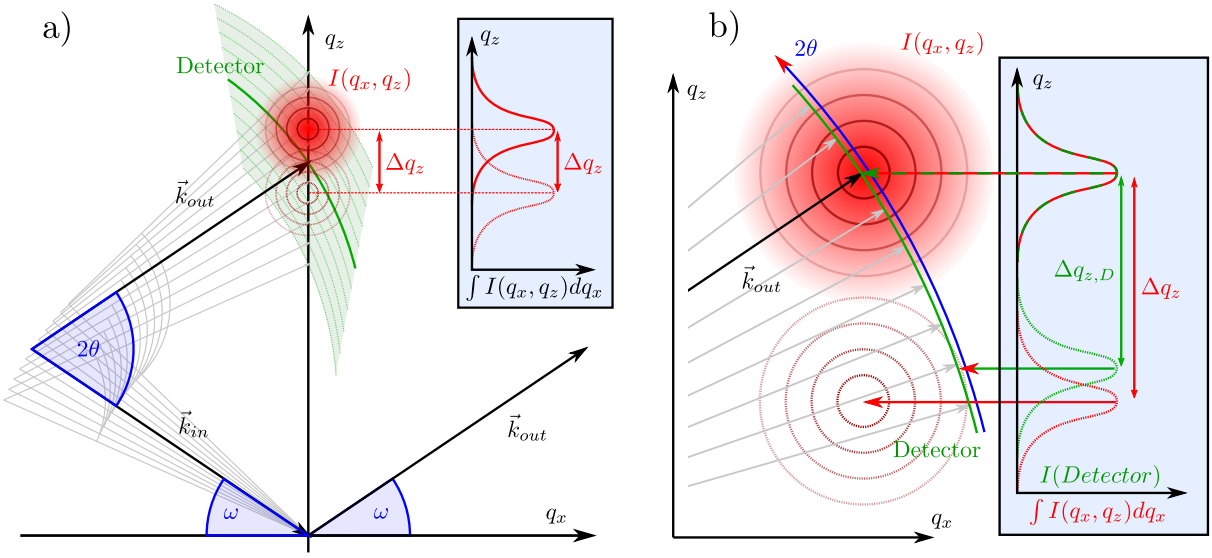

Figure 2.1.1: **Comparison of a): conventional reciprocal space mapping and b): reciprocal space slicing.** In **a)**, a symmetrical scattering geometry in the reciprocal space is depicted. The red area with concentric contour lines is the measured intensity distribution $I(q_x, q_z)$ in vicinity to the reciprocal lattice point. The contour lines shifted by Δq_z indicate the positional change of the lattice point due to strain. The green area is the area scanned by the green detector line during a reciprocal space scan, where ω and 2θ are moved in conjunction. The righthand diagram shows the integrated intensity of the diffracted intensity in reciprocal space for the two positions of the reciprocal lattice point. A close-up of the reciprocal lattice points and the detector line is depicted in **b)**. The detector measures the intensity in the reciprocal space at all points on the green line which thus acts as a 2θ-axis. In the righthand diagram, the intensity measured by the detector is compared to the integrated intensity of the reciprocal space for both positions of the reciprocal lattice point.

2.1.2 Combining UXRD and tr-MOKE

UXRD probes the crystal lattice and temperature and the tr-MOKE quantifies the magnetization change of a specimen [47, 48]. The combination of the two is particularly useful, since it yields experimental data sets which validate models encompassing both subsystems of solids and their interactions. This contains coherent and incoherent phonon dynamics, i.e. strain waves, lattice heating and thermal expansion [34], coherent and incoherent magnon dynamics, i.e. spin waves and thermally induced demagnetization and anisotropy changes [19]. Additionally, these models include phonon-magnon interactions such as (inverse) magnetostriction [7] and the thermodynamics of the coupled phonon and magnon heat-baths [11]; All on an ultrafast timescale. When conducting experiments combining UXRD and tr-MOKE under identical excitation conditions, it is even possible to quantify phonon-magnon coupling strengths and time constants of various materials on a picosecond timescale.

I almost exclusively concerned myself with the investigation of magnetic materials such as the giant magnetostrictive ferrimagnet $TbFe_2$ (I), the magnetostrictive ferro- and antiferromagnet Dysprosium (II), the Invar-like ferromagnet FePt (IV) and Bi:YIG (III, V, VII, VIII), which exhibits a multitude of spin or magnetization dynamics on the picosecond timescale, see Sec. 2.2. While I was mostly responsible for the execution of the UXRD experiments and the subsequent data analysis, my colleagues and coworkers measured and modeled the magnetic dynamics by tr-MOKE measurements. Together, we were able to provide comprehensive insights about the interactions between the lattice and magnetic dynamics.

In article I we are able to allocate the periodic magnetization changes of a thin $TbFe_2$ film upon femtosecond laser excitation to a train of longitudinal strain pulses. We demonstrate, that due to inverse giant magnetostriction, the strain pulses change the magnetization state of the probed volume linearly with coincidental sign and amplitude [49, 50]. On the contrary, we observe in publication II that an energy entry into the magnetic subsystem of Dysprosium modifies the shape of the strain pulses succeeding a femtosecond laser excitation. The magnetostriction is modeled by a contractive stress originating from the spin system which counteracts the thermal expansion of the lattice, which is extensively discussed in the works of my colleague Alexander von Reppert [51, 52, 53]. A similar competition is discussed in article IV, as thin films of the technological relevant and Invar-like FePt with different morphologies yield contrasting strain responses upon laser excitation. Employing micromagnetic finite-element modeling, the strongly pump energy density dependent picosecond strain signatures are rationalized with a negative spin stress on the lattice [20, 54]. Anticipating the in-depth discussion about magnetoacoustics in Bi:YIG in Sec. 2.2, the publications III, V and VII demonstrate the role of the temperature and strain dynamics as well as the means of manipulation to trigger magnetic dynamics and spin waves in Bi:YIG [19, 29, 55].

However, one aspect remained a challenge in some cases. Since the UXRD and tr-MOKE measurements presented in this work were always measured in different laboratories, a quantitative comparison can be difficult due to inevitably differing experimental conditions. Different laser characteristics, pump angles and spot sizes as well as probe spots give rise to the uncertainty of pump energy densities and material properties which are parameters used in the modeling. Consequently, we decided to combine UXRD and tr-MOKE at a single experimental setup to propel future investigations such as the comparison of ultrafast thermometry via thermal expansion and the Debye-Waller effect as well as ultrafast de- and remagnetiaztion.

To my knowledge, the combination of UXRD and tr-MOKE at a single experimental setup is the first of its kind, although all-optical strain assessment in conjunction with tr-MOKE was performed already. However, my contributions illustrate that UXRD has mainly two upsides compared to all-optical strain-assessment via Brillouin scattering or transient reflection analysis. Those are the simultaneous collective and selective probing possibilities in thin film heterostructures. On the one hand, the X-ray probe penetrates the whole sample, so we can access every layer of the sample and are not mainly sensitive to highly reflective interfaces or just the surface in the case for metals and semiconductors. On the other

hand, the X-ray probe is diffracted to different Bragg angles for each unique crystalline structure, i.e. the different layers. Thus, UXRD simultaneously yields the strain transients for each individual layer independently, whereas the reflection or transmission signal in all-optical measurements can be a convolution of the signals from several layers and interfaces, and some buried layers may even be optically inaccessible.

I helped implementing and commissioning a tr-MOKE setup into the already existing UXRD setup in the PXS laboratory of the UDKM group at the University of Potsdam. The design and construction was spearheaded and executed mainly by Jan-Etienne Pudell during his PhD studies. An explicitly detailed and true to scale technical overview of the complete experimental setup is presented in his thesis [56]. I display a sketch of the experimental setup in Fig.2.1.2 and a short description to provide sufficient understanding of the mechanics and capabilities of the experimental setup in the scope of this thesis.

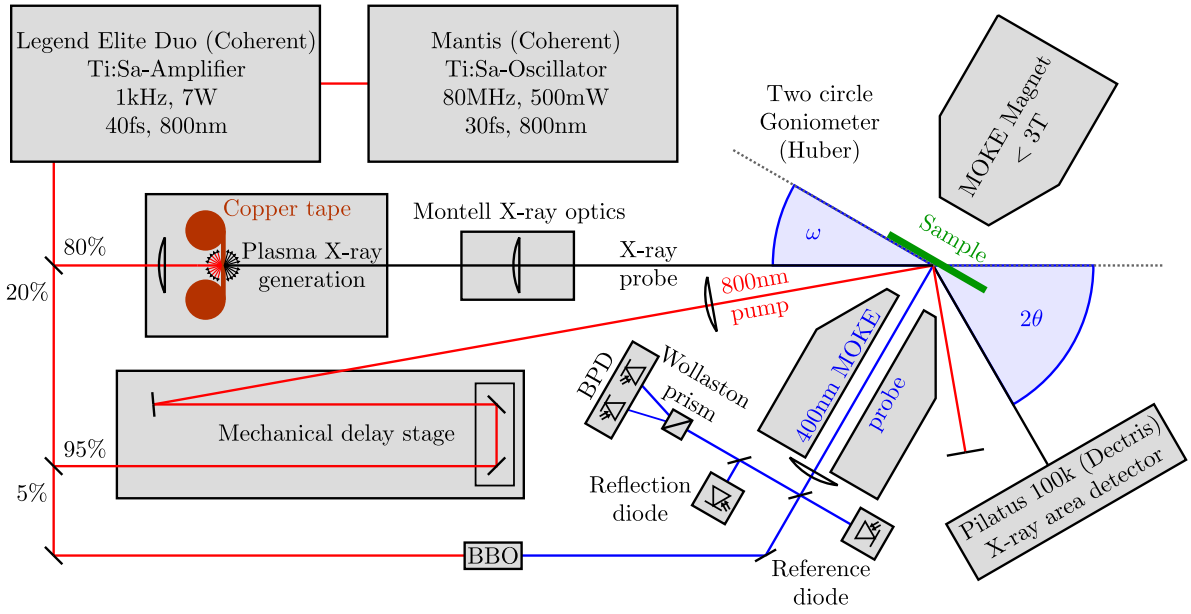

Figure 2.1.2: **Sketch of the combined experimental UXRD and tr-MOKE setup in the PXS laboratory at the university of Potsdam:** The Ti:Sa oscillator provides femtosecond 800 nm laser pulses to the two-stage amplifier, which generates 7 mJ pulses at a 1 kHz repetition rate via chirped pulse amplification. 80% of the laser power output is used for the X-ray pulse generation as the laser is focused onto a 15 μm copper tape producing copper plasma in vacuum and generating femtosecond X-ray pulses [57]. Those are focused with Montell optics [58] onto the sample in the center of the goniometer and the diffracted intensity is measured by the Pilatus area detector to probe the crystal lattice. To trigger ultrafast dynamics in the samples, up to 20% of the laser power is sent across a mechanical delay stage and focused onto the sample. 5% of the designated pump beam is separated and transformed via 2nd harmonic generation in a beta-barium borate (BBO) crystal into the 400 nm tr-MOKE probe. It is focused through one of the two poles of the magnet perpendicular onto the sample, the reflection is split up by a Wollaston prism and a balanced photo diode (BPD) detects changes in the polarization, which is a measure for the magnetic state of the sample due to the magneto-optical Kerr effect.

The UXRD setup in at the UDKM group at the University of Potsdam employs a laser-driven plasma X-ray source (PXS) for femtosecond x-ray diffraction [59, 60, 61]. With this, it is possible to generate up to 2 Mcounts/s of photon flux of the Cu-$K_{\alpha 1}$ and -$K_{\alpha 2}$ lines at 1.54 pm with a duration down to 100 fs at a 1 kHz repetition rate [57]. The X-rays are focused with a convergence of 0.3° onto the sample in the center of the goniometer with an angular resolution below one arcsecond and an angular range of 120°. The diffracted X-ray intensity is measured by the Pilatus 100k area detector (Dectris) with 487×195 pixels and a pixelsize of 172 μm which can be placed at a distance of 0.1 to 2 m from the sample. The

X-ray probe spot size is 0.3 mm measured at full width at half maximum (FWHM). The temporal delay between pump and probe pulse is set with the mechanical delay stage of the pump beam, which reaches up to 4 ns with an accuracy of 50 fs. The pump beam is focussed onto the sample with a variable spotsize of 2.5 mm to 0.5 mm set by a lens telescope. The incident pump energy density is set with a reflection polarizer with a range of 0.1 to 150 mJ/cm^2.

A detailed description of the tr-MOKE portion of the setup and its specifications can be found in the PhD thesis of Jan-Etienne Pudell and Lisa Willig, since the tr-MOKE setup is in principle a copy of the setup which she constructed and commissioned during her PhD studies in our group [56, 62]. We are solely able to pump and probe from the frontside of the sample and to perform polar tr-MOKE measurements, so the setup is exclusively sensitive to out-of-plane magnetization changes. The probe spot size is comparable with the X-ray spot at 0.3 mm and the pulse energy can be set by a waveplate-polarizer combination right before the 2nd harmonic generation and is optimally set to 0.1 μJ. With the installed magnet, it is possible to reach a homogeneous magnetic field of up to 2.5 A/m (3 T), which is sufficient to saturate the thin films of $TbFe_2$, Bi:YIG and FePt out-of-plane.

2.2 Ultrafast Magnetoacoustics in Bi:YIG

The picosecond magnetization dynamics of YIG and in particular Bi:YIG as well as other iron garnets have been rigorously investigated up to the present day [55, 63, 64, 65, 66, 67, 68]. Intelligently designed, Bi:YIG combines the low magnon damping of YIG with a large magneto-optical contrast due to the Bi-substitution, rendering it a workhorse in the research field of ultrafast spin dynamics [69, 70]. The ferromagnetic insulator exhibits reliable and easily manipulated response of the spin system in the form of a collective and coherent motion of the spins, so called spin waves [19, 29].

I studied the Bi:YIG thin film system with ultrafast X-ray diffraction to ascertain the role of coherent phonon packets and incoherent phonon excitations, i.e. sound waves and lattice heating, in the excitation of the coherent magnetization dynamics. Both were thought to be important, and we were able to confirm this. Additionally, we quantified the share and efficiency of both processes.

In this section I will present the lattice dynamics of Bi:YIG thin films upon femtosecond laser excitation. The excitation of the lattice, and subsequently the magnetization dynamics, are done directly via one or two photon absorption or indirectly with a metallic transducer. I will present both studies separately and eventually bring them together with a comprehensive model of the magnetoacoustic interactions in Bi:YIG.

2.2.1 Direct excitation via one and two photon absorption

Exciting a thin film with a femtosecond laser pulse eventually yields an ultrafast spatio-temporal deformation of the lattice which is in any case a superposition of at least two tightly connected but distinguishable phenomena; sound and heat [17]. In photoexcited Bi:YIG, disregarding magnetic and electronic stresses on the lattice, some of the energy absorbed by the electrons of the solid is transformed via electron-phonon coupling into phonons. The increased phonon population associated with an increase of the temperature exerts a stress on the lattice itself, the phonon pressure. According to the elasticity of solids, this results in an expansion, which is the thermal expansion in equilibrium [5]. Assuming a homogeneously excited volume, the expansion can only occur first at the surface of the material, as the pressure is isotropic. With the release of the stress into strain, the adjacent volume can subsequently expand. This strain wave propagates with the speed of sound, determined by the elastic properties of the material, deeper into the volume. To summarize, femtosecond laser excitation leads to thermal expansion of the sample due to heat and coherent phonon wave packets, i.e. strain pulses or sound waves [17, 71].

My experimental findings confirm a thermal expansion on the nanosecond time scale and picosecond bipolar strain pulses. In publication III, we present a comprehensive study of the picosecond strain dynamics in 150 and 135 nm thin Bi:YIG films measured at the PXS setup at the University of Potsdam and in article VII we show additional lattice dynamics measured at the KMC3-XPP-Beamline at BESSY II at HZB. Here, I describe and explain the mechanics of the picosecond strain dynamics in Bi:YIG by consulting the UXRD data and the results of a one temperature model and a one dimensional model of masses and springs, which are fitted to the data [39, 40]. The data and the fit are displayed in Fig. 2.2.1a), the spatio-temporal temperature and strain distributions which are calibrated by the data are displayed in Fig. 2.2.1c) and b), respectively. A schematic sketch of the sample and the pump-probe technique is shown in Fig. 2.2.1d).

The femtosecond laser excitation of the Bi:YIG thin film results in a sub-picosecond expansive response of the layer which linearly increases during the first few picoseconds to a local maximum, decreases subsequently to a quasi-static level of two thirds of the preceeding maximum and eventually decreases further on a nanosecond timescale, see Fig. 2.2.1a). The initial increasing expansion originates from the thermal stress acting onto the lattice, due to the energy deposited by the laser pulse and increasing the phonon temperature, see Fig. 2.2.1c). Since the laser-induced phonon pressure is more or less homogeneous in Bi:YIG, but essentially zero in air and the transparent, non-absorbing substrate, the expansion of the

lattice first takes place at the sample surface and the substrate interface, see Fig. 2.2.1b) [17]. Because this positive strain relieves the thermal stress on the one side, adjacent unit cells on the other side expand subsequently, proceeding deeper into the layer. The motion of the expansion is classified as a strain wave and is limited by the sound velocity in Bi:YIG $v_{s,B}$ [71]. Thus, the timing of the maximum average strain t_{max} is reached, when the strain waves from both sides of the layer traversed to the other side, leading to $t_{max} = \frac{d_B}{v_{s,B}}$, where d_B is the Bi:YIG layer thickness. At delays larger than t_{max}, the expansive strain wave from the sample surface is ejected into the substrate, trailing behind the initial compression and composing the bipolar strain pulse which propagates deeper into the sample substrate. The exit of the expansive wave denotes the decrease of the average strain in Bi:YIG after t_{max} which plateaus at the thermal expansion level corresponding to the increased phonon temperature in the layer. Eventually, the strain decreases on a nanosecond timescale due to a Fourier heat flow from the Bi:YIG layer into the substrate, triggered by the thermal gradient. The thermal conduction is slow compared to the acoustic processes, which is highlighted by the relatively constant temperature distribution in Fig. 2.2.1c). To keep the model as simple as possible, I did not include an interface heat resistance which slows down the heat in nanoscale heat transport [72]. This is why the strain decrease on a nanosecond timescale is slightly overestimated, which however does not alter the modeling of the magnetization dynamics in Sec. 2.2.3.

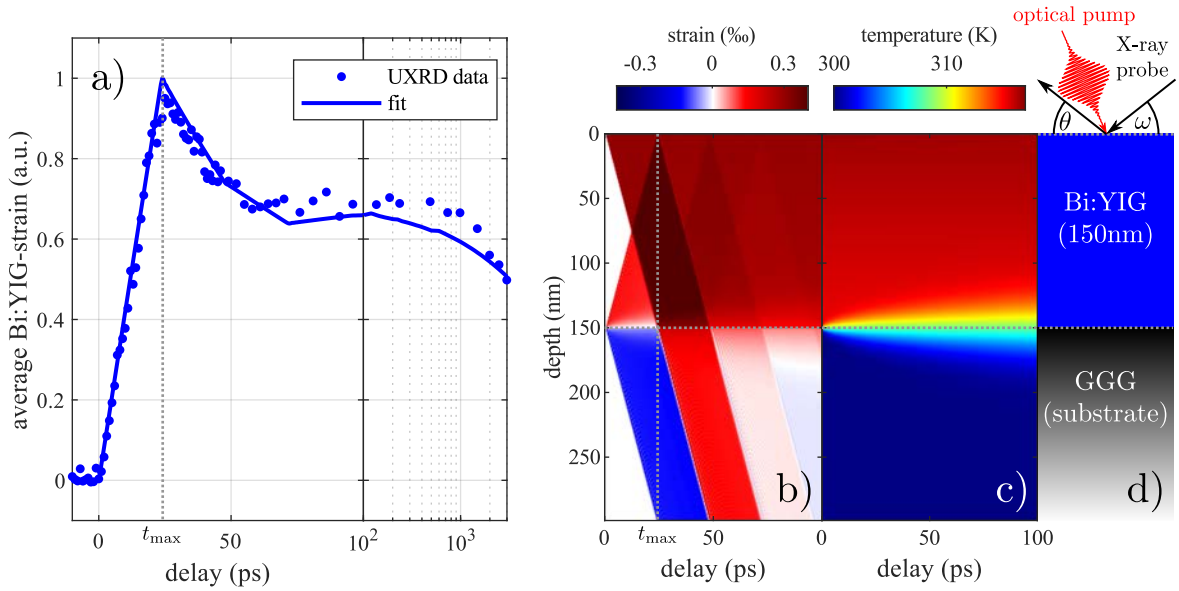

Figure 2.2.1: **a)**: Strain inside the Bi:YIG layer upon photoexcitation with 800 nm pump pulses, scaled to the maximum. The dots are the weighted average of the pulse duration series UXRD measurements from article III (Fig. 2c)). The line is the calculated average strain calculated from the spatio-temporal strain distribution in **b)**. **b)**: Modeled one dimensional depth resolved strain dynamics of Bi:YIG upon photoexcitation calculated with the udkm1d-sim toolbox using the parameters in Tab. 2.2.1. **c)**: Corresponding temperature distribution upon excitation. **d)**: Sketch of the sample structure and the pump-probe geometry for UXRD.

Going more into detail, the modeling is done with the udkm1D-sim toolbox which is fed with several parameters of the used materials, which are given in Tab. 2.2.1 [39, 40]. One of the parameters is the optical penetration depth of the pump pulse which is directly translated into the initial temperature profile of the heterostructure. In turn, this modifies the stress profile simulated with the toolbox and consequently the strain dynamics, in particular the shape of the strain pulse and the average strain transient displayed in Fig. 2.2.1a). The measured strain dynamics of publication III exhibit a linear increase after excitation and can be fitted with an optical penetration depth of 170 nm for 400 nm pump pulses. I used a penetration depth of 1800 nm for the 800 nm laser excitation, which exceeds the layer thickness

of 150 nm by far, resulting in the nearly homogeneous excitation of the layer. This corresponds to the absorption profile for a two photon absorption process with an incident intensity of 1 TW/cm^2, which was used in the measurements.

I have shown with article III and VII, that significant strain dynamics in thin Bi:YIG layers can be triggered directly with the full range of the visible spectrum. Using 400 nm pump pulses, thin Bi:YIG layers exhibit similar ultrafast lattice responses to common metal transducers although the excitation process is different. The strain amplitude is set linearly with the incident pump energy density in this case as a very rapid electron-phonon coupling heats the phonons. Using 800 nm pump pulses, the insulator can only be efficiently excited via a two photon absorption process at intensities above 0.1 TW/cm^2. Thus, the generated strain is depends quadratically on the pump energy density and inversely proportional to the pulse duration. Using 512 nm pulses, it is even possible to change the amount of absorbed energy by simply changing the polarization state of the pump pulse. In this one photon absorption process, the helicity directly alters the absorption efficiency due to the magnetic circular dichroism of Bi:YIG and consequently the strain amplitude. Those various possibilities to control and manipulate the photoexcited strain render Bi:YIG a promising candidate in the field of ultrafast magnetiaztion dynamics and its applications.

2.2.2 Transducer mediated indirect excitation via strain waves

Besides the lattice dynamics of directly photoexcited thin Bi:YIG films, as discussed in the previous section, I also analyzed the pico- to nanosecond strain dynamics of indirectly excited thin films. In this case, the same Bi:YIG thin film is buried underneath a 5 nm Pt transducer on top of a 110 nm Cu thin film, see Fig. 2.2.2 d), so the influence of an injected strain pulse onto the magnetization dynamics can be examined. It has been shown, that the direct as well as the indirect excitation process trigger standing spin waves efficiently [19, 29]. The comparison of the lattice dynamics gives information on the share and efficiency of either coherent or incoherent phonons, i.e. strain waves or heat, in the spin wave generation.

With the experimental configuration shown in Fig. 2.2.2 d), I observe a single cycle biploar strain wave during the first 75 picoseconds and an increasing thermal expansion on the nanosecond timescale in the Bi:YIG layer upon femtosecond laser excitation of the Pt surface transducer, see Fig. 2.2.2 a). The Cu layer directly underneath the Pt transducer on the other side exhibits a lattice response which is to be expected of a regular metal transducer, which is homogeneously excited [17, 71]. Comparing the strain signature of the Cu layer in this case (Fig. 2.2.2a)) and the strain of the Bi:YIG layer in the case of direct excitation (Fig. 2.2.1a)), reveals an identical response upon excitation, although the excitation processes are different. Unfortunately, it was not possible to measure the strain of the Pt layer with UXRD, since the diffracted intensity was on the noise level. In a different study on a similar heterostructure of Pt/Cu/Ni, my colleagues were able to directly measure the strain have shown that the Pt transducer does in fact generate a short and high amplitude strain pulse [13]. However, to trigger magnetization dynamics, the Cu layer is the more relevant transducer. This is why I will first focus mainly on the Cu layer dynamics and later comment on the role of the thin Pt transducer.

I simulated the processes in the heterostructure again with the udkm1D-sim toolbox [39, 40]. To account for the heat transport in metals, I utilized a two temperature model of the electrons and phonons. I used the same parameters for Bi:YIG as in the direct excitation and the same parameters for Pt and Cu of previous works of my group with the exception of the Bi:YIG layer thickness (Tab. 2.2.1). It is changed to 135 nm because the sample growers removed a small amount of Bi:YIG to prepare the surface for the Cu deposition on top. The resulting spatio temporal lattice temperature and strain distribution are displayed in Fig. 2.2.2 c) and b), respectively. Qualitatively, the strain distribution of the direct excitation in the previous section (Fig. 2.2.1b)) and indirect excitation here (Fig. 2.2.2b)) are very much alike. The important difference is that in the previous case, Bi:YIG acts as a transducer, injecting a bipolar strain pulse into the substrate. Here, in the indirect case, Cu acts as the transducer, injecting a bipolar strain pulse into the Bi:YIG layer. The role of the transducer has shifted from Bi:YIG to

Cu, which is why the average strain of Bi:YIG in the direct excitation (Fig. 2.2.1a)) looks so similar to the average strain of Cu in the indirect excitation (Fig. 2.2.2a)). Here, I denote t_{min} as the point in time, when the average strain in Bi:YIG is minimal, which coincides with the time span in which only a compression propagates in Bi:YIG, see Fig.2.2.2 a) and b). At this delay, the average strain in the Cu layer is maximal, marking the time when the trailing, expansive part of the strain wave starts to traverse into the Bi:YIG layer, consequently increasing the average strain there. After the transition of the strain wave into the $Gd_3Ga_5O_{12}$ - Gadolinium Gallium-Garnet (GGG) substrate, the Bi:YIG lattice relaxes to an almost undistorted state, where the average strain is close to zero. A small portion of the layer is merely heated, resulting in a thermal expansion, which continuously increases on a nanosecond timescale, as the heat eventually flows into the layer, see Fig.2.2.2 c).

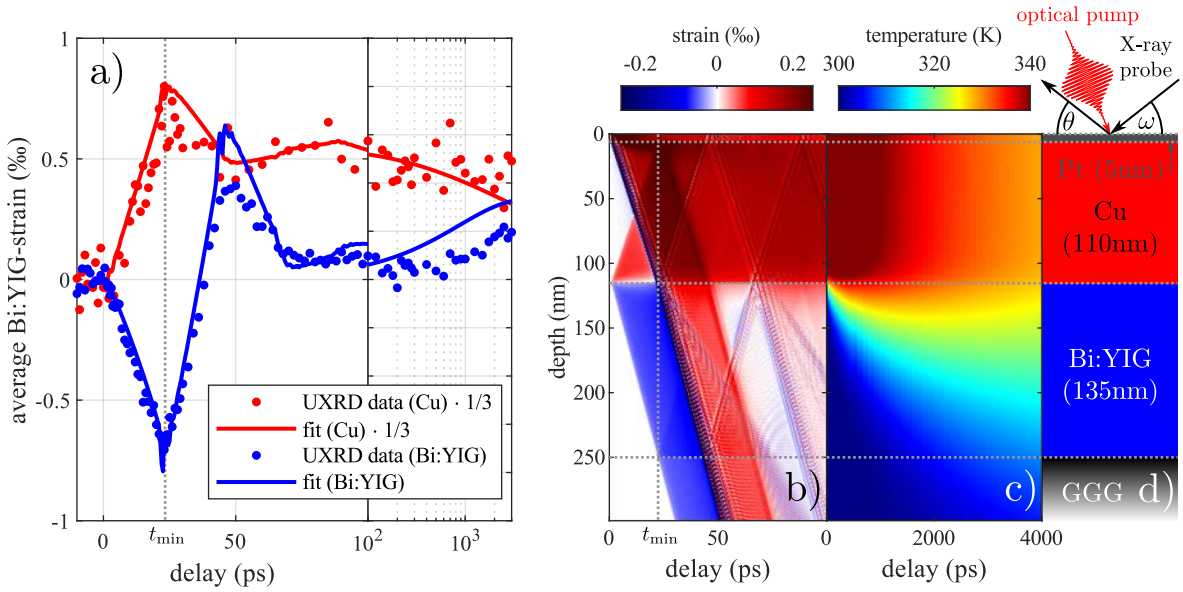

Figure 2.2.2: **a)**: Strain inside the Cu and Bi:YIG layer upon photoexcitation with 800 nm pump pulses, whereas the Cu transient are scaled with a factor of 1/3. The lines are the calculated average strains calculated from the spatio-temporal strain distribution in **b)** for each individual layer. **b)**: Modeled one dimensional depth resolved strain dynamics of the Pt/Cu/Bi:YIG heterostrucutre upon photoexcitation calculated with the udkm1d-sim toolbox using the parameters in Tab. 2.2.1. **c)**: Corresponding temperature distribution upon excitation. **d)**: Sketch of the sample structure and the pump-probe geometry for UXRD. The data and the simulation results in **a)**, **b)** and **c)** are the same as published article V (Fig. 1), but with a different layer thickness of $d_{\mathrm{Bi:YIG}} = 150$ nm, instead of 135 nm, used in the modeling.

To achieve a match of the model and the data, it is important to use a two temperature model in this case. With that, we visualized that the energy deposited initially mainly in the electrons of the Pt transducer is rapidly distributed over the whole Cu layer equally via electronic heat conduction. The strong electron-phonon coupling in Pt on a femtosecond time scale does in fact lead to a sub-picosecond expansion of the thin layer, injecting a strain pulse into Cu [13]. However, some of the pump energy is transported via electrons into the Cu layer, distributed equally within the first picosecond after excitation. This leads to an instantaneous rise of the lattice temperature of Cu due to electron-phonon coupling as if the Cu layer was homogeneously photoexcited. Consequently, at the interface to Bi:YIG, which does not receive energy immediately, the Cu layer reacts to the thermal stress with an expansion merely a picosecond after excitation, acting as a transducer and compressing the adjacent Bi:YIG layer. The strain pulse from the Pt layer is limited by the sound velocity in Cu and arrives at t_{min} in Bi:YIG. Thus, the initial strain dynamics in Bi:YIG can only be rationalized by an sub-picosecond electronic energy transport from Pt to Cu and a subsequent immediate expansion of Cu due to electronic and phononic pressure.

Initially, this sample structure was chosen to generate a short strain pulse with a large amplitude in Pt which then propagates through Cu into Bi:YIG to trigger magnetization dynamics [29]. The Cu layer was implemented as a isolation layer to suppress a direct optical excitation of Bi:YIG. Both intentions were met, but the electronic heat dynamics in Pt and Cu not only resulted in an additional much longer but less intense strain pulse but also to immediate although slow phonon heating in Bi:YIG, see Fig. 2.2.2 c). Without this study, those important facts might not have been considered in the generation process of spin waves in Bi:YIG.

	Pt	**Cu**	**Bi:YIG**	**GGG**
layer thickness d (nm)	5	110	150 (direct excitation) 135 (indirect excitation)	∞
sound velocity s_v ($\frac{\mathrm{nm}}{\mathrm{ps}}$)	4.2	5.2	6.3 [73]	6.3 [74]
opitcal penetration depth ξ (nm)	2.8	20	1800	∞
mass density ρ ($\frac{\mathrm{g}}{\mathrm{cm^3}}$)	21.4	9.0	5.9 [73]	7.1 [75]
linear thermal expansion α ($\frac{10^{-5}}{\mathrm{K}}$)	1.85	3.0	1.0 [76]	0.92 [76]
Poisson ratio	2.2	1.7	1.8 [77, 78]	1.8 [78]
phonon heat capacity C_{ph} ($\frac{\mathrm{J}}{\mathrm{kg\ K}}$)	133	384	570 [79]	381 [75]
phonon heat conductivity κ_{ph} ($\frac{\mathrm{W}}{\mathrm{m\ K}}$)	5.0	5.0	7.4 [79]	7.05 [75]
phonon Grüneisen constant Γ_{ph}	2.5	2.1	1 [80]	1 [80]
electron phonon coupling g ($\frac{\mathrm{PW}}{\mathrm{m^3K}}$)	400	63	-	-
Sommerfeld constant γ_{S} ($\frac{\mathrm{mJ}}{\mathrm{cm^3K^2}}$)	0.74	0.1	-	-
electronic heat conductivity κ_{el} ($\frac{\mathrm{W}}{\mathrm{m\ K}}$)	66	396	-	-
electronic Grüneisen constant Γ_{el}	0.9	1.1	-	-

Table 2.2.1: **Experimental, elastic and thermophysical parameters used in the udkm1Dsimtoolbox simulations.** The Poisson ratio is a factor to scale the strain arising from thermal expansion in ultrafast thin film experiments, as the system can be approximated as a one-dimensional if in-plane dynamics are not considered. The discrepancy of the Bi:YIG layer thickness comes from the surface preparation of the sample before Cu is put onto the Bi:YIG layer. The electronic parameters for Bi:YIG and GGG are empty, since those materials are insulators and thus do not contribute to the electronic energy and heat dynamics of the heterostructure. All parameters of Pt and Cu are set to the same parameters used in a previous study in our group, with a similar sample structure of Pt/Cu/Ni [13].

To conclude, I will shortly address the mismatches of the data and the modeling results. First, there is the overestimation of the heat flow out of the Cu layer into the Bi:YIG layer. This can be seen in Fig.2.2.2 a), where the calculated strain in Cu is smaller and in Bi:YIG is larger than the measured strain. This could be corrected by introducing an empirical interface resistivity for thermal transport. Acoustic reflections and other scattering mechanisms at the interface slow down the heat flow across material interfaces is slowed down which results in a slower heating and smaller effect of the thermal expansion for Bi:YIG [72]. The second mismatch of the modeling and the data is the asymmetrical shape of the bipolar strain pulse in the data, which is not reproduced by the simulation. This needs to be investigated further but possible reasons might be an increased scattering of the coherent phonons launched at the Pt/Cu interface due to a large incoherent phonon population due to heat or a mismatch of the acoustic impedances at the Cu/Bi:YIG interface, underestimating the reflection of the expansive strain wave.

On a side note, this analysis indicates the importance of buried detection layers in UXRD experiments to monitor and sample strain signatures in nanoscale heterostructes, as discussed in article I. This is

because there is no feature in the Bi:YIG UXRD data that suggests the passage of the short and intense strain pulse from the Pt layer thorugh Bi:YIG, in contrast to the study on a Pt/Cu/Ni hetero structure of our group [13]. Even the simulation, which clearly exhibits the bipolar strain pulse traversing through Cu, see Fig. 2.2.2 b), does not clearly exhibit the strain pulse in the average strain over the whole layer, see Fig. 2.2.2 a). The small ripples at t_{min} and 50 ps are the only signature of the Pt strain pulse and repeating the simulation without a Pt layer just results in the qualitatively same average strain signature with smooth extrema without the ripples. This effect is not detectable, since the layer is too thick for a short but strain pulse to change the average strain significantly. Also, the average strain due to the biploar strain pulse is zero, which makes it impossible to detect via the shift of the Bragg peak, when it is inside the layer. To find a remedy, it is practical to implement a significantly thinner layer with which it is possible to sample even short strain pulses.

2.2.3 Generation of standing spin waves with sound and heat

Having investigated the lattice response of Bi:YIG upon femtosecond laser excitation, I will now present the results of publication VIII, in which we disect the excitation process of standing spin waves observed with tr-MOKE via coherent and incoherent phonons observed with UXRD. This is done by first fitting the UXRD data with the modeling described in the previous two sections to generate the spatio-temporal temperature and strain profiles, $T(z,t)$ and $\epsilon(z,t)$. Those are subsequently implemented into a micromagnetic model, describing the effective field $H_{\mathrm{eff}}(z,t)$ in Bi:YIG, acting on the magnetization $\vec{m}(z,t)$ at any given point in time and space. Furthermore, utilizing the Landau-Lifschitz-Gilbert (LLG) equation, we simulate the expected spin dynamics and compare them in terms of a spectral analysis with the measured standing spin waves in Bi:YIG. All calculations concerning magnetization dynamics were done by Xi-Guang Wang from the Nonequilibrium Many-Body Systems group of Jamal Berakdar at the Martin-Luther-University Halle-Wittenberg [81]. A flow chart of this procedure is presented in Fig. 2.2.3. As we put the strain and temperature profiles into the micromagnetic modeling, we are able select very specific stimuli, for example exclusively a temperature increase without any strain dynamics. With this, it is possible isolate the impact of coherent or incoherent phonons on the spin excitations.

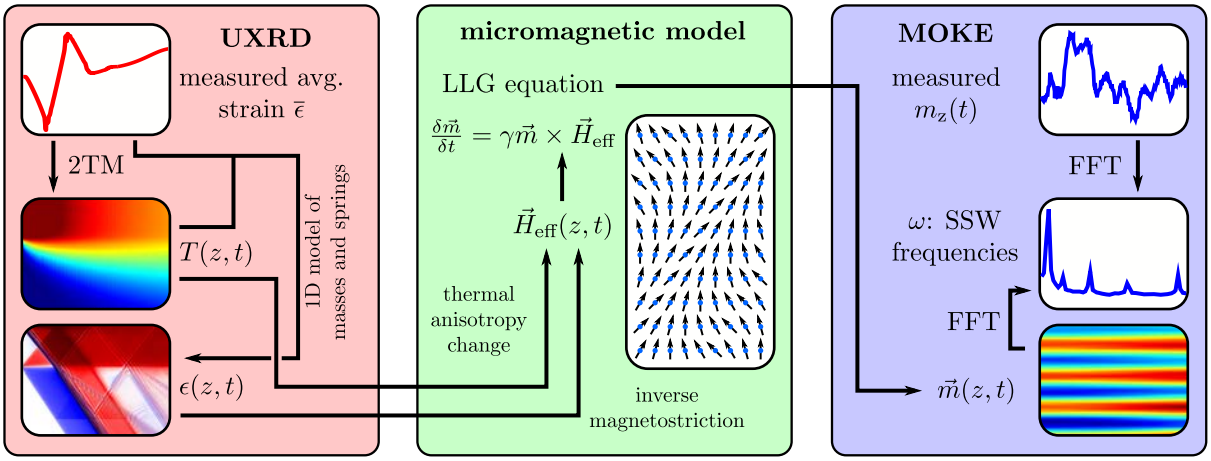

Figure 2.2.3: **Flowchart of the modeling process of SSWs in Bi:YIG thin films excited via coherent and incoherent phonons, see article [8].** The samples which exhibit SSWs are characterized with UXRD to generate spatio-temporal temperature and strain profiles which fit the data (red). Via anisotropy change and inverse magnetostriction, $T(z,t)$ and $\epsilon(z,t)$ modify the effective field which is part of the LLG equation (green). The latter is numerically solved to generate a spatio-temporal magnetization profile $\vec{m}(z,t)$. This is spectrally compared with the MOKE measurements (blue), conducted under similar excitation conditions as the UXRD measurements.

The initial question was to quantify the role of sound and heat in the generation of SSW in photoex-

cited Bi:YIG thin films. The UXRD studies show that an expansive strain pulse together with a nearly homogeneous phonon heating is introduced by the direct laser excitation. For the case of the indirect excitation, a bipolar strain wave is injected into the buried Bi:YIG thin film, accompanied by an instant phonon heating at the Cu/Bi:YIG interface. We show that the heating and the strain waves in both cases generate higher order SSWs in Bi:YIG. Also, we found that the two generation processes of sound and heat excite the ferromagnetic resonance mode (FMR) with opposite phases in both excitation configurations. This leads to a significant reduction of the FMR mode amplitude when considering both, the thermal anisotropy change due to phonon heating and the inverse magnetostriction due to the strain waves and thermal expansion. With this, we are able to model the relative amplitudes of the SSWs, since the FMR mode's amplitude has the same order of magnitude as the higher order modes.

Chapter 3

Articles

In this chapter, I will list all articles I authored or co-authored during my PhD studies. With that, I will shortly describe my contributions and those of my co-authors in the given publication. Also, I will comment on every article, which includes additional information and interpretations, references to contemporary research, emphasis of specific details and summaries of the main messages.

I Tracking picosecond strain pulses in heterostructures that exhibit giant magnetostriction

Steffen Peer Zeuschner, Tymur Parpiiev, Thomas Pezeril, Arnaud Hillion, Karine Dumesnil, Abdelmadjid Anane, Jan-Etienne Pudell, Lisa Willig, Matthias Rössle, Marc Herzog, Alexander von Reppert and Matias Bargheer

Structural Dynamics 6, 024302 (2019)

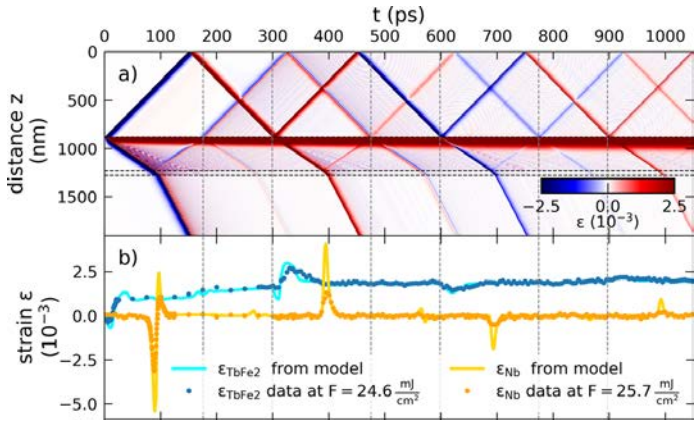

Abstract We combine ultrafast X-ray diffraction (UXRD) and time-resolved Magneto-Optical Kerr Effect (MOKE) measurements to monitor the strain pulses in laser-excited $TbFe_2$/Nb heterostructures. Spatial separation of the Nb detection layer from the laser excitation region allows for a background-free characterization of the laser-generated strain pulses. We clearly observe symmetric bipolar strain pulses if the excited $TbFe_2$ surface terminates the sample and a decomposition of the strain wavepacket into an asymmetric bipolar and a unipolar pulse, if a SiO_2 glass capping layer covers the excited $TbFe_2$ layer. The inverse magnetostriction of the temporally separated unipolar strain pulses in this sample leads to a MOKE signal that linearly depends on the strain pulse amplitude measured through UXRD. Linear chain model simulations accurately predict the timing and shape of UXRD and MOKE signals that are caused by the strain reflections from multiple interfaces in the heterostructure.

Contributions to the work

I performed the ultrafast X-ray diffraction experiments collaboratively with Alexander von Reppert and Jan-Etienne Pudell. Together with Alexander, I evaluated and displayed the data, performed the simulations with the udkm1D-Sim toolbox and wrote the manuscript. The timeresolved magneto-optical Kerr-Effect measurements were conducted by Tymur Parpiiev and the samples were provided by Karine Dumesnil and her group.

Comments

This article is the first of our group in which we actually combined UXRD and tr-MOKE results. We were able to show that the highly magnetostrictive $TbFe_2$ exhibits a linear response of the magnetization with the distortion of the lattice due to strain pulses, which we monitored with the buried Nb detection layer. The ultrasonic strain pulses arise, as it is usually the case in picosecond ultrasonics, from an ultrafast expansion of a transducer lattice due to heat [17, 71]. In this case, the transducer is $TbFe_2$ and the impact of the long lasting thermal expansion itself on the magnetization and consequently on the tr-MOKE signal was not discussed in detail in the paper. In contrast, we subtracted the thermal demagnetization background in the publication to filter out the coherent dynamics. However, I will now present a more complete investigation about the thermal dynamics of the lattice and the spin system with the assumption of linear inverse magnetostriction. With this, I can attribute a portion of the demagnetization to magnetostriction due to thermal expansion and the remaining part of the tr-MOKE signal to exactly two exponential decays with significantly different timescales which can be thought to

be two distinct spin heat flows.

To do so, I used the UXRD measurements of $TbFe_2$ and Nb presented in the paper to create a spatio-temporal strain map $\epsilon(z,t)$, which attributes a relative change of the lattice constant to any given point in space and time. This is done by fitting the data with the one-dimensional model of masses and springs of the udkm1Dsim-toolbox as displayed and discussed in the paper [39, 40]. An excerpt of the strain map is depicted in Fig. I.1c) next to the sample structure for orientation in Fig. I.1b). Assuming a linear dependence of the magnetization, and thus the tr-MOKE signal, on the strain, I weighted the strain map with the penetration profile of the tr-MOKE probe $S(z) := e^{(-z-d_1)/\xi}$, where $z = 0$ is the sample surface, z increases with the depth, $d_1 = 882$ nm is the Silicium Dioxide (SiO_2) layer thickness and $\xi = 18$ nm the tr-MOKE probe penetration depth, see Fig. I.1d). Since the intensity of the probe decreases with increasing depth, the sensitivity of the probe decreases accordingly. The penetration profile $S(z)$ thus acts as a sensitivity function to scale the measureable response in the tr-MOKE experiment, similar to the work of my colleague Tymur Parpiiev [50]. Subsequently, I integrated the weighted strain map over the $TbFe_2$ layer, from $z = d_1$ to $z = d_1 + d_2$, which results in the time dependent signal I_{ME} depicted in blue in Fig. I.1a). Immediately one recognizes the qualitative similarities between I_{ME} and the tr-MOKE signal, which are the exponential-like decay as well as the timing and relative amplitude of local extrema due to the strain pulses. With that, I_{ME} denotes the magnetoacoustic contribution to the tr-MOKE signal, assuming a linear inverse magnetostriction. Moreover, it is possible to fit the tr-MOKE signal completely by first scaling I_{ME} (blue transient) by the amplitude of the local strain pulse extrema at 300 and 600 ps seen in the tr-MOKE signal (black transient). Secondly, the difference I_{ME} and the tr-MOKE signal can be fitted by the sum of two exponential terms $A \cdot e^{-t/\tau_1} + B \cdot e^{-t/\tau_2}$ with $A = 0.56$, $B = 0.36$, $\tau_1 = 81$ ps and $\tau_2 = 830$ ps. As a crosscheck, the sum of I_{ME} and the two exponential functions is displayed (red) in Fig. I.1a) and precisely fits the tr-MOKE signal qualitatively and quantitatively.

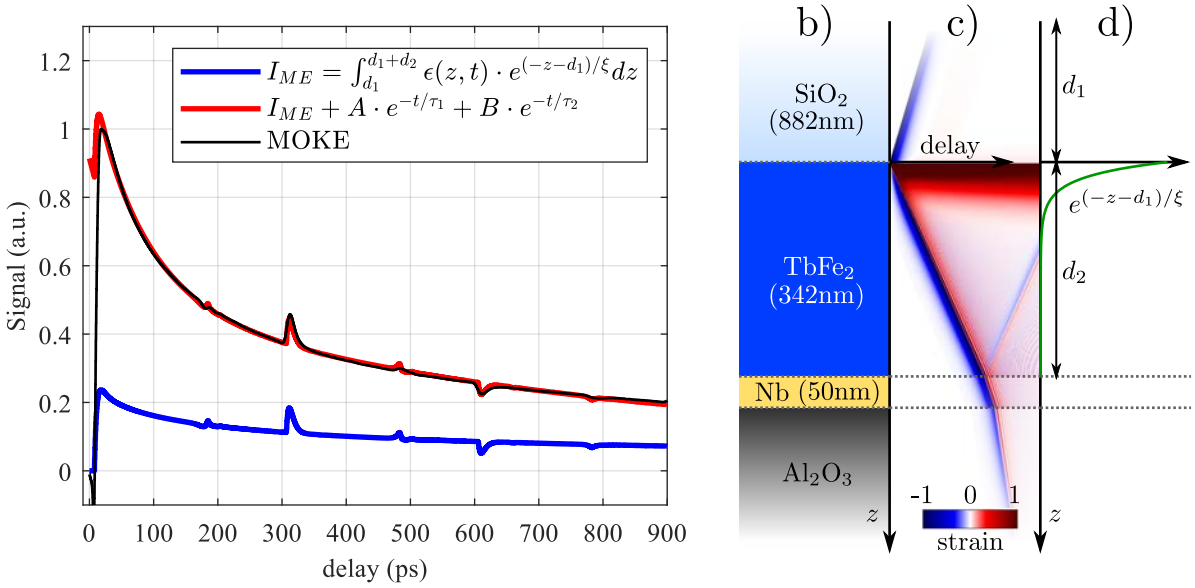

Figure I.1: **a):** Timeresolved signatures of the tr-MOKE measurement in black, the convolution of the strain map $\epsilon(z,t)$ inside the $TbFe_2$ layer ($d_1 < z < d_1 + d_2$) with the sensitivity function of the tr-MOKE probe ($e^{(-z-d_1)/\xi}$) in blue and with the addition of two exponential fitting terms in red. The convolution and the tr-MOKE signal are scaled to the amplitudes of the strain pulse echoes at 300 and 600 ps. **b):** Sketch of the sample structure along the depth (z), giving the material compositions and layer thicknesses. **c):** Spatio-temporal strain map $\epsilon(z,t)$ **d):** Sketch of the sensitivity function in green, where ξ is the optical penetration depth of the tr-MOKE probe and d_1 and d_2 are the layer thicknesses of SiO_2 and $TbFe_2$, respectively.

With this, I show that upon femtosecond laser excitation a significant portion of the magnetization change in $TbFe_2$ measured by tr-MOKE is rationalized by thermal expansion, which matches similar contemporary studies [82]. The ultrafast de- and remagnetization is a combination of inverse magnetostriction manifesting by thermal expansion of the lattice as well as thermal dynamics of the spin system itself. Accounting for the magnetization changes due to inverse magnetostriction, I found a two-fold exponential remagnetization with timescales differing by an order of magnitude, explicitly 81 and 830 ps, which contribute comparably in their amplitude. A possible explanation for two different timescales is the distinction between a spin heat flow deeper into the sample due to a spatial heat gradient and an energy conversion of spin heat into phonon or lattice heating. Regardless, this example consolidates the importance of monitoring the strain in addition to the magnetization in magnetostrictive materials on an ultrafast timescale. Otherwise, one runs the risk of missinterpreting tr-MOKE transients as sole responses of the magnetic subsystem.

On a much different note, this paper presents interesting possibilities for the research field of picosecond ultrasonics. With the present choice of thin film arrangement (SiO_2/$TbFe_2$/ Nb/Al_2O_3), it is possible to create unipolar strain pulses arriving at equidistant times after an initial asymmetrical bipolar strain pulse. The shape of a strain pulse originating from a thin film transducer ($TbFe_2$) after femtosecond laser excitation is usually bipolar and symmetrical. Putting a transparent capping layer (SiO_2) on top of the transducer prevents an unhindered expansion of the transducer layer surface. The transducer pushes the capping layer right after excitation, injecting a compressive unipolar strain pulse into the capping layer, which is reflected back and forth injecting fractions of itself into the transducer each roundtrip. The energy stored in the injected unipolar strain pulse is missing in the initial bipolar strain pulse, which explains its asymmetry. In the case of the SiO_2/$TbFe_2$-interface, the reflection and transmission coefficients of strain waves are roughly 50%. Another combination of acoustic impedances, the product of mass density and sound velocity $Z = \rho v_{\mathrm{sound}}$, would yield different coefficients and thus other strain transients [78].

On a final note, we also discussed the amplitude of the strain pulses besides the shape and timing of the strain signatures. As written in the publication, we were not able to fit our dissipation free modelling simultaneously to the strain amplitude in $TbFe_2$ and Nb and addressed that by acoustic damping and scattering. In the more recent publication VI, we show that the strain data of the Nb-layer of this publication is actually underestimated by up to 25%, because of the measurement routine of the reciprocal space slicing, see Sec. 2.1.1. However, this detail does not impact any drawn conclusions, interpretations or results.

Structural Dynamics ARTICLE scitation.org/journal/sdy

Tracking picosecond strain pulses in heterostructures that exhibit giant magnetostriction

Cite as: Struct. Dyn. 6, 024302 (2019); doi: 10.1063/1.5084140
Submitted: 4 December 2018 · Accepted: 26 February 2019 ·
Published Online: 20 March 2019

S. P. Zeuschner,[1,2] T. Parpiiev,[3] T. Pezeril,[3] A. Hillion,[4] K. Dumesnil,[4] A. Anane,[5] J. Pudell,[2] L. Willig,[2] M. Rössle,[1] M. Herzog,[2] A. von Reppert,[2,a)] and M. Bargheer[1,2]

AFFILIATIONS

[1]Helmholtz-Zentrum Berlin, Wilhelm-Conrad-Röntgen-Campus, BESSY II, Albert-Einstein-Straße 15, 12489 Berlin, Germany
[2]Institute of Physics and Astronomy, University of Potsdam, Karl-Liebknecht-Straße 24-25, 14476 Potsdam, Germany
[3]Institut des Molécules et Matériaux du Mans (UMR CNRS 6283), Université du Maine, 72085 Le Mans Cedex, France
[4]Institut Jean Lamour (UMR CNRS 7198), Université de Lorraine, 54000 Nancy, France
[5]Unité Mixte de Physique, CNRS, Thales, Univ. Paris-Sud, Université Paris-Saclay, 91767, Palaiseau, France

[a)]reppert@uni-potsdam.de

ABSTRACT

We combine ultrafast X-ray diffraction (UXRD) and time-resolved Magneto-Optical Kerr Effect (MOKE) measurements to monitor the strain pulses in laser-excited $TbFe_2$/Nb heterostructures. Spatial separation of the Nb detection layer from the laser excitation region allows for a background-free characterization of the laser-generated strain pulses. We clearly observe symmetric bipolar strain pulses if the excited $TbFe_2$ surface terminates the sample and a decomposition of the strain wavepacket into an asymmetric bipolar and a unipolar pulse, if a SiO_2 glass capping layer covers the excited $TbFe_2$ layer. The inverse magnetostriction of the temporally separated unipolar strain pulses in this sample leads to a MOKE signal that linearly depends on the strain pulse amplitude measured through UXRD. Linear chain model simulations accurately predict the timing and shape of UXRD and MOKE signals that are caused by the strain reflections from multiple interfaces in the heterostructure.

I. INTRODUCTION

The generation, propagation, and detection of laser-induced strain waves contain rich physics that has been studied extensively since the seminal work of Thomsen *et al.*, which exploited photoelasticity for detection.[1,2] Ingenious all-optical probing schemes for GHz to THz phonons have since then been used to investigate strain waves in multiple materials,[3–6] vibrational modes of nanoparticles,[7] shear waves,[8] nonlinear propagation effects,[9,10] and acoustic solitons.[11,12] Strain waves that originate from coherent phonon excitation can attain transient stresses on the order of GPa, which have been shown to interact with other phenomena such as phase transitions,[13,14] quantum well bandgaps,[15] piezo-[16]/ferroelectricity,[17] and magnetism.[18–22] Such interactions are not only of fundamental interest but may also become relevant for applications as soon as the understanding allows for controllability.[23,24]

In order to study the response to pure strain pulses, it is beneficial to spatially separate the laser excited transducer from the probed layer. The inherent limitation given by the finite optical penetration of the visible light in the transducer is often circumvented by backside probing schemes.[10,21] The development of (sub)-picosecond hard X-ray diffraction has opened the possibility to directly obtain the time-resolved strain amplitude[25–28] with penetration depths in the few μm regime. The separation of the layer peaks in reciprocal space allows for material specific probing of the energy flow[29,30] and strain evolution[31,32] in nanoscopic, crystalline heterostructures.

The envisioned manipulation of the polarization and magnetization states in ferroic materials via strain relies on a strong coupling between spin or electronic degrees of freedom and the atomic lattice.[23,33] In this regard, rare-earth-based alloys such as Terfenol ($TbFe_2$) have attracted attention due to the discovery of "giant magnetostriction,"[34,35]

Structural Dynamics ARTICLE scitation.org/journal/sdy

i.e., lattice strains in excess of 10^{-3} caused by magnetization change. Among the binary rare-earth alloys, $TbFe_2$ exhibits the largest magnetostriction.[36] It combines the large exchange interaction of the 3*d* orbital in Iron (Fe) with the large magnetic moment of $9\mu_B$ per Tb atom and the large spin-orbit coupling associated with 4*f* orbitals. The exchange coupling results in a ferrimagnetic alignment of the Fe and Tb moments with the Curie point ($T_C \approx 700$ K) considerably above room temperature.[37] $TbFe_2$ crystallizes in a cubic C_{15} Laves phase structure, where the $\langle 111 \rangle$-direction is the magnetic easy axis, which can be modeled by the cubic crystalline anisotropy constants $K_1 = -1.2 \times 10^8$ erg/cm^3 and $K_2 = 2.08 \times 10^7$ erg/cm^3.[38] The resulting high coercivity is often reduced for application purposes by introducing Dy ($\langle 001 \rangle$ easy axis) to obtain the ternary alloy Terfenol-D ($Tb_xDy_{1-x}Fe_2$). The desired low coercivity with large magnetostriction that is favorable for magneto-acoustic transduction applications can be tailored by different ratios *x*, where $x = 0.27$ is found to be optimal at room temperature.[39] Despite the potentially rich, coupled magnetization, and lattice dynamics in this magnetostrictive ferrimagnet, there have been only a few reports[8,23] that aim at quantifying and correlating the strain evolution and its coupling to the magnetization by time-resolved measurements in binary rare-earth alloys.

Here, we display the different capabilities of table-top ultrafast X-ray diffraction (UXRD) and all-optical methods to probe the strain propagation and evolution in a layered magnetostrictive heterostructure. Femtosecond laser pulses are used to excite the rare-earth alloy $TbFe_2$, which serves as a transducer for strain waves into adjacent layers. UXRD measurements observe the arrival and shape of the strain waves in a thin, buried detection layer. From this, we extract the stress profile that generates the strain wave in the inhomogeneously excited $TbFe_2$ layer. The timings of the observed experimental features are rationalized by modeling the strain propagation in this multilayer sample using a 1-dimensional linear chain model of masses and springs. The modeling is shown to be particularly useful when the transducer is capped by a transparent layer so that the conventional symmetric bipolar strain pulse is split into an asymmetric bipolar pulse travelling into the transducer and a unipolar strain pulse that is reflected at the sample-surface after a time determined by the transparent layer thickness. Complementary to the UXRD data, we employ an all-optical polarization sensitive measurement that probes the strain propagation in a transparent silica (SiO_2) acoustic delay line. Time-resolved magneto-optical-Kerr-effect (MOKE) measurements are shown to be a very sensitive probe for the arrival of the multiple strain echoes at the top of the laser-excited $TbFe_2$ layer, which can be used to complement the bulk sensitive UXRD.

II. EXPERIMENTAL DETAILS

We investigate laser-excited samples that consist of (110) oriented Terfenol ($TbFe_2$) layers grown by MBE on $(11\bar{2}1)$ oriented Sapphire (Al_2O_3) with a buried Niobium (Nb) (110) buffer layer as previously described.[38,40] The basic sample structure is only capped by a 2 nm thin protective Titanium (Ti) layer, which does not significantly contribute to the experimental transients. We therefore refer to sample 1 as uncapped. The second sample was instead capped with an 885 nm thick amorphous silica (SiO_2) layer. The UXRD measurements are carried out at a laser-driven, plasma-based diffraction setup (PXS) that supplies 200 fs X-ray pulses at Cu K_α-energy.[41] The table-top laser-pump X-ray-probe setup uses *p*-polarized excitation pulses at a central wavelength of 800 nm, with a 1 kHz repetition rate and a full width at half maximum spot size of a 2-dimensional Gaussian function of 1.4 mm × 1.5 mm for the laser pulses and 0.3 mm × 0.3 mm spot size of the X-ray pulses. Using the top-hat approximation with the $1/e$ width for the laser excitation profile and the pulse energy, we calculate the fluence for the $TbFe_2$ and Nb experiments, respectively. The pump-fluence at the Nb angle is approximately 4% larger compared to the $TbFe_2$ experiments since the 1.6° larger diffraction angle leads to a smaller laser footprint, whereas the Fresnel reflection coefficient for the *p*-polarized laser light decreases by approximately 1.4%.

A representative reciprocal-space map (RSM) of the uncapped sample structure obtained at the PXS alongside the static X-ray diffraction curve and the temporal evolution of the material specific Bragg peaks are displayed in Fig. 1. In the probed RSM volume, we find three separated peaks with their maximum intensity at the out-of-plane reciprocal space coordinate $q_z = 2.42$ Å^{-1}, 2.64 Å^{-1}, and 2.69 Å^{-1}, which are attributed to $TbFe_2$ (220), Al_2O_3 $(11\bar{2}1)$, and Nb (110), respectively, according to their bulk lattice plane spacings. The layer thicknesses set by the sample growth are 500 nm $TbFe_2$ on top of 50 nm Nb and 330 μm Al_2O_3 as schematically depicted in Fig. 1(e).

The $TbFe_2$ diffraction peak is significantly broadened along the in-plane reciprocal space coordinate q_x compared to the instrument function limited Al_2O_3 substrate peak. This is a hallmark for microcrystalline domains that in this case exhibit a large mosaic spread of 1.5° around the bulk diffraction angle,[40] very similar to previously reported UXRD experiments on ferroelectric samples.[42,43] The presence of such structural imperfections in the $TbFe_2$ becomes evident by comparison to the diffraction peak of the Nb layer, which exhibits a much smaller width in q_x. The blue and orange lines in Fig. 1(b) represent the reciprocal space slices that are probed in our setup for two fixed angles of incidence (AOI) ω that are chosen to be selectively sensitive to the $TbFe_2$ and Nb lattice strains, respectively.

The combination of an optic that focuses X-rays onto the sample with a convergence of $\Delta\omega \approx 0.3°$ (Montel optic from Layertec) and an X-ray area pixel detector (Dectris PILATUS-100k) allows for swift data acquisition that avoids time-consuming mesh scans of the AOI (ω) and the diffraction angle (θ). Each pixel of the X-ray area detector is mapped to reciprocal space coordinates q_x and q_z using the mapping routine described in a previous publication,[42] which is applicable in the thin film regime. Using this fixed angle detection scheme, the flux of 10^6 photons/s incident on the sample is sufficient to probe the evolution of the material specific diffraction peaks and the laser excited heterostructure with subpicosecond time resolution within few hours. The X-ray diffraction curves of the unexcited sample at the Nb and $TbFe_2$ AOI are indicated by orange and blue solid lines in Fig. 1(a) and their time evolution is represented by Figs. 1(c) and 1(d) for Nb and $TbFe_2$, respectively. The dashed lines in Figs. 1(c) and 1(d) indicate the temporal evolution of the peak center that is extracted by fitting the diffraction signal with a Gaussian line profile at each delay. This extracted Bragg peak position in reciprocal space is inversely proportional to the lattice constant *d* of the material via $q_{z,\mathrm{Fit}}(t) = \frac{2\pi}{d_{\mathrm{Fit}}(t)}$. UXRD thus probes the time-resolved strain $\varepsilon(t)$, defined as the change of the average lattice constant *d* relative to the unexcited sample $\varepsilon = \frac{d(t) - d(t<0)}{d(t<0)}$. The presented UXRD measurements were carried out without the external magnetic field. The application of static magnetic fields on the order of $\mu_0 H = 500$ mT in- and out-of-plane only leads

Structural Dynamics ARTICLE scitation.org/journal/sdy

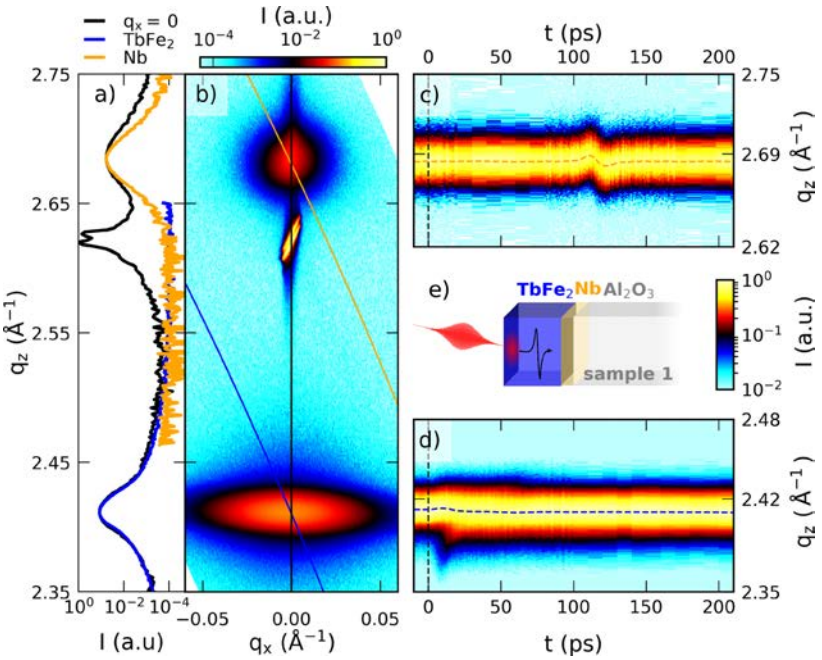

FIG. 1. Characterization of sample 1 via X-ray diffraction: (a) slice of the reciprocal space map shown in (b) at $q_x = 0$ (black line). The blue and orange lines in (a) correspond to the probed reciprocal slice when using the convergent beam of the X-ray focusing optic and area detector at the lab-based diffraction setup at a fixed angle of incidence. (c) and (d) depict the temporal evolution of the Nb and TbFe$_2$ peak at 13.3 mJ/cm^2, respectively, with the fitted peak position indicated by dashed lines. (e) Schematic depiction of the uncapped sample structure.

to minor modification of the UXRD signals consistent with a slightly increased sound velocity.

III. ANALYSIS AND DISCUSSION OF THE RESULTS

A. Signatures from the sample without SiO_2 capping

Before discussing the transient strain of the SiO_2 capped Terfenol (TbFe$_2$) structures, it is instructive to rationalize the signals seen in the UXRD experiment on the uncapped sample 1 that is schematically depicted in Fig. 1(e) for a fluence of 12.7 mJ/cm^2 and 13.3 mJ/cm^2 for the TbFe$_2$ and Nb, respectively. At first we discuss the strain evolution in the directly excited, approximately 500 nm thick TbFe$_2$ layer shown in Fig. 2(a). The blue data points show the experimentally obtained strain from Gaussian fits to the diffraction curves. The representative fits and raw time-resolved data from Figs. 1(c) and 1(d) are shown in Fig. S1 of the supplementary material. Beyond 20 ps, we observe an expansion that manifests in a shift of the diffraction peaks to smaller q_z. Within the first 20 ps, one observes a transient shift of the majority of the Bragg peak to larger q_z, which coincides with the appearance of a shoulder at smaller q_z. Between 40 and 80 ps, we detect a pronounced, triangular shaped strain increase and subsequent decrease in addition to an overall rising background.

No background is observed in the strain response of the 50 nm thin, buried Nb layer displayed in Fig. 2(b). The strain in the Nb layer is close to zero up to 4 ns (not shown), except for the very pronounced, nearly symmetric bipolar strain pulse that starts with a contraction at approximately 90 ps, reverses sign at 117 ps, and ceases at approximately 150 ps. The diffraction peak evolution of the thin Nb layer displayed in Fig. 1(c) exhibits a large peak shift that corresponds to a

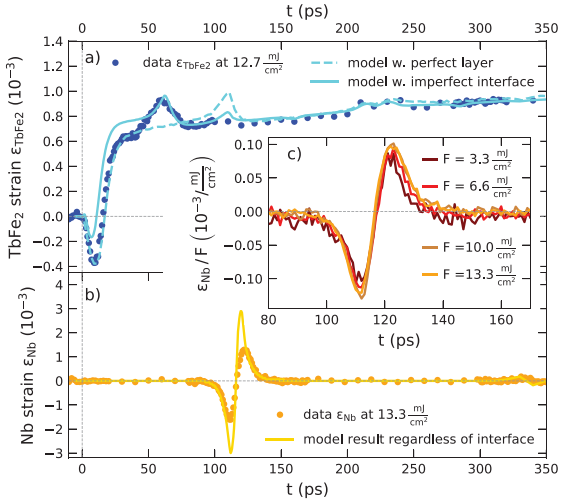

FIG. 2. Transient strain signatures of sample 1 without SiO_2 capping: (a) and (b) display transient strains extracted from the average peak shift via Gaussian lineshape fits and the simulated strain response using the udkm1Dsim toolbox as lines. The dashed line in (a) corresponds to a model with a full single-crystalline TbFe$_2$ layer whereas the solid line takes a disordered TbFe$_2$ layer at the TbFe$_2$/Nb interface into account. Inset (c) depicts the transient strain pulse in the Nb layer normalized to the different excitation fluences.

Structural Dynamics ARTICLE scitation.org/journal/sdy

strain amplitude of 1.5‰, which is only present during a short time window. The inset (c) in Fig. 2 shows the strain oscillation in Nb for different pump fluences, normalized to the fluence of the laser pulses. Since the transient strain curves nearly coincide, our data evidence a linear fluence dependence for this strain oscillation feature in Nb up to 13.3 mJ/cm^2.

The interpretation of the UXRD data from the thick $TbFe_2$ layer is based on the insights into ultrafast lattice response of photoexcited thin films studied by UXRD, which were previously discussed by Schick *et al.*[44] The laser illumination leads to the excitation of coherent and incoherent phonons, which superimpose in the strain response of the absorbing layer.[2] The strain pulse composed of the coherent excitation of phonons subsequently propagates at the longitudinal acoustic phonon velocity whereas the thermal energy leaves the excited layer by a slower diffusion process.

Our experiment represents the limiting case of an inhomogeneously excited transducer since the $TbFe_2$ layer thickness is approximately 25 times larger than the 19.9 nm light intensity penetration depth at 800 nm, which we obtain from ellipsometry measurements using a commercial setup and analyzing software (SENTECH), as discussed in Sec. III of the supplementary material. The appearance of a marked shoulder in the $TbFe_2$ diffraction signal on the lower q_z side for the main diffraction in Fig. 1(d) signals the existence of a highly strained surface layer on top of the nearly unperturbed $TbFe_2$. Schick *et al.*[44] have analyzed in detail that the exponential stress profile originating from inhomogeneous laser heating leads to an initial compression of the majority of the layer. Since the Gaussian fit is most sensitive to the central region of the diffraction peak, we observe the leading compressive strain front as a shift of the Bragg peak maximum to larger angles in the first 15 ps. When the free surface expansion propagates into the material at the speed of sound, the strong expansive component finally shifts the Bragg peak maximum to smaller angles. We attribute the remaining slope to the heat transport that equilibrates the inhomogeneous temperature profile within the $TbFe_2$ layer on a timescale of hundreds of picoseconds to several nanoseconds.

The strain response of the Nb layer seen in Fig. 2(b) confirms that the thermal transport occurs mainly within the $TbFe_2$ layer since we observe no thermal expansion that would appear as a background within our 4 ns measurement window. The bipolar strain pulse marks the delayed passage of the coherently excited phonon wave packet, which is launched at the sample-air interface, through the buried Nb layer. The detected diffraction peak shift of the 50 nm thick detection layer thus shows a background-free signal of the strain pulse, consisting of a compressive leading edge, which is followed by an expansive trailing edge as it is known from previous picosecond acoustic investigations.[2,45] The smaller layer thickness leads to higher average strain signals and sharper features as compared to the strain detected in the thick transducer layer.

The signature of the exit of the bipolar strain pulse from the probed $TbFe_2$ layer is an increase in the average layer strain followed by a decrease back to the thermal expansion background since the leading compressive edge exits while the trailing expansive part is still in the layer. In our experiment, we observe a pronounced delay between the exit of the strain wave from the $TbFe_2$ layer, at approximately 40 ps and its arrival in the adjacent Nb at 90 ps. This 50 ps delay of the signatures can only be rationalized if the strain pulse traverses a $TbFe_2$ layer that does not contribute significantly to the X-ray diffraction signal. Using $v_{sound} = 3.94$ nm/ps, known for polycrystalline $TbFe_2$,[46] this corresponds to a layer with a thickness of approximately 187 nm $TbFe_2$ that has a considerably different texture. Structural inhomogeneities are in-line with the mosaic peak broadening and the comparably small X-ray diffraction intensity of the $TbFe_2$ peak. The existence of a structurally imperfect interface layer at the $TbFe_2$-Nb interface is further supported by Atomic Force microscopy measurements that observed that the rare-earth alloy layer growth proceeds first as separated 3-dimensional islands that only coalesce to form a continuous film for thicknesses on the order of 100 nm and above.[38] The large in-plane lattice-constant mismatch of 11.6% between the underlying Nb template and the $TbFe_2$ is reduced by a thin FeNb layer but is probably the origin for the large mosaicity and for the limited coherence length along the growth direction,[47] which amounts to 50 nm in the present $TbFe_2$ film.

Modeling the excitation and propagation of picosecond acoustic strain pulses is achieved by solving the partial differential equation for the time-dependent local strain in which the given spatio-temporal stress profile acts as source term.[2,44,48] The thin film geometry reduces this to a 1-dimensional problem as the laser excitation spot is much larger than the film thickness of the nanostructure and the probed X-ray spot. Numerical solutions for the strain evolution in nanoscopic layers are frequently applied in nanoscopic heterostructure geometries where multiple interface reflections complicate analytical solutions.[32,48,49] In Figs. 2(a) and 2(b), we compare the UXRD data to simulation results obtained with the udkm1Dsim toolbox package that we used to calculate the time-resolved strain response based on a linear chain model of masses and springs. Although details of the software are given in the reference publication,[50] we briefly outline the workflow of the modeling. Upon input of the thermophysical material properties and the known sample geometry that are listed in Table I of the supplementary material, we first calculate the absorbed optical energy density and temperature profiles according to the heat diffusion equation[51] with unit cell resolution. The resulting spatio-temporal temperature profile represents the thermoelastic stress that drives a linear chain of masses and springs, where the masses represent individual unit cells. In the last simulation step, the obtained time-resolved strains are used as an input for the computation of the time-dependent dynamical X-ray diffraction signal.[52] The resulting diffraction peaks are fitted with a Gaussian line profile to yield the strain signal displayed as lines in Figs. 2(a) and 2(b).

The dashed line in Fig. 2(a) shows the modeled strain of a structurally perfect 436 nm thick $TbFe_2$ layer on top of a 50 nm Nb layer attached to an Al_2O_3 substrate. The simulation data represented by the solid line assume only 249 nm structurally perfect $TbFe_2$ on top of a 187 nm $TbFe_2$ layer with substantial disorder. The improved fit of the model regarding the triangular feature beginning at 40 ps substantiates the evidence for a structurally different $TbFe_2$ layer at the Nb interface. The total $TbFe_2$ layer thickness is determined by the arrival time of the bipolar strain pulse in Nb using the directionally averaged speed of sound of $v_{sound} = 3.94$ nm/ps for polycrystalline $TbFe_2$,[46] due to the lack of exact elastic constants for single-crystalline $TbFe_2$. Despite the agreement between the simulated and experimental strains in the $TbFe_2$ layer, the simulation substantially overestimates the bipolar strain pulse amplitude in the Nb layer. This may be accounted for by taking into account a slowly rising stress profile in $TbFe_2$ and acoustic damping as well as scattering of the coherent phonons at the interface.[53–55]

Structural Dynamics ARTICLE scitation.org/journal/sdy

B. Signals in the SiO_2 capped sample

The central experimental result of this work is summarized in Fig. 3. Here, we combine the experimental results from a sample capped by an amorphous SiO_2 layer as sketched in the inset of Fig. 3(e). Figure 3(a) shows the spatio-temporal strain profile that is obtained within the linear chain model for the second sample structure with the stacking sequence 882 nm SiO_2 / 342 nm $TbFe_2$ / 50 nm Nb / Al_2O_3 substrate, which is solved by the udkm1Dsim toolbox.[50] Red and blue colors correspond to regions of expansive and compressive strain, respectively. One observes that the expansion of the laser-heated region slowly spreads as the heat diffuses within the $TbFe_2$ layer. Now, the bipolar strain pulse that is launched towards the substrate is clearly asymmetric, where a large-amplitude leading compressive part is followed by a smaller expansive tail. In addition, a unipolar compression pulse propagates in the SiO_2 capping layer towards the surface where it is converted into an expansion. The simulated strain in Fig. 3(a) clarifies that for a very thin capping layer, the expansive unipolar wave reflected at the surface would superimpose with the small expansive tail of the asymmetric bipolar wave to form the symmetric bipolar wave observed in sample 1, see Fig. 2. Multiple reflections of the strain pulses occur at the material interfaces indicated by horizontal dashed lines where the reflection and transmission arise due to the acoustic impedance mismatch.[2,56,57] A direct comparison of the simulation results is presented in Sec. IV of the supplementary material.

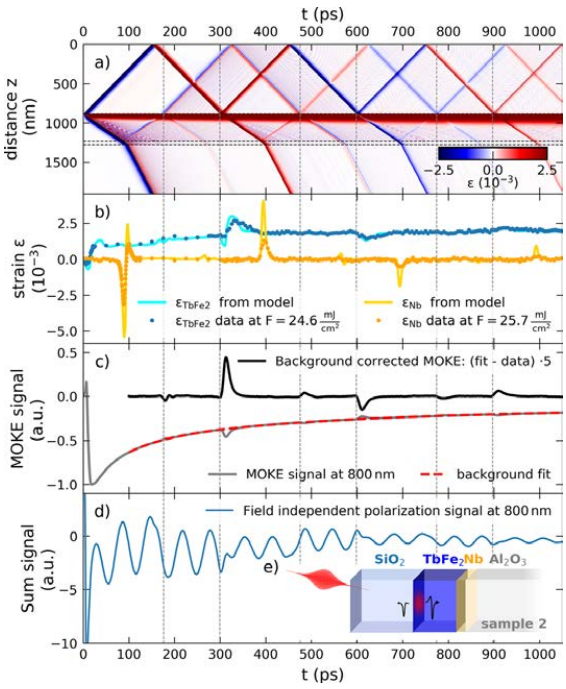

FIG. 3. Time-resolved signals from the SiO_2 capped sample structure: (a) spatio-temporal strain simulation result that highlights the occurrence of multiple echoes from bipolar and unipolar strain pulses. Horizontal dashed lines indicate the layer interfaces of the schematic sample geometry displayed in (e). (b) Comparison of the strain signal from UXRD measurements and udkm1Dsim toolbox simulations. (c) Time-resolved all-optical MOKE signal S: $[S(H_{up}) - S(H_{down})]$. The background subtracted signal shows pronounced peaks when strain pulses traverse the SiO_2/$TbFe_2$ interface, which are marked by vertical dashed lines. The field-independent polarization change $[S(H_{up}) + S(H_{down})]$ shown in (d) is dominated by oscillations of the time-resolved Brillouin scattering signal of the strain pulses within the SiO_2 capping.

The occurrence of multiple unipolar strain pulse echoes that traverse the $TbFe_2$ and Nb layers at different timings is readily seen in the UXRD data presented in Fig. 3(b). The modeled average strain shown as solid lines accurately predicts the timing and shape of the observed features but the amplitude of the Nb strain is substantially overestimated. This may indicate a finite electron-phonon-coupling time and scattering of the coherent phonons in $TbFe_2$ from structural imperfections, which are both not captured in the current modeling. The presented UXRD data were obtained under identical excitation conditions as the experiments on the uncapped sample except for the larger pump-fluence 24.6 mJ/cm^2, which leads to an increase in the detected strain amplitudes.

In the following, we discuss the results of time-resolved MOKE measurements, which probe the change of the polarization state of the probe light upon reflection due to the permanent magnetization of the sample. The measurement displayed in Fig. 3(c) was carried out close to the polar MOKE geometry with an external out-of-plane magnetic field of $\mu_0 H = 800$ mT using 200 fs laser pulses at a central wavelength of approximately 800 nm, a repetition rate of 250 kHz, and a pump fluence of approximately 2.7 mJ/cm^2. In these measurements, the difference of the polarization changes for opposite external field orientations $[S(H_{up}) - S(H_{down})]$ is probed using the reflection of 800 nm probe-light-pulses analyzed by a half-wave plate in combination with a Wollaston-prism and a balanced photo-diode. Lock-in detection using an acousto-optical modulation of the pump beam intensity at 50 kHz was employed. The resulting polar MOKE signal displayed as a solid grey line essentially probes the out-of-plane magnetization component of the $TbFe_2$ layer within the 19.9 nm optical penetration depth and is probably sensitive to the Fe sub-lattice.[58] Subtraction of the slowly varying thermal background approximated by a double-exponential decay (red line) from the MOKE signal (grey line) reveals multiple sharp peaks in the residual black curve. By comparison with the linear chain model results in Fig. 3(a), it becomes obvious that the observed features occur at the time when the longitudinal strain pulse echoes traverse the top few nanometers of the $TbFe_2$ layer given by the penetration depth of the probe pulse. Note that the sign of the peaks correlates with the sign of the (unipolar) strain-pulse echoes and that even the small reflections from the $TbFe_2$/Nb interface produce observable MOKE signatures at around 180, 485, and 790 ps.

Figure 3(d) displays the time-resolved polarization analysis signal of the reflected 800 nm probe beam independent of the magnetization state, which is obtained from the sum signal $[S(H_{up}) + S(H_{down})]$ of the balanced detection. Similar time-resolved Brillouin scattering experiments have shown that the observed oscillations originate from the interference of the reflected light from the traveling strain pulse in the transparent SiO_2 medium and the static interfaces.[59,60] Pronounced phase jumps in this Brillouin signal occur when the strain pulses invert their sign due to the reflection at the SiO_2/air interface.[56,61]

Consequently, the strain propagation as modeled by the 1-dimensional-linear chain model accurately predicts the timings of all

Structural Dynamics ARTICLE scitation.org/journal/sdy

the experimental signals we observed in this heterostructure. We have employed a single temperature model for the driving stress on the lattice. This certainly oversimplifies the equilibration process of the electron-, lattice-, and spin-subsystems to occur instantaneously. A detailed analysis of the dynamics prior to the equilibration is beyond the scope of the current investigation as it requires the knowledge of the thermophysical properties for each sub-system as well as the coupling constants of this largely unexplored material.

C. Experimental results from the buried detection layer

In the henceforth presented data analysis, we put the focus on the qualitative and quantitative information that can be directly extracted from the UXRD signal in the buried Nb detection layer. In Fig. 4(a), we see that the normalized, background-subtracted MOKE signal originating from $TbFe_2$ matches the normalized Nb strain when shifted by 84 ps, which is the longitudinal acoustic propagation time through the $TbFe_2$ layer. This agreement proves a linear relation between the lattice strain and the observed MOKE signal. The slight discrepancies at 485 and 790 ps probably originate from the fact that the MOKE signal results from a superposition of the strain pulses reflected at the surface and at the $TbFe_2$/Nb interface, which traverse the top $TbFe_2$ layer simultaneously [see Fig. 3(a)]. Since only part of the reflection at the $TbFe_2$/Nb interface is again reflected at the $TbFe_2/SiO_2$ interface, the Nb layer senses a different strain wave composition. It will be important for future experiments investigating the interaction of shear waves with the magnetization to accurately identify also the small longitudinal acoustic pulse echoes in such multilayered structures. Previous picosecond acoustic investigations in magnetic samples have observed that strain pulses can exert a torque on the sample magnetization $\vec{M}$ via a transient modification of the crystalline anisotropy, often resulting in a damped precessional motion of $\vec{M}$.[18,62,63] Although a torque on the magnetization by the strain pulse is expected, the absence of precessional oscillations challenges the theoretical interpretation of the observed MOKE signal based on the Landau-Lifshitz-Gilbert model. Crystalline defects in the $TbFe_2$, resulting in small magnetic domains,[63] in combination with a magneto-crystalline anisotropy and damping could drastically suppress the coherent precessional signal. The signal might have contributions from a modulation of the reflectivity driven by the photoelastic effect;[21] however, the reflectivity signal does not exhibit significant spikes at the echo positions. In any case, the striking resemblance of the detected strain pulses in the Nb layer to extracted features in the MOKE measurements demonstrates a high sensitivity of MOKE for probing strain pulses arriving at the $TbFe_2$ surface.

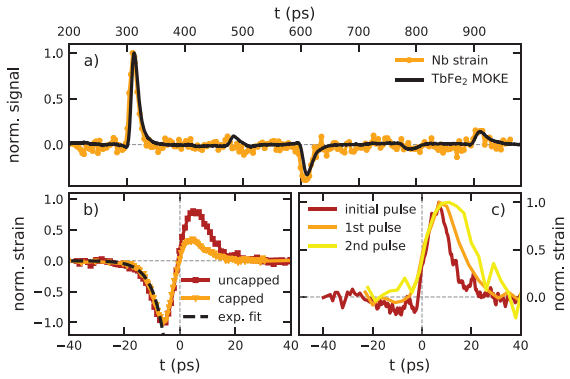

FIG. 4. Analysis of the strain pulse signatures: (a) comparison of the coherent phonon strain contribution seen in the MOKE and UXRD signal, scaled to the maximum amplitude and shifted to overlap in time. (b) Comparison of the initial asymmetric bipolar strain pulse in the capped sample 2 and the symmetric bipolar strain in the uncapped sample 1, to an exponential fit with a time-constant of 4.56 ps. (c) Evolution of the strain pulse after passing the SiO_2 layer multiple times.

In Fig. 4(b), we compare the initial bipolar strain pulses from the capped and uncapped samples, normalized to their compressive part. We observe that the leading, compressive parts coincide, whereas the expansive parts in the SiO_2 capped sample 2 are strongly reduced. The black dashed line indicates a single exponential fit to the falling edge of the compressive strain with a time constant of 4.6 ps, which translates to a spatial extension of approximately 18 nm using $v_{sound} = 3.94$ nm/ps. This value provides an estimation of the spatial extension of the driving stress profile.[3,64] This matches the optical penetration depth obtained from ellipsometry, which shows that potential hot-electron diffusion does not substantially increase the excitation profile length.

The evolution of the unipolar strain pulse within the SiO_2 capping is shown in Fig. 4(c), where we compare the first and second unipolar strain echoes that traverse the Nb layer at 396 ps and 695 ps to the initial pulse launched into the SiO_2 capping. The latter is extracted from the difference between the bipolar strain pulses observed on the capped and uncapped samples. In this analysis, we assume that the laser generated stress profile is identical in the capped and uncapped $TbFe_2$ samples and that the difference of the initially detected bipolar strain pulse seen in Fig. 4(b) originates solely from partial reflection of the expansion at the top $TbFe_2$ interface. The FWHM of the detected strain signals increases from 9 to 16 and 21 ps. The modeling does not include any broadening mechanisms and reports echoes with a constant width of 8 ps FWHM. Anharmonic interactions in the lattice potential have been shown to change the shape and broaden high amplitude coherent phonon wavepackets.[65] Contributions from the SiO_2 surface roughness should also be taken into account.

IV. CONCLUSION

In this work, we have combined multiple techniques to follow the trajectory of strain pulses that are generated by femtosecond laser pulses exploiting the giant magnetostriction material Terfenol ($TbFe_2$) as a transducer. MOKE measurements in $TbFe_2$ are shown to provide a surface sensitive method to probe strain pulses at the top of the metallic $TbFe_2$ that is complementary to bulk sensitive X-ray diffraction.

Probing the strain pulse in a thin, buried detection layer adjacent to an optically opaque transducer via UXRD allows for a characterization of the coherent strain pulse separately from heat expansion without frontside-pump backside-probe schemes. By detecting the strain pulse in the buried and perfect Nb layer, we demonstrate how UXRD can clearly locate the structurally imperfect fraction of the $TbFe_2$ layer in this opaque heterostructure. Contrary to all-optical methods, UXRD provides a quantitative measure of the average lattice strain that does not require detailed knowledge of photo elastic coefficients and optical properties. In combination with 1-dimensional-linear chain models, UXRD can provide quantitative information on realistic strains with unit cell resolution, which can be

Structural Dynamics ARTICLE scitation.org/journal/sdy

used as input for modeling strain-assisted magnetization switching approaches.[23] The obtained maximum strain amplitude in $TbFe_2$ of 2‰ is well below the deterministic switching limit of a few percent strain, but the local heating substantially lowers the anisotropy[66] as it is known from heat-assisted magnetic recording schemes.

The combination of MOKE and UXRD outlines a potential path towards an experimental calibration of the magneto-elastic coefficient, i.e., the magnetization change per strain amplitude for picosecond acoustic pulses. Such a quantity is not only relevant for testing fundamental research that models magneto-elastic couplings but also represents a valuable input for application-oriented research.

We believe that probing the strain-pulse in a buried detection layer is a versatile method for studying the stress generation profile as it separates coherent from incoherent phonon excitations. It will be especially useful in situations where multiple mechanisms with different spatial or temporal characteristics superimpose in the strain generation process as it is the case in (anti-)ferromagnetic[67,68] materials. The use of an acoustic delay line further introduces the possibility to study the evolution of the strain pulse shape and to calibrate the magnetization response to unipolar compression and expansion pulses. This will support important future steps towards a full understanding of the demagnetization process especially in high-anisotropy, giant magnetostriction materials. A combination of time-resolved probes that monitor different degrees of freedom within the same experiment will foster the understanding of the intricate couplings between electron-, spin-, and lattice systems in solids, which forms the basis for many useful devices.

SUPPLEMENTARY MATERIAL

See supplementary material for the details of the time evolution of the $TbFe_2$ and Nb Bragg peaks (S1) and the material parameters used in the modeling (S2). Furthermore, we provide the complex index of refraction and the resulting optical properties that were extracted from spectroscopic ellipsometry on the uncapped $TbFe_2$ sample (S3) as well as a section that compares the modeling results for the strain propagation in the capped and uncapped samples (S4).

ACKNOWLEDGMENTS

We gratefully acknowledge the BMBF for the financial support via 05K16IPA and the DFG via BA 2281/8-1 and BA 2281/11-1, the Open Access Publishing Fund of University of Potsdam, and Agence Nationale de la Recherche under Grant No. ANR-14-CE26-0008. We are thankful to Marwan Deb and Gregory Malinowski for stimulating discussions.

REFERENCES

[1]C. Thomsen *et al.*, "Coherent phonon generation and detection by picosecond light pulses," Phys. Rev. Lett. **53**, 989–992 (1984).
[2]C. Thomsen, H. T. Grahn, H. J. Maris, and J. Tauc, "Surface generation and detection of phonons by picosecond light pulses," Phys. Rev. B **34**, 4129–4138 (1986).
[3]O. B. Wright and K. Kawashima, "Coherent phonon detection from ultrafast surface vibrations," Phys. Rev. Lett. **69**, 1668–1671 (1992).
[4]T. Saito, O. Matsuda, and O. B. Wright, "Picosecond acoustic phonon pulse generation in nickel and chromium," Phys. Rev. B **67**(20), 205421 (2003).
[5]Y. Sugawara *et al.*, "Watching ripples on crystals," Phys. Rev. Lett. **88**, 185504 (2002).
[6]O. B. Wright, "Ultrafast nonequilibrium stress generation in gold and silver," Phys. Rev. B **49**, 9985–9988 (1994).
[7]G. V. Hartland, "Coherent vibrational motion in metal particles: Determination of the vibrational amplitude and excitation mechanism," J. Chem. Phys. **116**, 8048–8055 (2002).
[8]T. Pezeril, "Laser generation and detection of ultrafast shear acoustic waves in solids and liquids," Opt. Laser Technol. **83**, 177–188 (2016).
[9]A. Bojahr *et al.*, "Second harmonic generation of nanoscale phonon wave packets," Phys. Rev. Lett. **115**, 195502 (2015).
[10]C. Klieber, V. E. Gusev, T. Pezeril, and K. A. Nelson, "Nonlinear acoustics at GHz frequencies in a viscoelastic fragile glass former," Phys. Rev. Lett. **114**, 065701 (2015).
[11]H.-Y. Hao and H. J. Maris, "Experiments with acoustic solitons in crystalline solids," Phys. Rev. B **64**, 64302 (2001).
[12]P. J. S. van Capel and J. I. Dijkhuis, "Time-resolved interferometric detection of ultrashort strain solitons in sapphire," Phys. Rev. B **81**, 144106 (2010).
[13]P. Ruello, S. Zhang, P. Laffez, B. Perrin, and V. Gusev, "Laser-induced coherent acoustical phonons mechanisms in the metal-insulator transition compound $NdNiO_3$: Thermal and nonthermal processes," Phys. Rev. B **79**, 94303 (2009).
[14]S. H. Kim, B. J. Kim, T. Y. Jeong, Y. S. Lee, and K. J. Yee, "Coherent phonon spectroscopy of the phase transition in VO_2 single crystals and thin films," J. Appl. Phys. **117**, 163107 (2015).
[15]A. V. Akimov, A. V. Scherbakov, D. R. Yakovlev, C. T. Foxon, and M. Bayer, "Ultrafast band-gap shift induced by a strain pulse in semiconductor heterostructures," Phys. Rev. Lett. **97**(3), 037401 (2006).
[16]M. R. Armstrong *et al.*, "Observation of terahertz radiation coherently generated by acoustic waves," Nat. Phys. **5**, 285–288 (2009).
[17]C. K. Schmising *et al.*, "Coupled ultrafast lattice and polarization dynamics in ferroelectric nanolayers," Phys. Rev. Lett. **98**, 257601 (2007).
[18]J.-W. Kim, M. Vomir, and J.-Y. Bigot, "Ultrafast magnetoacoustics in nickel films," Phys. Rev. Lett. **109**, 166601 (2012).
[19]J. V. Jäger *et al.*, "Picosecond inverse magnetostriction in galfenol thin films," Appl. Phys. Lett. **103**, 032409 (2013).
[20]V. N. Kats *et al.*, "Ultrafast changes of magnetic anisotropy driven by laser-generated coherent and noncoherent phonons in metallic films," Phys. Rev. B **93**, 214422 (2016).
[21]L. Thevenard *et al.*, "Effect of picosecond strain pulses on thin layers of the ferromagnetic semiconductor (Ga,Mn)(As,P)," Phys. Rev. B **82**, 104422 (2010).
[22]M. Deb *et al.*, "Picosecond acoustic-excitation-driven ultrafast magnetization dynamics in dielectric Bi-substituted yttrium iron garnet," Phys. Rev. B **98**, 174407 (2018).
[23]O. Kovalenko, T. Pezeril, and V. V. Temnov, "New concept for magnetization switching by ultrafast acoustic pulses," Phys. Rev. Lett. **110**, 266602 (2013).
[24]A. V. Scherbakov *et al.*, "Ultrafast control of light emission from a quantum-well semiconductor microcavity using picosecond strain pulses," Phys. Rev. B **78**, 241302(R) (2008).
[25]C. Rose-Petruck *et al.*, "Picosecond-milliangstrom lattice dynamics measured by ultrafast X-ray diffraction," Nature **398**, 310–312 (1999).
[26]A. M. Lindenberg *et al.*, "Time-resolved x-ray diffraction from coherent phonons during a laser-induced phase transition," Phys. Rev. Lett. **84**, 111–114 (2000).
[27]D. A. Reis *et al.*, "Probing impulsive strain propagation with x-ray pulses," Phys. Rev. Lett. **86**, 3072–3075 (2001).
[28]T. Henighan *et al.*, "Generation mechanism of terahertz coherent acoustic phonons in Fe," Phys. Rev. B **93**, 220301(R) (2016).
[29]M. Highland *et al.*, "Ballistic-phonon heat conduction at the nanoscale as revealed by time-resolved x-ray diffraction and time-domain thermoreflectance," Phys. Rev. B **76**, 075337 (2007).
[30]A. Koc *et al.*, "Ultrafast x-ray diffraction thermometry measures the influence of spin excitations on the heat transport through nanolayers," Phys. Rev. B **96**, 014306 (2017).
[31]M. Bargheer *et al.*, "Coherent atomic motions in a nanostructure studied by femtosecond X-ray diffraction," Science **306**, 1771–1773 (2004).
[32]J. Pudell *et al.*, "Layer specific observation of slow thermal equilibration in ultrathin metallic nanostructures by femtosecond X-ray diffraction," Nat. Commun. **9**, 3335 (2018).

[33]W. Eerenstein, N. D. Mathur, and J. F. Scott, "Multiferroic and magnetoelectric materials," Nature **442**, 759–765 (2006).
[34]A. E. Clark and H. S. Belson, "Giant room-temperature magnetostrictions in $TbFe_2$ and $DyFe_2$," Phys. Rev. B **5**, 3642–3644 (1972).
[35]N. C. Koon, A. I. Schimdler, and F. L. Carter, "Giant magnetostriction in cubic rare earth-iron compounds of the type RFe_2," Phys. Lett. A **37**, 413–414 (1971).
[36]A. Clark and D. Crowder, "High temperature magnetostriction of $TbFe_2$ and $Tb_{.27}Dy_{.73}Fe_2$," IEEE Trans. Magn. **21**, 1945–1947 (1985).
[37]K. H. J. Buschow and R. P. van Stapele, "Magnetic properties of some cubic rare-earth-iron compounds of the type RFe_2 and $R_xY_{1-x}Fe_2$," J. Appl. Phys. **41**, 4066–4069 (1970).
[38]A. Mougin, C. Dufour, K. Dumesnil, and P. Mangin, "Strain-induced magnetic anisotropy in single-crystal RFe_2 (110) thin films (R = Dy, Er, Tb, $Dy_{0.7}$ $Tb_{0.3}$, Sm, Y)," Phys. Rev. B **62**, 9517–9531 (2000).
[39]R. Bergstrom *et al.*, "Morphotropic phase boundaries in ferromagnets: $Tb_{1-x}Dy_xFe_2$ alloys," Phys. Rev. Lett. **111**, 017203 (2013).
[40]V. Oderno, C. Dufour, K. Dumesnil, P. Mangin, and G. Marchal, "Epitaxial growth of (110) $DyFe_2$, $TbFe_2$ and $Dy_{0.7}Tb_{0.3}Fe_2$ thin films by molecular beam epitaxy," J. Cryst. Growth **165**, 175–178 (1996).
[41]D. Schick *et al.*, "Normalization schemes for ultrafast x-ray diffraction using a table-top laser-driven plasma source," Rev. Sci. Instrum. **83**, 025104 (2012).
[42]D. Schick *et al.*, "Ultrafast reciprocal-space mapping with a convergent beam," J. Appl. Crystallogr. **46**, 1372–1377 (2013).
[43]D. Schick *et al.*, "Following strain-induced mosaicity changes of ferroelectric thin films by ultrafast reciprocal space mapping," Phys. Rev. Lett. **110**, 095502 (2013).
[44]D. Schick *et al.*, "Ultrafast lattice response of photoexcited thin films studied by X-ray diffraction," Struct. Dyn. **1**, 064501 (2014).
[45]P. Ruello and V. E. Gusev, "Physical mechanisms of coherent acoustic phonons generation by ultrafast laser action," Ultrasonics **56**, 21–35 (2015).
[46]A. E. Clark, H. S. Belson, and R. E. Strakna, "Elastic properties of rare-earth-iron compounds," J. Appl. Phys. **44**, 2913–2914 (1973).
[47]A. Mougin *et al.*, "Strain in single-crystal RFe_2 (110) thin films (R = Y, Sm, Gd, Tb, $Dy_{0.7}Tb_{0.3}$, Dy, Er, Lu)," Phys. Rev. B **59**, 5950–5959 (1999).
[48]M. Nicoul, U. Shymanovich, A. Tarasevitch, D. von der Linde, and K. Sokolowski-Tinten, "Picosecond acoustic response of a laser-heated gold-film studied with time-resolved x-ray diffraction," Appl. Phys. Lett. **98**, 191902 (2011).
[49]M. Herzog *et al.*, "Analysis of ultrafast X-ray diffraction data in a linear-chain model of the lattice dynamics," Appl. Phys. A **106**, 489–499 (2012).
[50]D. Schick *et al.*, "udkm1Dsim—A simulation toolkit for 1D ultrafast dynamics in condensed matter," Comput. Phys. Commun. **185**, 651–660 (2014).
[51]I. A. Veres, T. Berer, and P. Burgholzer, "Numerical modeling of thermoelastic generation of ultrasound by laser irradiation in the coupled thermoelasticity," Ultrasonics **53**, 141–149 (2013).
[52]S. A. Stepanov *et al.*, "Dynamical x-ray diffraction of multilayers and superlattices: Recursion matrix extension to grazing angles," Phys. Rev. B **57**, 4829–4841 (1998).
[53]M. Hase, Y. Miyamoto, and J. Tominaga, "Ultrafast dephasing of coherent optical phonons in atomically controlled $GeTe/Sb_2Te_3$ superlattices," Phys. Rev. B **79**, 174112 (2009).
[54]M. Hase and M. Kitajima, "Interaction of coherent phonons with defects and elementary excitations," J. Phys. Condens. Matter **22**, 073201 (2010).
[55]G. Chen *et al.*, "Increased phonon scattering by nanograins and point defects in nanostructured silicon with a low concentration of germanium," Phys. Rev. Lett. **102**(19), 196803 (2009).
[56]D. Royer and E. Dieulesaint, *Elastic Waves in Solids I* (Springer, 1996), Chap. I.
[57]A. I. H. Persson, H. Enquist, A. Jurgilaitis, B. P. Andreasson, and J. Larsson, "Real-time observation of coherent acoustic phonons generated by an acoustically mismatched optoacoustic transducer using x-ray diffraction," J. Appl. Phys. **118**, 185308 (2015).
[58]A. R. Khorsand *et al.*, "Element-specific probing of ultrafast spin dynamics in multisublattice magnets with visible light," Phys. Rev. Lett. **110**, 107205 (2013).
[59]M. Lejman *et al.*, "Ultrafast acousto-optic mode conversion in optically birefringent ferroelectrics," Nat. Commun. **7**, 12345 (2016).
[60]A. Bojahr *et al.*, "Brillouin scattering of visible and hard X-ray photons from optically synthesized phonon wavepackets," Opt. Express **21**, 21188 (2013).
[61]E. Pavlenko *et al.*, "Azobenzene-functionalized polyelectrolyte nanolayers as ultrafast optoacoustic transducers," Nanoscale **8**, 13297 (2016).
[62]A. V. Scherbakov *et al.*, "Coherent magnetization precession in ferromagnetic (Ga,Mn)As induced by picosecond acoustic pulses," Phys. Rev. Lett. **105**, 117204 (2010).
[63]T. L. Linnik *et al.*, "Theory of magnetization precession induced by a picosecond strain pulse in ferromagnetic semiconductor (Ga,Mn)As," Phys. Rev. B **84**, 214432 (2011).
[64]J. Pudell *et al.*, "Ultrafast negative thermal expansion driven by spin-disorder," Phys. Rev. B (to be published).
[65]A. Bojahr, M. Herzog, D. Schick, I. Vrejoiu, and M. Bargheer, "Calibrated real-time detection of nonlinearly propagating strain waves," Phys. Rev. B **86**, 144306 (2012).
[66]A. Clark, R. Abbundi, and W. Gillmor, "Magnetization and magnetic anisotropy of $TbFe_2$, $DyFe_2$, $Tb_{0.27}Dy_{0.73}Fe_2$ and $TmFe_2$," IEEE Trans. Magn. **14**, 542–544 (1978).
[67]A. von Reppert *et al.*, "Persistent nonequilibrium dynamics of the thermal energies in the spin and phonon systems of an antiferromagnet," Struct. Dyn. **3**, 054302 (2016).
[68]A. von Reppert *et al.*, "Ultrafast laser generated strain in granular and continuous FePt thin films," Appl. Phys. Lett. **113**, 123101 (2018).

II Unconventional picosecond strain pulses resulting from the saturation of magnetic stress within a photoexcited rare earth layer

Alexander von Reppert, Maximilian Mattern, Jan-Etienne Pudell, Steffen Peer Zeuschner, Karine Dumesnil and Matias Bargheer

Structural Dynamics 7, 024303 (2020)

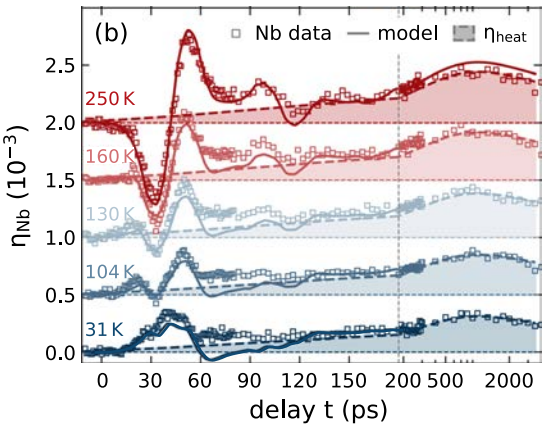

Abstract Optical excitation of spin-ordered rare earth metals triggers a complex response of the crystal lattice since expansive stresses from electron and phonon excitations compete with a contractive stress induced by spin disorder. Using ultrafast x-ray diffraction experiments, we study the layer specific strain response of a dysprosium film within a metallic heterostructure upon femtosecond laser-excitation. The elastic and diffusive transport of energy to an adjacent, non-excited detection layer clearly separates the contributions of strain pulses and thermal excitations in the time domain. We find that energy transfer processes to magnetic excitations significantly modify the observed conventional bipolar strain wave into a unipolar pulse. By modeling the spin system as a saturable energy reservoir that generates substantial contractive stress on ultrafast timescales, we can reproduce the observed strain response and estimate the time- and space dependent magnetic stress. The saturation of the magnetic stress contribution yields a non-monotonous total stress within the nanolayer, which leads to unconventional picosecond strain pulses.

Contributions to the work

Togehter with Alexander von Reppert, Jan-Etienne Pudell and Maximilian Mattern, I performed ultrafast X-Ray diffraction measurements. Additionally, I commented on the manuscript. The samples were provided by Karine Dumesnil.

Comments

This publication illustrates an ingenious possibility to tailor unusual picosecond strain pulses. Conventional metal transducers produce symmetrical and bipolar shaped strain pulses upon femtosecond laser excitation [17, 71]. In those cases, the leading part of the strain pulse is compressive followed by the expansion, since the stress on the lattice is largest at the excited surface right after the excitation and thus the ultrafast thermal expansion pushes a contraction forward into the sample. In multilayered samples with fitting acoustic impedances, it is even possible to generate alternating unipolar strain pulses, see Article I. In this publication, we show that it is possible to remove the initial compression and generate a unipolar strain pulse by utilizing dynamic stresses of the sample's subsystems. To do so, we employed Dysprosium which exhibits negative thermal expansion between 90 and 180 K due to the antiferromagnetic ordering [83]. The excitation of the spins exerts a negative stress onto the lattice, counteracting the positive stress of the increasing phonon pressure with rising temperature. This leads to an ultrafast contraction at the surface right after the excitation, which erases the initial contraction in the launched strain pulse.

Structural Dynamics ARTICLE scitation.org/journal/sdy

Unconventional picosecond strain pulses resulting from the saturation of magnetic stress within a photoexcited rare earth layer

Cite as: Struct. Dyn. **7**, 024303 (2020); doi: 10.1063/1.5145315
Submitted: 17 January 2020 · Accepted: 9 March 2020 ·
Published Online: 27 March 2020

A. von Reppert,[1] M. Mattern,[1] J.-E. Pudell,[1,2] S. P. Zeuschner,[1,2] K. Dumesnil,[3] and M. Bargheer[1,2,a)]

AFFILIATIONS

[1]Institut für Physik & Astronomie, Universität Potsdam, Karl-Liebknecht-Str. 24-25, 14476 Potsdam, Germany
[2]Helmholtz Zentrum Berlin, Albert-Einstein-Str. 15, 12489 Berlin, Germany
[3]Institut Jean Lamour (UMR CNRS 7198), Université Lorraine, 54000 Nancy, France

[a)]Author to whom correspondence should be addressed: bargheer@uni-potsdam.de

ABSTRACT

Optical excitation of spin-ordered rare earth metals triggers a complex response of the crystal lattice since expansive stresses from electron and phonon excitations compete with a contractive stress induced by spin disorder. Using ultrafast x-ray diffraction experiments, we study the layer specific strain response of a dysprosium film within a metallic heterostructure upon femtosecond laser-excitation. The elastic and diffusive transport of energy to an adjacent, non-excited detection layer clearly separates the contributions of strain pulses and thermal excitations in the time domain. We find that energy transfer processes to magnetic excitations significantly modify the observed conventional bipolar strain wave into a unipolar pulse. By modeling the spin system as a saturable energy reservoir that generates substantial contractive stress on ultrafast timescales, we can reproduce the observed strain response and estimate the time- and space dependent magnetic stress. The saturation of the magnetic stress contribution yields a non-monotonous total stress within the nanolayer, which leads to unconventional picosecond strain pulses.

I. INTRODUCTION

Experiments that probe the strain response of the atomic lattice that results from the light-matter interaction of a femtosecond optical pulse with an opto-acoustic transducer material can be subsumed as picosecond ultrasonics.[1,2] They yield fundamental insights into physical processes within the laser-excited thin film, such as electron-phonon coupling,[3–5] hot electron propagation,[6,7] and electron–hole pair generation.[8,9] This is possible because the lattice strain is the deterministic, elastic response to a physical stress that itself contains the time- and length-scales of the energy transfer processes within the transducer region. Research in this field has developed from studying the elementary processes in metals[3,4] and semiconductors[8,10] to the point that various thermal and non-thermal mechanisms for the stress generation have been distinguished.[11]

Picosecond ultrasonics within magnetic materials offers a route to study spin-lattice interactions in the time domain. An additional motivation comes from the prospect that strain assisted magnetization manipulation could lead to faster, potentially field-free data storage techniques, with increased storage densities.[12,13] Recent experiments have shown that electronically generated surface-acoustic-waves are able to switch the magnetization by nanosecond strain pulses.[14,15] Precession of the magnetization due to traversing picosecond strain pulses that transiently modify the crystal field anisotropy has been observed in many common and technologically relevant magnets such as nickel,[16,17] GaMnAs,[18,19] galfenol,[20] and doped yttrium–iron–garnet.[21,22] The inverse effect, i.e., lattice stress that originates from the change of the magnetic state, is less explored by time-resolved investigations although examples, such as the metamagnetic phase-transition in FeRh[23,24] and the change in the tetragonality of FePt[25,26] and $SrRuO_3$,[27] exist. For static and low frequency applications, it is known that metallic, magnetostrictive transducers complement the frequently used piezoelectric ceramics with the advantage of increased conductivity and ductility.[28] The class of heavy rare earth elements exhibits an exceptionally large magnetostriction[29] where the stress that can be generated by spin disorder is not only contractive but also dominates over the expansive phonon contribution as we have confirmed by

Structural Dynamics ARTICLE scitation.org/journal/sdy

probing the structural response of laser-excited gadolinium,[30] holmium,[31] and dysprosium (Dy).[32,33] Ultrafast x-ray diffraction (UXRD) is a suitable tool for quantitatively probing the strain generation and propagation as well as the accompanying heat flow in crystalline heterostructures that are either inseparable or potentially opaque to all-optical probing schemes.[34–36]

Here, we present the ultrafast lattice response of a laser-excited Dy thin film within a metallic heterostructure, where we use a buried niobium (Nb) layer for separating strain pulses from the lattice expansion that results from heat diffusion. We systematically analyze the lattice dynamics as a function of the temperature-dependent magnetic order and the laser excitation energy density. The strain-pulse observed in the Nb detection layer changes upon cooling well below $T_{Néel}$ from a bipolar compression-expansion feature that is characteristic of a fast expansive stress to an almost unipolar expansion that results from a slowly rising contractive stress within the transducer. By modeling the strain response of the heterostructure, we obtain separated spatio-temporal stress-profiles for both the expansive phonon stress and the contractive magnetic stress. The stress within the Dy layer changes from expansive to contractive because the energy conversion to the spin system is saturated only in the strongly excited near surface region. To reproduce the observed low-temperature strain-response within a one dimensional elastic model, we have to assume a contractive stress contribution that rises nearly instantaneously and counteracts the quasi-instantaneous expansive, thermoelastic stress from hot phonons and electrons. In addition, a second contractive contribution is needed that rises with an ≈15 ps time constant. These timescales match the sub-picosecond electron-spin coupling and the subsequent phonon-spin coupling that were reported by previous demagnetization experiments in heavy rare earth elements.[37–39] For high excitation densities, we observe an additional increase in the spin-stress on a longer timescale. We attribute this to phonon mediated energy transport processes from surface-near regions of complete demagnetization to regions with partial magnetic order deeper in the sample, which have been photoexcited less. The energy transfer to the magnetic system removes energy from the phonon system. The storage of heat in spin disorder in Dy is documented by a reduced thermal expansion of the buried Nb detection layer, which only accepts heat from electrons and phonons.

The presented experiments extend our previous works[32,33] that mainly discuss the evolution of the average Dy layer strain on timescales $t > 45$ ps, by an analysis of the initial picosecond strain response for $t < 180$ ps. The main experimental novelty is the use of a dedicated non-magnetic and non-excited detection layer that allows for a clear separation of elastic waves and thermal expansion following the diffusion of heat. In addition, we now discuss a spatially resolved model for the magnetic stress evolution and its saturation within the Dy layer, which is at the origin of the unconventional picosecond strain response.

This paper consists of three main parts: in Sec. II, we present the sample characterization and the temperature dependent lattice expansion of the transducer and detection layer and introduce the concept of Grüneisen constants that are central to the following analysis. Section III contains the main experimental findings on the temperature and excitation energy dependent strain within the transducer and detection layer studied by UXRD. Section IV is devoted to the modeling of the spatiotemporal stress profile and corroborates the experimental findings.

II. STATIC PROPERTIES

In the following, we provide a brief overview over the relevant properties that are later probed by time-resolved experiments. We depict a representative x-ray diffraction pattern and discuss the material specific thermal expansion response that shows fingerprints of the magnetic phase-transition within the Dy layer. We introduce the thermodynamic concept of a Grüneisen constant that relates the energy density for phonons and magnetic excitations to their stress on the crystal lattice.

A. Sample characterization by x-ray diffraction

The static and temperature dependent characterization of the Dy sample by x-ray diffraction is provided in Fig. 1. In the inset of Fig. 1(b), we display a schematic of the investigated metallic heterostructure. It consists of a 80 nm (0001)-oriented Dy transducer layer grown in between two yttrium (Y) hcp-(0001) layers (22 nm on top of and 5 nm below Dy) on-top of a 102 nm niobium (Nb) body centered cubic (110)-oriented film that enables the crystalline growth on a sapphire (Al_2O_3) hcp-(11–20) substrate[40] and serves as an additional strain detection layer. X-ray diffraction, using a microfocus Cu − K_α radiation source, yields a reciprocal space projection that is depicted in Fig. 1(c), where the four different diffraction maxima that correspond to the material specific lattice constants are clearly separated along the out-of-plane reciprocal-space coordinate q_z. These Bragg-peaks are seen as diffraction intensity maxima in Fig. 1(a), where we show the

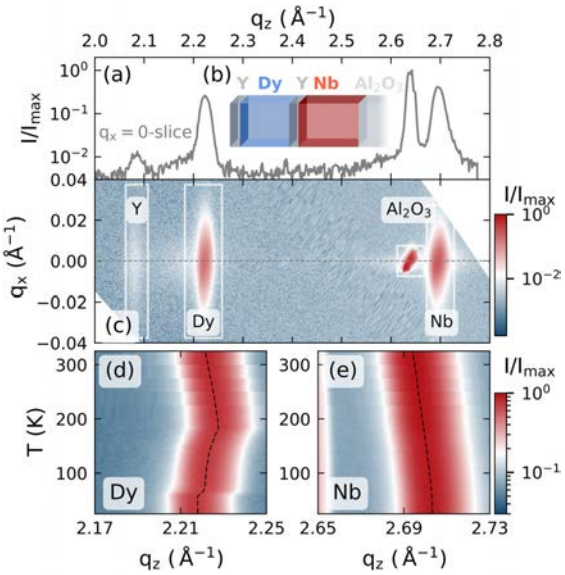

FIG. 1. Static x-ray diffraction results: (a) x-ray diffraction intensity of the sample structure that is schematically depicted in the inset (b). The material specific Bragg peaks are labeled in the reciprocal space map shown in (c). The temperature dependent peak-shifts that contrast the negative thermal expansion in the FM and AFM phase of dysprosium to the monotonous peak shift of the PM niobium are depicted in (d) and (e), respectively.

Structural Dynamics ARTICLE scitation.org/journal/sdy

slice of the reciprocal space at $q_x = 0$. In the main experiments, we observe the time-dependent shift of the Dy and Nb diffraction peaks after laser-excitation and extract the resulting average lattice strain η of these materials in a laser-pump, x-ray diffraction-probe scheme, with a time-resolution of approximately 200 fs as described previously.[35,41,42]

An important reference for our interpretation of the lattice response upon laser-excitation is the equilibrium thermal expansion and contraction during heating of the sample structure. The temperature dependent peak-shift that we extract by heating from 25 K to 350 K is depicted in Figs. 1(d) and 1(e) for Dy and Nb, respectively, where the dashed lines indicate the peak center positions as obtained by Gaussian fits. The monotonous shift of the niobium peak to smaller q_z represents the common positive thermal expansion behavior. This contrasts with the thermal expansion seen in the dysprosium peak that exhibits a pronounced negative thermal expansion (NTE) between 40 K and 180 K as well as a change between expansion and contraction at 180 K.

B. Temperature-dependent material properties

The temperature dependent lattice strain $\eta = (c(T) - c_0)/c_0)$ of the c-axis with $c_0 = c(T = 250\,\mathrm{K})$ in the hcp unit cell of the investigated thin Dy film is depicted in Fig. 2. For comparison, we relate it to the lattice constant change[43] [Fig. 2(a)] and to the heat capacity[44] of bulk Dy [Fig. 2(b)]. Changes in the thermal expansion are known to coincide with changes within the magnetic order and magnetic

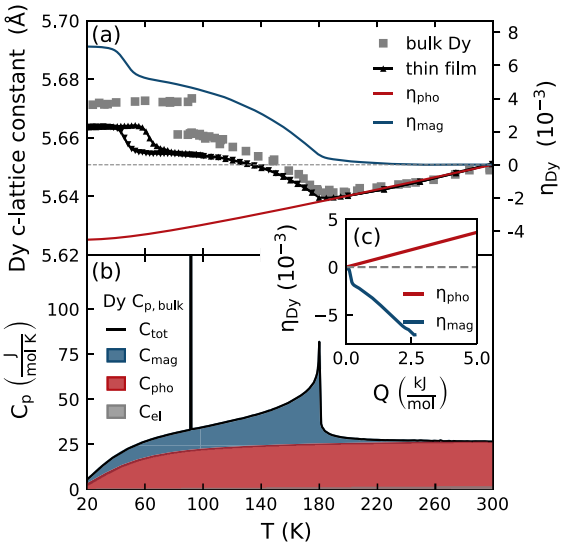

FIG. 2. Subsystem separation of (a) the static strain and (b) heat capacity contributions in Dy: The temperature-dependent c-axis of Dy and the heat capacity show a pronounced change at the AFM-PM phase transition at $T_{Néel} \approx 180$ K. The FM-AFM phase transition that occurs at $T_{Curie} \approx 90$ K for bulk Dy is shifted to lower temperatures in the used thin film sample. The inset in (c) shows the strain per deposited energy, which results from the separation of the strain and heat capacity into the contributions of phonon and spin excitations, which are indicated in red and blue, respectively.

contributions to the strain can exceed 10^{-3}.[29,45] Elemental Dy has one of the highest magnetic moments of 10.64 μ_B per atom, which order ferromagnetically (FM) below $T_{Curie,bulk} \approx 90$ K and antiferromagnetically (AFM) between T_{Curie} and $T_{Néel} \approx 180$ K above which Dy becomes paramagnetic (PM).[46–48] The large magnetic moment originates mainly from the localized magnetic moments of the partially filled 4f-electron orbitals that interact via the delocalized 5d6s-conduction band electrons by the Ruderman -Kittel -Kasuya -Yosida (RKKY)-mechanism.[47,48] The magnetic easy axis in the FM phase lies along the a-axis in the basal plane of the hexagonal unit cell and the AFM phase exhibits a helical spin ordering that is characterized by a finite turn angle between the magnetic moments for neighboring unit cells along the c-axis direction.[46]

Magnetostriction in rare earth elements is often discussed within the so-called standard model of magnetostriction pioneered by Callen and Callen.[49,50] This formalism takes both single-ion and two-ion interactions into account.[50,51] Single-ion contributions originate from the interaction of the crystal field with the anisotropic 4f-orbitals, which leads to a lattice deformation upon magnetization change due to the intrinsic spin–orbit coupling.[51,52] The case of vanishing orbital momentum, that is realized in Gadolinium, demonstrates the importance of the exchange-striction mechanism that explains the occurrence of magnetostriction even for spherically symmetric charge distributions.[51] Exchange-striction is a two-ion contribution that originates from a distance-dependent magnetic interaction energy (here provided by the oscillatory RKKY-interaction[53]) that in turn affects the equilibrium position of the magnetic ions based on their alignment.[51,52] A unified, potentially even microscopic model that explains the temperature and field dependent magnetostriction for the entire class of heavy rare earth elements does not exist.[51,52]

C. Grüneisen concept

In the discussion of the time-resolved strain, we employ a macroscopic, thermodynamic approach that approximates the laser-generated stresses to be directly proportional to the energy densities deposited in the corresponding subsystems. We introduce the main idea at first for the static thermal expansion of Dy. The origin of our approach dates back to 1912 when Grüneisen recognized that the contributions of the lattice vibrations to the volumetric thermal expansion coefficient $\beta(T)$ of elemental solids and their heat capacity $C_V(T)$ at constant volume V share the same temperature dependence, so that their ratio can be simplified to a dimensionless, nearly temperature-independent parameter.[54] The concept of this Grüneisen constant Γ has been employed continuously and was further generalized for the discussion of the thermal expansion in solids.[55–57] The thermodynamic derivation yields the macroscopic Γ as[55]

$$\Gamma = KV\frac{\beta(T)}{C_V(T)}, \tag{1}$$

wherein K represents the bulk modulus. This approach can be extended to account for different excitations that contribute energy reservoirs r in a solid by introducing dedicated Γ_r.[55] The generalization to the case of anisotropic expansion requires the use of anisotropic linear thermal expansion coefficients $\alpha_i(T)$ and anisotropic Grüneisen constants Γ_i as well as the proper directional elastic constants c_{ij} (Ref. 55) as exemplified for the rare earth Holmium.[58] For simplicity,

Structural Dynamics ARTICLE scitation.org/journal/sdy

we consider the elastic strain response to be purely one-dimensional. This is justified if the probed region is homogeneously excited along the lateral dimension, so that its picosecond response shows no in-plane strain. We thus limit the discussion to the out-of-plane response of the materials so that we will drop the directional indices for the out-of-plane stress $\sigma_3 = c_{33}\eta_3$ in the following. For sufficiently small ΔT, Eq. (1) can be transformed to the linear relation

$$\sigma_r = \Gamma_r \rho_r^Q \tag{2}$$

between the stress σ_r and the laser-induced energy density $\rho_r^Q(\Delta T) = \int_T^{T+\Delta T} C_r(T')\mathrm{d}T'$, wherein the subscript, r, denotes one of the energy reservoirs. For the case of Dy, we separate the total strain response to stress contributions from electronic excitations (r = el), phonons (r = pho), and magnetic excitations (r = mag).

In Fig. 2, we demonstrate the separation of the subsystem contributions to the equilibrium lattice strain and heat capacity in Dy from which we subsequently extract the ratio of the Grüneisen parameters for the combined electron-phonon and magnetic excitations. Using the heat capacity of the chemically equivalent non-magnetic heavy rare earth Lutetium, scaled according to the Debye temperature of Dy, provides an estimate for the combined electron and phonon contribution to the specific heat.[59] This is indicated by the red shading in Fig. 2(b). The estimated electronic contribution to the heat capacity C corresponds to the very small gray shaded area in Fig. 2(b), which we obtain from a Sommerfeld model [$C_{el} = \gamma_{Dy} T$ with $\gamma_{Dy} = 4.9$ mJ/(mol K)].[60] Electronic excitations thus only store a sizeable energy fraction at high electron temperatures that are attained only directly after laser-excitation. For that reason, we label the combined electron-phonon subsystem in the following as phonon contribution (r = pho) unless stated otherwise.

Assuming a constant Grüneisen parameter for the phonon contribution, we obtain an estimate for the thermal expansion of non-magnetic Dy (η_{pho}) that we represent by the red line in Fig. 2(a). By subtracting η_{pho} and C_{pho} from the measured lattice strain and the combined heat capacity, we obtain the contribution of magnetic excitations to the strain and heat capacity, which are indicated by the blue line in Fig. 2(a) and blue shaded area in Fig. 2(b), respectively. From this separation, we can directly extract the strain per deposited energy for the phonon and magnetic subsystem, which is displayed in the inset in Fig. 2(c). Indeed, the linear slope of the magnetic strain in Fig. 2(c) reconfirms the linear relation of stress and energy density of Eq. (2) for the spin system. The linear strain-energy-density relation for the phonon strain is in agreement with previous analysis of the thermal expansion of solids[55,61] and in particular, the non-magnetic rare earth Lutetium[62] where Grüneisen parameters Γ are found that are nearly constant over an extended range of temperatures even when $C(T)$ and $\beta(T)$ are T-dependent. Recently, this was extended to the separated magnetic and nonmagnetic contributions of the thermal expansion of Dy.[32,33] The slope of the resulting curves is proportional to the Grüneisen parameter since the relevant elastic constant c_{33} changes by less than 10% across the displayed temperature region.[63] The ratio of the Grüneisen constants $\Gamma_{mag}/\Gamma_{pho} \approx -3$ indicates that magnetic excitations in Dy are three times more efficient in the stress generation per deposited energy as compared to phonons.

As opposed to the AFM-PM transition that is of second order, the FM-AFM transition is a first order phase transition with a latent heat of 50.7 J/mol.[44] In our thin film sample, we see that this phase transition occurs between 60 K and 75 K upon heating. We attribute the shift and broadening of the phase transition to epitaxial strains. The FM-AFM phase transition leads to orthorhombic in-plane distortions that are clamped near the interfaces. Since a measurement of the temperature-dependent heat capacity of the Dy transducer within our heterostructure is not possible, we can only specify that the observed negative strain per deposited energy of the spin system is potentially even larger in the region of the FM-AFM transition. Note, however, that this contraction results mainly from the FM-AFM phase transition, since within the FM phase the lattice expands for rising temperatures.

The presented subsystem separation can be applied to gadolinium[30] and holmium,[31] which exhibit similarly large negative Grüneisen parameters for magnetic excitations. Heavy rare earth metals are an interesting class of materials for lattice dynamics since their magnetic heat capacity C_{mag} and the associated entropy of magnetic excitations $\delta S_{mag} = \Delta Q_{mag}/T$ are comparable to the phonon contribution over a large temperature region.[31,55,58] This renders Dy a suitable candidate for experiments that investigate the magnetic contributions, that lead to the NTE response, within a time-resolved experiment.

III. TIME-RESOLVED EXPERIMENTS

The main experimental results of our study are summarized in Figs. 3 and 4, which display representative picosecond strain responses for both the Dy transducer and the buried Nb detection layer at different starting temperatures T and excitation energy densities F. In our UXRD experiments, the sample is subjected to 110 fs-long, p-polarized laser pulses with a central wavelength of 800 nm at a repetition rate of 1 kHz. The laser excitation profile corresponds to a 2D-Gaussian contour with approximately $1.6 \times 1.2\,\mathrm{mm}^2$ full width at half maximum along its principal axis. The optical pump-pulses are incident under 36° for measuring the Dy response and 40° for the Nb measurements where the angle is given relative to the surface plane of the sample. The x-ray probe-pulses are generated using a laser-based plasma x-ray source,[64] monochromatized to Cu-K_α-radiation, and focused onto the sample using a Montel optic[65] with a diamond shaped $300 \times 300\,\mu\mathrm{m}^2$ beam focus on the sample. The sample temperature is monitored via a thermocouple adjacent to the sample and all reported fluence values are provided as incident energy density that is calculated from the incident laser power and the beam footprint.

A. Temperature dependent UXRD experiments

First, we discuss the results displayed in Fig. 3, where a fixed energy density of 7.2 mJ/cm^2 is used to excite the sample for different initial temperatures, sampling the different magnetic orders. The results obtained in the PM phase at $T = 250$ K are displayed by red open symbols and represent the non-magnetic response of the investigated metallic heterostructure. We find an expansion of the Dy layer that reaches its maximum within 30 ps, which corresponds to the time it takes to propagate strain from the air/Y interface through the Dy layer to the Dy/Y interface. After traversing the 5 nm Y interlayer, this expansion enters the Nb layer at approximately 31.5 ps. This expansion pulse is preceded by a compression that results from the fast rise of the spatially inhomogeneous expansive stress. The resulting bipolar shape of the propagating strain pulse is well known in picosecond

Structural Dynamics ARTICLE scitation.org/journal/sdy

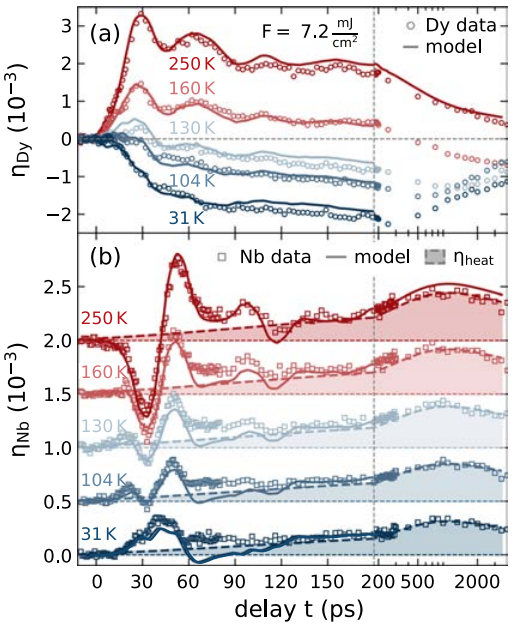

FIG. 3. Temperature-dependent strain response of (a) the Dy transducer and (b) the Nb detection layer for a fixed excitation energy density of $F = 7.2$ mJ/cm^2. Open symbols represent the average strain of the layers extracted from the Bragg peak shift observed by UXRD. Solid lines represent the simulated UXRD response obtained from a one-dimensional elastic model subjected to time-dependent phonon and magnetic stresses that are detailed in the modeling Sec. IV. The shaded region in (b) indicates the estimated thermal contribution to the Nb strain. The linear to logarithmic axis break (vertical, dashed line) allows the simultaneous comparison of the picosecond strain pulse and the subsequent thermal expansion. Nb curves are offset for clarity.

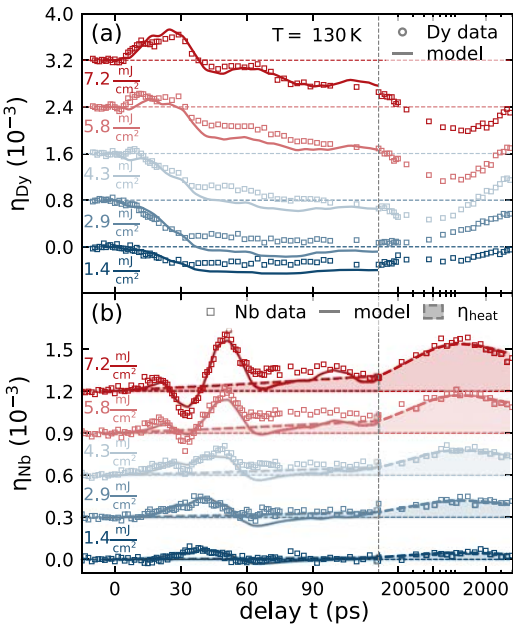

FIG. 4. Same depiction as in Fig. 3 used for the excitation energy density dependent strain response of (a) the Dy transducer and (b) the Nb detection layer for the fixed $T = 130$ K. All curves are offset for clarity. The initial transducer response changes from contraction to expansion as the excitation energy is increased, which coincides with the appearance of the delayed bipolar strain feature in the coherent phonon response of the buried detection layer.

acoustics; however, optical detection schemes often probe the wave returning back to the surface after a reflection.[1,2,5]

UXRD experiments can monitor the bipolar strain pulse traversing a buried detection layer: The classical bipolar wave first leads to a negative average strain in this layer and before it turns positive, a zero average strain indicates equal expansive and contractive parts in this layer.[35,66] The nearly bipolar shape of the Nb strain in Fig. 3(b) within the first 75 ps is characteristic of a symmetric strain pulse that is generated by a total stress that rises fast compared to the strain-propagation time through the laser-excited transducer. Echos of the laser-generated picosecond strain pulses that occur due to the partial reflection at the layer interfaces lead to a damped oscillation of the average strain in the Dy transducer and a second bipolar feature in the Nb detection layer between 80 ps and 125 ps.

In addition to these signatures of the coherent phonon wave packets, we observe a slowly increasing strain that originates from the excitation of incoherent phonons in the materials. This thermal expansion contribution of the excited Dy transducer is observed to decay on a nanosecond timescale by heat diffusion toward the substrate. This diffusion leads to a transient thermal expansion in the Nb detection layer that exhibits its maximum at approximately 1 ns after the excitation. To highlight the contribution of heat transport to the Nb expansion, we added dashed lines and shaded areas to Fig. 3(b). These lines are all scaled copies $A(T)\bar{\eta}_{\mathrm{heat}}(t)$ of the transient average strain $\bar{\eta}_{\mathrm{heat}}(t)$ in the Nb layer, which fit the 250 K data. This line could be drawn through the data by averaging out any coherent oscillations, but here we used the simulated expansion according to a Fourier heat law model discussed below. The temperature dependent factor $A(T)$ is determined by scaling the temperature-independent $\bar{\eta}_{\mathrm{heat}}(t)$ to the Nb data between 200 ps and 3 ns. $A(T)$ decreases significantly with temperature T, indicating that part of the energy density is stored in magnetic excitations that become accessible below $T_{\mathrm{Néel}}$ within the Dy transducer. The details of the modeling including a plot of $A(T)$ are discussed in Sec. IV.

Looking at the short timescale, we find that the magnetic excitations accessible upon lowering the temperature transform the transducer response continuously from a rapid expansion to a relatively slow contraction [Fig. 3(a)]. The coherent phonon oscillations in Dy become significantly weaker. In the Nb-detection layer [Fig. 3(b)], this coherent picosecond strain wave is observed to change from a large bipolar shape with a leading compression to a weaker unipolar expansion. At intermediate temperatures, a bipolar strain wave with reduced amplitude compared to the PM phase is preceeded by an expansion, which we attribute to contractive stress at the back side of the Dy layer, which absorbs the smallest energy density.

Structural Dynamics ARTICLE scitation.org/journal/sdy

B. Excitation density dependent strain-response

This hypothesis was checked by the excitation-density dependent measurements that we depict in Fig. 4. We repeated the UXRD experiment for a systematic variation of excitation fluences at a fixed initial sample temperature of $T = 130$ K in the AFM phase of Dy. The increase in the deposited energy in the heterostructure can be seen directly as an increase in the transient thermal expansion of the Nb detection layer beyond 100 ps. The shaded area in Fig. 4(b) again indicates our estimate of the incoherent strain contribution that we obtain by scaling the strain $\bar{\eta}_{\mathrm{heat}}(t)$ from the PM phase to approximate the data between 0.2 and 3 ns. The resulting amplitude $A(130\,\mathrm{K}, F)$ scales super-linearly with F, indicating a saturation of the energy transfer to magnetic excitations (cf. Sec. IV E). Note that the magnetic contribution to the specific heat C_{mag} above $T_{\mathrm{Néel}}$ is small but finite [Fig. 2(b)]. According to the equilibrium analysis, the Grüneisen constant Γ_{mag} has the same value above $T_{\mathrm{Néel}}$, as the slope in Fig. 2(c) remains constant toward the end. Similar to the temperature dependent experiments, we find a strong qualitative change of the picosecond strain response in our heterostructure. For low excitation energies $F < 4.3$ mJ/cm^2, we observe an average contraction of the Dy transducer that goes along with the unipolar expansion of the Nb layer. For $F > 4.3$ mJ/cm^2, we observe an initial expansion of the Dy transducer that changes to an average contraction at delays much larger than the 30 ps that it takes for strain propagation through the layer.

The strain pulse measured in the Nb detection layer [Fig. 4(b)] exhibits a unipolar expansion feature for low excitation energy densities. For higher fluences, this expansion is superimposed by a bipolar strain response expected for the excitation of phonons, i.e., the dominant signal in the PM phase. However, here we confirm that the bipolar strain pulse is preceded by an expansion. Since this leading expansion is rationalized by a contractive stress at the backside of the Dy transducer, the high fluence data directly show that the magnetic excitations at the back side of the Dy transducer are not saturated. The simultaneous expansion at the Dy front side, however, triggers the bipolar waveform which is observed in the detection layer with a delay given by the sound propagation. This waveform confirms a saturation of the magnetic excitation in the Dy front part, because it is the trailing part of the strain pulse, which is considerably changed by the increasing fluence. The fraction of the transducer, where expansive stress from the combined electron-phonon system dominates over the contractive stress, extends over a thicker part of the layer for higher excitation energy densities.

Before discussing the resulting quantitative findings and the modeling approach, we briefly summarize the experimental conclusions that can be drawn directly from the presented UXRD data. For low excitation energies and temperatures, we observe that the magnetic rare earth transducer contracts on average as opposed to the expansion that is observed in the PM phase. For intermediate temperatures, we can infer that the front of the transducer expands while its backside contracts. This behavior can be rationalized by a spatially dependent saturation of the magnetic stress that originates from the inhomogeneous energy deposition profile. We find that the strain propagation maps the stress profile onto a nearly background-free, time-dependent signal of the average strain in the buried Nb detection layer. Since heat diffusion takes longer than strain waves, detecting the propagated strain wave in the detection layer separates the strain contribution of coherent and incoherent phonons, which are superimposed within the photoexcited Y and Dy layer. The additional layer thus provides a nanometric depth-resolution of the UXRD experiments using hard x-rays, which otherwise exhibit an extinction length on the order of few μm. The heat transport observed via the thermal expansion of the adjacent Nb layer is found to be reduced below the magnetic ordering temperatures. This can be directly seen in the area under the curve for the average strain in Nb [Fig. 4(b)], which is smaller at low temperatures. This is quantitatively depicted in Fig. S1(c) of the supplementary material.

IV. MODELING SPATIO-TEMPORAL STRESS

Our modeling approach is designed to identify the ingredients that are necessary to rationalize the observed temperature- and excitation fluence-dependent strain-response of the magnetic rare earth transducer. To that end, we model a time- and space dependent driving stress $\sigma_{\mathrm{tot}}(z,t) = \sigma_{\mathrm{pho}}(z,t) + \sigma_{\mathrm{mag}}(z,t)$ generated by energy transfer to magnetic excitations that acts in addition to the electron-phonon stress calibrated by the response in the PM phase. The measured average strain $\bar{\eta}$ for $t > 100$ ps only encodes the average stress in the Nb layer originating from the heat diffusion. The qualitative analysis of the strain wave detected in Nb for $t < 100$ ps already indicated that we are able to extract temporal variations $\sigma(z,t)$ of the spatial stress profile in the Dy by modeling the strain wave launched into the Nb detection layer. As shown in Figs. 3 and 4, we find qualitative and quantitative agreement between our model and data.

In the following, we first discuss the general assumptions of our modeling approach before we specify the simulation steps and assumptions for the modeled electron-phonon stress and the magnetic stress contributions.

A. General model assumptions

We assume the energy transfer processes between the stress-contributing subsystems schematically shown in Fig. 5(a), with coupling-times that correspond to the stress rise-times depicted in Fig. 5(b). The spatial stress profiles in the Dy layer are exemplified in Fig. 5(c) for the parameters $T = 130$ K and $F = 7.2$ mJ/cm^2 that are representative of the AFM sample response. The total energy provided by the laser pulse is distributed between electron-phonon excitations that exert an expansive stress and magnetic-excitations that exert a contractive stress within the Dy layer. The energy is assumed to be deposited with the same inhomogeneous spatial profile to phonon- and magnetic excitations. The magnetic excitations however induce a contractive stress whose amplitude is three times larger than the expansive stress that is generated by electron-phonon excitations with the same energy density, according to the static Grüneisen analysis [Fig. 2(c)]. We keep as many simulation parameters as possible constant throughout the modeling. This includes the three coupling times illustrated in Fig. 5, the ratio of the initial energy redistribution from electrons to spins and phonons, and the maximum value for the spin energy density given by the saturation value $\rho^{\mathrm{sat}}_{\mathrm{mag}}$. We assume that the spatial energy distribution in the magnetic subsystem follows the profile of the phonon energy-density obtained by modeling the PM phase. This profile changes in time according to the heat diffusion, and we implicitly assume that the coupling of energy from phonons to spins is effective enough to prevent different spatial profiles of the contributing excitations. However, when the magnetic energy density exceeds the saturation value $\rho^{\mathrm{sat}}_{\mathrm{mag}}$, we truncate it. This truncation yields the

Structural Dynamics ARTICLE scitation.org/journal/sdy

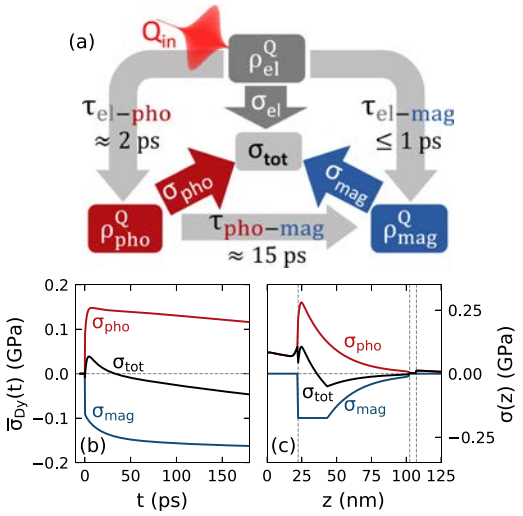

FIG. 5. (a) Schematic stress contributions used in the modeling approach. Arrows and labels indicate the modeled energy transfer processes between the subsystems and the assumed coupling-timescales τ. The resulting time-dependence of the spatially averaged stress contributions in Dy (b) and the used stress profile 100 fs after excitation (c) are shown exemplarily for $T = 130$ K and $F = 7.2$ mJ/cm^2. Vertical dashed lines in (c) indicate interfaces of the Y/Dy/Y/Nb heterostructure. This illustrates that the total stress evolution is a superposition of the expansive electron-phonon stress and the contractive magnetic stress both in the space- and time-domain.

non-monotonous spatial variation of the total driving stress as a function of temperature and excitation fluence. The temporal variation owes to the fact that the fraction of energy coupled rapidly to the phonon system is larger than into the magnetic system. Therefore, the additional 15 ps spin-phonon coupling time leads to a slow rise of the spin excitation and a decay of the phonon excitation.

We limit the modeling time to 180 ps since we expect remagnetization effects to significantly contribute to the strain at later times via magnetostriction. A full description would require a detailed model for the recovery of the magnetic order including both thermal transport and nucleation, growth, and coalescence of magnetic domains. This is beyond the scope of our one-dimensional thermodynamical approach. We furthermore refrain from a time- and space-dependent three-temperature model that has been previously used to rationalize the demagnetization of the magnetic specimen,[67,68] because it would require many, potentially temperature dependent, material constants for all layers in our heterostructure that are not known with the required accuracy. To what extend a three temperature model would capture the demagnetization and remagnetization of both the itinerant (5*d*6*s*) conduction band electrons and the localized 4*f* electrons in heavy rare earth metals is a matter of current research debate.[39,69,70]

B. Simulated spatio-temporal stress contributions

The modeled time-dependent stress profiles, separated into the expansive, contractive and the total stress contributions are displayed in Figs. 6(a)–6(o). The first row [Figs. 6(a)–6(e)] shows the expansive electron-phonon stress (σ_{pho}). In the PM-phase (250 K), σ_{pho} is identical to the total stress (σ_{tot}), shown in the third row. For the low temperature magnetic phases, the energy transfer to magnetic excitations reduces the amplitude of σ_{pho} [Figs. 6(b)–6(e)] without changing the relative spatio-temporal form, and at the same time, it creates the magnetic-stress contribution (σ_{mag}) shown in the second row [Figs. 6(f)–6(j)]. The resulting total stress σ_{tot} [Figs. 6(k)–6(o)] strongly depends on the initial temperature and excitation energy. This is supported by the modeled spatiotemporal stress profile and strain response for the excitation energy density dependent experiments at $T = 130$ K that we display in Sec. S5 of the supplementary material. The modeled strain response [Figs. 6(p)–6(t)] contains the propagating strain pulses that are launched at gradients of the driving stress in addition to the strain contribution of the local driving stress.

While the saturation level of the magnetic stress changes for the *T*-dependent measurements, *F*-dependent measurements vary the deposited energy density for a fixed maximum magnetic stress. In both cases, we observe that the absolute value of the total stress that acts on the lattice is reduced in comparison to the competing contributions from magnetic- and phonon excitations. Even though the total stress is contractive at the end of most simulation scenarios, the maximum contraction is attained slower than the magnetic stress rise time due to the time-dependent balance of phonon and magnetic stresses. The reappearance of the bipolar strain pulse in the detection layer response for high excitation energies thus occurs since the total stress at the top Y/Dy interface is dominated by an unbalanced electron-phonon stress.

C. Simulation steps

We use the modular UDKM1DSIM[71] MATLAB library to model the time-dependent energy density, strain, and x-ray reflectivity of the non-magnetic heterostructure response. The solid, dark-red line in Figs. 3(a) and 3(b) corresponds to the strain that we obtain from the simulated transient x-ray diffraction peak shift. In the first step, we calculate the time-dependent temperature changes upon laser excitation using a one-dimensional Fourier heat diffusion model from the thermophysical properties of the materials in the PM phase that we list in Sec. S3 of the supplementary material. The resulting spatiotemporal energy density is subsequently translated to a stress that acts as the driving force on a linear chain of masses and springs, which calculates the time-resolved layer strain with unit-cell resolution. The final simulation step employs a transfer matrix algorithm that yields the Bragg-peak evolution of the strained sample according to dynamical x-ray diffraction theory. Section S3 of the supplementary material shows a flow chart of the simulation steps including the relevant equations. The good quantitative agreement between UXRD data and simulation indicates that our model is a suitable representation of the sample properties and non-magnetic processes (i.e., layer thicknesses, optical excitation parameters, stress profiles, and rise-times) in the PM phase of Dy. We keep all the parameters given in Table I of the supplementary material fixed throughout the modeling, even in the FM and AFM phase, since these parameters describe the electron-phonon system. Section IV E describes how we added the contractive negative stress according to Eq. (2) for excitation in the AFM and FM phase.

Structural Dynamics ARTICLE scitation.org/journal/sdy

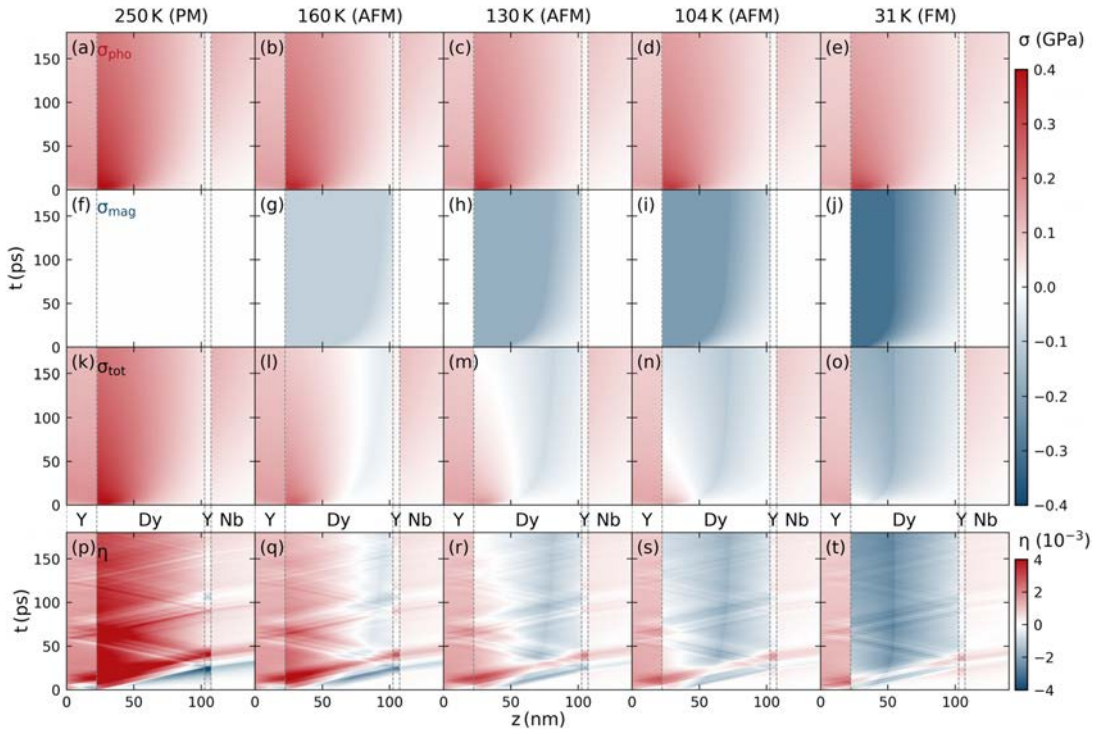

FIG. 6. Modeled spatiotemporal stress and strain response in our heterostructure for a fixed excitation with $F = 7.2$ mJ/cm^2 at different starting temperatures. The phonon-stress contributions (a)–(e) and the magnetic-stress contributions (f)–(j) in the first and second row add to the total stress provided in the third row (k)–(o). This illustrates the temperature and time-dependent energy transfer and the saturation effects due to the finite amount of energy that can be transferred to magnetic excitations. The resulting strain response of a linear chain of masses and springs model that contains contributions from both coherent and incoherent phonons is shown at the bottom (p)–(t). These strain maps are used to simulate the time-dependent Bragg peak shift that yields the modeled Dy and Nb strain response in Fig. 3. Vertical dashed lines indicate the interfaces within the Y/Dy/Y/Nb heterostructure.

D. Electron-phonon stress contribution

Both the Dy and the Nb strain responses in the PM-phase are used to calibrate the electron-phonon stress contribution. The electron-phonon coupling is included by a 2 ps time-constant of the expansive stress and a ratio between the Grüneisen constants $\Gamma_{el}/\Gamma_{pho} = 0.5$ for both the Y and Dy layers. These parameters are chosen to fit the observed expansion of the Dy layer and the coherent phonon oscillation amplitude of the PM response and are fixed for the subsequent modeling. To illustrate the effect of the stress rise time on the shape of the strain pulse seen by UXRD in the detection layer, we present the elastic-response-simulations of the average strain within a simplified structure that contains only a transducer and a detection layer in Sec. S2 of the supplementary material. To recover the observed direct rise of the Dy strain after laser excitation, we have to assume a reduced absorption and thermal expansion in the 21 nm thick Y capping layer, which would otherwise compress the adjacent Dy. Although the estimated expansion of the Y layer is reduced by 40% compared to the literature value, we stress that this parameter is kept fixed for all subsequent simulations that focus on the T-dependent magnetic response. One possible explanation for this deviation could be a partial oxidation of the capping layer since the metallic sample was kept at ambient conditions prior to the measurements.

To match the slow nanosecond decay of the Dy strain as well as the delayed rise of the expansion in the Nb layer, we use an effective thermal conductivity value for the Dy layer that is reduced by approximately 40% compared to the bulk literature value to account for thermal interface resistance effects. Using the material-specific elastic constants, we can then transform the energy densities ρ_r into an estimated spatiotemporal profile of the driving stress $\sigma_r = \Gamma_r \rho_r$ according to the Grüneisen concept [Figs. 6(a) and 6(k)]. This stress drives the elastic response shown in Fig. 6(p). The modeled strain matches both the Dy transducer and Nb detection layer response qualitatively and quantitatively over the entire 3.5 ns simulation time as shown in Fig. 3.

E. Magnetic stress contribution

To minimize the number of parameters for the simulations in the AFM and FM phase, we not only keep all thermophysical parameters describing the e-ph system fixed. We also use the shape of the

Structural Dynamics ARTICLE scitation.org/journal/sdy

spatiotemporal phonon stress-profile $\eta_{heat}(z,t)$ extracted in the PM phase. We reduce its amplitude in all layers (Y, Dy and Nb) according to the fraction of the energy that is transferred to magnetic excitations that is shown in Fig. 7 as red squares. The blue squares represent $1-\eta_{heat}$, which is proportional to the fraction of energy that is stored in the magnetic system of Dy on the few ns timescale. The lines in Fig. 7 show the relative weight of the energy densities in the phonon (red) and magnetic system (blue) in our model. We find a qualitative agreement with the data if locally a fraction of 25% of the excitation energy is deposited instantaneously into the magnetic system to account for subpicosecond electron-spin couplings and additionally a second energy fraction of 25% of the excitation energy is subsequently transferred from phonon to magnetic excitations by the phonon-spin coupling. Only when this energy transfer locally exceeds the maximum energy density ρ^{sat}_{mag} in the spin system, we truncate the energy transfer from phonons to spins. Thus, to account for the experimentally observed reduced energy transport to the adjacent layer in the magnetic phase of Dy, we reduce the energy density in the Nb and Y layers and add the removed fraction to the Dy layer where the energy is distributed between magnetic and phonon excitation. We use ρ^{sat}_{mag} as a free parameter in the modeling and find the best agreement with our data with $\rho^{sat}_{mag}(T_{start}) = 0.81\int_{T_{start}}^{\infty} C_{mag}(T')dT'$, using the literature bulk values for $C_{mag}(T')$. We believe that either the thin film value for $C_{mag}(T')$ is smaller compared to the bulk value, or only a reduced fraction of the magnetic heat capacity of the thin film is accessible upon ultrafast laser excitation. Our model reproduces the trends of the experimentally observed reduced energy flow in Fig. 7 as a function of the starting temperature and the fluence correctly. The energy fraction that is not detected in Nb persists in the magnetic excitations of Dy that act as a saturable heat sink. The saturation can be seen by the reduced energy fraction in the magnetic excitations closer to $T_{Néel}$ and the decrease in the magnetic energy fraction for higher excitation densities. The blue lines representing the fraction of heat in the magnetic system around 180 ps in our model report a systematically larger value than the blue squares derived from the experiment of the Nb strain

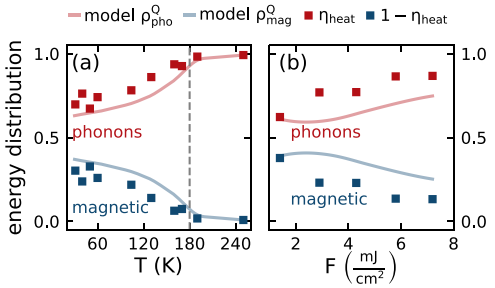

FIG. 7. Estimated energy distribution between magnetic- and phonon excitations within the rare earth transducer for the presented temperature- (a) and excitation energy dependent (b) measurements at fixed $F = 7.2$ mJ/cm^2 and $T = 130$ K, respectively. Data points correspond to the fitted amplitude $A(T, F)$ of the thermal expansion $A(T,F)\eta_{heat}(t)$ of the Nb detection layer (shaded areas in Figs. 3 and 4), normalized to the PM phase value $A(250\,K)$. Solid lines represent the energy distribution at the last time step $t = 180$ ps of the spatiotemporal stress–strain simulation. The fraction of deposited energy in the spin system decreases when approaching $T_{Néel}$ from low temperatures as well as for higher fluences.

between 0.2 and 3 ns. This is in line with the previous analysis of persistent magnetic excitations in Dy decaying within a few ns.[32]

We use energy transfer times that are in agreement with recent ultrafast demagnetization studies in AFM-dysprosium[38] and holmium.[39] The resonant diffraction studies independently report both a subpicosecond demagnetization, which is attributed to electron-spin coupling and a second demagnetization timescale on the order of 15 ps, which is attributed to phonon-spin coupling. Systematic modeling of our data yields that both timescales are necessary to capture the early time strain response of the transducer. A substantial fraction of the magnetic stress needs to be present within the first ps to balance the otherwise expansive electron-phonon response. However, our modeling shows that not all energy is instantaneously transferred to magnetic excitations since the resulting stress would drive a contraction that is significantly faster than the observed response.

In addition to these two intrinsic demagnetization timescales, we observe a contraction of the Dy transducer for larger pump-probe delays. This effect is most pronounced at high excitation densities and T close to and above $T_{Néel}$. Our simulations show that this can be rationalized by two energy transport effects within the inhomogeneously excited heterostructure. First there is thermal diffusion of phonon excitations within the inhomogeneously heated Dy. This transports energy from the near surface region where spin-excitations are saturated into the depth of the transducer, where the spin energy density is below the saturation threshold. The coupling of energy from phonons to the spins decreases the expansive phonon stress and increases the contractive magnetic stress contribution. The transport of phonon heat out of the Dy layer into the Nb reduces the expansion further. This allows us to model the spatial spin-stress profile. Although the quantitative link between the magnetic stress and the sublattice magnetization in the time-domain is largely unexplored, we can argue qualitatively that the saturation of the spin-stress will be linked to regions of complete demagnetization. For static thermal expansion experiments, it has been reported that the magnetostrictive stress is proportional to the square of the sublattice-magnetization.[43,72] Thus, we can speculate that the modeled magnetic stress profile is qualitatively similar to the demagnetization profile. More precisely, we assume that the observed magnetic stress profile reflects the demagnetization of the 4*f*-electrons of the heavy rare earth. These anisotropic orbitals carry large, localized magnetic moments that distinguish rare earth materials from 3*d*-transition metals that exhibit by far smaller magnetostriction.

The color code of Fig. 6 provides a qualitative overview over the temperature dependent stress contributions that we focus on in the current report. For a more quantitative comparison, we refer the reader to Sec. S5 of the supplementary material. There we show outlines of the modeled spatial stress profiles at 6 ps, 45 ps, and 180 ps alongside the time dependence of the modeled stress contributions for both the *T*- and *F*-dependent experiments.

Our current modeling provides a plausible scenario for the driving stress. A satisfactory agreement between the data and modeling definitively requires three energy transfer timescales to the spin system. The first energy transfer to the magnetic excitations has to rise equally fast or faster than the electron-phonon stress to cancel the expansive electron-phonon stress in the first few ps. The second timescale has to be in the range of 10–20 ps to model the contraction of the Dy layer and the unipolar expansion wave observed in the Nb layer.

Structural Dynamics ARTICLE scitation.org/journal/sdy

The third process on a timescale larger than 40 ps is given by thermal transport within the Dy layer. This is the simplest possible temporal behavior of the stress that is consistent with our data.

So far, we have also treated the FM and AFM response equally although there exists an additional first order phase-transition in the low temperature phase and the demagnetization of the ferromagnetic phase was reported to occur slower than in the antiferromagnetic Dy.[38] We attribute the reasonable agreement for the FM phase at $T = 31$ K to the use of a large excitation energy density that drives mainly spin excitations with the calibrated Grüneisen constant of the AFM phase. These magnetic-excitations seem to dominate the magnetostrictive response at high excitation energy densities compared to the potential contribution of the latent heat that is necessary to undergo the metamagnetic FM-AFM transition. A detailed study of the magnetostriction at the FM-AFM transition is deferred to future investigations.

V. CONCLUSION

The presented picosecond strain dynamics in a laser-excited heterostructure containing a rare-earth transducer shows strong magnetic contributions to the lattice response. Both the picosecond strain pulse and the thermal transport are affected by energy transfer processes to magnetic excitations. The transient strain observed in a buried detection layer directly shows the saturation of the contractive magnetic stress component, which occurs when an increasing fraction of the Dy layer is excited across its magnetic phase transition. The spatially varying sign of the stress within the Dy layer triggers unconventional strain pulses, which exhibit a leading expansive part in front of the conventional bipolar strain pulse. Our modeling yields an estimate for the time- and space-dependent profile of the additional magnetic stress contribution to the lattice dynamics. The magnetic excitations act as a saturable heat reservoir, which stores a significant fraction of the excitation energy and exerts a contractive stress that dominates over the phonon contribution. We expect this finding to be generic for the magnetic phase in the class of heavy rare earth materials in the periodic table of elements $_{64}$Gd–$_{69}$Tm. The observed energy transfer timescales are in agreement with recent demagnetization experiments. This indicates that the magnetostrictive response can be used to probe the time-dependent evolution of the sublattice magnetization.

Our investigation demonstrates the capabilities of UXRD experiments in a transducer-detector geometry to observe non-trivial spatial stress profiles. We emphasize that extracting the stress profile in the transducer by UXRD from an adjacent crystalline detection layer can be applied to investigate non-crystalline transducer films. The combination of picosecond acoustics experiment, UXRD detection, and elastic modeling can be used to study the strain generation by energy transfer to other degrees of freedom. This comprises, in particular, phase-transition effects such as studies of ferroelectric and charge order transition as well as investigations of other magnetostrictive materials, which may hold hitherto unknown functionalities.

SUPPLEMENTARY MATERIAL

See the supplementary material for a complete overview of the UXRD results (Sec. S1) and simulations (Sec. S2) that illustrate the effect of the stress rise time, stress profile length, and the detection layer thickness for the strain response in a simplified transducer-detector heterostructure. Section S3 provides an overview of the mathematical relations relevant for the strain simulation and a list of the relevant thermophysical material properties, including a description of the Poisson correction factor for the Grüneisen constant. Section S4 shows a detailed plot of the spatiotemporal stress contributions for the T- and F-dependent modeling that comprises stress-profiles at selected times and the time dependent average stress within the Dy layer.

ACKNOWLEDGMENTS

We gratefully acknowledge the BMBF for the financial support via No. 05K16IPA and the DFG via Nos. BA 2281/8-1 and BA 2281/11-1. We acknowledge the pre-characterization of the crystalline thin lms at the XPP-KMC3 synchrotronradiation beamline D13.2 at the BESSY II electron storage ring operated by the Helmholtz-Zentrum Berlin.

REFERENCES

[1]C. Thomsen, H. T. Grahn, H. J. Maris, and J. Tauc, "Surface generation and detection of phonons by picosecond light pulses," Phys. Rev. B **34**, 4129–4138 (1986).
[2]O. Matsuda, M. C. Larciprete, R. Li Voti, and O. B. Wright, "Fundamentals of picosecond laser ultrasonics," Ultrasonics **56**, 3–20 (2015).
[3]M. Nicoul, U. Shymanovich, A. Tarasevitch, D. von der Linde, and K. Sokolowski-Tinten, "Picosecond acoustic response of a laser-heated gold-film studied with time-resolved x-ray diffraction," Appl. Phys. Lett. **98**, 191902 (2011).
[4]O. B. Wright, "Ultrafast nonequilibrium stress generation in gold and silver," Phys. Rev. B **49**, 9985–9988 (1994).
[5]T. Saito, O. Matsuda, and O. B. Wright, "Picosecond acoustic phonon pulse generation in nickel and chromium," Phys. Rev. B **67**, 205421 (2003).
[6]G. Tas and H. J. Maris, "Electron diffusion in metals studied by picosecond ultrasonics," Phys. Rev. B **49**, 15046–15054 (1994).
[7]M. Lejman, V. Shalagatskyi, O. Kovalenko, T. Pezeril, V. V. Temnov, and P. Ruello, "Ultrafast optical detection of coherent acoustic phonons emission driven by superdiffusive hot electrons," J. Opt. Soc. Am. B **31**, 282 (2014).
[8]O. B. Wright, O. Matsuda, B. Perrin, and V. E. Gusev, "Ultrafast carrier diffusion in gallium arsenide probed with picosecond acoustic pulses," Phys. Rev. B **64**, 3–6 (2001).
[9]E. S. Young, A. V. Akimov, R. P. Campion, A. J. Kent, and V. Gusev, "Picosecond strain pulses generated by a supersonically expanding electron-hole plasma in GaAs," Phys. Rev. B **86**, 1–13 (2012).
[10]O. B. Wright and V. E. Gusev, "Acoustic generation in crystalline silicon with femtosecond optical pulses," Appl. Phys. Lett. **66**, 1190–1192 (1995).
[11]P. Ruello and V. E. Gusev, "Physical mechanisms of coherent acoustic phonons generation by ultrafast laser action," Ultrasonics **56**, 21–35 (2015).
[12]O. Kovalenko, T. Pezeril, and V. V. Temnov, "New concept for magnetization switching by ultrafast acoustic pulses," Phys. Rev. Lett. **110**, 266602 (2013).
[13]W. Li, B. Buford, A. Jander, and P. Dhagat, "Acoustically assisted magnetic recording: A new paradigm in magnetic data storage," IEEE Trans. Magn. **50**, 37–40 (2014).
[14]L. Thevenard, I. S. Camara, S. Majrab, M. Bernard, P. Rovillain, A. Lemaître, C. Gourdon, and J.-Y. Duquesne, "Precessional magnetization switching by a surface acoustic wave," Phys. Rev. B **93**, 134430 (2016).
[15]I. S. Camara, J. Y. Duquesne, A. Lemaître, C. Gourdon, and L. Thevenard, "Field-free magnetization switching by an acoustic wave," Phys. Rev. Appl. **11**, 1 (2019).
[16]J.-W. Kim, M. Vomir, and J.-Y. Bigot, "Ultrafast magnetoacoustics in nickel films," Phys. Rev. Lett. **109**, 166601 (2012).
[17]J. W. Kim, M. Vomir, and J. Y. Bigot, "Controlling the spins angular momentum in ferromagnets with sequences of picosecond acoustic pulses," Sci. Rep. **5**, 1–7 (2014).

Structural Dynamics ARTICLE scitation.org/journal/sdy

[18]A. V. Scherbakov, A. S. Salasyuk, A. V. Akimov, X. Liu, M. Bombeck, C. Brüggemann, D. R. Yakovlev, V. F. Sapega, J. K. Furdyna, and M. Bayer, "Coherent magnetization precession in ferromagnetic (Ga,Mn)As induced by picosecond acoustic pulses," Phys. Rev. Lett. **105**, 1–4 (2010).
[19]M. Bombeck, J. V. Jäger, A. V. Scherbakov, T. Linnik, D. R. Yakovlev, X. Liu, J. K. Furdyna, A. V. Akimov, and M. Bayer, "Magnetization precession induced by quasitransverse picosecond strain pulses in (311) ferromagnetic (Ga,Mn)As," Phys. Rev. B **87**, 1–5 (2013).
[20]J. V. Jäger, A. V. Scherbakov, T. L. Linnik, D. R. Yakovlev, M. Wang, P. Wadley, V. Holy, S. A. Cavill, A. V. Akimov, A. W. Rushforth, and M. Bayer, "Picosecond inverse magnetostriction in galfenol thin films," Appl. Phys. Lett. **103**, 032409 (2013).
[21]Y. Hashimoto, D. Bossini, T. H. Johansen, E. Saitoh, A. Kirilyuk, and T. Rasing, "Frequency and wavenumber selective excitation of spin waves through coherent energy transfer from elastic waves," Phys. Rev. B **97**, 1–5 (2018); arXiv:1710.08087.
[22]M. Deb, E. Popova, M. Hehn, N. Keller, S. Mangin, and G. Malinowski, "Picosecond acoustic-excitation-driven ultrafast magnetization dynamics in dielectric Bi-substituted yttrium iron garnet," Phys. Rev. B **98**, 174407 (2018); arXiv:1807.00610.
[23]S. O. Mariager, F. Pressacco, G. Ingold, A. Caviezel, E. Möhr-Vorobeva, P. Beaud, S. L. Johnson, C. J. Milne, E. Mancini, S. Moyerman, E. E. Fullerton, R. Feidenhans'l, C. H. Back, and C. Quitmann, "Structural and magnetic dynamics of a laser induced phase transition in FeRh," Phys. Rev. Lett. **108**, 87201 (2012).
[24]F. Quirin, M. Vattilana, U. Shymanovich, A.-E. El-Kamhawy, A. Tarasevitch, J. Hohlfeld, D. von der Linde, and K. Sokolowski-Tinten, "Structural dynamics in FeRh during a laser-induced metamagnetic phase transition," Phys. Rev. B **85**, 20103 (2012).
[25]A. H. Reid, X. Shen, P. Maldonado, T. Chase, E. Jal, P. W. Granitzka, K. Carva, R. K. Li, J. Li, L. Wu, T. Vecchione, T. Liu, Z. Chen, D. J. Higley, N. Hartmann, R. Coffee, J. Wu, G. L. Dakovski, W. F. Schlotter, H. Ohldag, Y. K. Takahashi, V. Mehta, O. Hellwig, A. Fry, Y. Zhu, J. Cao, E. E. Fullerton, J. Stöhr, P. M. Oppeneer, X. J. Wang, and H. A. Dürr, "Beyond a phenomenological description of magnetostriction," Nat. Commun. **9**, 388 (2018).
[26]A. von Reppert, L. Willig, J.-E. Pudell, M. Rössle, W. Leitenberger, M. Herzog, F. Ganss, O. Hellwig, and M. Bargheer, "Ultrafast laser generated strain in granular and continuous FePt thin films," Appl. Phys. Lett. **113**, 123101 (2018).
[27]C. von Korff Schmising, A. Harpoeth, N. Zhavoronkov, Z. Ansari, C. Aku-Leh, M. Woerner, T. Elsaesser, M. Bargheer, M. Schmidbauer, I. Vrejoiu, D. Hesse, and M. Alexe, "Ultrafast magnetostriction and phonon-mediated stress in a photoexcited ferromagnet," Phys. Rev. B **78**, 60404 (2008).
[28]E. D. T. De Lacheisserie, *Magnetostriction: Theory and Applications of Magnetoelasticity* (CRC, 1993).
[29]F. Darnell, "Temperature dependence of lattice parameters for Gd, Dy, and Ho," Phys. Rev. **130**, 1825–1828 (1963).
[30]A. Koc, M. Reinhardt, A. von Reppert, M. Rössle, W. Leitenberger, M. Gleich, M. Weinelt, F. Zamponi, and M. Bargheer, "Grueneisen-approach for the experimental determination of transient spin and phonon energies from ultrafast x-ray diffraction data: Gadolinium," J. Phys.: Condens. Matter **29**, 264001 (2017).
[31]J. Pudell, A. von Reppert, D. Schick, F. Zamponi, M. Rössle, M. Herzog, H. Zabel, and M. Bargheer, "Ultrafast negative thermal expansion driven by spin disorder," Phys. Rev. B **99**, 094304 (2019); arXiv:pudell2019a.
[32]A. von Reppert, J. Pudell, A. Koc, M. Reinhardt, W. Leitenberger, K. Dumesnil, F. Zamponi, and M. Bargheer, "Persistent nonequilibrium dynamics of the thermal energies in the spin and phonon systems of an antiferromagnet," Struct. Dyn. **3**, 054302 (2016).
[33]A. Koc, M. Reinhardt, A. von Reppert, M. Rössle, W. Leitenberger, K. Dumesnil, P. Gaal, F. Zamponi, and M. Bargheer, "Ultrafast x-ray diffraction thermometry measures the influence of spin excitations on the heat transport through nanolayers," Phys. Rev. B **96**, 014306 (2017); arXiv:1701.05918.
[34]J. Pudell, A. Maznev, M. Herzog, M. Kronseder, C. Back, G. Malinowski, A. von Reppert, and M. Bargheer, "Layer specific observation of slow thermal equilibration in ultrathin metallic nanostructures by femtosecond x-ray diffraction," Nat. Commun. **9**, 3335 (2018); arXiv:1803.04034.
[35]S. P. Zeuschner, T. Parpiiev, T. Pezeril, A. Hillion, K. Dumesnil, A. Anane, J. Pudell, L. Willig, M. Rössle, M. Herzog, A. von Reppert, and M. Bargheer, "Tracking picosecond strain pulses in heterostructures that exhibit giant magnetostriction," Struct. Dyn. **6**, 024302 (2019).
[36]Y. Gao, Z. Chen, Z. Bond, A. Loether, L. E. Howard, S. LeMar, S. White, A. Watts, B. C. Walker, and M. F. DeCamp, "Reconstructing longitudinal strain pulses using time-resolved x-ray diffraction," Phys. Rev. B **88**, 525A (2013).
[37]A. Eschenlohr, M. Sultan, A. Melnikov, N. Bergeard, J. Wieczorek, T. Kachel, C. Stamm, and U. Bovensiepen, "Role of spin-lattice coupling in the ultrafast demagnetization of gd 1- x tb x alloys," Phys. Rev. B **89**, 214423 (2014).
[38]N. Thielemann-Kühn, D. Schick, N. Pontius, C. Trabant, R. Mitzner, K. Holldack, H. Zabel, A. Föhlisch, and C. Schüßler-Langeheine, "Ultrafast and energy-efficient quenching of spin order: antiferromagnetism beats ferromagnetism," Phys. Rev. Lett. **119**, 197202 (2017); arXiv:1703.03689.
[39]L. Rettig, C. Dornes, N. Thielemann-Kühn, N. Pontius, H. Zabel, D. L. Schlagel, T. A. Lograsso, M. Chollet, A. Robert, M. Sikorski, S. Song, J. M. Glownia, C. Schüßler-Langeheine, S. L. Johnson, and U. Staub, "Itinerant and localized magnetization dynamics in antiferromagnetic Ho," Phys. Rev. Lett. **116**, 257202 (2016).
[40]K. Dumesnil, C. Dufour, P. Mangin, G. Marchal, and M. Hennion, "Magnetic structure of dysprosium in epitaxial Dy films and in Dy/Er superlattices," Phys. Rev. B **54**, 6407–6420 (1996).
[41]D. Schick, M. Herzog, A. Bojahr, W. Leitenberger, A. Hertwig, R. Shayduk, and M. Bargheer, "Ultrafast lattice response of photoexcited thin films studied by x-ray diffraction," Struct. Dyn. **1**, 064501 (2014).
[42]D. Schick, R. Shayduk, A. Bojahr, M. Herzog, C. von Korff Schmising, P. Gaal, and M. Bargheer, "Ultrafast reciprocal-space mapping with a convergent beam," J. Appl. Crystallogr. **46**, 1372–1377 (2013).
[43]F. J. Darnell and E. P. Moore, "Crystal structure of dysprosium at low temperatures," J. Appl. Phys. **34**, 1337–1338 (1963).
[44]V. Pecharsky, K. Gschneidner, and D. Fort, "Superheating and other unusual observations regarding the first order phase transition in Dy," Scr. Mater. **35**, 843–848 (1996).
[45]S. Legvold, J. Alstad, and J. Rhyne, "Giant magnetostriction in dysprosium and holmium single crystals," Phys. Rev. Lett. **10**, 509–511 (1963).
[46]W. C. Koehler, "Magnetic properties of rare earth metals and alloys," J. Appl. Phys. **36**, 1078–1087 (1965).
[47]R. Elliott, *Magnetic Properties of Rare Earth Metals* (Springer Science & Business Media, 1972).
[48]J. Jensen and A. R. Mackintosh, *Rare Earth Magnetism* (Clarendon, Oxford, 1991).
[49]E. R. Callen and H. B. Callen, "Static magnetoelastic coupling in cubic crystals," Phys. Rev. **129**, 578–593 (1963).
[50]E. Callen and H. B. Callen, "Magnetostriction, forced magnetostriction, and anomalous thermal expansion in ferromagnets," Phys. Rev. **139**, A455–A471 (1965).
[51]M. Doerr, M. Rotter, and A. Lindbaum, "Magnetostriction in rare-earth based antiferromagnets," Adv. Phys. **54**, 1–66 (2005).
[52]L. Benito, J. Arnaudas, M. Ciria, C. de La Fuente, and A. del Moral, "The magnetostriction of Tb, Dy and Ho revisited," J. Phys.: Condens. Matter **16**, 7151 (2004).
[53]W. Nolting and A. Ramakanth, *Quantum Theory of Magnetism* (Springer Science & Business Media, 2009).
[54]E. Grüneisen, "Theorie des festen zustandes einatomiger elemente," Ann. Phys. **344**, 257–306 (1912).
[55]T. Barron, J. Collins, and G. K. White, "Thermal expansion of solids at low temperatures," Adv. Phys. **29**, 609–730 (1980).
[56]J. Chen, L. Hu, J. Deng, and X. Xing, "Negative thermal expansion in functional materials: Controllable thermal expansion by chemical modifications," Chem. Soc. Rev. **44**, 3522–3567 (2015); arXiv:1612.08814.
[57]M. T. Dove and H. Fang, "Negative thermal expansion and associated anomalous physical properties: Review of the lattice dynamics theoretical foundation," Rep. Prog. Phys. **79**, 066503 (2016).
[58]G. K. White, "Phase transitions and the thermal expansion of holmium," J. Phys.: Condens. Matter **1**, 6987–6992 (1989).
[59]L. D. Jennings, R. E. Miller, and F. H. Spedding, "Lattice heat capacity of the rare earths. Heat capacities of yttrium and lutetium from 15–350K," J. Chem. Phys. **33**, 1849–1852 (1960).

[60]W. M. Haynes, *CRC Handbook of Chemistry and Physics*, CRC Handbook of Chemistry and Physics, 93rd ed. (Taylor & Francis, 2012).
[61]T. Barron, "Grüneisen parameters for the equation of state of solids," Ann. Phys. **1**, 77–90 (1957).
[62]J. J. Tonnies, K. A. Gschneidner, and F. H. Spedding, "Elastic moduli and thermal expansion of lutetium single crystals from 4.2 to 300k," J. Appl. Phys. **42**, 3275–3283 (1971).
[63]S. B. Palmer and E. W. Lee, "The elastic constants of dysprosium and holmium," Proc. R. Soc. A **327**, 519–543 (1972).
[64]D. Schick, A. Bojahr, M. Herzog, C. v K. Schmising, R. Shayduk, W. Leitenberger, P. Gaal, and M. Bargheer, "Normalization schemes for ultrafast x-ray diffraction using a table-top laser-driven plasma source," Rev. Sci. Instrum. **83**, 025104 (2012).
[65]M. Bargheer, N. Zhavoronkov, R. Bruch, H. Legall, H. Stiel, M. Woerner, and T. Elsaesser, "Comparison of focusing optics for femtosecond x-ray diffraction," Appl. Phys. B: Lasers Opt. **80**, 715–719 (2005).
[66]C. Rose-Petruck, R. Jimenez, T. Guo, A. Cavalleri, C. W. Siders, F. Rksi, *et al.*, "Picosecond -milliångström lattice dynamics measured by ultrafast X-ray diffraction," Nature **398**(6725), 310–312 (1999).
[67]E. Beaurepaire, J.-C. Merle, A. Daunois, and J.-Y. Bigot, "Ultrafast spin dynamics in ferromagnetic nickel," Phys. Rev. Lett. **76**, 4250–4253 (1996).
[68]B. Koopmans, G. Malinowski, F. Dalla Longa, D. Steiauf, M. Fähnle, T. Roth, M. Cinchetti, and M. Aeschlimann, "Explaining the paradoxical diversity of ultrafast laser-induced demagnetization," Nat. Mater. **9**, 259–265 (2010).
[69]B. Frietsch, J. Bowlan, R. Carley, M. Teichmann, S. Wienholdt, D. Hinzke, U. Nowak, K. Carva, P. M. Oppeneer, and M. Weinelt, "Disparate ultrafast dynamics of itinerant and localized magnetic moments in gadolinium metal," Nat. Commun. **6**, 8262 (2015).
[70]K. Bobowski, M. Gleich, N. Pontius, C. Schüßler-Langeheine, C. Trabant, M. Wietstruk, B. Frietsch, and M. Weinelt, "Influence of the pump pulse wavelength on the ultrafast demagnetization of Gd(0 0 0 1) thin films," J. Phys. Condens. Matter **29**, 234003 (2017).
[71]D. Schick, A. Bojahr, M. Herzog, R. Shayduk, K. C. von Schmising, and M. Bargheer, "udkm1Dsim—A simulation toolkit for 1D ultrafast dynamics in condensed matter," Comput. Phys. Commun. **185**, 651 (2014).
[72]C. Kittel, "Model of exchange-inversion magnetization," Phys. Rev. **120**, 335–342 (1960).

III Measurement of transient strain induced by two-photon excitation

Steffen Peer Zeuschner, Jan-Etienne Pudell, Alexander von Reppert, Marwan Deb, Elena Popova, Niels Keller, Matthias Rössle, Marc Herzog and Matias Bargheer

Physical Review Research 2, 022013(R) (2020)

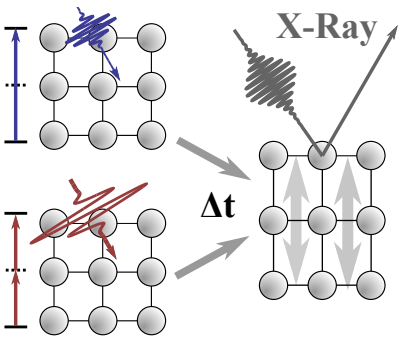

Abstract By ultrafast x-ray diffraction we quantify the strain from coherent and incoherent phonons generated by one- and two-photon absorption. We investigated the ferrimagnetic insulator bismuth-doped yttrium iron garnet, which is a workhorse for laser-induced spin dynamics that may be excited indirectly via phonons. We identify the two-photon absorption by the quadratic intensity dependence of the transient strain and confirm a short lifetime of the intermediate state via the inverse proportional dependence on the pump-pulse duration. We determine the two-photon absorption coefficient using the linear relation between strain and absorbed energy density. For large intensities of about 1 TW/cm^2 considerable strain amplitudes of 0.1 % are driven exclusively by two-photon absorption.

Contributions to the work

I performed the ultrafast X-Ray diffraction experiments together with Alexander von Reppert and Jan-Etienne Pudell. Jan and I modelled the data and I wrote the manuscript with the help and comments from the Co-authors. The samples were provided by Elena Popova and Niels Keller.

Comments

I rate this publication to be part of the most important results of my PhD studies. Not only because it is the first direct strain assessment of femtosecond laser excited Bi:YIG and the proof of two photon absorption processes. But also because this article emphasizes the importance of a precise analysis of the excitation process in ferromagnetic insulators and in extension exemplifies a two-photon excitation process in the ultrafast dynamics community.

Preceding works on Bi:YIG as a promising candidate to generate, examine and manipulate coherent spin oscillations assumed that incoherent and coherent phonons played a major role in the excitation process of those spin waves [19, 29]. Even in the case of 800 nm pump pulses, a thermal excitation process was considered, necessarily via a two-photon absorption process hence the 2.6 eV band gap of Bi:YIG. In the all-optical experiments, the Brillouin oscillation of strain waves was measurable, which proves the existence of coherent phonons. Usually, a transducer which expands due to an absorption induced thermal expansion serves as a basis for a picosecond strain waves, which was quantified directly via UXRD in this paper. In conjunction with previous publications of my colleague Marwan Deb, we prove that a high efficiency two-photon absorption process dominates the generating process of the spin waves in Bi:YIG [19, 29]. This renders it a thermal excitation process, unlike non-thermal processes like inverse Faraday and Cotton-Mouton effects or photoinduced magnetic anisotropy [84, 85].

For the presented results, we used relatively high pump energy densities, which was outlined in the review process, where it was described as an exotic example in the field of ultrafast dynamics of ferromagnetic insulators. Thus it was challenged, that the thermal exication process via a two-photon absorption process needs to be widely considered in this field of research. However, it is important to

understand that not only the pump energy density F is the relevant quantity to compare in ultrafast experiments, it is the peak intensity I as well, which scales the two-photon absorption efficiency quadratically. Thus it is of utmost importance to additionally compare the pulse length τ of the pump laser pulses, since $I \sim \frac{F}{\tau}$. Besides, there are in fact multiple examples of impactful publications on ferromagnetic insulators with comparably large pump energy densities and peak intensities which do not always consider a thermal excitation process, see Tab. III.1.

Publication	**Material**	$F\ \left(\frac{\mathbf{mJ}}{\mathbf{cm^2}}\right)$	τ **(fs)**	λ **(nm)**	$I\ \left(\frac{\mathbf{TW}}{\mathbf{cm^2}}\right)$
[86] PRL 116, 097401 (2016)	$DyFeO_3$	660	60	800	10.3
[87] PRL 122, 027202 (2019)	Bi:YIG	370	100	400	3.5
[68] PRB 97, 140404(R) (2018)	Bi:LuIG	300	100	800	2.8
[67] Nature 542, 71–74 (2017)	Co:YIG	220	50	1150 to 1450	4.1
[88] JoP Cond. Mat. 28, 276002 (2016)	Bi:YIG	130	40	800	3.0
This manuscript (2020)	Bi:YIG	100	80	800 and 400	1.2
[89] PRB 81, 214440 (2010)	Co:YIG	80	100	800	0.75
[90] PRL 112, 147403 (2014)	$FeBO_3$	60	200	800	0.28
[91] PRB 78, 104301 (2008)	$FeBO_3$	60	150	800	0.38
[19] PRL 123, 027202 (2019)	Bi:YIG	15	35	800	0.27

Table III.1: **Overview of relevant publications in the field of ultrafast magnetization dynamics in ferromagnetic insulators** with comparable pump energy densities F, pulse durations τ and thus peak intensities I. The list is ordered by the peak intensity from the highest to the lowest. It is clearly visible, that this publication as part of this PhD thesis is in fact one example of a multitude of publications working with similar excitation conditions as those for which we observed dominant two-photon absorption and consequently thermal excitation of spin dynamics.

Having shown that it is necessary to be mindful of possible thermal excitation processes in ferromagnetic insulators, this extends to the whole research field of ultrafast dynamics. Nonlinear light-matter interactions such as multi-photon absorption or absorption saturation are relevant for this research field as a whole, since the peak intensities or photon densities are always orders of magnitudes larger than those of CW sources which are used to calibrate the absorption properties of samples and materials, for example ellipsometry.

PHYSICAL REVIEW RESEARCH **2**, 022013(R) (2020)

Rapid Communications

Measurement of transient strain induced by two-photon excitation

S. P. Zeuschner,[1,2] J.-E. Pudell,[1,2] A. von Reppert,[1] M. Deb,[1] E. Popova,[3] N. Keller,[3] M. Rössle,[2] M. Herzog,[1] and M. Bargheer[1,2,*]

[1]*Institute of Physics and Astronomy, University of Potsdam, Karl-Liebknecht-Str. 24-25, 14476 Potsdam, Germany*

[2]*Helmholtz-Zentrum Berlin für Materialien und Energie GmbH, Wilhelm-Conrad-Röntgen Campus, BESSY II, 12489 Berlin, Germany*

[3]*Groupe d'Etude de la Matiére Condensée (GEMaC), CNRS UMR 8635, Université Paris-Saclay, 78035 Versailles, France*

(Received 20 November 2019; accepted 17 March 2020; published 13 April 2020)

By ultrafast x-ray diffraction we quantify the strain from coherent and incoherent phonons generated by one- and two-photon absorption. We investigated the ferrimagnetic insulator bismuth-doped yttrium iron garnet, which is a workhorse for laser-induced spin dynamics that may be excited indirectly via phonons. We identify the two-photon absorption by the quadratic intensity dependence of the transient strain and confirm a short lifetime of the intermediate state via the inverse proportional dependence on the pump-pulse duration. We determine the two-photon absorption coefficient using the linear relation between strain and absorbed energy density. For large intensities of about 1 TW/cm^2 considerable strain amplitudes of 0.1% are driven exclusively by two-photon absorption.

DOI: 10.1103/PhysRevResearch.2.022013

Lattice dynamics is a unifying theme common to all laser-excited condensed matter systems, since their phonon subsystem provides a large bath for energy, entropy, and angular momentum transfer [1–4]. The ultrafast increase of the energy density in materials drives coherent atomic motion, i.e., sizable picosecond strain pulses [5–7], that add to the incoherent thermal expansion. Ultrafast x-ray diffraction (UXRD) has quantified these strain amplitudes generated in various materials, with a dependence on the incident fluence that is usually linear [5–8] or sublinear if saturation effects play a role [9]. In semiconductors and insulators the excitation of electrons across the band gap drives lattice strain [10–12]. However, the stresses by hot phonons often prevail [13]. In GaAs a nonlinear contribution to the fluence dependence of the strain adds to the saturating one-photon absorption [14]. Various time-resolved magneto-optical experiments in metallic magnets demonstrate the possibility to trigger and control magnetization precession [15–18], using laser-induced strain pulses. In contrast, most research on magnetic insulators, mainly oxides, emphasizes energy-efficient magnetization switching schemes [19,20] and nonthermal spin manipulation by the inverse Faraday effect [21], the inverse Cotton-Mouton effect [22], and photoinduced magnetic anisotropy [23]. Since these oxides have large band gaps, the processes are thought to proceed without absorption, and the generation of phonons is not always mentioned as a mechanism to drive spins. In some materials hybrid magnetoelastic modes are identified as the relevant excitations [24,25]. Among the magnetic oxides, yttrium iron garnet (YIG) provides the lowest magnon damping. Below the charge-transfer transitions identified with the band gap of YIG, there are weaker crystal-field *d-d* transitions down to about 800 nm [26,27]. A large magneto-optical contrast is achieved by bismuth substitution [28], which connects this workhorse of magnon spintronics [29,30] and spin caloritronics [31] to optomagnetism. Recent publications on ferrimagnetic garnets reported magnetization dynamics via thermally induced crystalline anisotropy modification [23,32,33], similar to previous work in antiferromagnets [34–36]. More specifically, optically excited coherent and incoherent phonons are reported to generate spin waves (SWs) [27,37,38]. A quadratic fluence dependence of the spin-wave amplitude was discovered in several garnets already with moderate fluences below 15 mJ/cm^2 [25,38].

Here, we present nondestructive UXRD measurements on the very same Bi:YIG film [38], to quantify the lattice dynamics upon below-band-gap femtosecond laser excitation with fluences up to 100 mJ/cm^2. This corresponds to intensities, which are typical of experiments that manipulate magnetization in insulators by femtosecond light pulses [19,33,37,38], and we find a pronounced quadratic fluence dependence of the strain amplitude that quantifies coherent and incoherent phonons as propagating strain pulses and localized thermal expansion, respectively. The strain amplitude is inversely proportional to the pump pulse duration, which indicates a short lifetime of the intermediate state during the two-photon excitation. This is a quantitative and direct structural measurement of transient strain generated dominantly by two-photon absorption. We contrast this two-photon absorption process with direct above-band-gap excitation using near-ultraviolet (NUV) pulses. In this case, the lattice strain η depends linearly on the excitation fluence.

We investigate two similar (100)-oriented thin films of 150 and 135 nm $Bi_xY_{3-x}Fe_5O_{12}$ (Bi:YIG) with $x = 1$ and 2, respectively, grown on a (100)-oriented $Gd_3Ga_5O_{12}$ (GGG) substrate, schematically pictured in Fig. 1(b). The single-crystalline films were grown by pulsed laser deposition.

*bargheer@uni-potsdam.de

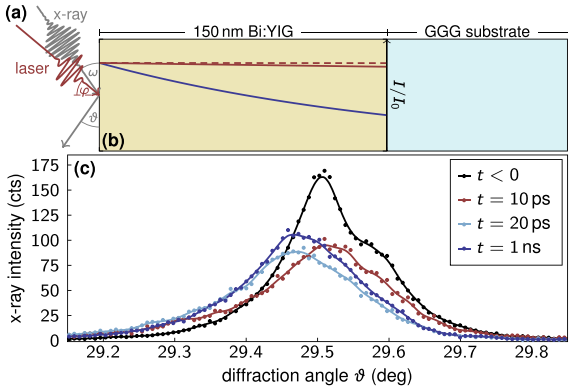

FIG. 1. (a) Sketched pump-probe geometry. (b) Sample structure and spatial intensity profiles in Bi:YIG for NUV (blue) and NIR illumination (red). For NIR light the linear absorption is negligible (dashed line) and it remains small (solid line) when including two-photon absorption, assuming an intensity of 1 TW/cm^2. (c) Scattered x-ray intensity is plotted as a function of ϑ, showing the (800) Bragg reflection of $Bi_2Y_1Fe_5O_{12}$ before 8 mJ/cm^2 NUV excitation and for a selection of pump-probe delays.

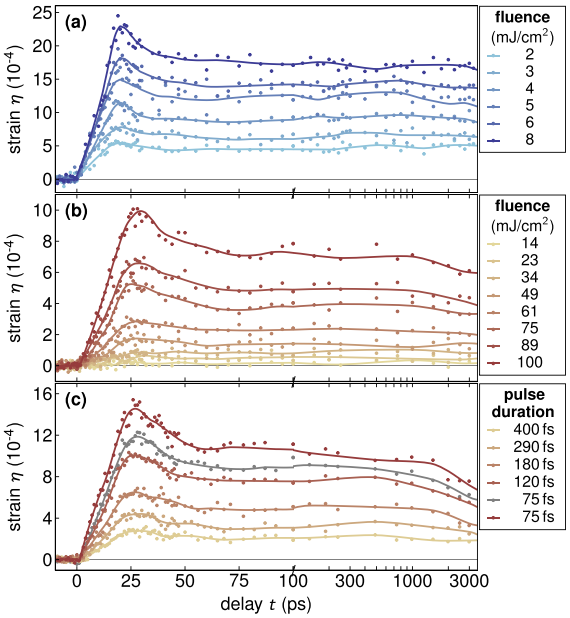

FIG. 2. Transient lattice strain η for different excitation parameters, measured with UXRD. Solid lines act as a guide to the eye. (a) Fluence series for $Bi_2Y_1Fe_5O_{12}$ with femtosecond NUV excitation. For $Bi_1Y_2Fe_5O_{12}$ we show (b) the fluence series with 120 fs NIR excitation and (c) the pulse duration series with 100 mJ/cm^2 NIR excitation. The gray data set has a similar pulse duration but opposite linear chirp.

X-ray diffraction and spectroscopic ellipsometry reveal similar structural and optical properties of both Bi:YIG samples. Although the bismuth substitution enhances the electronic d-d transition probabilities for photon energies just below the band-gap energy [39], the optical properties are essentially identical for both samples at the excitation wavelengths $\lambda_{NUV} = 400$ nm and $\lambda_{NIR} = 800$ nm of our experiments. This is verified by ellipsometry, which yields an optical penetration depth of 170 nm at λ_{NUV}. For λ_{NIR} ellipsometry only yields a lower bound for the penetration depth which is consistent with the literature value of 65 μm [26–28]. The intensity profiles for both excitation wavelengths are depicted true to scale in Fig. 1(b). For our experiments the relevant difference of the samples is the higher elastic constant for the lower bismuth concentration. The larger speed of sound is partially compensated by the increased layer thicknesses such that we qualitatively find the same transient response to laser excitation. The increased lattice constant upon doping [40] does not affect our results as we examine solely the relative changes of the lattice. Thus the two samples allow us to crosscheck the amplitudes and timings of the photoinduced strain transients.

The UXRD data, exemplarily depicted in Fig. 1(c), are measured at the laser-driven table-top plasma x-ray source (PXS) [41] at the University of Potsdam with a 200-fs x-ray pulse duration at a wavelength of 154 pm (Cu $K\alpha$). The samples are excited at a 1 kHz repetition rate by p-polarized NUV pulses at 400 nm or NIR pulses at 800 nm under an angle of $\varphi = 40^\circ$ [see Fig. 1(a)]. The incident fluence F_i is changed by a combination of a wave plate and polarizer. Changes in the spot size resulting from self-focusing at higher intensities, however, led us to adjust the full width at half maximum (FWHM) of the Gaussian-shaped pump pulses between 1.5 and 0.7 mm diameter, as controlled by a beam profiler. F_i is calculated by the top-hat approximation with the $1/e$ width for the laser excitation profile. The laser pulse duration is determined by a single-shot autocorrelator. X-ray pulses with a 0.3-mm-diam spot size probe the samples at delays up to $t = 3$ ns at a Bragg angle of $\omega = 29.5^\circ$ [see Fig. 1(a)], associated with the symmetric (800) reflection for both samples. In Fig. 1(c), the scattered x-ray intensity of Bi:YIG around $\omega = \vartheta$, detected with a Pilatus 100k area detector from Dectris, is exemplarily displayed for four different pump-probe delays after an 8 mJ/cm^2, NUV femtosecond excitation. The transient angular shift $\Delta\vartheta(t)$ of the Bragg reflection is calculated by the center-of-mass change of the scattered intensity before and after excitation [42]. From this, we calculate the mean transient out-of-plane strain (i.e., the relative change of the layer thickness) in the Bi:YIG layer, $\eta(t)$, via Bragg's law modified by a geometric scaling factor f. According to our diffraction geometry, with the sample and area detector at fixed diffraction angles, and for a convergent x-ray beam we use $f \approx 2$ [43,44],

$$\eta(t) = -f\,\Delta\vartheta(t)\cot(\omega). \tag{1}$$

First, we investigated the transient strain of Bi:YIG as a function of the excitation fluence for NUV illumination to determine the response to an above-band-gap excitation. The results for $Bi_2Y_1Fe_5O_{12}$ are shown in Fig. 2(a) and yield the typical linear scaling of the strain amplitude with the fluence in accordance with other studies on semiconductors and insulators [12,45]. This dependence is analyzed by the blue linear fit in Fig. 3(a), where the average strain $\overline{\eta}$ in

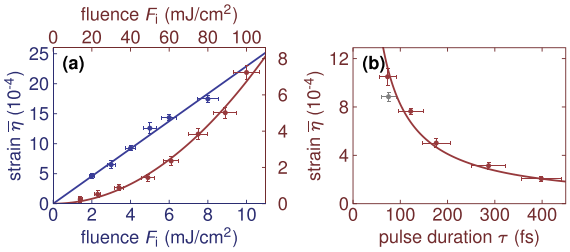

FIG. 3. Averaged lattice strain $\overline{\eta}$ in Bi:YIG between 75 ps and 1 ns evaluated from the data set in Fig. 2. (a) $\overline{\eta}$ as a function of the fluence at NUV excitation of $Bi_2Y_1Fe_5O_{12}$ (blue) and NIR excitation of $Bi_1Y_2Fe_5O_{12}$ (red). The NUV data are fitted with a linear function and a quadratic fluence dependence is observed for the NIR excitation as predicted by the presented modeling [see Eq. (7)]. (b) Pulse duration dependence of $\overline{\eta}$ upon NIR excitation of $Bi_1Y_2Fe_5O_{12}$. The gray data point was obtained under different chirp conditions. The solid line results from Eq. (7) with the same parameters as in (a). The vertical error bars are the standard deviation of η and the horizontal error bars are estimated from the pump spot size fluctuation and the GDD of the mirrors.

Bi:YIG from 75 ps to 1 ns is displayed as a function of the NUV fluence. The transient strain data in Fig. 2 exhibit multiple features characteristic of coherent and incoherent phonons. During the first 50 ps, the rising edge, the local maximum at 25 ps, and the falling edge are associated with a coherent and bipolar phonon wave packet launched by the absorption of an ultrashort laser pulse [12]. The time to reach the maximum expansion/strain is governed by the sound velocity in Bi:YIG and the film thickness. The falling edge relates to the movement of the expansive part of the bipolar wave packet out of the Bi:YIG layer [12]. The exact temporal behavior of the measured average strain depends on the spatial form of the wave packet [12]. The strain beyond 50 ps arises from heating, which is proportional to the absorbed energy [1,46,47]. Within our measurement window of 3 ns the thermal expansion shows almost no relaxation because of the slow heat transport out of Bi:YIG, as expected from the low thermal conductivity of garnet [48,49]. The dynamics of the film with $x = 1$ is identical when we scale the timing according to the different sound velocity and thickness.

Following the experiments for the excitation of spin waves [24,25,38,50], we excited Bi:YIG with NIR light with a short pulse duration (150 fs) and incident fluences up to 100 mJ/cm^2. We used the very same $x = 1$ sample as Deb *et al.* [38]. At fluences comparable to the NUV excitation no significant strain was detected. The results for fluences larger than 10 mJ/cm^2 are displayed in Fig. 2(b) and show a quadratic dependence of $\eta(t)$ on the fluence. Substantiated by the red line in Fig. 3(a), this quadratic fluence dependence indicates a two-photon strain generation process. Although the transient strain response for NIR excitation shown in Figs. 2(b) and 2(c) is very similar to the above-band-gap excitation shown in Fig. 2(a), three small differences in the observed strain signatures require discussion. The maximum at 25 ps in Fig. 2(b) is slightly delayed, because the higher sound velocity $v_1 = 6.3$ nm/ps for $x = 1$ as compared to $v_2 = 5.4$ nm/ps for $x = 2$ [40,51] is overcompensated by the layer thickness d. Second, the subsequent falling edge shows an almost linear strain decrease from 25 to 50 ps for NIR excitation, whereas for NUV excitation the slope shows an exponential-like decrease. This is observed for both samples and is due to the nearly homogeneous nonlinear absorption in contrast to the steeper intensity profile for linear absorption, displayed in Fig. 1(b). The absorption profiles lead to different stress profiles inside the layer. Consequently, a rectangular-shaped bipolar strain wave is launched upon NIR excitation and a semiexponential-shaped bipolar strain wave is launched upon NUV excitation [8]. The average strain in the Bi:YIG layer is shaped accordingly [52], which we monitor directly with UXRD [3,8,53]. The different intensity profiles also determine the deposition of heat. This explains the third difference observed at timescales beyond 1 ns when $\eta(t)$ retains a constant value for NUV excitation and decreases at NIR excitation. We attribute this to a stronger heat gradient at the Bi:YIG/GGG interface and faster cooling to the substrate for NIR excitation.

We conclude our measurements with a variation of the NIR pulse duration to examine the lifetime of the transient state of the two-photon process. At a fluence of 100 mJ/cm^2 we tuned the pump pulse duration from $\tau = 75$ to 400 fs. The transient strain response, depicted in Fig. 2(c), is qualitatively very similar to the data in Fig. 2(b). The dependence of the average strain $\overline{\eta}(\tau)$ on the pulse duration τ is analyzed in Fig. 3(b). The fit shows an inverse proportionality between $\overline{\eta}$ and τ. The two-photon absorption for the shortest pulse durations of 75 fs with opposite linear chirp show deviations which we attribute to a higher-order chirp. The fit in Fig. 3(b) only includes the red data points which have the same sign of the linear chirp which was controlled by the grating compressor of the laser system. We corrected the pulse durations measured at the autocorrelator according to the group delay dispersion GDD $\approx -500 \pm 200$ fs^2 of the mirrors between the autocorrelator and the sample.

Both the fluence and pulse duration dependence of the strain are consistent with a model which is based on one- and two-photon absorption processes. In the following we present the modeling to fit the strain data in Fig. 3 and to determine the two-photon absorption coefficient β of Bi:YIG for NIR light. Lambert-Beer's law can be modified by a second-order term to account for two-photon absorption [see Eq. (2)] [54,55]. Starting from the attenuation of light in matter at the depth z due to one- and two-photon absorption, we solve the following equation for the intensity I,

$$\frac{\partial I}{\partial z} = -\alpha I - \beta I^2, \tag{2}$$

where α is the one- and β the two-photon absorption coefficient. In the case of linear one-photon absorption, i.e., for NUV light, we set $\beta = 0$, which results in Lambert-Beer's law [see Eq. (3)]. In the case of NIR light, we set $\alpha = 0$ to model the strain generated solely by two-photon absorption as suggested by the data in Fig. 3(a). If I_0 is the incident intensity on the Bi:YIG layer, the solutions of Eq. (2) are

$$I(z) = \begin{cases} I_0 e^{-\alpha z} & \text{for NUV,} \\ \frac{I_0}{1+\beta I_0 z} & \text{for NIR.} \end{cases} \tag{3}$$

Since the layer thickness is much smaller than the penetration depth of the NIR light, we may Taylor-expand Eq. (3) at $z = 0$, i.e., $I(z) = I_0 - \beta I_0^2 z + O(z^2)$. The linear spatial intensity dependence is a good approximation for NIR light [see Fig. 1(b)]. For time-resolved measurements, the incident intensity I_0 is time dependent. In this experiment, the excitation pulse can be well approximated by a Gaussian envelope $I_0(t) = 2\sqrt{\ln 2/\pi}\, F_\mathrm{i}/\tau \exp(-4 \ln 2\, t^2/\tau^2)$, where F_i is the incident fluence, and τ is the pulse duration at FWHM. The absorbed fluence inside the Bi:YIG layer $F_\mathrm{a}(F_\mathrm{i}, \tau)$ is calculated via temporal integration of the intensity difference from the sample surface ($z = 0$) to the layer-substrate interface ($z = d$)

$$F_\mathrm{a}(F_\mathrm{i}, \tau) = \int_{-\infty}^{\infty} I_0(t) - I(z = d, t)dt \tag{4}$$

$$= \begin{cases} (1 - e^{-\alpha d})F_\mathrm{i} & \text{for NUV,} \\ \sqrt{\frac{\ln 4}{\pi}}\beta d \frac{F_\mathrm{i}^2}{\tau} - O\left(\frac{F_\mathrm{i}^3}{\tau^2}\right) & \text{for NIR.} \end{cases} \tag{5}$$

The stress σ on the lattice resulting from the energy density deposited by the pump pulse $\rho^\mathrm{Q} = F_\mathrm{a}/d$ is given by the macroscopic Grüneisen parameter Γ via $\sigma = \Gamma \rho^\mathrm{Q}$ [3,46,47,56]. In the one-dimensional (1D) geometry of a homogeneously excited thin film with a cubic symmetry aligned to the sample surface, the strain response perpendicular to the surface is given by $\eta = \sigma / C_{11}$, where C_{11} is the cubic elastic constant. We estimate the mean strain in the Bi:YIG layer via the linear NUV absorption ($\beta = 0$),

$$\overline{\eta}_\mathrm{NUV} = \frac{\Gamma}{C_{11} d}(1 - e^{-\alpha d})F_\mathrm{i}. \tag{6}$$

The 2.1×10^{-4} per mJ/cm^2 calculated from Eq. (6) is in reasonable agreement with the strain $\overline{\eta}_\mathrm{NUV} = 2.3 \times 10^{-4}$ per mJ/cm^2 extracted from the blue line in Fig. 3(a). Here, we used a film thickness of $d = 135$ nm, the linear absorption coefficient for NUV light $\alpha = 6 \times 10^4$ cm^{-1}, the elastic constant $C_{11} = 190$ GPa for $Bi_2Y_1Fe_5O_{12}$, and the Grüneisen parameter of YIG, $\Gamma \approx 1$, reported in the literature [26,40,51,57]. The lattice strain $\overline{\eta}$ generated via nonlinear NIR absorption can also be calculated in the same manner with a different value of $C_{11} = 230$ GPa for $Bi_1Y_2Fe_5O_{12}$,

$$\overline{\eta}_\mathrm{NIR} = \frac{\Gamma}{C_{11}} \sqrt{\frac{\ln 4}{\pi}} \beta \frac{F_\mathrm{i}^2}{\tau}. \tag{7}$$

This equation describes the functional dependence of the strain on the fluence F_i and the pulse duration τ which we discovered experimentally upon NIR excitation. The red curves in Fig. 3 are calculated with Eq. (7), fitting the data precisely if we use $\beta = 2.4$ cm/GW as the two-photon absorption coefficient. We visualized the spatial intensity profile according to two-photon absorption in Fig. 1(b) by the red solid line. As a crosscheck we note that $\alpha I < \beta I^2$, already for comparably low intensities of $I = 0.1$ TW/cm^2 if we use the literature value $\alpha = 150$ cm^{-1} for NIR light [26]. This justifies neglecting the linear absorption term during the evaluation of the NIR data, since βI^2 is orders of magnitude larger than αI at intensities higher than $I = 1$ TW/cm^2.

A two-photon absorption coefficient of $\beta_\mathrm{YIG} = 130$ cm/GW was reported for undoped YIG at photon energies of $(1.17 + 1.93)$ eV $= 3.1$ eV [58]. Mainly, a two-step process via the ${}^6A_{1g}({}^6S) \rightarrow {}^4T_{1g}({}^4G)$ and subsequent ${}^4T_{1g}({}^4G) \rightarrow {}^4T_{1g}({}^4P)$ Fe^{3+}-ion transitions in YIG and Bi:YIG accounts for the two-photon absorption in both materials [27,59,60], i.e., the two-photon transition proceeds via real and short-lived levels. The bismuth substitution affects the electronic and optical properties of YIG, e.g., increasing spin-orbit coupling, absorption, and even second-harmonic generation (SHG) efficiency [39,61,62]. In particular, the very weak ${}^6A_{1g}({}^6S) \rightarrow {}^4T_{1g}({}^4G)$ transition energy shifts with doping and therefore modulates the one- and two-photon absorption coefficients. According to our modeling the previously reported β_YIG would yield a strain of 4% and an absorption of 60% at large peak intensities of 1 TW/cm^2, which contradicts the measured values of 0.1% strain and less than 5% absorption.

To summarize, we used UXRD to directly measure the strain in nanolayered Bi:YIG excited via one- and two-photon absorption. We identify the two-photon process by the quadratic fluence dependence and the inversely proportional pulse duration dependence of the photoexcited strain. The latter also proves that the intermediate state is short lived. We substantiate our findings by a quantitative fit with Lambert-Beer's law with a two-photon absorption extension in combination with the Grüneisen approach, where the absorbed energy is proportional to the lattice strain, independent of how the photon energy is absorbed. From this, we determine the two-photon absorption coefficient $\beta \approx 2$ cm/GW for exciting $Bi_1Y_2Fe_5O_{12}$ at 800 nm. We believe that our quantitative evaluation of the strain generated by two-photon absorption is particularly important for a full understanding of light-driven spin manipulation in magnetic insulators [23,27,32–38], but it has more general relevance for ultrafast science on supposedly nonabsorbing or transparent matter. The large peak intensities around 1 TW/cm^2 necessary to drive 0.1% strain can be achieved both by high pump fluences and short pulse durations.

We acknowledge the BMBF for the financial support via 05K16IPA and the DFG via BA 2281/8-1 and BA 2281/11-1. M.D. thanks the Alexander von Humboldt Foundation for financial support. We acknowledge the precharacterization of the crystalline thin films at the XPP-KMC3 synchrotron-radiation beamline D13.2 at the BESSY II electron storage ring operated by the Helmholtz-Zentrum Berlin.

[1] J. Pudell, A. A. Maznev, M. Herzog, M. Kronseder, C. H. Back, G. Malinowski, A. von Reppert, and M. Bargheer, Layer specific observation of slow thermal equilibration in ultrathin metallic nanostructures by femtosecond X-ray diffraction, Nat. Commun. **9**, 3335 (2018).

[2] M. Highland, B. C. Gundrum, Y. K. Koh, R. S. Averback, D. G. Cahill, V. C. Elarde, J. J. Coleman, D. A. Walko, and E. C. Landahl, Ballistic-phonon heat conduction at the nanoscale as revealed by time-resolved x-ray diffraction and time-domain thermoreflectance, Phys. Rev. B **76**, 075337 (2007).

[3] J. Pudell, A. von Reppert, D. Schick, F. Zamponi, M. Rössle, M. Herzog, H. Zabel, and M. Bargheer, Ultrafast negative thermal expansion driven by spin disorder, Phys. Rev. B **99**, 094304 (2019).

[4] C. Dornes, Y. Acremann, M. Savoini, M. Kubli, M. J. Neugebauer, E. Abreu, L. Huber, G. Lantz, C. A. F. Vaz, H. Lemke, E. M. Bothschafter, M. Porer, V. Esposito, L. Rettig, M. Buzzi, A. Alberca, Y. W. Windsor, P. Beaud, U. Staub, D. Zhu *et al.*, The ultrafast Einstein–de Haas effect, Nature (London) **565**, 209 (2019).

[5] C. Thomsen, H. T. Grahn, H. J. Maris, and J. Tauc, Surface generation and detection of phonons by picosecond light pulses, Phys. Rev. B **34**, 4129 (1986).

[6] P. Ruello and V. E. Gusev, Physical mechanisms of coherent acoustic phonons generation by ultrafast laser action, Ultrasonics **56**, 21 (2015).

[7] O. Matsuda, M. C. Larciprete, R. Li Voti, and O. B. Wright, Fundamentals of picosecond laser ultrasonics, Ultrasonics **56**, 3 (2015).

[8] D. Schick, M. Herzog, A. Bojahr, W. Leitenberger, A. Hertwig, R. Shayduk, and M. Bargheer, Ultrafast lattice response of photoexcited thin films studied by X-ray diffraction, Struct. Dyn. **1**, 064501 (2014).

[9] D. Daranciang, M. J. Highland, H. Wen, S. M. Young, N. C. Brandt, H. Y. Hwang, M. Vattilana, M. Nicoul, F. Quirin, J. Goodfellow, T. Qi, I. Grinberg, D. M. Fritz, M. Cammarata, D. Zhu, H. T. Lemke, D. A. Walko, E. M. Dufresne, Y. Li, J. Larsson *et al.*, Ultrafast Photovoltaic Response in Ferroelectric Nanolayers, Phys. Rev. Lett. **108**, 087601 (2012).

[10] C. Rose-Petruck, R. Jimenez, T. Guo, A. Cavalieri, C. W. Siders, F. Rksi, J. A. Squier, B. C. Walker, K. R. Wilson, and C. P. J. Barty, Picosecond-milliangstrom lattice dynamics measured by ultrafast X-ray diffraction, Nature (London) **398**, 310 (1999).

[11] K. Sokolowski-Tinten, C. Blome, C. Dietrich, A. Tarasevitch, M. Horn von Hoegen, D. von der Linde, A. Cavalleri, J. Squier, and M. Kammler, Femtosecond X-Ray Measurement of Ultrafast Melting and Large Acoustic Transients, Phys. Rev. Lett. **87**, 225701 (2001).

[12] D. Schick, M. Herzog, H. Wen, P. Chen, C. Adamo, P. Gaal, D. G. Schlom, P. G. Evans, Y. Li, and M. Bargheer, Localized Excited Charge Carriers Generate Ultrafast Inhomogeneous Strain in the Multiferroic $BiFeO_3$, Phys. Rev. Lett. **112**, 097602 (2014).

[13] M. Bargheer, N. Zhavoronkov, J. C. Woo, D. S. Kim, M. Woerner, and T. Elsaesser, Excitation mechanisms of coherent phonons unravelled by femtosecond X-ray diffraction, Phys. Status Solidi A **243**, 2389 (2006).

[14] G. J. Williams, S. Lee, D. A. Walko, M. A. Watson, W. Jo, D. R. Lee, and E. C. Landahl, Direct measurements of multi-photon induced nonlinear lattice dynamics in semiconductors via time-resolved x-ray scattering, Sci. Rep. **6**, 39506 (2016).

[15] J. V. Jäger, A. V. Scherbakov, T. L. Linnik, D. R. Yakovlev, M. Wang, P. Wadley, V. Holy, S. A. Cavill, A. V. Akimov, A. W. Rushforth, and M. Bayer, Picosecond inverse magnetostriction in galfenol thin films, Appl. Phys. Lett. **103**, 032409 (2013).

[16] J.-W. Kim, M. Vomir, and J.-Y. Bigot, Ultrafast Magnetoacoustics in Nickel Films, Phys. Rev. Lett. **109**, 166601 (2012).

[17] J.-W. Kim, M. Vomir, and J.-Y. Bigot, Controlling the spins angular momentum in ferromagnets with sequences of picosecond acoustic pulses, Sci. Rep. **5**, 8511 (2015).

[18] D. Afanasiev, I. Razdolski, K. M. Skibinsky, D. Bolotin, S. V. Yagupov, M. B. Strugatsky, A. Kirilyuk, T. Rasing, and A. V. Kimel, Laser Excitation of Lattice-Driven Anharmonic Magnetization Dynamics in Dielectric $FeBO_3$, Phys. Rev. Lett. **112**, 147403 (2014).

[19] A. Stupakiewicz, K. Szerenos, D. Afanasiev, A. Kirilyuk, and A. V. Kimel, Ultrafast nonthermal photo-magnetic recording in a transparent medium, Nature (London) **542**, 71 (2017).

[20] F. Hansteen, A. Kimel, A. Kirilyuk, and T. Rasing, Femtosecond Photomagnetic Switching of Spins in Ferrimagnetic Garnet Films, Phys. Rev. Lett. **95**, 047402 (2005).

[21] A. V. Kimel, A. Kirilyuk, P. A. Usachev, R. V. Pisarev, A. M. Balbashov, and T. Rasing, Ultrafast non-thermal control of magnetization by instantaneous photomagnetic pulses, Nature (London) **435**, 655 (2005).

[22] C. Tzschaschel, K. Otani, R. Iida, T. Shimura, H. Ueda, S. Günther, M. Fiebig, and T. Satoh, Ultrafast optical excitation of coherent magnons in antiferromagnetic NiO, Phys. Rev. B **95**, 174407 (2017).

[23] A. Stupakiewicz, A. Maziewski, I. Davidenko, and V. Zablotskii, Light-induced magnetic anisotropy in Co-doped garnet films, Phys. Rev. B **64**, 064405 (2001).

[24] Y. Hashimoto, S. Daimon, R. Iguchi, Y. Oikawa, K. Shen, K. Sato, D. Bossini, Y. Tabuchi, T. Satoh, B. Hillebrands, G. E. W. Bauer, T. H. Johansen, A. Kirilyuk, T. Rasing, and E. Saitoh, All-optical observation and reconstruction of spin wave dispersion, Nat. Commun. **8**, 15859 (2017).

[25] Y. Hashimoto, D. Bossini, T. H. Johansen, E. Saitoh, A. Kirilyuk, and T. Rasing, Frequency and wavenumber selective excitation of spin waves through coherent energy transfer from elastic waves, Phys. Rev. B **97**, 140404(R) (2018).

[26] G. B. Scott, D. E. Lacklison, and J. L. Page, Absorption spectra of $Y_3Fe_5O_{12}$ (YIG) and $Y_3Ga_5O_{12}$:Fe^{3+}, Phys. Rev. B **10**, 971 (1974).

[27] M. Deb, P. Molho, B. Barbara, and J.-Y. Bigot, Controlling laser-induced magnetization reversal dynamics in a rare-earth iron garnet across the magnetization compensation point, Phys. Rev. B **97**, 134419 (2018).

[28] J. M. Robertson, S. Wittekoek, T. J. A. Popma, and P. F. Bongers, Preparation and optical properties of single crystal thin films of bismuth substituted iron garnets for magneto-optic applications, Appl. Phys. **2**, 219 (1973).

[29] A. V. Chumak, V. Vasyuchka, A. Serga, and B. Hillebrands, Magnon spintronics, Nat. Phys. **11**, 453 (2015).

[30] A. A. Serga, A. V. Chumak, B. Hillebrands, A. A. Serga, B. Hillebrands, A. V. Chumak, and T. Neumann, YIG magnonics, J. Phys. D **43**, 264002 (2010).

[31] G. E. W. Bauer, E. Saitoh, and B. J. van Wees, Spin caloritronics, Nat. Mater. **11**, 391 (2012).

[32] L. A. Shelukhin, V. V. Pavlov, P. A. Usachev, P. Y. Shamray, R. V. Pisarev, and A. M. Kalashnikova, Ultrafast laser-induced changes of the magnetic anisotropy in a low-symmetry iron garnet film, Phys. Rev. B **97**, 014422 (2018).

[33] C. S. Davies, K. H. Prabhakara, M. D. Davydova, K. A. Zvezdin, T. B. Shapaeva, S. Wang, A. K. Zvezdin, A. Kirilyuk, T. Rasing, and A. V. Kimel, Anomalously Damped

Heat-Assisted Route for Precessional Magnetization Reversal in an Iron Garnet, Phys. Rev. Lett. **122**, 027202 (2019).

[34] A. V. Kimel, A. Kirilyuk, A. Tsvetkov, R. V. Pisarev, and T. Rasing, Laser-induced ultrafast spin reorientation in the antiferromagnet $TmFeO_3$, Nature (London) **429**, 850 (2004).

[35] A. M. Kalashnikova, A. V. Kimel, R. V. Pisarev, V. N. Gridnev, A. Kirilyuk, and T. Rasing, Impulsive Generation of Coherent Magnons by Linearly Polarized Light in the Easy-Plane Antiferromagnet $FeBO_3$, Phys. Rev. Lett. **99**, 167205 (2007).

[36] A. M. Kalashnikova, A. V. Kimel, R. V. Pisarev, V. N. Gridnev, P. A. Usachev, A. Kirilyuk, and T. Rasing, Impulsive excitation of coherent magnons and phonons by subpicosecond laser pulses in the weak ferromagnet $FeBO_3$, Phys. Rev. B **78**, 104301 (2008).

[37] B. Koene, M. Deb, E. Popova, N. Keller, T. Rasing, and A. Kirilyuk, Spectrally resolved optical probing of laser induced magnetization dynamics in bismuth iron garnet, J. Phys.: Condens. Matter **28**, 276002 (2016).

[38] M. Deb, E. Popova, M. Hehn, N. Keller, S. Petit-Watelot, M. Bargheer, S. Mangin, and G. Malinowski, Femtosecond Laser-Excitation-Driven High Frequency Standing Spin Waves in Nanoscale Dielectric Thin Films of Iron Garnets, Phys. Rev. Lett. **123**, 027202 (2019).

[39] M. Deb, E. Popova, A. Fouchet, and N. Keller, Magneto-optical Faraday spectroscopy of completely bismuth-substituted $Bi_3Fe_5O_{12}$ garnet thin films, J. Phys. D **45**, 455001 (2012).

[40] G. G. Siu, C. M. Lee, and Y. Liu, Magnons and acoustic phonons in $Y_{3-x}Bi_xFe_5O_{12}$, Phys. Rev. B **64**, 094421 (2001).

[41] D. Schick, A. Bojahr, M. Herzog, C. Von Korff Schmising, R. Shayduk, W. Leitenberger, P. Gaal, and M. Bargheer, Normalization schemes for ultrafast x-ray diffraction using a table-top laser-driven plasma source, Rev. Sci. Instrum. **83**, 025104 (2012).

[42] The double-peak structure of the unexcited sample results from the $K\alpha_1$ and $K\alpha_2$ photons emitted by the source. The inhomogeneous excitation results in a broadening of the maxima.

[43] D. Schick, R. Shayduk, A. Bojahr, M. Herzog, C. von Korff Schmising, P. Gaal, and M. Bargheer, Ultrafast reciprocal-space mapping with a convergent beam, J. Appl. Crystallogr. **46**, 1372 (2013).

[44] M. Kozina, T. Hu, J. S. Wittenberg, E. Szilagyi, M. Trigo, T. A. Miller, C. Uher, A. Damodaran, L. Martin, A. Mehta, J. Corbett, J. Safranek, D. A. Reis, and A. M. Lindenberg, Measurement of transient atomic displacements in thin films with picosecond and femtometer resolution, Struct. Dyn. **1**, 034301 (2014).

[45] H. Wen, P. Chen, M. P. Cosgriff, D. A. Walko, J. H. Lee, C. Adamo, R. D. Schaller, J. F. Ihlefeld, E. M. Dufresne, D. G. Schlom, P. G. Evans, J. W. Freeland, and Y. Li, Electronic Origin of Ultrafast Photoinduced Strain in $BiFeO_3$, Phys. Rev. Lett. **110**, 037601 (2013).

[46] A. von Reppert, J. Pudell, A. Koc, M. Reinhardt, W. Leitenberger, K. Dumesnil, F. Zamponi, and M. Bargheer, Persistent nonequilibrium dynamics of the thermal energies in the spin and phonon systems of an antiferromagnet, Struct. Dyn. **3**, 054302 (2016).

[47] T. Henighan, M. Trigo, S. Bonetti, P. Granitzka, D. Higley, Z. Chen, M. P. Jiang, R. Kukreja, A. Gray, A. H. Reid, E. Jal, M. C. Hoffmann, M. Kozina, S. Song, M. Chollet, D. Zhu, P. F. Xu, J. Jeong, K. Carva, P. Maldonado *et al.*, Generation mechanism of terahertz coherent acoustic phonons in Fe, Phys. Rev. B **93**, 220301(R) (2016).

[48] N. P. Padture and P. G. Klemens, Low thermal conductivity in garnets, J. Am. Ceram. Soc. **80**, 1018 (2005).

[49] G. A. Slack and D. W. Oliver, Thermal conductivity of garnets and phonon scattering by rare-earth ions, Phys. Rev. B **4**, 592 (1971).

[50] I. Razdolski, A. Alekhin, N. Ilin, J. P. Meyburg, V. Roddatis, D. Diesing, U. Bovensiepen, and A. Melnikov, Nanoscale interface confinement of ultrafast spin transfer torque driving non-uniform spin dynamics, Nat. Commun. **8**, 15007 (2017).

[51] M. Deb, E. Popova, M. Hehn, N. Keller, S. Mangin, and G. Malinowski, Picosecond acoustic-excitation-driven ultrafast magnetization dynamics in dielectric Bi-substituted yttrium iron garnet, Phys. Rev. B **98**, 174407 (2018).

[52] D. Schick, P. Gaal, A. Bojahr, W. Leitenberger, R. Shayduk, A. Hertwig, I. Vrejoiu, M. Herzog, and M. Bargheer, Ultrafast x-ray diffraction studies of photoexcited coherent phonons in $SrRuO_3$ thin films, arXiv:1301.3324.

[53] S. P. Zeuschner, T. Parpiiev, T. Pezeril, A. Hillion, K. Dumesnil, A. Anane, J. Pudell, L. Willig, M. Rössle, M. Herzog, A. von Reppert, and M. Bargheer, Tracking picosecond strain pulses in heterostructures that exhibit giant magnetostriction, Struct. Dyn. **6**, 24302 (2019).

[54] M. Bass, E. W. van Stryland, D. R. Williams, and W. L. Wolfe, *Handbook of Optics Volume I*, 2nd ed. (McGraw-Hill, New York, 1995).

[55] J.-C. Diels and W. Rudolph, *Ultrashort Laser Pulse Phenomena: Fundamentals, Techniques, and Applications on a Femtosecond Time Scale*, 2nd ed. (Elsevier/Academic, Amsterdam, 2006), p. 652.

[56] A. Koc, M. Reinhardt, A. von Reppert, M. Rössle, W. Leitenberger, M. Gleich, M. Weinelt, F. Zamponi, and M. Bargheer, Grueneisen-approach for the experimental determination of transient spin and phonon energies from ultrafast x-ray diffraction data: Gadolinium, J. Phys.: Condens. Matter **29**, 264001 (2017).

[57] G. A. Saunders, S. C. Parker, N. Benbattouche, and H. L. Alberts, Elastic and nonlinear acoustic properties of the terbium iron garnet $Tb_3Fe_5O_{12}$ in relation to those of other garnets, Phys. Rev. B **46**, 8756 (1992).

[58] S. I. Shablaev and R. V. Pisarev, Two-photon absorption spectroscopy of electronic states in yttrium iron garnet $Y_3Fe_5O_{12}$, J. Magn. Soc. Jpn. **11**, 19 (1987).

[59] J. F. Dillon, Optical absorptions and rotations in the ferrimagnetic garnets, J. Phys. Radium **20**, 374 (1959).

[60] K. A. Wickersheim and R. A. Lefever, Absorption spectra of ferric iron-containing oxides, J. Chem. Phys. **36**, 844 (1962).

[61] T. Oikawa, S. Suzuki, and K. Nakao, First-principles study of spin-orbit interactions in bismuth iron garnet, J. Phys. Soc. Jpn. **74**, 401 (2005).

[62] G. Petrocelli, S. Martellucci, and M. Richetta, Bismuth induced enhancement of the second-harmonic generation efficiency in bismuth-substituted yttrium iron garnet films, Appl. Phys. Lett. **63**, 3402 (1993).

IV Spin stress contribution to the lattice dynamics of FePt

Alexander von Reppert, Lisa Willig, Jan-Etienne Pudell, Steffen Peer Zeuschner, Gabriel Sellge, Fabian Ganss, Olav Hellwig, Jon Ander Arregi, Vojteč Uhlíř, Aurélien Crut and Matias Bargheer

Science Advances Vol.6, No.28 (2020)

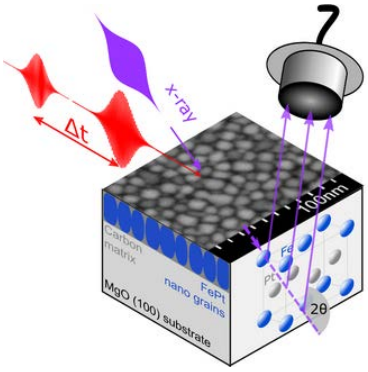

Abstract Invar-behavior occurring in many magnetic materials has long been of interest to materials science. Here, we show not only invar behavior of a continuous film of FePt but also even negative thermal expansion of FePt nanograins upon equilibrium heating. Yet, both samples exhibit pronounced transient expansion upon laser heating in femtosecond x-ray diffraction experiments. We show that the granular microstructure is essential to support the contractive out-of-plane stresses originating from in-plane expansion via the Poisson effect that add to the uniaxial contractive stress driven by spin disorder. We prove the spin contribution by saturating the magnetic excitations with a first laser pulse and then detecting the purely expansive response to a second pulse. The contractive spin stress is reestablished on the same 100 ps time scale that we observe for the recovery of the ferromagnetic order. Finite-element modeling of the mechanical response of FePt nanosystems confirms the morphology dependence of the dynamics.

Contributions to the work

I supported Alexander von Reppert to perform the X-Ray diffraction measurements and to commission the double-pulse excitation setup. I commented on the manuscript. The samples were provided by the group of Olav Hellwig.

Comments

In this publication we investigated the ultrafast response of the popular ferromagnetic material FePt with three motivations in mind. On the one side, it is investigated due to its Invar-behavior [92]. This means that it does not expand with increasing temperature due to conventional thermal expansion nor contract due to a dominating magnetic stress as it is the case for Dysprosium, see Article II. Instead, the lattice dimensions stay constant over a wide range of temperatures due to cancellation of an expansive phonon- and compressive spin-stress. On the other side, FePt is already used in the new HAMR technology, see Sec. 1.2, as it exhibits a large and strongly temperature dependent magnetic anisotropy which is paramount for HAMR storage devices [25, 27]. Finally, we investigated the Poisson effect on an ultrafast timescale, which leads to different lattice expansions, depending on the morphology of the sample [54, 93].

We found, that the lattice response upon femtosecond laser excitation is not Invar-like and that it depends on the morphology of the sample, if an initial contraction or expansion is observed. Furthermore, the interpretation of the ultrafast lattice dynamics can not be thought without an interplay of the contractive magnetic stress and the expansive incoherent phonon pressure, which leads to the Invar-behavior in equilibrium. I want to highlight, that it was possible for us to quantify the contribution of the magnetic stress onto the lattice with the double-pulse technique [56, 53]. In this ingenious experimental configuration, the sample is pumped twice to first heat the phonon and spin system simultaneously above the Curie temperature which switches off any magnetic stress contributions in the second excitation pulse. The difference of the initial and second lattice response thus yields the impact of the spin system onto the lattice via inverse magnetostriction on an ultrafast timescale.

SCIENCE ADVANCES | RESEARCH ARTICLE

PHYSICS

Spin stress contribution to the lattice dynamics of FePt

A. von Reppert[1], L. Willig[1,2], J.-E. Pudell[1,2], S. P. Zeuschner[1,2], G. Sellge[3,4], F. Ganss[3], O. Hellwig[3,4], J. A. Arregi[5], V. Uhlíř[5,6], A. Crut[7], M. Bargheer[1,2]*

Invar-behavior occurring in many magnetic materials has long been of interest to materials science. Here, we show not only invar behavior of a continuous film of FePt but also even negative thermal expansion of FePt nanograins upon equilibrium heating. Yet, both samples exhibit pronounced transient expansion upon laser heating in femtosecond x-ray diffraction experiments. We show that the granular microstructure is essential to support the contractive out-of-plane stresses originating from in-plane expansion via the Poisson effect that add to the uniaxial contractive stress driven by spin disorder. We prove the spin contribution by saturating the magnetic excitations with a first laser pulse and then detecting the purely expansive response to a second pulse. The contractive spin stress is reestablished on the same 100-ps time scale that we observe for the recovery of the ferromagnetic order. Finite-element modeling of the mechanical response of FePt nanosystems confirms the morphology dependence of the dynamics.

INTRODUCTION

Invar materials exhibit almost zero thermal expansion over a wide temperature range (*1*). Although the discovery of a 10-fold reduction of the thermal expansion of the $Fe_{0.65}Ni_{0.35}$ alloy compared to its pure elements (*2*) dates back to 1897, its origin remained an active area of solid-state research over the next century (*3*–*5*). Invar behavior requires a mechanism that counteracts the thermal expansion resulting from anharmonic phonon-phonon interactions. For magnetic invar materials, it is found that the required contractive stress originates from an increased volume for the spin-ordered state compared to the disordered state that can now be predicted in different ab initio approaches (*4*, *5*). Quantitative, time-resolved studies of the structural dynamics have recently started to explore the response of the lattice to magnetic stresses (*6*–*12*), which are attributed to the transfer of angular momentum (*6*, *7*), energy (*8*, *12*), and entropy (*9*) from and to the spin system. In this context, it is interesting to ask how invar materials respond to laser-induced heating on the picosecond time scale and to determine the lattice dynamics induced by counteracting contributions of phonon and spin stresses.

One approach for the separation of the magnetic response from the ever-present phonon contribution to the lattice dynamics in laser-excited metals is to compare the structural response above and below the magnetic ordering temperature (*8*–*10*). This is sometimes prohibited by irreversible modifications of the material under heating. A demagnetized state can also be created transiently by femtosecond laser excitation (*13*, *14*) and characterized by applying a pump-probe sequence, where a second pump pulse excites the nonequilibrium state generated by the first pump pulse. Double-pulse excitation experiments not only have been used to demonstrate intriguing coherent control of the magnetization (*15*–*17*) and lattice dynamics (*18*, *19*) but they also revealed that the induced magnetization dynamics, (*20*) total transient demagnetization (*21*), and magnetic anisotropy (*22*) critically depend on the pulse-to-pulse separation.

Invar behavior is found in many Fe-containing alloys (*1*, *23*). The magnetic recording medium FePt in the fully ordered $L1_0$ phase is receiving particular attention due to its large uniaxial magnetic anisotropy energy ($K_u > 4.5$ J/cm^3) (*24*), which sustains nanoscopic magnetically stable bits with perpendicular magnetization. The envisioned heat-assisted magnetic recording scheme (*25*) aims at improving the magnetic information densities to exceed 2 Tb/in^2 in commercial products of the near future (*26*). The possibility to grow magnetic, oriented nanograins with a high degree of structural order makes this material an ideal candidate for studying the lattice using time-resolved diffraction techniques. In a recent ultrafast x-ray diffraction (UXRD) study, we have found a short-lived lattice contraction along the short out-of-plane *c* axis of the tetragonal unit cell of a nanogranular FePt film on a substrate, whereas continuous epitaxial thin films merely expanded under otherwise identical excitation conditions (*27*). Previously, ultrafast electron diffraction experiments had reported a transient *c*-axis contraction and in-plane expansion for freestanding FePt nanograins (*11*). Spin-polarized density functional theory consistently predicts this tetragonal distortion when comparing the spin-ordered ferromagnetic ground state to the paramagnetic phase with full spin disorder (*11*). In the same paper, a strongly anisotropic phonon stress was predicted, seven times larger in-plane than out-of-plane (*11*). In all three cases the material is the $L1_0$ phase of FePt. Therefore, the variability of the measured ultrafast dynamics suggests that the morphology and substrate-induced strain must have an important influence on the lattice dynamics at ultrafast time scales.

Here, we use fluence-dependent UXRD experiments on granular FePt thin films to show experimentally that the initial contraction originates from spin entropy, as it saturates for high fluence when the spin system is disordered. Weak excitation pulses trigger an initial contraction driven by spin stress, but expansive lattice stresses prevail after about 3 ps. The direct connection of spin disorder with the contractive stress is revealed by double-pulse excitation scenarios. When a strong first excitation pulse has essentially disordered the

[1]Institute of Physics and Astronomy, University of Potsdam, Karl-Liebknecht-Str. 24-25, 14476 Potsdam, Germany. [2]Helmholtz-Zentrum Berlin für Materialien und Energie GmbH, Wilhelm-Conrad-12 Röntgen Campus, BESSY II, Albert-Einstein-Str. 15, 12489 Berlin, Germany. [3]Institut für Physik, Technische Universität Chemnitz, Reichenhainer Str. 70, 09126 Chemnitz, Germany. [4]Institut für Ionenstrahlphysik und Materialforschung, Helmholtz-Zentrum Dresden-Rossendorf, Bautzner Landstrasse 400, 01328 Dresden, Germany. [5]CEITEC BUT, Brno University of Technology, Purkyňova 123, 612 00 Brno, Czechia. [6]Institute of Physical Engineering, Brno University of Technology, Technická 2, 616 69 Brno, Czechia. [7]FemtoNanoOptics Group, Institut Lumière Matière, Université de Lyon, CNRS-Université Lyon 1, 69622 Villeurbanne, France.
*Corresponding author. Email: bargheer@uni-potsdam.de

spin system, a second excitation pulse applied after a short delay only triggers expansion.

However, if the second pulse arrives about 100 ps later, the spin order has partially recovered, and the second pulse yields a contraction. This time scale for the recovery of the contractive stress is dictated by thermal transport and identical to the time scale of remagnetization observed in time-resolved magneto-optical Kerr effect (tr-MOKE) measurements. We model the coupled out-of-plane and in-plane lattice response of the nanograins using finite-element modeling (FEM) by varying the amplitude of the uniaxial contractive stress component $\sigma_{\perp}^{sp}$ associated with the spin disorder, which is the essential parameter for describing the two-pulse experiments. To provide a solid experimental basis for our interpretation, we compare granular films composed of FePt grains in a carbon matrix to continuous films, where the in-plane expansion on the picosecond time scale is forbidden by symmetry.

RESULTS

Time-resolved and static expansion

We first discuss the lattice response of FePt to laser excitation and equilibrium heating. Figure 1 (A and B) compares the lattice response of a granular and a continuous film of similar thickness to 100-fs pump laser pulses for incident laser fluences ranging from F_{in} = 1.4 to 11 mJ/cm^2 (see Materials and Methods for details). To show that lattice expansion beyond 3 ps is approximately proportional to F_{in} and thus to the energy density, we have normalized the observed out-of-plane strain $\eta_{\perp}$ to the incident laser fluence. Because the phonon system hosts most of the energy density at this time, the strain per fluence is approximately the same, and variations are due to energy absorbed in the spin system. The central finding for the granular film (Fig. 1A) is the pronounced contraction in the first 2 ps. Its absolute value is maximized for medium laser fluences, and the contraction disappears upon increasing the laser fluence further (see Supplementary Materials for the unscaled data). This already hints at the spin disorder as the driving mechanism of the contraction. The UXRD results in Fig. 1B show that the contraction is essentially absent for the continuous FePt film at all fluences. The small delay of the expansion observed in Fig. 1B for low laser fluences suggests that expansive and contractive out-of-plane stresses have different time dependences. Although the thermal expansion of bulk FePt solid solutions of different composition has been studied (*28*–*31*), static characterization of the out-of-plane expansion for continuous and granular $L1_0$-ordered thin films approaching the Curie temperature $T_C \approx 700$ K was, so far, not available. Our results in Fig 1C show that the out-of-plane dimension of $L1_0$-FePt behaves invar-like for the continuous film and even exhibits negative thermal expansion (NTE) for the granular FePt sample. The in-plane thermal expansion coefficient of FePt matches the value 1×10^{-5} K^{-1} of the MgO substrate (see Supplementary Materials), so that epitaxial stresses on the thin film upon equilibrium heating are expected to be small (*11*, *29*, *31*). Figure 1 thus directly contrasts that the FePt out-of-plane strain $\eta_{\perp}$ exhibits a pronounced difference between equilibrium heating, which shows NTE and invar behavior for granular and continuous FePt films, respectively, and ultrafast laser heating, where FePt mainly expands out-of-plane showing a positive strain $\eta_{\perp} = \Delta c/c$. We attribute the differences in $\eta_{\perp}(t)$ for the nanogranular and continuous FePt to the different magnitudes of in-plane strain $\eta_{\parallel}(t)$. The probed region is almost homogeneously heated as the excitation spot is three times

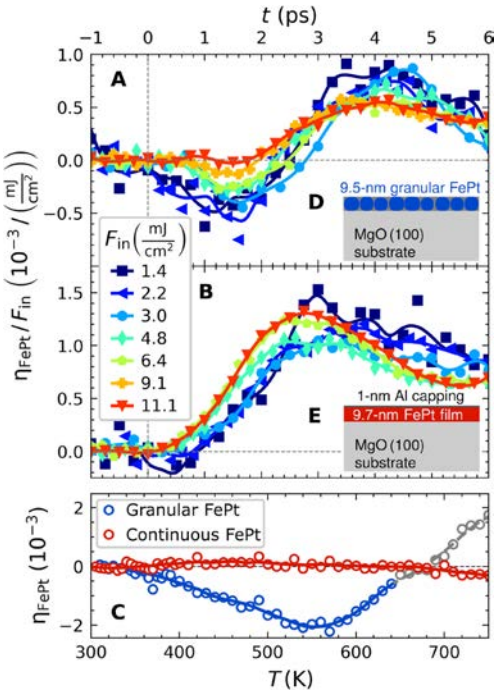

Fig. 1. Comparison of granular and continuous FePt film responses to laser excitation and equilibrium heating. (**A**) Normalized transient out-of-plane strain $\eta_{\perp}$ in FePt derived from the Bragg peak shift in UXRD experiments involving excitation of the granular FePt film with various incident fluences F_{in}. The observed strain is normalized to F_{in}. (**B**) Same for the continuous film. (**C**) Out-of-plane strain $\eta_{\perp}$ upon equilibrium heating for both samples. Points above 650 K are grayed out, because the Bragg peak intensity decrease by 20% of the granular sample may indicate a slight sample degradation. Solid lines serve as guide to the eye. The insets (**D**) and (**E**) schematically depict the sample structures.

larger than the probe pulses. Any in-plane stresses are therefore balanced by the adjacent unit cells for the continuous FePt film. The in-plane strain propagation from the edge of the excitation region to the probed region at the sound velocity sets the 100-ns time scale (much longer than those investigated in the time-resolved experiments) on which this in-plane fixation is relieved. For the granular FePt film, the inhomogeneity at the carbon-FePt interface enables transverse stresses and strains even on picosecond time scales, whereas they are forbidden by symmetry in the continuous film case. Under static heating conditions, both the substrate and the thin film can relax in-plane, which creates additional contractive elastic stresses out-of-plane via the Poisson effect. Thus, the static out-of-plane NTE of the granular film is reduced to an invar behavior in the continuous film, for which the in-plane expansion of FePt and hence the Poisson effect are limited by the epitaxial clamping to the substrate.

Double-pulse excitation: Spin stress tuning

The results of a double-pulse excitation scheme displayed in Fig. 2A confirm that the spin excitations drive the contraction in the granular FePt film. In these experiments, we use a first strong laser pulse (p_1) to saturate the spin excitations and a second, weaker laser pulse (p_2) for triggering subsequent dynamics with a delay Δt. The ultrashort

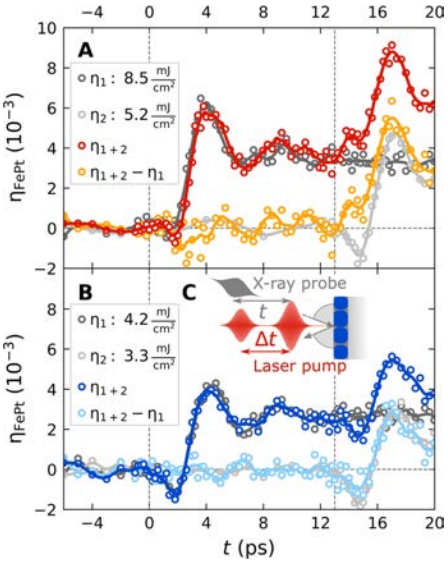

Fig. 2. UXRD with double-pulse excitation. (**A**) Transient strain $\eta(t)$ of the granular FePt film from UXRD with single- and double-pulse excitation. The first pulse at $t = 0$ has a fluence of $F_{in,1} = 8.5$ mJ/cm^2, and the second pulse at 13 ps is weaker ($F_{in,2} = 5.2$ mJ/cm^2). The nonequilibrium strains $\eta_{ne}(t) = \eta_{1+2}(t) - \eta_1(t)$ (orange) are derived by subtracting the dark gray curve from the red curve. This strain is induced by the photoexcitation in the nonequilibrium conditions set by the first pulse. (**B**) Same for weaker pump pulses $F_{in,1} = 4.2$ mJ/cm^2 and $F_{in,2} = 3.3$ mJ/cm^2, which only partially demagnetize the film. (**C**) Relative timing of the double-pulse excitation experiments.

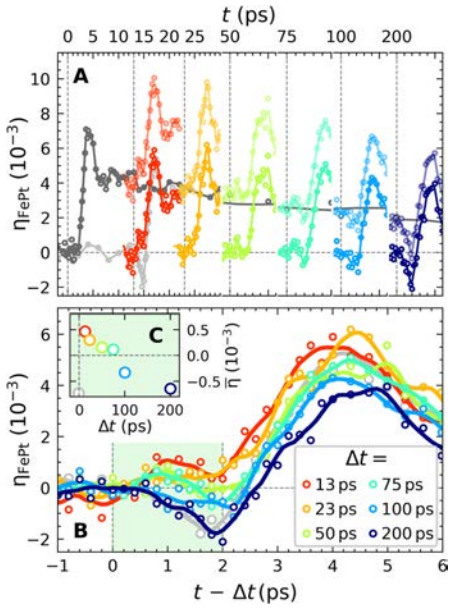

Fig. 3. Recovery of the spin entropy–driven lattice contraction. (**A**) Dark gray: transient strain $\eta_1(t)$ from UXRD with single-pulse excitation at $t = 0$ ($F_{in,1} = 8.5$ mJ/cm^2) for the granular film. Light-colored data: strain $\eta_{1+2}(t)$ observed for double-pulse excitation with the same first pulse and a second pulse with fluence ($F_{in,2} = 5.2$ mJ/cm^2) after $\Delta t = 13$, 23, 50, 75, 100, and 200 ps. The bright-colored data represent $\eta_{ne}(t) = \eta_{1+2}(t) - \eta_1(t)$. (**B**) Comparison of $\eta_{ne}(t - \Delta t)$ from (A) to the strain $\eta_2(t)$ obtained for excitation only with the second pulse (gray). (**C**) Average strain $\eta_{ne}(t - \Delta t)$ within the first 2 ps.

x-ray probe pulse detects the lattice dynamics $\eta_\perp(t)$ that is induced by this double-pulse excitation, as schematically depicted in Fig 2C. The dark gray data from Fig. 2A show the UXRD signal that characterizes the strain $\eta_1(t)$ due to a single strong pulse with $F_{in,1} = 8.5$ mJ/cm^2 at $t = 0$, which almost exclusively leads to expansion of the FePt film. In contrast, the light gray data representing the strain $\eta_2(t)$ generated by a weaker single pulse with $F_{in,2} = 5.2$ mJ/cm^2 arriving at $\Delta t = 13$ ps show a pronounced contraction at the onset of the second pulse, consistent with the fluence series in Fig. 1A. When both pulses excite the sample with the delay set to $\Delta t = 13$ ps, we observe the strain $\eta_{1+2}(t)$ (red data points). The orange points represent the additional strain $\eta_{ne}(t) = \eta_{1+2}(t) - \eta_1(t)$, which is induced by the photoexcitation of the sample in the nonequilibrium conditions previously set by the first pulse. It mainly differs from $\eta_2(t)$ (light gray curve in Fig. 2A) in the first 2 ps after the second laser pulse arrives. Clearly, there is no contraction at $t = 15$ ps just after the second pulse, if the sample was pre-excited with the first pulse. We conclude that the first pulse has essentially saturated the spin excitations. Figure 2B confirms this interpretation by reducing the fluences to $F_{in,1} = 4.2$ mJ/cm^2 and $F_{in,2} = 3.3$ mJ/cm^2 with the same timing. Now, $\eta_{ne}(t)$ shows approximately half of the contraction at $t = 15$ ps compared to $\eta_2(t)$ (light gray data) because the first pulse does not fully saturate the spin excitations.

Our double-pulse scheme also allows monitoring the recovery of the contractive stress by adjusting the timing between the excitation pulses for constant $F_{in,1}$ and $F_{in,2}$. Figure 3A depicts the results from Fig. 2A for tuning the double-pulse time delay Δt. Again, the gray line shows the strain induced only by the first pump pulse with $F_{in,1} = 8.5$ mJ/cm^2. Within 200 ps, the cooling of the FePt lattice reduces the transient strain from $\eta_\perp = 4 \times 10^{-3}$ to the half value. The light-colored lines show the strain $\eta_{1+2}(t)$ observed for double-pulse excitation, and the bright colors show the nonequilibrium strain $\eta_{ne}(t) = \eta_{1+2}(t) - \eta_1(t)$. Figure 3B reproduces these data on a time axis where $t = 0$ indicates the arrival of the second pulse and compares $\eta_{ne}(t - \Delta t)$ to $\eta_2(t)$ (light gray), i.e., the response to the second pulse with and without pre-excitation. For a pulse delay of $\Delta t = 200$ ps, $\eta_{ne}(t - \Delta t)$ and $\eta_2(t)$ nearly coincide in the first 3 ps, indicating a reordering of the spin system within this time scale. For time delays shorter than $\Delta t = 75$ ps, the lattice expansion prevails. The red line ($\Delta t = 13$ ps) transforms continuously into the dark blue line ($\Delta t = 200$ ps) with increasing time delay, indicating the emergence of the contractive stress as the spin system can be disordered again by the second pulse.

Magnetization dynamics and energy density

To corroborate our findings about the spin stress contribution to the lattice dynamics, we analyze the magnetic system. The spin stress contribution to the strain response must vanish if the magnetic system is in a state close to its maximal entropy that can be reached either thermally or via laser-induced demagnetization. According to recent FEM simulations of the field enhancement effects in the optical absorption of a similar nanogranular sample (*32*), the temperature change due to the inhomogeneous optical absorption of the irregularly shaped FePt nano-islands varies between 10 and

30%. For $F_{in,1}$ = 8.5 mJ/cm², we therefore estimate the temperature rise to be in the range ΔT = 300 to 700 K. The majority of the nanogranular FePt will be transiently heated above the Curie temperature, which is about $T_C \approx$ 650 to 700 K for the current particle size (*33*).

Figure 4A contains tr-MOKE data for three selected fluences. We assume nearly full demagnetization for the incident fluence of 11 mJ/cm², as the signal does not increase beyond this fluence. Consistent with literature, this sets the initial demagnetization for the pulses (8.5 mJ/cm²) used in the UXRD experiment from Figs. 3A and 2A at 85%. Because of the large out-of-plane anisotropy and the single-domain character of the grains (no domain wall propagation), we can use the tr-MOKE signal recorded with an external field of ±0.7 *T* as an estimation of the time-dependent average magnetization $M(t)$ of the sample (*34*). The static magnetization curve $M(T)$ of the granular FePt sample is depicted in Fig 4B. To relate the UXRD and tr-MOKE signal, we calculate an estimate for the spin contribution to the heat capacity (Fig. 4C) according to the mean field theory relation (*35*) $C_{sp} \propto \frac{\partial M^2}{\partial T} = M\frac{\partial M}{\partial T}$, which agrees reasonably well with recent theoretical predictions represented by the dashed line (*36*).

The colored dashed lines in Fig. 4 (A to C) indicate how the MOKE signal, which is proportional to $M(t)$, is related to the auxiliary temperature $T(t)$ of the spin system for the specific time $t = \Delta t$ of the UXRD experiment. This temperature is used to estimate the energy density $\Delta\rho^Q_{sp} = \int_T C_{sp}(T')\,dT'$, which would be required to fully saturate the heat capacity $C_{sp}(T)$ of the spin system. In a first-order analysis, the individual stresses from electrons, phonons, and spins $\sigma_{e,ph,sp} = \Gamma_{e,ph,sp}\rho^Q_{e,ph,sp}$ are directly proportional to the heat energy densities $\rho^Q_{e,ph,sp}$, and the dimensionless macroscopic Grueneisen coefficients $\Gamma_{e,\,ph,\,sp}$ describe the efficiency for generating stress from energy in each of the three systems (*8*).

To combine UXRD and tr-MOKE, we reproduce on the vertical axis of Fig. 4D the average lattice strain $\bar{\eta}$ from Fig. 3C, while the horizontal axis quantifies the fraction of the energy density $\Delta\rho^Q_{sp}(\Delta t)$ that the second pulse can still introduce into the spin system according to (Fig. 4C). For simplicity, we assume that after a short time delay Δt = 15 ps, the FePt is still nearly fully demagnetized (Fig. 4A), and almost no energy density $\Delta\rho^Q_{sp}$ can be deposited into the spin system. Hence, the second pulse only induces expansion, i.e., positive $\bar{\eta}(\Delta t)$ in Fig. 4D by exciting electrons and phonons. With increasing Δt, the contractive stress $\sigma_{sp} = \Gamma_{sp}\Delta\rho^Q_{sp}$ increases. The slope of Fig. 4D is proportional to the macroscopic Grueneisen constant Γ_{sp} of the spin system, which must, in fact, be negative to support the observed NTE or invar behavior (*3*, *37*).

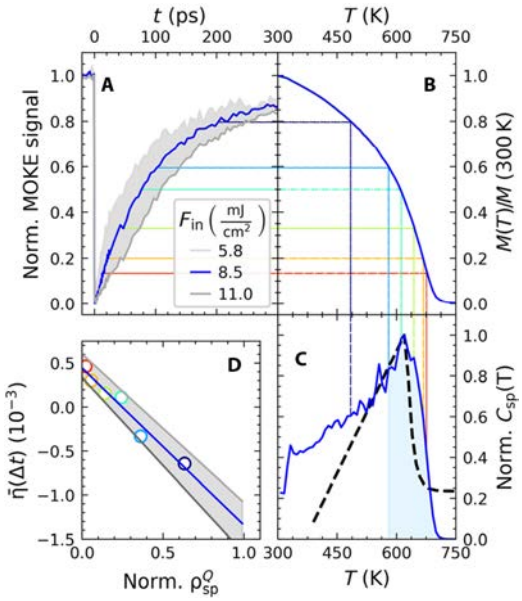

Fig. 4. Semiquantitative approximation of the remaining spin energy from tr-MOKE measurements. (**A**) Transient MOKE data for the granular FePt film for various fluences, normalized (Norm.) to their maximum demagnetization. (**B**) Equilibrium magnetization $M(T)$ measurement for a similarly prepared granular FePt film obtained by vibrating sample magnetometry (VSM). (**C**) Spin-specific heat as derived via $C_{sp} \approx M\frac{\partial M}{\partial T}$ (blue line) from $M(T)$ and calculations (*36*) (thick black dashed line). The colored dashed lines connect the graphs at selected times for which partial recovery of the spin entropy–driven contraction is observed (compare Fig 3). (**D**) Average strain $\bar{\eta}(\Delta t)$ in the first 2 ps after the second pulse (green area in Fig. 3B) as a function of the energy density $\Delta\rho^Q_{sp}(\Delta t)$ that this second pulse can still introduce into the spin system. The light blue shaded area in (C) visualizes $\Delta\rho^Q_{sp}$ for the case of T(100 ps) = 580 K, which gives rise to the light blue circle in (D).

Modeling

We experimentally find that the spin stress contribution recovers on a 100-ps time scale, consistent with the remagnetization of the grains. As domain wall propagation is not relevant within the nanoscopic grains on this time scale, the dynamics are governed by thermal transport to the carbon matrix and the substrate. Figure 4C illustrates that the energy density ρ^Q_{sp} and the associated spin entropy density $S_{sp} \propto \rho^Q_{sp}/T$ that can be induced by a second excitation after a given time delay Δt are finite. Statistical mechanics limits the maximum spin entropy to $S_{sp} = Nk_B \ln(2J + 1)$, where J is the angular momentum per magnetic atom. This saturation provides the necessary mechanism for the reduced contractive stress contribution at high fluences in the otherwise linear stress-strain relations. NTE generally requires an increasing entropy with decreasing volume (*23*).

The main features of the fluence-dependent responses observed for the continuous and granular films (Fig. 1) and of the two-pulse excitation experiments (Figs. 2 and 3) can be qualitatively understood in the light of a simplified equation of motion [see Materials and Methods for the full three-dimensional (3D) equation]

$$\rho\frac{\partial^2 u_\perp}{\partial t^2} = \frac{\partial}{\partial z}\left(\underbrace{C_{33}\frac{\partial u_\perp}{\partial z}}_{\text{elast.}\sigma_\perp} + \underbrace{2C_{31}\eta_\parallel}_{\text{elast.}\sigma_\perp^{\text{Poi}}} - \underbrace{\sigma_\perp^{sp}}_{<0} - \underbrace{\sigma_\perp^{e-ph}}_{>0}\right) \quad (1)$$

At equilibrium, negative strain $\eta_\perp = \frac{\partial u_\perp}{\partial z} < 0$ occurs only if a contractive spin stress $\sigma_\perp^{sp}$ and the elastic Poisson stress contribution $\sigma_\perp^{Poi}(t) \sim \eta_\parallel(t)$ induced by in-plane strain $\eta_\parallel$ add constructively to overcome the expansive out-of-plane stress $\sigma_\perp^{e-ph}$ imposed by hot electrons and phonons. Equation 1 is valid in the case of a thin FePt needle, i.e., a cylinder with radius much smaller than height ($r \ll d$), because this allows us to assume that in-plane strains $\eta_\parallel$ are relaxed and equal in x and y directions. The main reason for writing Eq. 1 is to see that it can be further simplified for the continuous film because $\sigma_\perp^{Poi}$ is absent at ultrafast time scales for which $\eta_\parallel = 0$ for symmetry reasons. Thus, on ultrafast time scales, Eq. 1 with $\sigma_\perp^{Poi} = 0$ is exact, and the Poisson stress makes the out-of-plane response of the granular film response substantially different.

We complement this simple analysis of the FePt deformation dynamics by FEM simulations using the actual FePt nanostructure dimensions and considering 3D, nonsimplified equations of motion (see Materials and Methods and Supplementary Materials for technical details). The results for the granular FePt film are shown in Fig. 5, while those obtained for continuous films and free grains can be found in the Supplementary Materials. In each case, various values of the relative amplitude A^{sp} of the spin stress contribution were used to mimic its variation in the context of fluence dependence (Fig. 1—saturation of the contraction) and two-pulse excitation (Figs. 2 and 3—time-dependent recovery of the spin stress). A complete reproduction of the measured time-resolved signals is challenging, as it would require to precisely take into account the morphological dispersion of the FePt grains and the heat transfer to the carbon. Nevertheless, enable a good qualitative reproduction of the strain dynamics measured for granular FePt films, as can be seen by comparing the measured strain (Figs. 1A and 3B) with the simulated strain in Fig. 5B.

Figure 5A illustrates the electron-phonon, spin, and Poisson stress contributions, which drive the out-of-plane strain dynamics of granular films (Eq. 1). As expected, in the absence of the contractive spin stress ($A^{sp} = 0$), the total stress almost always remains positive. The computed out-of-plane strain dynamics correspond to oscillations of the FePt nanostructure configuration around an expanded equilibrium, with a total absence of out-of-plane compression throughout the motion (Fig. 5B). These computed strain dynamics agree well with experimental strain data where the spin contribution is strongly reduced via the use of high-fluence light pulses (Figs. 1 to 3). Conversely, a sufficient amplitude of A^{sp} (e.g., $A^{sp} = 0.2$, as in Fig. 5A) creates a negative average value of the computed total stress enabling out-of-plane FePt contractions (Fig. 5B), in agreement with the experimental observation of a contraction at the beginning of the dynamics. Moreover, the computed strains shown in Fig. 5B qualitatively reproduce both the maximal contraction at 1.7 ps and maximal expansion at 4.5 ps, observed in the context of both low-fluence single-pump experiments (Fig. 1A) and double-pulse excitation with large delay between pump pulses, i.e., recovered spin order (Fig. 3B). The FePt deformation computed at these two instants is illustrated for $A^{sp} = 0.2$ in Fig. 5. For the same range of A^{sp}, our FEM modeling of a continuous film (see Supplementary Materials) reproduces the absence of a contraction and the 0.5-ps phase shift observed in Fig. 1B for increasing fluence. Conversely, the Poisson effect is enhanced for free FePt grains (see Supplementary Materials) because the in-plane displacement is unconstrained. Our simulations qualitatively reproduce the large out-of-plane contractions observed previously (*11*).

A systematic variation of the simulation parameters shows that a reasonable agreement with the experimental data can be obtained only by assuming an anisotropic electron-phonon stress, with nonequal out-of-plane and in-plane amplitudes $\sigma_{\perp}^{e-ph,0} = A^{ani}\,\sigma_{\parallel}^{e-ph,0}$. However, the optimal value of the anisotropy parameter $A^{ani} \approx 3$ used for the simulations shown in Fig. 5 is more than twice smaller than predicted (*11*). Including an in-plane expansion resulting from spin stress (*11*) would even reduce A^{ani} further. Although the overall agreement between simulations and experiments is good, the simulations systematically underestimate the expansion beyond 3 ps observed experimentally. This may be compensated for by adding expansive stress in the carbon shell resulting from heat transfer from the FePt, which would decrease the Poisson stress $\sigma_{\perp}^{Poi}$ acting on FePt on long time scales.

Our modeling shows that the difference in the response of free grains, a granular film, and the continuous film mainly originates from the different in-plane boundary conditions, which suppress or partially allow the Poisson effect. We can reproduce the essential conclusion drawn from the double-pulse experiment (Fig. 3) that the initial out-of-plane contraction is driven by spin stress.

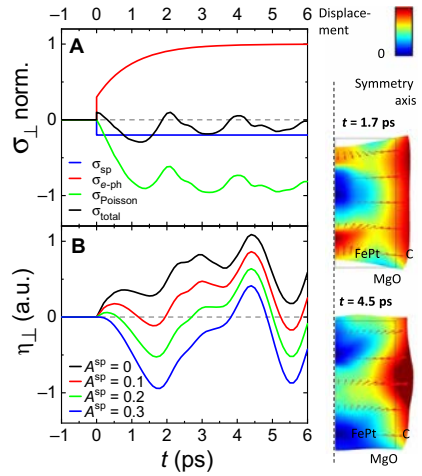

Fig. 5. FEM modeling of the mechanical response of a granular FePt film. (**A**) Time-dependent out-of-plane stresses $\sigma_{\perp}(t)$ acting on FePt for $A^{sp} = 0$ (no spin stress, solid lines) and $A^{sp} = 0.2$ (dashed lines). The Poisson stress component was deduced from the computed in-plane strains. (**B**) Average out-of-plane strain $\eta_{\perp}(t)$ in arbitrary units (a.u.) computed for various ratios A^{sp} of the spin and electron-phonon stress amplitudes. The computed FePt deformation at instants corresponding to maximal initial contraction and expansion for $A^{sp} = 0.2$ are illustrated at the right.

CONCLUSION

In conclusion, we have shown that laser-generated spin entropy drives a pronounced but short-lived lattice contraction of nanogranular FePt films in the $L1_0$ phase. In a double-pulse excitation scenario, the absence of a contraction after the second laser pulse quantifies the contractive stress contribution of the spin excitations, as they saturate when the FePt temperature approaches T_C. Fluence-dependent transient MOKE data confirm that the relaxation of the magnetization occurs on the same time scale as the spin entropy–driven contraction reappears.

Our elastic continuum modeling clarifies the important role of the Poisson effect in establishing the transient contraction of the granular film, which is not observed for the continuous film. We are confident that this double-pulse excitation scenario can be developed into a versatile tool for investigating coupled systems with many degrees of freedom, when a phase transition leads to the saturation for one of the driving stresses of the lattice response.

MATERIALS AND METHODS

X-ray and MOKE experiments

We performed laser-based UXRD pump-probe experiments with an x-ray pulse duration (*38*) of approximately 200 fs on two FePt thin films in the ordered $L1_0$ phase grown on MgO (001) oriented substrates. We observe the time-dependent evolution of the (002)

FePt diffraction peak, from which we deduce the time-resolved out-of-plane lattice strain of the FePt layer $\eta_\perp(t)$. The samples are excited by p-polarized pump pulses with a duration of 100 fs at a central wavelength of 800 nm, which are incident under 45° relative to the surface normal. The laser spot size of approximately 1.6 mm by 1.3 mm (full width at half maximum) ensures that a homogeneously excited sample area is probed by the x-rays that have rhombical 0.3 mm–by–0.3 mm profile (*39*). The tr-MOKE setup (*34*) uses comparable excitation parameters. For experimental details, see Supplementary Materials. Static x-ray diffraction measurements at different sample temperatures were recorded using a commercial diffraction setup (Rigaku SmartLab 9 kW system).

Sample preparation

A continuous FePt thin film was prepared by magnetron-sputtering Fe and Pt from a composite FePt target onto a substrate preheated to 500°C. Similarly, a granular FePt film was prepared at a slightly higher substrate temperature of 650°C by adding approximately 30 volume % of carbon to the sputtering target. X-ray reflectivity measured the sample thicknesses to be about d = 9.5 nm, where the continuous film is covered with an additional 1-nm layer of oxidized Al (*27*). According to scanning electron microscopy images of similarly prepared samples (see Supplementary Materials), the size distribution of the FePt nanograins segregated in a carbon matrix within the granular film is centered at approximately 8 nm. This nano-morphology yields a very large coercive field of approximately $\mu_0 H$ = 5 T, whereas the coercive field of the continuous film $\mu_0 H$ = 0.4 T is substantially smaller because of the possibility of domain wall motion that cannot occur in the nanogranular samples (*40*). The sample structures are schematically depicted as insets (C) and (D) in Fig. 1, and their properties and the measurement technique have been described in a previous publication (*27*).

FEM modeling

Finite-element simulations were performed using the Structural Mechanics Module of the COMSOL commercial software. It determines the spatiotemporal variations of displacement $u_i(x_1, x_2, x_3, t)$ by the numerical, approximation-free resolution of the continuum mechanics equation of motion in all Cartesian directions x_i

$$\rho\frac{\partial^2 u_i}{\partial t^2} = \sum_{j=1}^{3}\frac{\partial}{\partial x_j}\left(\sum_{k,l=1}^{3} C_{ijkl}\eta_{kl} - \sigma_{ij}^{ext}\right) \text{ with the strain } \eta_{kl} = \frac{1}{2}\left(\frac{\partial u_k}{\partial x_l} + \frac{\partial u_l}{\partial x_k}\right)$$

The simulation system was composed of a FePt cylinder with the radius r = 4 nm and d=10 nm height encapsulated by a cylindrical carbon shell of 2-nm thickness and same height supported on a MgO substrate. Note that the choice of such an axially symmetric geometry allowed us to perform 2D simulations, which are computationally much less expensive than 3D ones. Perfect mechanical contact was assumed at all internal interfaces of the system. Vanishing in-plane displacement was imposed on the lateral surface of the simulation domain, 6 nm away from its symmetry axis, to describe the absence of lateral contraction in films. Stress-free and low-reflecting boundary conditions were, respectively, used at the top of the FePt–carbon film and at the bottom of the MgO substrate.

FePt elastic anisotropy was neglected, and all materials were described by their density ρ, Young modulus Y, and Poisson ratio ν as listed in Table 1.

The time-dependent displacement fields $u_i(t)$ induced in this system by its sudden excitation were computed in the time domain, and the average out-of-plane strain in FePt $\eta_\perp(t) = \frac{\partial u_z(t)}{\partial z}$ was deduced by spatial integration.

The laser-induced excitation was described by a time-dependent diagonal matrix obtained by summing the contributions of an expansive, anisotropic electron-phonon stress with components $\sigma_{xx}^{e-ph}(t) = \sigma_{yy}^{e-ph}(t) = A^{ani}\sigma_{zz}^{e-ph}(t) = A^{ani}\sigma^{e-pho,0}\left(1 + \left(\frac{\gamma_e}{\gamma_{ph}} - 1\right)e^{-\frac{t}{\tau}}\right)\Theta(t)$ accounting for energy dissipation from electrons to phonons after selective excitation of the former by light (*41*) and an instantaneously rising contractive uniaxial spin stress $\sigma_{zz}^{sp}(t) = \sigma_\perp^{sp,0}\Theta(t)$, where Θ is the Heaviside function. A τ = 1 ps electron-phonon coupling time and a $\frac{\gamma_e}{\gamma_{ph}}$ = 0.3 ratio of electron and phonon Grüneisen constants were used in the modeling. We approximate both the contractive spin stress and the expansive electron stress as instantaneous, i.e., much shorter than the 200 fs time resolution of our UXRD experiment. This is consistent with recent ultrafast electron calorimetry, which has shown that the energy transfer to the spin system in nickel is effective within the first 20 fs (*42*).

Table 1. Elastic parameters used in the modeling.

	FePt	C	MgO
ρ (kg/m^3)	14,700	2000	3580
Y (GPa)	237	200	249
ν	0.31	0.2	0.18

SUPPLEMENTARY MATERIALS

Supplementary material for this article is available at http://advances.sciencemag.org/cgi/content/full/6/28/eaba1142/DC1

REFERENCES AND NOTES

1. E. F. Wasserman, Invar: Moment-volume instabilities in transition metals and alloys. *Handbook Ferromagn. Mater.* **5**, 237–322 (1990).
2. C. E. Guillaume, Recherches sur les aciers au nickel. Dilatations aux températures élevées; résistance électrique. *C. R. Acad. Sci.* **125**, 18 (1897).
3. R. J. Weiss, The origin of the `Invar'effect. *Proc. Phys. Soc.* **82**, 281 (1963).
4. M. Van Schilfgaarde, I. A. Abrikosov, B. Johansson, Origin of the invar effect in iron-nickel alloys. *Nature* **400**, 46–49 (1999).
5. S. Khmelevskyi, I. Turek, P. Mohn, Large negative magnetic contribution to the thermal expansion in iron-platinum alloys: Quantitative theory of the invar effect. *Phys. Rev. Lett.* **91**, 037201 (2003).
6. C. Dornes, Y. Acremann, M. Savoini, M. Kubli, M. J. Neugebauer, E. Abreu, L. Huber, G. Lantz, C. A. F. Vaz, H. Lemke, E. M. Bothschafter, M. Porer, V. Esposito, L. Rettig, M. Buzzi, A. Alberca, Y. W. Windsor, P. Beaud, U. Staub, D. Zhu, S. Song, J. M. Glownia, S. L. Johnson, The ultrafast Einstein–de Haas effect. *Nature* **565**, 209–212 (2019).
7. E. Jal, V. López-Flores, N. Pontius, T. Ferté, N. Bergeard, C. Boeglin, B. Vodungbo, J. Lüning, N. Jaouen, Structural dynamics during laser-induced ultrafast demagnetization. *Phys. Rev. B.* **95**, 184422 (2017).
8. A. von Reppert, J. Pudell, A. Koc, M. Reinhardt, W. Leitenberger, K. Dumesnil, F. Zamponi, M. Bargheer, Persistent nonequilibrium dynamics of the thermal energies in the spin and phonon systems of an antiferromagnet. *Struct. Dyn.* **3**, 054302 (2016).
9. J. Pudell, A. von Reppert, D. Schick, F. Zamponi, M. Rössle, M. Herzog, H. Zabel, M. Bargheer, Ultrafast negative thermal expansion driven by spin disorder. *Phys. Rev. B.* **99**, 094304 (2019).
10. C. von Korff Schmising, A. Harpoeth, N. Zhavoronkov, Z. Ansari, C. Aku-Leh, M. Woerner, T. Elsaesser, M. Bargheer, M. Schmidbauer, I. Vrejoiu, D. Hesse, M. Alexe, Ultrafast magnetostriction and phonon-mediated stress in a photoexcited ferromagnet. *Phys. Rev. B.* **78**, 060404 (2008).
11. A. H. Reid, X. Shen, P. Maldonado, T. Chase, E. Jal, P. W. Granitzka, K. Carva, R. K. Li, J. Li, L. Wu, T. Vecchione, T. Liu, Z. Chen, D. J. Higley, N. Hartmann, R. Coffee, J. Wu, G. L. Dakovski, W. F. Schlotter, H. Ohldag, Y. K. Takahashi, V. Mehta, O. Hellwig, A. Fry, Y. Zhu, J. Cao, E. E. Fullerton, J. Stöhr, P. M. Oppeneer, X. J. Wang, H. A. Dürr, Beyond a phenomenological description of magnetostriction. *Nat. Commun.* **9**, 388 (2018).

12. A. Koc, M. Reinhardt, A. von Reppert, M. Rössle, W. Leitenberger, M. Gleich, M. Weinelt, F. Zamponi, M. Bargheer, Grueneisen-approach for the experimental determination of transient spin and phonon energies from ultrafast x-ray diffraction data: Gadolinium. *J. Phys. Condens. Matter* **29**, 264001 (2017).
13. E. Beaurepaire, J.-C. Merle, A. Daunois, J.-Y. Bigot, Ultrafast spin dynamics in ferromagnetic nickel. *Phys. Rev. Lett.* **76**, 4250–4253 (1996).
14. J. Kimling, J. Kimling, R. B. Wilson, B. Hebler, M. Albrecht, D. G. Cahill, Ultrafast demagnetization of FePt:Cu thin films and the role of magnetic heat capacity. *Phys. Rev. B.* **90**, 224408 (2014).
15. T. Kampfrath, A. Sell, G. Klatt, A. Pashkin, S. Mährlein, T. Dekorsy, M. Wolf, M. Fiebig, A. Leitenstorfer, R. Huber, Coherent terahertz control of antiferromagnetic spin waves. *Nat. Photonics* **5**, 31–34 (2011).
16. F. Hansteen, A. Kimel, A. Kirilyuk, T. Rasing, Nonthermal ultrafast optical control of the magnetization in garnet films. *Phys. Rev. B.* **73**, 014421 (2006).
17. J. W. Kim, M. Vomir, J. Y. Bigot, Controlling the spins angular momentum in ferromagnets with sequences of picosecond acoustic pulses. *Sci. Rep.* **5**, 8511 (2014).
18. M. Sander, J. E. Pudell, M. Herzog, M. Bargheer, R. Bauer, V. Besse, V. Temnov, P. Gaal, Quantitative disentanglement of coherent and incoherent laser-induced surface deformations by time-resolved x-ray reflectivity. *Appl. Phys. Lett.* **111**, 261903 (2017).
19. D. C. Heinecke, O. Kliebisch, J. Flock, A. Bruchhausen, K. Köhler, T. Dekorsy, Selective excitation of zone-folded phonon modes within one triplet in a semiconductor superlattice. *Phys. Rev. B* **87**, 075307 (2013).
20. T. Cheng, J. Wu, T. Liu, X. Zou, J. Cai, R. W. Chantrell, Y. Xu, Dual-pump manipulation of ultrafast demagnetization in TbFeCo. *Phys. Rev. B.* **93**, 064401 (2016).
21. K. Bühlmann, R. Gort, G. Salvatella, S. Däster, A. Fognini, T. Bähler, C. Dornes, C. A. F. Vaz, A. Vaterlaus, Y. Acremann, Ultrafast demagnetization in iron: Separating effects by their nonlinearity. *Struct. Dyn.* **5**, 044502 (2018).
22. J. Y. Shi, M. Tang, Z. Zhang, L. Ma, L. Sun, C. Zhou, X. F. Hu, Z. Zheng, L. Q. Shen, S. M. Zhou, Y. Z. Wu, L. Y. Chen, H. B. Zhao, Impact of ultrafast demagnetization process on magnetization reversal in $L1_0$ FePt revealed using double laser pulse excitation. *Appl. Phys. Lett.* **112**, 082403 (2018).
23. G. D. Barrera, J. A. O. Bruno, T. H. K. Barron, N. L. Allan, Negative thermal expansion. *J. Phys. Condens. Matter* **17**, R217–R252 (2005).
24. O. Mosendz, S. Pisana, J. W. Reiner, B. Stipe, D. Weller, Ultra-high coercivity small-grain FePt media for thermally assisted recording (invited). *J. Appl. Phys.* **111**, 07B729 (2012).
25. D. Weller, G. Parker, O. Mosendz, A. Lyberatos, D. Mitin, N. Y. Safonova, M. Albrecht, Review article: FePt heat assisted magnetic recording media. *J. Vac. Sci. Technol.* **34**, 060801 (2016).
26. K. Hono, Y. K. Takahashi, G. Ju, J.-U. Thiele, A. Ajan, X. Yang, R. Ruiz, L. Wan, Heat-assisted magnetic recording media materials. *MRS Bull.* **43**, 93–99 (2018).
27. A. von Reppert, L. Willig, J.-E. Pudell, M. Rössle, W. Leitenberger, M. Herzog, F. Ganss, O. Hellwig, M. Bargheer, Ultrafast laser generated strain in granular and continuous FePt thin films. *Appl. Phys. Lett.* **113**, 123101 (2018).
28. K. Sumiyama, M. Shiga, M. Morioka, Y. Nakamura, Characteristic magnetovolume effects in Invar type Fe-Pt alloys. *J. Phys. F Met. Phys.* **9**, 1665–1677 (1979).
29. Y. Tsunoda, H. Kobayashi, Temperature variation of the tetragonality in ordered PtFe alloy. *J. Magn. Magn. Mater.* **272–276**, 776–777 (2004).
30. R. Nicula, O. Crisan, A. D. Crisan, I. Mercioniu, M. Stir, F. Vasiliu, Thermal stability, thermal expansion and grain-growth in exchange-coupled Fe–Pt–Ag–B bulk nanocomposite magnets. *J. Alloys Compd.* **622**, 865–870 (2015).
31. P. Rasmussen, X. Rui, J. E. Shield, Texture formation in FePt thin films via thermal stress management. *Appl. Phys. Lett.* **86**, 191915 (2005).
32. P. W. Granitzka, E. Jal, L. Le Guyader, M. Savoini, D. J. Higley, T. Liu, Z. Chen, T. Chase, H. Ohldag, G. L. Dakovski, W. F. Schlotter, S. Carron, M. C. Hoffman, A. X. Gray, P. Shafer, E. Arenholz, O. Hellwig, V. Mehta, Y. K. Takahashi, J. Wang, E. E. Fullerton, J. Stöhr, A. H. Reid, H. A. Dürr, Magnetic switching in granular FePt layers promoted by near-field laser enhancement. *Nano Lett.* **17**, 2426–2432 (2017).
33. O. Hovorka, S. Devos, Q. Coopman, W. J. Fan, C. J. Aas, R. F. L. Evans, X. Chen, G. Ju, R. W. Chantrell, The Curie temperature distribution of FePt granular magnetic recording media. *Appl. Phys. Lett.* **101**, 052406 (2012).
34. L. Willig, A. Von Reppert, M. Deb, F. Ganss, O. Hellwig, M. Bargheer, Finite-size effects in ultrafast remagnetization dynamics of FePt. *Phys. Rev. B.* **100**, 224408 (2019).
35. J. M. D. Coey, *Magnetism and Magnetic Materials* (Cambridge Univ. Press, 2012).
36. A. Lyberatos, G. J. Parker, Model of ballistic-diffusive thermal transport in HAMR media. *Jpn. J. Appl. Phys.* **58**, 045002 (2019).
37. T. H. K. Barron, J. G. Collins, G. K. White, Thermal expansion of solids at low temperatures. *Adv. Phys.* **29**, 609–730 (1980).
38. D. Schick, A. Bojahr, M. Herzog, C. von Korff Schmising, R. Shayduk, W. Leitenberger, P. Gaal, M. Bargheer, Normalization schemes for ultrafast x-ray diffraction using a table-top laser-driven plasma source. *Rev. Sci. Instrum.* **83**, 025104 (2012).
39. M. Bargheer, N. Zhavoronkov, R. Bruch, H. Legall, H. Stiel, M. Woerner, T. Elsaesser, Comparison of focusing optics for femtosecond x-ray diffraction. *Appl. Phys. B.* **80**, 715–719 (2005).
40. T. Shima, K. Takanashi, Y. K. Takahashi, K. Hono, Preparation and magnetic properties of highly coercive FePt films. *Appl. Phys. Lett.* **81**, 1050–1052 (2002).
41. A. von Reppert, R. M. Sarhan, F. Stete, J. Pudell, N. Del Fatti, A. Crut, J. Koetz, F. Liebig, C. Prietzel, M. Bargheer, Watching the vibration and cooling of ultrathin gold nanotriangles by ultrafast x-ray diffraction. *J. Phys. Chem. C* **120**, 28894–28899 (2016).
42. P. Tengdin, W. You, C. Chen, X. Shi, D. Zusin, Y. Zhang, C. Gentry, A. Blonsky, M. Keller, P. M. Oppeneer, H. Kapteyn, Z. Tao, M. Murnane, Critical behavior within 20 fs drives the out-of-equilibrium laser-induced magnetic phase transition in nickel. *Sci. Adv.* **4**, eaap9744 (2018).
43. D. Schick, R. Shayduk, A. Bojahr, M. Herzog, C. von Korff Schmising, P. Gaal, M. Bargheer, Ultrafast reciprocal-space mapping with a convergent beam. *J. Appl. Cryst.* **46**, 1372–1377 (2013).

Acknowledgments

Funding: We acknowledge the BMBF for the financial support via 05K16IPA and the DFG via BA 2281/8-1 and BA2281/11-1. Part of the work was carried out with the support of CEITEC Nano Research Infrastructure (MEYS CR, LM2018110). This work has received funding from the European Union's Horizon 2020 research and innovation program under the Marie Skłodowska-Curie program, and it is cofinanced by the South Moravian Region under grant agreement no. 665860. We acknowledge the precharacterization of the crystalline thin films at the XPP-KMC3 synchrotron radiation beamline D13.2 at the BESSY II electron storage ring operated by the Helmholtz-Zentrum Berlin. **Author contributions:** A.v.R. and M.B. conceived the experiment A.v.R., J.-E.P., and S.P.Z. performed the time-resolved x-ray experiments and analysis. F.G., G.S., and O.H. grew and characterized the samples. J.A.A. and V.U. performed and analyzed the T-dependent x-ray diffraction experiment. A.C. performed the FEM simulations. L.W. and A.v.R. performed the MOKE experiments and analysis. A.v.R. and M.B coordinated writing of the paper with contributions from all coauthors. **Competing interests:** The authors declare that they have no competing interests. **Data and materials availability:** All data needed to evaluate the conclusions in the paper are present in the paper and/or the Supplementary Materials. Additional data related to this paper may be requested from the authors.

Submitted 5 November 2019
Accepted 22 May 2020
Published 8 July 2020
10.1126/sciadv.aba1142

Citation: A. von Reppert, L. Willig, J.-E. Pudell, S. P. Zeuschner, G. Sellge, F. Ganss, O. Hellwig, J. A. Arregi, V. Uhlíř, A. Crut, M. Bargheer, Spin stress contribution to the lattice dynamics of FePt. *Sci. Adv.* **6**, eaba1142 (2020).

V Generation of spin waves via spin-phonon interaction in a buried dielectric thin film

Marwan Deb, Elena Popova, Steffen Peer Zeuschner, Michel Hehn, Niels Keller, Stéphane Mangin, Gregory Malinowski and Matias Bargheer

Physical Review B 103, 024411 (2021)

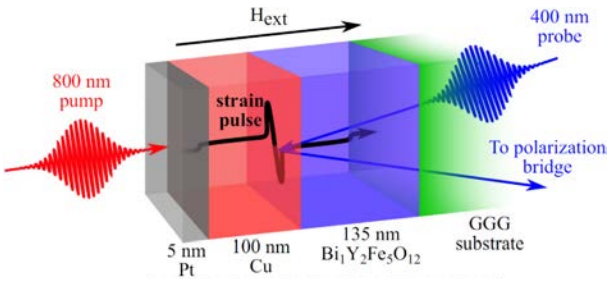

Abstract In this paper, we investigate the magnetic, optical, and lattice responses of a $Pt/Cu/Bi_1Y_2Fe_5O_{12}/\ Gd_3Ga_5O_{12}$ heterostructure to femtosecond laser excitation of the opaque Pt/Cu metallic bilayer. The electronic excitation generates coherent and incoherent phonons, which trigger high-frequency standing spin waves (SWs) in the dielectric $Bi_1Y_2Fe_5O_{12}$ layer via a phonon-induced change of magnetic anisotropy. We find that the incoherent phonons (heat) can induce a fast (<1 ps) and slow (>1000 ps) decrease of the magnetic order by different spin-phonon interaction scenarios. These results open perspectives for generating high-frequency SWs in buried magnetic garnets.

Contributions to the work

Togehter with Alexander von Reppert I performed the ultrafast X-Ray difffraction measurements for the characterization of the sample. I modelled the temperature and the strain in the heterostructe with the udkm1D-Sim toolbox and commented on the manuscript. The samples were provided by Elena Popova and Niels Keller.

Comments

This publication is the second work in which I investigated the ferromagnetic insulator Bi:YIG. In contrast to article III, the sample structure is modified so that a 5 nm thin Pt transducer above a 100 nm Cu layer is grown onto the Bi:YIG layer. The aim was that the Pt transducer injects a high amplitude strain pulse into the Cu and subsequently Bi:YIG layer, in which standing spin waves are triggered via anisotropy changes and inverse magnetostriction. At the same time, the Cu layer was meant to isolate the Bi:YIG from the incident femtosecond laser pulse, so no energy is deposited in the Bi:YIG layer via photons. With this, previous works on this system assumed an excitation of the spin waves solely via the strain pulse, i.e. sound not heat [29].

However, we found out that this is just half of the truth. With the UXRD measurements we show, that the Bi:YIG layer is compressed in less than a picosecond after excitation, far too fast for the strain pulse from the Pt transducer which is limited by the sound velocity in Cu. The reason behind this is that the electrons in the Pt and Cu layer equilibrate thermally during the first picosecond which leads to an ultrafast thermal expansion of the whole Cu layer in addition to the Pt layer, consequently compressing the adjacent Bi:YIG volume immediately. So, the Cu layer works unintentionally as a transducer as well, injecting a strain pulse with much larger wavelength but significantly smaller amplitude into the Bi:YIG. Also, the copper adjacent to Bi:YIG is heated, which results in a significant unintended heat flow into the Bi:YIG at a picosecond timescale as well.

To conclude, this publication illustrates once again that UXRD is exceptionally useful for characterizing any ultrafast magnetization dynamics which are thought to be triggered by coherent or incoherent

phonons, i.e. sound or heat.

PHYSICAL REVIEW B **103**, 024411 (2021)

Generation of spin waves via spin-phonon interaction in a buried dielectric thin film

Marwan Deb,[1,*] Elena Popova,[2] Steffen Peer Zeuschner,[1,3] Michel Hehn,[4] Niels Keller,[2] Stéphane Mangin,[4] Gregory Malinowski,[4] and Matias Bargheer[1,3]

[1]*Institut für Physik und Astronomie, Universität Potsdam, Karl-Liebknecht-Straße 24–25, 14476 Potsdam, Germany*
[2]*Groupe d'Etude de la Matière Condensée (GEMaC), CNRS UMR 8635, Université Paris-Saclay, 78035 Versailles, France*
[3]*Helmholtz Zentrum Berlin für Materialien und Energie GmbH, Albert-Einstein-Straße 15, 12489 Berlin, Germany*
[4]*Institut Jean Lamour (IJL), CNRS UMR 7198, Université de Lorraine, 54506 Vandœuvre-lès-Nancy, France*

(Received 23 October 2020; revised 21 December 2020; accepted 23 December 2020; published 11 January 2021)

In this paper, we investigate the magnetic, optical, and lattice responses of a $Pt/Cu/Bi_1Y_2Fe_5O_{12}/Gd_3Ga_5O_{12}$ heterostructure to femtosecond laser excitation of the opaque Pt/Cu metallic bilayer. The electronic excitation generates coherent and incoherent phonons, which trigger high-frequency standing spin waves (SWs) in the dielectric $Bi_1Y_2Fe_5O_{12}$ layer via a phonon-induced change of magnetic anisotropy. We find that the incoherent phonons (heat) can induce a fast (<1ps) and slow (>1000 ps) decrease of the magnetic order by different spin-phonon interaction scenarios. These results open perspectives for generating high-frequency SWs in buried magnetic garnets.

DOI: 10.1103/PhysRevB.103.024411

I. INTRODUCTION

Controlling the spin dynamics at the fastest speed and with the highest efficiency has always been one of the ultimate goals of modern magnetism, as it constitutes a fundamentally important challenge with a potential high impact on data storage and processing technologies. Since the discovery of the subpicosecond demagnetization in nickel [1], laser-induced ultrafast magnetization dynamics have attracted a lot of attention and have become the rapidly developing field of femtomagnetism [2,3]. Indeed, over the past 25 years, it was shown that femtosecond laser pulses can trigger many important magnetic phenomena such as all-optical magnetization switching [4,5], ultrafast magnetic phase transition [6–8], and the generation of collective spin oscillations [9,10]. These results have provided important insight about fundamental mechanisms behind the excitation of spins with light. It was demonstrated that thermal effects play an important role in the majority of ultrafast magnetic processes induced in conducting [1,11,12] and semiconducting [13–16] magnets, while in magnetic insulators, the ultrafast control of spin dynamics can occur via nonthermal mechanisms like the inverse Faraday effect [10,17,18], the Cotton-Mouton effect [19], and the photo-induced magnetic anisotropy [20–23].

These results have motivated researchers to explore alternative possibilities to control the magnetization using other ultrashort stimuli like picosecond strain pulses and hot-electron pulses. For instance, the propagation of an ultrashort hot-electron pulse in conducting magnets can induce an ultrafast demagnetization [24–26] and a full magnetization reversal [25,26] via thermal effects. Picosecond acoustic pulses can trigger a homogeneous collective spin oscillation ($k = 0$, i.e., ferromagnetic resonance mode) via inverse magnetostriction in conducting [27–29], semiconducting [30], and insulating [31] magnetic materials. Very recently, the geometry for exciting spin dynamics indirectly via pumping a Pt/Cu bilayer that protects a magnetic layer from optical excitation [24,25] was investigated by ultrafast x-ray diffraction (UXRD) [32]. These experiments quantify the arrival of hot electrons, strain waves, and vibrational heat in a magnetic Ni layer.

The collective spin oscillations, known also as spin waves (SWs) or magnons, represent one of the most promising approaches toward the development of more energy-efficient and faster data transport and processing technology than the current charge-based semiconductor-based technology [33]. This is due to their very useful physical properties at room temperature, such as the low-energy dissipation, the high-frequency spectrum from GHz to THz, and the tunable wavelength down to nanoscales [34]. A key requirement for high-speed applications is to generate SWs that combine low damping with high frequency. Nanoscale thin films of yttrium iron garnet ($Y_3Fe_5O_{12}$, YIG) with its intrinsic low magnetic damping constant [35] are particularly interesting for these applications. The frequency of exchange standing SW (SSW) modes increases quadratically with the mode number n and with decreasing thickness d of the nanolayer. A moderate exchange stiffness D_{ex} can thus support the high frequency $\sim D_{ex}(\pi n/d)^2$ required by applications [36,37].

Generating SSWs requires nonuniform excitation across the film thickness [38], which is very challenging to induce using conventional microwave antennae [38–40]. On the other hand, for around 15 years, the excitation of SSWs with femtosecond laser pulses has been limited to conducting [9,41,42] and semiconducting [13,15,16] magnets. In our recent papers, we demonstrated that a femtosecond laser pulse can excite SSWs in insulating magnetic films of bismuth-substituted

*Corresponding author: madeb@uni-potsdam.de

YIG with high in-plane magnetic anisotropy [43,44]. In this context, an important fundamental study is to investigate the possibility to take advantage of femtosecond laser pulses to trigger high-frequency SSWs in bismuth-substituted YIG films buried below a thick metallic structure. This configuration is of utmost importance since it allows exploring the effects of picosecond strain excitation and heat transfer across a normal metal-magnetic insulator interface on the magnetic properties.

Here, we report an experimental investigation of the ultrafast magnetization dynamics in a dielectric film of $Bi_1Y_2Fe_5O_{12}$ (Bi-YIG) with high in-plane magnetic anisotropy and buried below a thick Cu/Pt metallic bilayer. We demonstrate that the indirect excitation of the Bi-YIG layer via exclusive absorption of light in the metal triggers high-frequency SSWs in the insulating Bi-YIG. Two mechanisms mediate this indirect excitation of SSWs: (i) Inverse magnetostriction changes the magnetic anisotropy proportional to lattice constant changes in the form of propagating strain waves. (ii) The lattice-heating additionally changes the magnetic anisotropy via the temperature dependence of the anisotropy constants. The strain pulse (coherent phonon) launched in the metal, traversing the Bi-YIG layer within 50 ps, and the rapid propagation of heat (incoherent phonons) can both excite SSWs. We suggest that phonons created at the Cu/Bi-YIG interface via hot electrons reflected at the metal-insulator interface additionally induce a fast (<1 ps) change of the magnetic order. The slower timescale (>1 ns) on which the magnetic order is further reduced can be attributed to a combination of slow phonon-spin coupling and heat transport into the Bi-YIG layer. Our model is based on the experimental results from time-resolved magneto-optical Kerr effect (TR-MOKE) and UXRD.

II. SAMPLE CHARACTERIZATION AND EXPERIMENTAL METHODS

The sample studied in this paper was based on a 135-nm-thick $Bi_1Y_2Fe_5O_{12}$ single crystalline film grown by pulsed laser deposition on a gadolinium gallium garnet (GGG) (100) substrate [45]. To address the effect of a phononic excitation on ultrafast magnetization dynamics that excludes optical excitation, we deposited a thick Pt (5 nm)/Cu (100 nm) nonmagnetic metallic bilayer on top of the Bi-YIG film using direct current magnetron sputtering [Fig. 2(b)]. The top Pt layer was added due to its high absorption at 800 nm compared with Cu, which also ensured an efficient generation of a hot-electron pulse [24,25,32]. Experimentally, the transmission of the pump light was less than 10^{-3}. The Cu was chosen for its high hot-electron lifetime [24,25,46]. Thus, the 100-nm-thick Cu layer protected the Bi-YIG film from the direct light excitation, while the hot-electron pulses propagated until reaching the back side of the Cu layer [24,25,32].

Figure 1 shows the UXRD study of the heterostructure, performed with femtosecond x-ray diffraction using a tabletop laser-driven plasma source [47]. In full analogy to the recent publication on a Pt/Cu/Ni heterostructure [32], we were able to model the time-resolved strain in Pt, Cu, and Bi-YIG with a two-temperature model in combination with a one-dimensional masses-and-springs model, using the

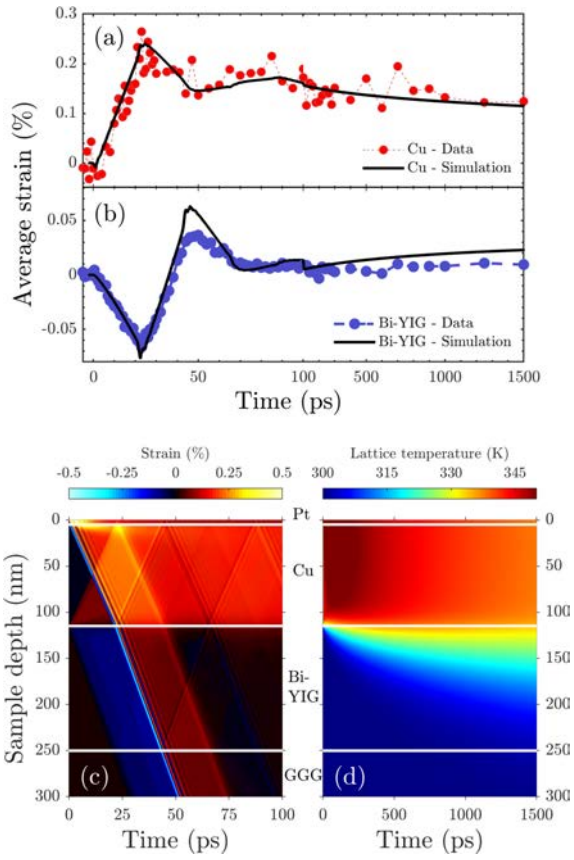

FIG. 1. Laser-induced lattice dynamics in the Pt/Cu/$Bi_1Y_2Fe_5O_{12}$/$Gd_3Ga_5O_{12}$ heterostructure. Average strain in (a) the Cu layer and (b) BI-YIG layer as measured by ultrafast x-ray diffraction (UXRD). Calculated spatiotemporal maps of (c) the strain and (d) temperature in the heterostructure. The solid lines in (a) and (b) are results of our modeling. The UXRD measurements were performed at room temperature with a pump wavelength of 800 nm, a pulse duration of 50 fs, and an incident pump energy density of 5 mJ/cm^2.

software package *udkm1Dsim-toolbox* [48]. The two-temperature model includes an enhanced electronic heat conductivity $\kappa_e = \kappa_0 \times T_e/T_{ph}$ compared with the equilibrium value κ_0. This enhancement is due to the reduction of the electron-phonon scattering channel if the lattice of Cu is cold compared with its electronic system [32]. The main difference to the previous paper is that the magnetic layer now is the insulating Bi-YIG, which cannot accept the thermal energy in the form of hot electrons. Instead, the hot electrons in Cu can excite optical phonons in Bi-YIG when they scatter at the interface, which quickly decay. In addition, heat can be transported into the Bi-YIG film via incoherent acoustic phonons from the Cu. Figures 1(a) and 1(b) show the measured time-resolved average strains $\bar{\eta}_{\mathrm{Cu}}(t)$ of the Cu layer and $\bar{\eta}_{\mathrm{Bi-YIG}}(t)$ of the Bi-YIG layer. As a first approximation, we disregard the direct transfer of energy from Cu electrons to Bi-YIG phonons and calculate the spatiotemporal lattice strain $\eta(z,t)$ from the

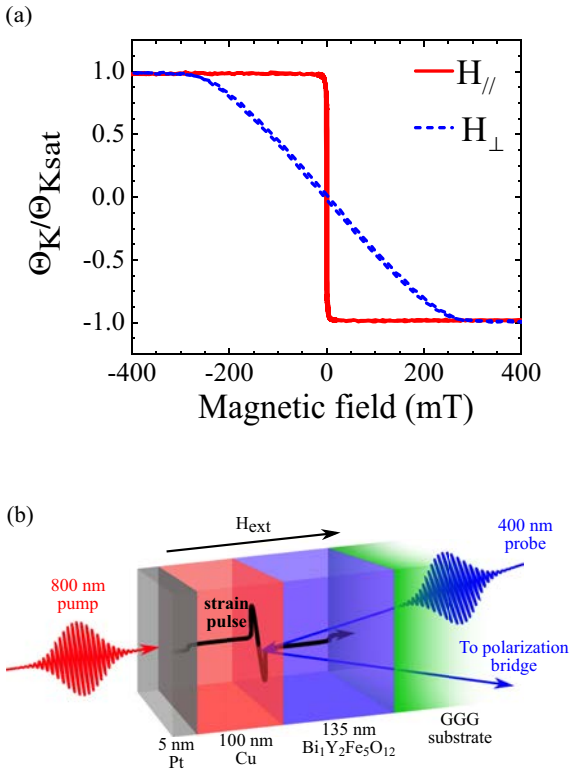

FIG. 2. Static room temperature magnetic properties of the garnet sample and the experimental configuration. (a) Normalized hysteresis loop measured in polar (dashed line) and longitudinal (solid line) configurations. (b) Sketch of the pump-probe time-resolved magneto-optical configuration that allows studying the ultrafast magnetization dynamics induced by coherent and incoherent phonons. The sketch also shows a snapshot of the bipolar strain pulse that traverses the Bi-YIG layer as modeled in Fig. 1(c). It contains a bipolar pulse with a broad, low-amplitude contribution from Cu excitation and a sharp high-amplitude contribution from Pt excitation.

temperature $T(z,t)$ in the heterostructure [see Figs. 1(c) and 1(d)]. In our simulation, we used the same parameters for Pt and Cu in Ref. [32] except that the Cu thickness was 110 nm to match the timings of the coherent strain signals. For Bi-YIG, we used a longitudinal sound velocity $V^L_{\mathrm{Bi-YIG}} = 6300$ m/s [49,50], a phonon heat capacity $C^{ph}_{\mathrm{Bi-YIG}} = 2.9\ \mathrm{J/m^3K}$ [51], a phonon heat conductivity $\kappa^{ph}_{\mathrm{Bi-YIG}} = 6\ \mathrm{W/mK}$ [51], and a Grüneisen constant $\Gamma^s_{\mathrm{Bi-YIG}} = 1$ [50]. The modeling of the average lattice strain is plotted as solid lines in Figs. 1(a) and 1(b), showing a reasonable agreement with the experimental data. We can use the transient temperature and strain which was calibrated to the UXRD experiment to discuss the excitation channels of the SWs. In Fig. 2(b), we display the calculated shape of the strain pulse that traverses the Bi-YIG layer, i.e., the time-dependent local strain that modulates each unit cell. It is a vertical cut through Fig. 1(c) at 25 ps. It contains a low-amplitude feature originating from the expansion of the Cu layer [Fig. 1(a)], which induces the immediate decrease of the strain in Fig. 1(b), starting within less than 1 ps. At this time, the heat energy transported by the hot electrons through Cu arrived at the Bi-YIG interface. The sharper high-amplitude feature originated from the expansion of the thin Pt transducer. Both features of the strain pulse together with the thermal expansion are shown in the strain map of Fig. 1(c), which highlights the spatiotemporal dynamics of the lattice strain in the heterostructure. The heat diffusion is illustrated by the phonon temperature profile [Fig. 1(d)]. This phonon heat energy density was the main component of the stress that drove the strain [32,48,50]. More importantly, Fig. 1(d) shows that the heating of the Bi-YIG layer is strongly inhomogeneous. Although the diffusion reached the back end of the Bi-YIG layer only at ∼2 ns, the temperature rose by more than 40 K within 100 ps in the first 10 nm behind the Cu interface [see Fig. 1(d)].

The static magnetic properties of the sample are characterized using the MOKE. The normalized polar and longitudinal Kerr hysteresis loops are shown in Fig. 2(a). The out-of-plane normalized remanence (M_r/M_s) was about 0.02, which is very small compared with the in-plane one of 0.85. The out-of-plane saturation field (∼260 mT) was about 50 times larger than the in-plane one (∼5 mT). These results reveal a strong in-plane magnetic anisotropy. The origin of this in-plane easy axis of magnetization is a large growth-induced anisotropy field [52,53], which has the value of −83 mT in the case of our film. The TR-MOKE and reflectivity measurements were investigated with the all-optical pump-probe configuration sketched in Fig. 2(b). We have employed a femtosecond laser pulse issued from an amplified Ti-Sapphire laser system operating at a 5-kHz repetition rate and delivering 35-fs pulses at 800 nm to generate the pump and the probe beams. The pump beam was kept at the fundamental wavelength of the amplifier at 800 nm and excited the sample at normal incidence from the Pt side. The probe beam was frequency doubled to 400 nm using a beta-barium borate (BBO) crystal and incident with a small angle of 6° onto the GGG substrate. Both beams were linearly polarized and focused onto the sample in spot diameters of ∼260 μm for the pump and ∼60 μm for the probe. The probe wavelength was well above the optical absorption edge of the GGG, which allowed the probe pulses to penetrate the substrate and reach the Bi-YIG layer. After interacting with the Bi-YIG, the reflected probe pulses allowed measuring the differential changes of the magneto-optical polar Kerr rotation $\Delta\Theta_K(t)$ and reflectivity $\Delta R(t)$ induced by the excitation pulse as a function of the time delay t between the pump and probe pulses using a lock-in detection scheme. The external magnetic field H_{ext} was applied perpendicular to the plane of the film. All measurements were performed at room temperature.

III. RESULTS AND DISCCUSSION

Figure 3(a) shows the TR-MOKE induced by an incident pump energy density of $E_{\mathrm{pump}} = 9.4\ \mathrm{mJcm^{-2}}$ for $H_{\mathrm{ext}} = 164$ mT. Three important features can be clearly distinguished. First, the $\Delta\Theta_K$ signal shows a small ultrafast decrease within the first picosecond after the arrival of hot electrons at the Cu/Bi-YIG interface, followed by a recovery toward the initial state in the next few picoseconds, as

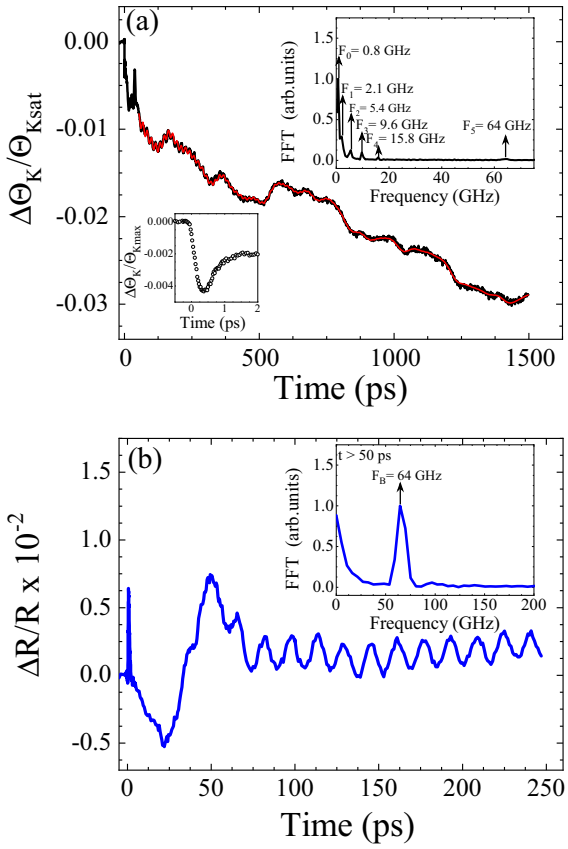

FIG. 3. Dynamics of spin and reflectivity in the $Bi_1Y_2Fe_5O_{12}$/GGG(100) buried below thick Pt/Cu bilayers. $\Delta\Theta_K/\Theta_K$ and $\Delta R/R$ induced by a pump energy density of $E_{pump} = 9.4\,mJcm^{-2}$ for $H_{ext} = 164\,mT$. The solid red line in (a) is the fit using Eq. (1). Insets: (a) Fourier transform spectrum of the $\Delta\Theta_K/\Theta_K$ data for the time delay $t \geqslant 50\,ps$ (top) and a magnified view of the $\Delta\Theta_K/\Theta_K$ signal (bottom) around the zero time delay. (b) Fourier transform spectrum of the $\Delta R/R$ data for the time delay $t \geqslant 50\,ps$ (top).

highlighted in the bottom inset of Fig. 3(a). Second, a gradual slow decrease of the $\Delta\Theta_K$ signal started at ∼5 ps and reached a large value at 1500 ps. Third, very complex oscillations are superimposed on the slow exponential change of the $\Delta\Theta_K$ signal. The characteristic times of the fast and slow decrease of the TR-MOKE are $\tau_{fast} = 0.4 \pm 0.09\,ps$ and $\tau_{slow} = 1220 \pm 60\,ps$. On the other hand, the complex oscillations are formed by six modes with different amplitudes in the frequency range between 0.8 and 64 GHz, as seen in the fast Fourier transform (FFT) spectrum in the top inset of Fig. 3(a). To study these modes in more detail, the TR-MOKE measurements are fitted with the following time damped oscillators:

$$\Delta\Theta_K(t > 41\ ps) = \sum_{i=0}^{5} A_i e^{-t/\tau_i} \sin(2\pi f_i t - \phi_i) + Be^{-t/\tau_{slow}} + C \quad (1)$$

Where A_i, f_i, ϕ_i, and τ_i are, respectively, the amplitude, frequency, initial phase, and decay time characterizing the oscillation of the mode i ($i = 0$, 1, 2, 3, 4, and 5). The term $Be^{-t/\tau_{slow}}$ represents the slow exponential change with the characteristic time τ_{slow} and C is an offset. The corresponding fitting with Eq. (1) is plotted in Fig. 3(a) with a red solid line, showing a good agreement with the experimental data. It yields the frequencies $f_0 = 0.8$ GHz, $f_1 = 2.2$ GHz, $f_2 = 5.4$ GHz, $f_3 = 9.6$ GHz, $f_4 = 15.5$ GHz, and $f_5 = 64$ GHz, which are similar to the ones obtained by the FFT analysis.

To have more information about these modes, we measured the pump-induced change in the reflectivity signal [see Fig. 3(b)]. Clear oscillations with a frequency of ∼64 GHz are observed from the time delay $t = 41$ ps, as seen in the FFT spectrum displayed in the inset of Fig. 3(b). These oscillations can be related to the time-domain Brillouin scattering, which originates from the interference of the probe beam reflected from the Bi-YIG surface with the reflection from the longitudinal strain pulse propagating into the GGG. Indeed, the observed frequency perfectly matches the value $f_{GGG} = 2V^L_{GGG}\sqrt{n^2 - \sin^2\theta}/\lambda = 63.9$ GHz, calculated from the probe wavelength $\lambda = 400\,nm$, the longitudinal sound velocity $V^L_{GGG} = 6400$ m/s of GGG [54], its refractive index $n \approx 2$ [55], and the angle of incidence $\theta = 6°$. Based on these observations, we can conclude that the highest frequency mode in the TR-MOKE is due to the propagation of the longitudinal acoustic pulse in the GGG substrate, since it has the same frequency as the Brillouin oscillation. We note that the observation of Brillouin oscillations in a TR-MOKE signal was previously reported in the literature [29–31,56]. It can be understood considering a small difference in the reflection of right (σ^+) and left (σ^-) helicity of light induced by the acoustic pulse during its propagation in the sample [30,56].

The frequencies of the low-frequency modes are in the range of SW frequencies in Bi-YIG films [43,44,57,58]. To clarify the nature of these modes, we investigated their frequencies as a function of the mode number. Interestingly, the precession frequencies of these modes have a quadratic dependence on the mode number. Such a variation is well described by the dispersion relation of SSW [36,37], which is written in the case of our experimental configuration as [36,37]:

$$\omega(k) = \omega_0 + \gamma D_{ex} k^2, \quad (2)$$

where ω is the angular precession frequency, ω_0 is the angular frequency of the fundamental mode which depends on H_{ext} and the effective magnetic anisotropy field, γ is the gyromagnetic ratio, D_{ex} is the exchange stiffness, and $k = n\pi/d$ represents the wave-vector of the standing SWs given by $d = 135$ nm. Indeed, a fit of experimental data with Eq. (2) using $(\gamma/2\pi) = 28$ GHz/T yields an excellent agreement with the experimental results (Fig. 4). We obtained an exchange stiffness $D_{ex} = (5.9 \pm 0.2)\ 10^{-17}\,T\,m^2$ in good agreement with those reported in the literature for YIG and Bi-YIG [49,59,60]. This clearly demonstrates the SSW nature of the observed magnetic resonance modes. It also shows that we can excite SSWs with a frequency up to 15 GHz, which is

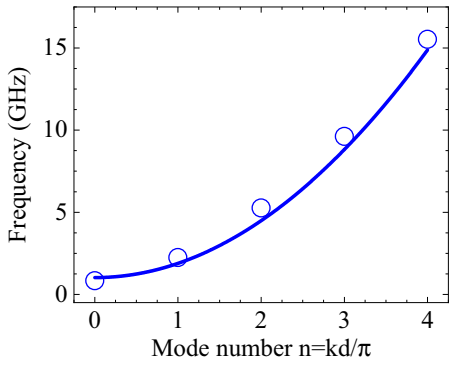

FIG. 4. Spin precession frequency as a function of the mode number. The solid line is the fit obtained using Eq. (2).

15 times higher than the one associated with the ferromagnetic resonance mode (i.e., $n = 0$). The general excitation mechanism of the SSWs can be related to an ultrafast change of magnetic anisotropy via coherent and incoherent phonons. The coherent phonons correspond to the strain wave shown in Fig. 1(c), and it changes the magnetic anisotropy via the inverse magnetostriction. The incoherent phonons correspond to the phonon-temperature change shown in Fig. 1(d). They change the magnetic anisotropy due to the temperature dependence of magnetic anisotropy constants. We discuss below that the physics behind the generation of incoherent phonons should combine the heat energy directly deposited by the hot-electron pulse at the Bi-YIG surface together with the heat energy transferred from Cu to Bi-YIG.

Let us now discuss the fast and slow decrease in the $\Delta\Theta_K$ signal. To give a comprehensive discussion of possible mechanisms behind these phenomena, it is worth mentioning first that the fast decrease and recovery in the $\Delta\Theta_K$ signal are similar to the ultrafast demagnetization process usually induced in metallic magnetic films by ultrashort laser [1] and hot-electron [24] excitations. The exact mechanism of this ultrafast demagnetization is still under debate, but different models have been proposed with the most used being the so-called three-temperature model [1]. This model is purely phenomenological and based on the heat transfer between three interacting subsystems representing electrons, lattice (i.e., phonon), and spins. Such an energy transfer leads to an ultrafast increase of spin temperature, which results in an ultrafast decrease of the magnetic order according to the dependence of the magnetization on the temperature. In magnetic insulators where no free electrons are present, the heating of the spin occurs mainly via the phonon-magnon coupling, which is very weak in the case of iron garnets [61–63]. Therefore, this mechanism cannot be the origin of the subpicosecond decrease of the magnetic order. However, the weak phonon-magnon coupling characterizing iron garnets is in good agreement with the slow decrease in the $\Delta\Theta_K$ signal, which can therefore be related to a slow demagnetization process. These slow demagnetization dynamics are consistent with the generation and propagation of incoherent phonons (heat) into the Bi-YIG layer [see Fig. 1(d)]. We note that Fig. 1(d) does not include the process of generating incoherent phonons directly deposited by the hot-electron pulse at the Bi-YIG surface. Including this process in the simulations is a complex task and will essentially increase the temperature in the first nanometer of Bi-YIG, which could compensate a reduced interface conductance for acoustic phonons at the metal-insulator contact. Due to the absence of free electrons in insulators, heat transport in Bi-YIG is identical to incoherent phonon transport. The decrease of the magnetic order is expected to be inhomogeneous across the Bi-YIG thickness and follow the phonon temperature gradient [Fig. 1(d)] with much larger demagnetization close to the Cu interface.

Apart from the phenomenological three-temperature model, the ultrafast demagnetization dynamics are explained from a microscopic point of view using processes involving fundamental interactions at the origin of magnetism: the spin-orbit interaction and the exchange interaction [64–67]. The spin-orbit interaction should only make a small contribution to the ultrafast loss of the magnetic order observed in our sample. Similar ultrafast decrease in the $\Delta\Theta_K/\Theta_{Kmax}$ signal, i.e., amplitude and timescale, have been measured in heterostructures based on a $Bi_1Y_2Fe_5O_{12}$ or a $Bi_3Fe_5O_{12}$ (not shown), in which different spin-orbit couplings are present due to various Bi concentrations. The large difference in spin-orbit coupling has been experimentally verified in $Bi_xY_{3-x}Fe_5O_{12}$, in which a huge increase of the MO properties was reported when increasing the Bi concentration [68,69]. We therefore suggest that the ultrafast change of the magnetic order is induced by an ultrafast modulation of the exchange interaction [67]. This mechanism has been recently suggested to explain subpicosecond magnetization dynamics induced in YIG and Bi/Ga-substituted YIG by resonant lattice excitation with an ultrashort terahertz pulse and theoretically supported via atomistic spin-dynamics simulations [67]. The scenario behind the modulation of the exchange interaction can be illustrated as follows. The excited incoherent phonons modulate the distance of adjacent atoms, in particular oxygen atoms. Since the superexchange interaction mediated by these atoms is distance dependent, this perturbation leads to an ultrafast modulation of the superexchange interaction between the two iron sublattices, which result in subpicosecond demagnetization dynamics [67].

To investigate further the ultrafast magnetization dynamics, we studied the fast and slow decrease of the magnetic order as a function of the pump energy density and the external magnetic field (see Fig. 5). The amplitude of both processes linearly increases with increasing E_{pump}. This is in good agreement with the expected dependence of the heat energy density of hot electrons on E_{pump}, since it is the main origin of the heat energy generated in our structure. The small nonlinearity in the heat transport originating from the temperature-dependent electronic heat transport is not relevant here, as confirmed by our UXRD studies [32]. On the other hand, we show that the magnetic field dependence of these amplitudes is the same as the static magnetization of the sample [see Fig. 2(a)]. Indeed, they saturate at $H_{ext} \sim 260$ mT, which is the magnetization saturation field characterizing the Bi-YIG film. These results clearly confirm our prediction about the magnetic origin of these phenomena. It is worth mentioning here that the amplitude of the fast demagnetization is about one order of magnitude smaller than the slow

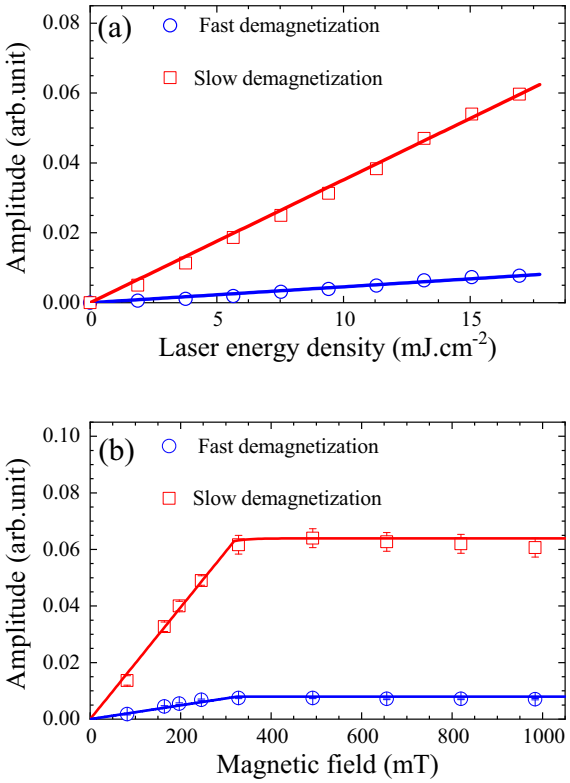

FIG. 5. Amplitude of the fast (circle) and slow (square) demagnetization processes as a function of (a) the pump energy density and (b) the external magnetic field. The solid lines are guides to the eye.

demagnetization for all measured values of H_{ext} and E_{pump}. This is consistent with a very small amplitude of the motion of oxygen atoms, which is in good agreement with the high stiffness and stability characterizing the garnet structure [70,71].

IV. CONCLUSIONS

We have studied the magnetic, optical, and lattice responses of a $Pt/Cu/Bi_1Y_2Fe_5O_{12}/Gd_3Ga_5O_{12}$ heterostructure upon femtosecond laser excitation of the opaque Pt/Cu bilayers. We find that coherent and incoherent phonons generated by the laser-excited metal electrons trigger high-frequency SSWs in the $Bi_1Y_2Fe_5O_{12}$ layer via phonon-induced change of the magnetic anisotropy. The incoherent phonons can induce a fast (<1 ps) and slow (>1000 ps) decrease of the magnetic order. We explain these two timescales by considering scenarios based on spin-phonon interaction. Our findings highlight the possibility of triggering high-frequency SWs in magnetic garnets embedded in complex heterostructure devices.

ACKNOWLEDGMENTS

This paper was supported by the French Investments for the Future Program (PIA) project "Lorraine Université d'Excellence", reference ANR-15-IDEX-04-LUE, the Bundesministerium für Bildung und Forschung Project Grant No. 05K16IPA, and the Deutsche Forschungsgemeinschaft Grant No. BA 2281/11-1. M.D. acknowledges the Alexander von Humboldt Foundation for financial support.

[1] E. Beaurepaire, J. C. Merle, A. Daunois, and J. Y. Bigot, Ultrafast Spin Dynamics in Ferromagnetic Nickel, Phys. Rev. Lett. **76**, 4250 (1996).

[2] U. Bovensiepen, Femtomagnetism: magnetism in step with light, Nat. Phys. **5**, 461 (2009).

[3] G. Zhang, W. Hübner, E. Beaurepaire, and J.-Y. Bigot, in *Spin Dynamics in Confined Magnetic Structures I*, edited by B. Hillebrands and K. Ounadjela (Springer Berlin Heidelberg, Berlin, Heidelberg, 2002).

[4] C. D. Stanciu, F. Hansteen, A. V. Kimel, A. Kirilyuk, A. Tsukamoto, A. Itoh, and T. Rasing, All-Optical Magnetic Recording with Circularly Polarized Light, Phys. Rev. Lett. **99**, 047601 (2007).

[5] S. Mangin, M. Gottwald, C. H. Lambert, D. Steil, V. Uhlíř, L. Pang, M. Hehn, S. Alebrand, M. Cinchetti, G. Malinowski, Y. Fainman, M. Aeschlimann, and E. E. Fullerton, Engineered materials for all-optical helicity-dependent magnetic switching, Nat. Mater. **13**, 286 (2014).

[6] E. Beaurepaire, M. Maret, V. Halté, J. C. Merle, A. Daunois, and J. Y. Bigot, Spin dynamics in $CoPt_3$ alloy films: A magnetic phase transition in the femtosecond time scale, Phys. Rev. B **58**, 12134 (1998).

[7] G. Ju, J. Hohlfeld, B. Bergman, R. J. M. van de Veerdonk, O. N. Mryasov, J.-Y. Kim, X. Wu, D. Weller, and B. Koopmans, Ultrafast Generation of Ferromagnetic Order via a Laser-Induced Phase Transformation in FeRh Thin Films, Phys. Rev. Lett. **93**, 197403 (2004).

[8] J. A. de Jong, I. Razdolski, A. M. Kalashnikova, R. V. Pisarev, A. M. Balbashov, A. Kirilyuk, T. Rasing, and A. V. Kimel, Coherent Control of the Route of an Ultrafast Magnetic Phase Transition via Low-Amplitude Spin Precession, Phys. Rev. Lett. **108**, 157601 (2012).

[9] M. van Kampen, C. Jozsa, J. T. Kohlhepp, P. LeClair, L. Lagae, W. J. M. de Jonge, and B. Koopmans, All-Optical Probe of Coherent Spin Waves, Phys. Rev. Lett. **88**, 227201 (2002).

[10] A. V. Kimel, A. Kirilyuk, P. A. Usachev, R. V. Pisarev, A. M. Balbashov, and T. Rasing, Ultrafast non-thermal control of magnetization by instantaneous photomagnetic pulses, Nature **435**, 655 (2005).

[11] K. Vahaplar, A. M. Kalashnikova, A. V. Kimel, D. Hinzke, U. Nowak, R. Chantrell, A. Tsukamoto, A. Itoh, A. Kirilyuk, and T. Rasing, Ultrafast Path for Optical Magnetization Reversal via a Strongly Nonequilibrium State, Phys. Rev. Lett. **103**, 117201 (2009).

[12] T. A. Ostler *et al.*, Ultrafast heating as a sufficient stimulus for magnetization reversal in a ferrimagnet, Nat. Commun. **3**, 666 (2012).

[13] P. Němec, V. Novák, N. Tesařová, E. Rozkotová, H. Reichlová, D. Butkovičová, F. Trojánek, K. Olejník, P. Malý, R. P. Campion, B. L. Gallagher, J. Sinova, and T. Jungwirth, The essential role of carefully optimized synthesis for elucidating intrinsic material properties of (Ga,Mn)As, Nat. Commun. **4**, 1422 (2013).

[14] R. R. Subkhangulov, H. Munekata, T. Rasing, and A. V. Kimel, Laser-induced spin dynamics in ferromagnetic (In,Mn)As at magnetic fields up to 7 T, Phys. Rev. B **89**, 060402(R) (2014).

[15] S. Shihab, H. Riahi, L. Thevenard, H. J. V. Bardeleben, A. Lemaître, and C. Gourdon, Systematic study of the spin stiffness dependence on phosphorus alloying in the ferromagnetic semiconductor (Ga,Mn)As, Appl. Phys. Lett. **106**, 142408 (2015).

[16] S. Shihab, L. Thevenard, A. Lemaître, and C. Gourdon, Counter-rotating standing spin waves: a magneto-optical illusion, Phys. Rev. B **95**, 144411 (2017).

[17] F. Hansteen, A. Kimel, A. Kirilyuk, and T. Rasing, Femtosecond Photomagnetic Switching of Spins in Ferrimagnetic Garnet Films, Phys. Rev. Lett. **95**, 047402 (2005).

[18] M. Deb, P. Molho, B. Barbara, and J.-Y. Bigot, Temperature and magnetic field dependence of rare-earth ↔ iron exchange resonance mode in a magnetic oxide studied with femtosecond magneto-optical kerr effect, Phys. Rev. B **94**, 054422 (2016).

[19] A. M. Kalashnikova, A. V. Kimel, R. V. Pisarev, V. N. Gridnev, A. Kirilyuk, and T. Rasing, Impulsive Generation of Coherent Magnons by Linearly Polarized Light in the Easy-Plane Antiferromagnet $FeBO_3$, Phys. Rev. Lett. **99**, 167205 (2007).

[20] F. Hansteen, A. Kimel, A. Kirilyuk, and T. Rasing, Nonthermal ultrafast optical control of the magnetization in garnet films, Phys. Rev. B **73**, 014421 (2006).

[21] M. Deb, M. Vomir, J.-L. Rehspringer, and J.-Y. Bigot, Ultrafast optical control of magnetization dynamics in polycrystalline bismuth doped iron garnet thin films, Appl. Phys. Lett. **107**, 252404 (2015).

[22] A. B. Chizhik, I. I. Davidenko, A. Maziewski, and A. Stupakiewicz, High-temperature photomagnetism in Co-doped yttrium iron garnet films, Phys. Rev. B **57**, 14366 (1998).

[23] A. Stupakiewicz, K. Szerenos, D. Afanasiev, A. Kirilyuk, and A. V. Kimel, Ultrafast nonthermal photo-magnetic recording in a transparent medium, Nature **542**, 71 (2017).

[24] N. Bergeard, M. Hehn, S. Mangin, G. Lengaigne, F. Montaigne, M. L. M. Lalieu, B. Koopmans, and G. Malinowski, Hot-Electron-Induced Ultrafast Demagnetization in Co/Pt Multilayers, Phys. Rev. Lett. **117**, 147203 (2016).

[25] Y. Xu, M. Deb, G. Malinowski, M. Hehn, W. Zhao, and S. Mangin, Ultrafast magnetization manipulation using single femtosecond light and hot-electron pulses, Adv. Mater. **29**, 1703474 (2017).

[26] R. B. Wilson, J. Gorchon, Y. Yang, C.-H. Lambert, S. Salahuddin, and J. Bokor, Ultrafast magnetic switching of GdFeCo with electronic heat currents, Phys. Rev. B **95**, 180409(R) (2017).

[27] J.-W. Kim, M. Vomir, and J.-Y. Bigot, Ultrafast Magnetoacoustics in Nickel Films, Phys. Rev. Lett. **109**, 166601 (2012).

[28] J.-W. Kim, M. Vomir, and J.-Y. Bigot, Controlling the spins angular momentum in ferromagnets with sequences of picosecond acoustic pulses, Sci. Rep.-Uk **5**, 8511 (2015).

[29] T. L. Linnik, V. N. Kats, J. Jäger, A. S. Salasyuk, D. R. Yakovlev, A. W. Rushforth, A. V. Akimov, A. M. Kalashnikova, M. Bayer, and A. V. Scherbakov, The effect of dynamical compressive and shear strain on magnetic anisotropy in a low symmetry ferromagnetic film, Phys. Scripta **92**, 054006 (2017).

[30] A. V. Scherbakov, A. S. Salasyuk, A. V. Akimov, X. Liu, M. Bombeck, C. Brüggemann, D. R. Yakovlev, V. F. Sapega, J. K. Furdyna, and M. Bayer, Coherent Magnetization Precession in Ferromagnetic (Ga,Mn)As Induced by Picosecond Acoustic Pulses, Phys. Rev. Lett. **105**, 117204 (2010).

[31] M. Deb, E. Popova, M. Hehn, N. Keller, S. Mangin, and G. Malinowski, Picosecond acoustic-excitation-driven ultrafast magnetization dynamics in dielectric Bi-substituted yttrium iron garnet, Phys. Rev. B **98**, 174407 (2018).

[32] J.-E. Pudell, M. Mattern, M. Hehn, G. Malinowski, M. Herzog, and M. Bargheer, Heat transport without heating?—An ultrafast x-ray perspective into a metal heterostructure, Adv. Funct. Mater. **30**, 2004555 (2020).

[33] I. L. Markov, Limits on fundamental limits to computation, Nature **512**, 147 (2014).

[34] A. G. Gurevich and G. A. Melkov, *Magnetization Oscillations and Waves* (CRC Press, Boca Raton, 1996).

[35] A. A. Serga, A. V. Chumak, and B. Hillebrands, YIG magnonics, J. Phys. D: Appl. Phys. **43**, 264002 (2010).

[36] C. Kittel, *Introduction to Solid State Physics* (John Wiley & Sons, New York, 1986).

[37] A. H. Morrish, *The Physical Principles of Magnetism* (IEEE, New York, 2001).

[38] I. S. Maksymov and M. Kostylev, Broadband stripline ferromagnetic resonance spectroscopy of ferromagnetic films, multilayers and nanostructures, Physica E **69**, 253 (2015).

[39] Y. Ding, T. J. Klemmer, and T. M. Crawford, A coplanar waveguide permeameter for studying high-frequency properties of soft magnetic materials, J. Appl. Phys. **96**, 2969 (2004).

[40] H. Yu, O. d' Allivy Kelly, V. Cros, R. Bernard, P. Bortolotti, A. Anane, F. Brandl, F. Heimbach, and D. Grundler, Approaching soft x-ray wavelengths in nanomagnet-based microwave technology, Nat. Commun. **7**, 11255 (2016).

[41] J. Walowski, M. D. Kaufmann, B. Lenk, C. Hamann, J. McCord, and M. Münzenberg, Intrinsic and non-local Gilbert damping in polycrystalline nickel studied by Ti : sapphire laser fs spectroscopy, J. Phys. D: Appl. Phys. **41**, 164016 (2008).

[42] B. Lenk, G. Eilers, J. Hamrle, and M. Münzenberg, Spin-wave population in nickel after femtosecond laser pulse excitation, Phys. Rev. B **82**, 134443 (2010).

[43] M. Deb, E. Popova, M. Hehn, N. Keller, S. Petit-Watelot, M. Bargheer, S. Mangin, and G. Malinowski, Femtosecond Laser-Excitation-Driven High Frequency Standing Spin Waves in Nanoscale Dielectric Thin Films of Iron Garnets, Phys. Rev. Lett. **123**, 027202 (2019).

[44] M. Deb, E. Popova, M. Hehn, N. Keller, S. Petit-Watelot, M. Bargheer, S. Mangin, and G. Malinowski, Damping of Standing Spin Waves in Bismuth-Substituted Yttrium Iron Garnet as Seen via the Time-Resolved Magneto-Optical Kerr Effect, Phys. Rev. Appl. **12**, 044006 (2019).

[45] E. Popova, L. Magdenko, H. Niedoba, M. Deb, B. Dagens, B. Berini, M. Vanwolleghem, C. Vilar, F. Gendron, A. Fouchet,

J. Scola, Y. Dumont, M. Guyot, and N. Keller, Magnetic properties of the magnetophotonic crystal based on bismuth iron garnet, J. Appl. Phys. **112**, 093910 (2012).

[46] M. Bauer, A. Marienfeld, and M. Aeschlimann, Hot electron lifetimes in metals probed by time-resolved two-photon photoemission, Prog. Surf. Sci. **90**, 319 (2015).

[47] D. Schick, A. Bojahr, M. Herzog, C. V. K. Schmising, R. Shayduk, W. Leitenberger, P. Gaal, and M. Bargheer, Normalization schemes for ultrafast x-ray diffraction using a table-top laser-driven plasma source, Rev. Sci. Instrum. **83**, 025104 (2012).

[48] D. Schick, A. Bojahr, M. Herzog, R. Shayduk, C. von Korff Schmising, and M. Bargheer, UDKM1DSIM—A simulation toolkit for 1D ultrafast dynamics in condensed matter, Comput. Phys. Commun. **185**, 651 (2014).

[49] G. G. Siu, C. M. Lee, and Y. Liu, Magnons and acoustic phonons in $Y_{3-x}Bi_xFe_5O_{12}$, Phys. Rev. B **64**, 094421 (2001).

[50] S. P. Zeuschner, J. E. Pudell, A. von Reppert, M. Deb, E. Popova, N. Keller, M. Rössle, M. Herzog, and M. Bargheer, Measurement of transient strain induced by two-photon excitation, Phys. Rev. Res. **2**, 022013 (2020).

[51] M. Schreier, A. Kamra, M. Weiler, J. Xiao, G. E. W. Bauer, R. Gross, and S. T. B. Goennenwein, Magnon, phonon, and electron temperature profiles and the spin seebeck effect in magnetic insulator/normal metal hybrid structures, Phys. Rev. B **88**, 094410 (2013).

[52] S. A. Manuilov, S. I. Khartsev, and A. M. Grishin, Pulsed laser deposited $Y_3Fe_5O_{12}$ films: nature of magnetic anisotropy I, J. Appl. Phys. **106**, 123917 (2009).

[53] S. A. Manuilov and A. M. Grishin, Pulsed laser deposited $Y_3Fe_5O_{12}$ films: nature of magnetic anisotropy II, J. Appl. Phys. **108**, 013902 (2010).

[54] V. F. Kitaeva, E. V. Zharikov, and I. L. Chistyi, The properties of crystals with garnet structure, Phys. Status Solidi A **92**, 475 (1985).

[55] D. L. Wood and K. Nassau, Optical properties of gadolinium gallium garnet, Appl. Optics **29**, 3704 (1990).

[56] L. Thevenard, E. Peronne, C. Gourdon, C. Testelin, M. Cubukcu, E. Charron, S. Vincent, A. Lemaître, and B. Perrin, Effect of picosecond strain pulses on thin layers of the ferromagnetic semiconductor (Ga,Mn)(As,P), Phys. Rev. B **82**, 104422 (2010).

[57] S. Klingler, V. Amin, S. Geprägs, K. Ganzhorn, H. Maier-Flaig, M. Althammer, H. Huebl, R. Gross, R. D. McMichael, M. D. Stiles, S. T. B. Goennenwein, and M. Weiler, Spin-Torque Excitation of Perpendicular Standing Spin Waves in Coupled YIG/Co Heterostructures, Phys. Rev. Lett. **120**, 127201 (2018).

[58] H. Qin, S. J. Hämäläinen, and S. van Dijken, Exchange-torque-induced excitation of perpendicular standing spin waves in nanometer-thick YIG films, Sci. Rep.-Uk **8**, 5755 (2018).

[59] A. Gurevich and A. Anisimov, Intrinsic spin wave relaxation processes in yttrium iron garnets, Sov. Phys. JETP **41**, 336 (1975).

[60] S. Klingler, A. V. Chumak, T. Mewes, B. Khodadadi, C. Mewes, C. Dubs, O. Surzhenko, B. Hillebrands, and A. Conca, Measurements of the exchange stiffness of YIG films using broadband ferromagnetic resonance techniques, J. Phys. D Appl. Phys. **48**, 015001 (2014).

[61] E. G. Spencer and R. C. LeCraw, Spin-Lattice Relaxation in Yttrium Iron Garnet, Phys. Rev. Lett. **4**, 130 (1960).

[62] D. L. Huber, Spin-magnon relaxation in rare-earth iron garnets, Phys. Rev. **136**, A500 (1964).

[63] G. F. Dionne and G. L. Fitch, Temperature dependence of spin-lattice relaxation in rare-earth iron garnets, J. Appl. Phys. **87**, 4963 (2000).

[64] B. Koopmans, G. Malinowski, F. Dalla Longa, D. Steiauf, M. Fahnle, T. Roth, M. Cinchetti, and M. Aeschlimann, Explaining the paradoxical diversity of ultrafast laser-induced demagnetization, Nat. Mater. **9**, 259 (2010).

[65] K. Krieger, J. K. Dewhurst, P. Elliott, S. Sharma, and E. K. U. Gross, Laser-induced demagnetization at ultrashort time scales: predictions of TDDFT, J. Chem. Theory Comput. **11**, 4870 (2015).

[66] G. P. Zhang, M. S. Si, Y. H. Bai, and T. F. George, Magnetic spin moment reduction in photoexcited ferromagnets through exchange interaction quenching: beyond the rigid band approximation, J. Phys. Condens. Matter **27**, 206003 (2015).

[67] S. F. Maehrlein, I. Radu, P. Maldonado, A. Paarmann, M. Gensch, A. M. Kalashnikova, R. V. Pisarev, M. Wolf, P. M. Oppeneer, J. Barker, and T. Kampfrath, Dissecting spin-phonon equilibration in ferrimagnetic insulators by ultrafast lattice excitation, Sci. Adv. **4**, eaar5164 (2018).

[68] P. Hansen and J. P. Krumme, Magnetic and magneto-optical properties of garnet films, Thin Solid Films **114**, 69 (1984).

[69] S. Wittekoek, T. J. A. Popma, J. M. Robertson, and P. F. Bongers, Magneto-optic spectra and the dielectric tensor elements of bismuth-substituted iron garnets at photon energies between 2.2-5.2 eV, Phys. Rev. B **12**, 2777 (1975).

[70] G. D. Winkler, *Magnetic Garnets*, (Vieweg, Braunschweig, 1981).

[71] G. F. Dionne, *Magnetic Oxides*, (Springer, New York, 2009).

VI Reciprocal space slicing: A time-efficient approach to femtosecond x-ray diffraction

Steffen Peer Zeuschner, Maximilian Mattern, Jan-Etienne Pudell, Alexander von Reppert, Matthias Rössle, Wolfram Leitenberger, Jutta Schwarzkopf, Jos Emil Boschker, Marc Herzog and Matias Bargheer

Structural Dynamics 8, 014302 (2021)

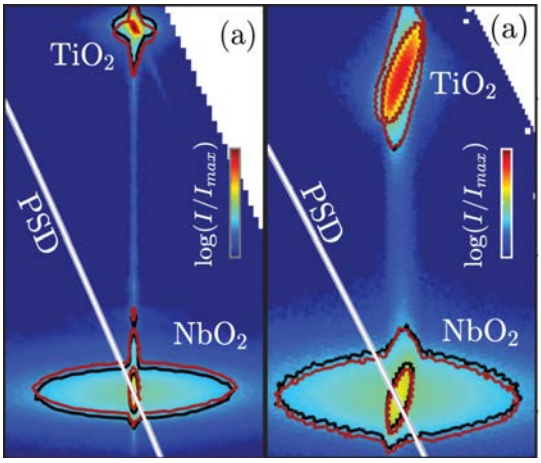

Abstract An experimental technique that allows faster assessment of out-of-plane strain dynamics of thin film heterostructures via x-ray diffraction is presented. In contrast to conventional high-speed reciprocal space-mapping setups, our approach reduces the measurement time drastically due to a fixed measurement geometry with a position-sensitive detector. This means that neither the incident (ω) nor the exit (2θ) diffraction angle is scanned during the strain assessment via x-ray diffraction. Shifts of diffraction peaks on the fixed x-ray area detector originate from an out-of-plane strain within the sample. Quantitative strain assessment requires the determination of a factor relating the observed shift to the change in the reciprocal lattice vector. The factor depends only on the widths of the peak along certain directions in reciprocal space, the diffraction angle of the studied reflection, and the resolution of the instrumental setup. We provide a full theoretical explanation and exemplify the concept with picosecond strain dynamics of a thin layer of NbO_2.

Contributions to the work

I performed the ultrafast X-Ray diffraction measurements at the PXS with the help of Maximilian Mattern. The static, temperature resolved data were measured by Matthias Rössle and Wolfram Leitenberger at the Synchrotron BESSY II of the HZB. I developed the modelling, performed the calculations and wrote the manuscript with the help and comments of the Co-authors. The Ssmples were provided by Jos Emil Boschker and Jutta Schwarzkopf.

Comments

I consider the development, presentation and implementation of the reciprocal space slicing technique to be part of the most important projects during my PhD studies. It clearly states a significant improvement of the experimental procedures of XRD and UXRD in particular. As mentioned in Section 2.1.1, the low number and availability of ultrashort X-ray pulse sources render measurement time a scarce and expensive resource and the RSS technique reduces the necessary time significantly. RSS can be applied and implemented at synchrotrons and FELs and in extension even at other diffraction experiments, such as electron- or neutron diffraction.

In the UDKM group at the University of Potsdam, we almost exclusively use the RSS technique in the UXRD experiments at the Plasma driven X-ray source to accelerate the measurements, since the photon flux is limited to 2 Mcounts/s. In Section 2.1.1 I will give a short summary of the mechanics of the RSS technique which is described in detail in this publication.

Structural Dynamics ARTICLE scitation.org/journal/sdy

Reciprocal space slicing: A time-efficient approach to femtosecond x-ray diffraction

Cite as: Struct. Dyn. 8, 014302 (2021); doi: 10.1063/4.0000040
Submitted: 25 September 2020 · Accepted: 21 December 2020 ·
Published Online: 21 January 2021

S. P. Zeuschner,[1,2,a] M. Mattern,[1] J.-E. Pudell,[1,2] A. von Reppert,[1] M. Rössle,[2] W. Leitenberger,[1] J. Schwarzkopf,[3] J. E. Boschker,[3] M. Herzog,[1] and M. Bargheer[1,2,a]

AFFILIATIONS

[1]Institut für Physik und Astronomie, Universität Potsdam, 14476 Potsdam, Germany
[2]Helmholtz-Zentrum Berlin für Materialien und Energie GmbH, Wilhelm-Conrad-Röntgen Campus, BESSY II, 12489 Berlin, Germany
[3]Leibniz-Institut für Kristallzüchtung, 12489 Berlin, Germany

[a]Authors to whom correspondence should be addressed: szeuschn@uni-potsdam.de and bargheer@uni-potsdam.de

ABSTRACT

An experimental technique that allows faster assessment of out-of-plane strain dynamics of thin film heterostructures via x-ray diffraction is presented. In contrast to conventional high-speed reciprocal space-mapping setups, our approach reduces the measurement time drastically due to a fixed measurement geometry with a position-sensitive detector. This means that neither the incident (ω) nor the exit (2θ) diffraction angle is scanned during the strain assessment via x-ray diffraction. Shifts of diffraction peaks on the fixed x-ray area detector originate from an out-of-plane strain within the sample. Quantitative strain assessment requires the determination of a factor relating the observed shift to the change in the reciprocal lattice vector. The factor depends only on the widths of the peak along certain directions in reciprocal space, the diffraction angle of the studied reflection, and the resolution of the instrumental setup. We provide a full theoretical explanation and exemplify the concept with picosecond strain dynamics of a thin layer of NbO_2.

I. INTRODUCTION

Modern crystallography and strain assessment at the nanoscale cannot be imagined without x-ray diffraction. This nondestructive and widely available tool to determine interatomic distances in crystalline specimen has been proven to be particularly useful in the ultrafast dynamics of condensed matter.[1–4] Technological progress relies on the development of novel and faster procedures to transfer energy between subsystems and a decreasing size of the devices. This implies the importance of quantifying strain in nanoscale specimens of technologically relevant materials on the picosecond timescale.[5–10]

Ultrafast x-ray diffraction (UXRD) setups are sensitive to changes in the diffraction pattern, which map out the reciprocal space (RS) of the specimen in which lattice dynamics have been triggered.[11] To access details of the crystalline order in the reciprocal space, all the diffracted intensity needs to be spatially quantified as a function of the angular relation between the incoming x-ray beam, the sample, and the detector.[11,12] Scanning both angles of a point detector and the sample takes a large amount of time, especially if multiple reciprocal space maps (RSMs) need to be recorded for time-resolved measurements.

With the introduction of position-sensitive detectors, i.e., pixel-area or pixel-line detectors, it became possible to measure the diffracted intensity on a linear subset of the reciprocal space simultaneously.[12–14] Consequently, the time for full reciprocal space mapping decreased drastically, e.g., for time-resolved strain assessment. A detection scheme with a fixed detector has been used in the context of high repetition rate UXRD experiments at synchrotrons.[15]

In this paper, we discuss an experimental method to determine the strain perpendicular to the surface of nanoscale heterostructures, which reduces the acquisition time even more. The data acquisition routine, which we call reciprocal space slicing (RSS), constantly monitors just a subset of the reciprocal space of a specimen with an area detector and a fixed diffraction geometry (see Sec. II). We analyze theoretically that reciprocal space slicing is sufficient to monitor strain dynamics perpendicular to the surface of most thin, layered specimen without scanning the diffraction angles. This applies for diffraction setups with monochromatic and parallel or convergent x-rays (see Sec. III A or Sec. IV A, respectively).

Structural Dynamics ARTICLE scitation.org/journal/sdy

We test our theory experimentally at the KMC-3 XPP Beamline at the BESSY II synchrotron of the HZB[16,17] for parallel x-rays in Sec. III B. For a convergent x-ray beam, reciprocal space slicing is validated experimentally at the femtosecond x-ray diffraction setup with a laser-based plasma x-ray source (PXS)[18,19] (see Sec. IV B). With both setups, we demonstrate the slicing by examination of a sample fabricated by pulsed laser deposition a thin layer of NbO_2 on top of a TiO_2 substrate.[20] NbO_2 exhibits an insulator-metal phase transition, accompanied by a transition in the crystalline ordering at 1070 K.[21] This renders NbO_2 and its alloys a promising material class for electrical switching and even memory applications at high temperatures.[22–24] Future ultrafast strain assessment during the phase transition using UXRD may reveal novel insight into the transition and promote application development in electronics, complementing all-optical studies.[25] For this publication, however, the NbO_2 sample was mainly selected because of its particular shape in reciprocal space, displaying a high-contrast twofold nature of the Bragg reflections, due to a particular domain structure resulting in a large discrepancy of the structural, in-plane coherence length. This sample is, thus, ideal to demonstrate the advantages and limitations of reciprocal space slicing for narrow and broad Bragg reflections in a single measurement.

II. RECIPROCAL SPACE SLICING

Generally, the measured intensity in reciprocal space ($I(\vec{Q})$) is a convolution of the reciprocal space (RS) of the specimen and the instrument's resolution area (RA),[11]

$$I(\vec{Q}) = (RS * RA)(\vec{Q}). \quad (1)$$

The shape of the resolution area is determined by the energy distribution and the trajectories of the x-ray photons used for diffraction. In reciprocal space, this translates into the length and directions of the incident x-ray wave vectors $\vec{k}_{in}$. Since RA is different for the two presented experimental setups in this paper, we evaluate the role of RA in Secs. III A and IV A. But the shape of the reciprocal space is determined by the coherence length of the scattering periodic structure of the specimen.[11] As we use the same sample throughout this paper, RS is the same and is modeled as follows.

For thin films, the reciprocal space $RS(\vec{Q})$ in the vicinity of $\vec{G}$ can be approximated by a Gaussian function. In this paper, we visualize the 3D reciprocal space by a 2D projection onto the q_x/q_z-plane since we only discriminate between the in- and out-of-plane directions. Here, q_z is aligned perpendicular and q_x parallel to the sample surface and diffraction plane. Thus, we model $RS(\vec{Q})$ of a thin layer, by a 2D-Gaussian function,

$$RS(q_x, q_z) = A_{RS} \exp\left(-\frac{(q_x - g_x)^2}{2\sigma_x^2} - \frac{(q_z - g_z - \Delta q_z)^2}{2\sigma_z^2}\right), \quad (2)$$

where σ_x and σ_z are the widths along q_x and q_z, which are inversely proportional to the in-plane and out-of-plane coherence lengths, respectively. The amplitude A_{RS} is proportional to the structure factor, and g_x and g_z are the components of $\vec{G}$, which has an absolute value that is inversely proportional to the lattice spacing in real space. In our case, g_x is close to 0, as we analyze lattice planes parallel to the sample surface. The shift of $\vec{G}$ resulting from out-of-plane strain is given by Δq_z. A contour line of this particular intensity in the q_x/q_z-plane is an ellipse, in which both semi-axis lengths correspond to the widths σ_x and σ_z. In Figs. 1(a) and 1(b), $I(q_x, q_z)$ is visualized for opposing σ_x/σ_z ratios by ellipses to provide an intuitive geometric approach.

In a symmetric diffraction geometry, with the center of the position sensitive detector set to twice the Bragg angle of the probed material ($2\theta_B$), the detector intersects the corresponding reciprocal lattice point $\vec{G}$, which is positioned at $\vec{G} = \vec{Q} := \vec{k}_{out} - \vec{k}_{in}$ in the reciprocal space map (RSM).[11,19] This means that the area detector slices the intensity distribution in reciprocal space (RS) in the center (Fig. 1), as the pixels record a large 2θ range of the diffracted signal.

Strain of the specimen perpendicular to the surface results in a change in the q_z-component of $\vec{G}$. Conventionally, this is detected by comparing an RSM of the strained sample with an RSM of a reference state. In this process, the RSMs are assembled by the reciprocal space slices recorded at different combinations of the diffraction angle ω and the 2θ range of the detector area.[11] Here, ω is the angle between $\vec{k}_{in}$

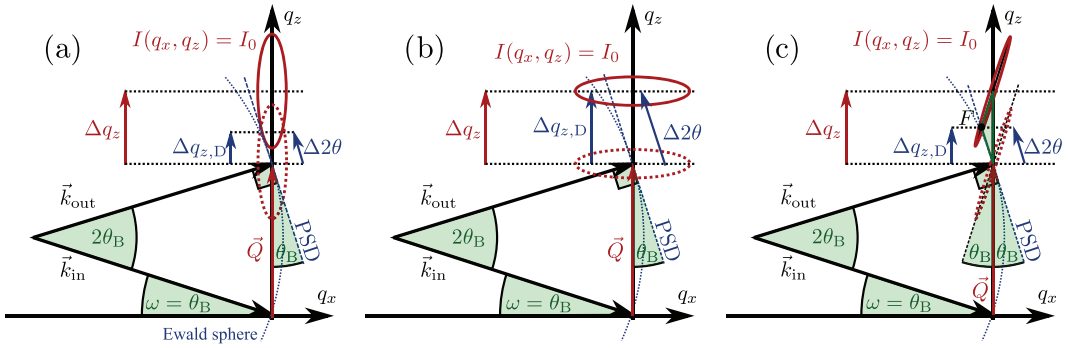

FIG. 1. Schematic sketch of a symmetric diffraction geometry set to the Bragg angle θ_B for different shaped intensity distributions surrounding $\vec{Q} = \vec{G}$. q_x is aligned along the sample surface. The red dashed and solid ellipses represent contour lines of the intensity distribution $I(q_x, q_z)$ surrounding $\vec{G}$ before and after the shift along q_z, respectively. The dotted blue line represents the Ewald sphere on which the detector is positioned. We approximate the arc by a straight line, indicated by the dashed blue line, labeled PSD. (a) I is elongated along q_z, which results in a small visible $\Delta 2\theta$ on the detector. (b) I is elongated along q_x, which leads to $\Delta q_{z,D} \approx \Delta q_z$. (c) $2\Delta q_{z,D} \approx \Delta q_z$, for reflections with high crystalline quality at the PXS setup (see Sec. IV).

Structural Dynamics ARTICLE scitation.org/journal/sdy

and the lattice planes of the corresponding $\vec{G}$, which are chosen to be parallel to the sample surface in this paper. 2θ denotes the angle enclosed by $\vec{k}_{in}$ and $\vec{k}_{out}$.

In contrast to full reciprocal space mapping, the diffraction geometry is fixed during reciprocal space slicing, which means, in particular, that ω and 2θ are set and fixed to θ_B and $2\theta_B$. This decreases the measurement time significantly, because no angular scans are required. The resulting Δq_z of a strained material manifests itself in a shift of the diffracted intensity distribution on the position sensitive detector ($\Delta 2\theta$) (see Fig. 1). The projection of $\Delta 2\theta$ onto the q_z axis $\Delta q_{z,D}$ is proportional to Δq_z, and the proportionality factor S depends on the diffraction geometry, the resolution area of the experimental setup (RA), and the reciprocal space of the specimen (RS) in proximity to $\vec{G}$. Consequently, we are able to determine the strain η by just scaling the shift of the 1D intensity distribution on the detector with the factor S. Since the detector area is tangent to the 2θ-circle, the strain η is proportional to the change in the diffraction angle $\Delta 2\theta$ on the detector and S,

$$\eta = -\frac{\Delta q_z}{|\vec{G}| + \Delta q_z} = -S\frac{\Delta q_{z,D}}{|\vec{G}| + \Delta q_z} = -S\frac{\Delta 2\theta}{2}\cot(\theta'_B), \tag{3}$$

where θ'_B is the Bragg angle after the shift occurred. For small strains below a few %, we can approximate $\theta'_B \approx \theta_B$ and $|\vec{G}| + \Delta q_z \approx |\vec{G}|$.

In Secs. III–IV, we will give a quantitative evaluation of the functional dependence of the desired observable Δq_z on the shift observed on the detector $\Delta 2\theta$. For this, we put in different RAs for the two different experimental setups and model the intensity distribution on the detector as a function of the shift Δq_z.

III. RECIPROCAL SPACE SLICING AT SYNCHROTRONS

A. The role of position sensitive detectors in RSS

First, we assume a resolution area, which corresponds to a monochromatic and parallel x-ray beam, which means that the resolution area can be approximated by a δ-function in the wave vector and energy space. Thus, the RSM is equal to the reciprocal space of the specimen: $I(\vec{Q}) = RS(\vec{Q})$, according to Eq. (2).

The intensity distribution measured by a detector line (I_D) is a one-dimensional subset of the intensity distribution $I(q_x, q_z)$, namely, an arc with the radius k_{in}, i.e., a fraction of the Ewald sphere for symmetric diffraction.[11,19] We approximate this arc as a line, as the size of the intensity distribution around $\vec{G}$ is typically comparably small with respect to the wave vector. Even for a minimal coherence length of $L_c = \pi/(\sqrt{2\ln 2}\sigma_q) = 1$ nm, the width $\sigma_q \approx 0.3$ Å^{-1} of the distribution $RS(\vec{Q})$ in the corresponding direction is an order of magnitude smaller than usual hard x-ray wave vectors that are on the order of $|\vec{k}_{in}| \approx 4$ Å^{-1} (8 keV). With this, the detector can be described by a linear parametric function, which defines a subset of the reciprocal space via Eq. (4), which is indicated by a dashed blue line in Fig. 1,

$$q_z = -\frac{q_x}{\tan(\theta_B)} + g_z. \tag{4}$$

Since this defines all pairs (q_x, q_z) at which the detector measures the intensity, we substitute q_x in Eq. (2) with Eq. (4) to get the measured intensity on the detector line I_D as a function of q_z only, which is again a 1D Gaussian function,

$$\begin{aligned} I_D(q_z) &:= I(-(q_z - g_z)\tan(\theta_B), q_z) \\ &= A_{RS}\exp\left(-\frac{\tan(\theta_B)^2(q_z - g_z)^2}{2\sigma_x^2} - \frac{(q_z - g_z - \Delta q_z)^2}{2\sigma_z^2}\right) \\ &\stackrel{!}{=} A_D\exp\left(-\frac{(q_z - g_z - \Delta q_{z,D})^2}{2\sigma_D^2}\right), \end{aligned} \tag{5}$$

where A_D is a scaled amplitude, σ_D is the width, and $\Delta q_{z,D}$ is the shift of the intensity distribution on the detector line projected onto the q_z axis. The relation between the strain-induced change of $\vec{G}$ (Δq_z) and the shift that is measured ($\Delta q_{z,D}$) is, therefore, given by

$$\Delta q_z = \Delta q_{z,D}\underbrace{\left(1 + \frac{\sigma_z^2}{\sigma_x^2}\tan(\theta_B)^2\right)}_{=:S}. \tag{6}$$

In the experiments with a fixed diffraction geometry and a δ-shaped instrument function, it is thus possible to derive the change in $\vec{G}$ and hence, the strain by just scaling the shift of the 1D intensity distribution on the detector with the factor S. However, this is only applicable for broad intensity distributions in reciprocal space. For very narrow Bragg reflections, e.g., as typical of substrates, even small shifts along q_z lead to a massive intensity loss on the fixed detector so that the diffracted intensity quickly becomes impossible to detect.

In Figs. 1(a) and 1(b), we display the two limits of this result with which we illustrate several important implications. In (a), $\sigma_x < \sigma_z$, which is the case for a single-crystalline thin film, results in a rather large intensity loss but only a small shift of the intensity distribution on the detector $\Delta q_{z,D}$ compared to the real shift of the intensity maximum Δq_z. In (b), on the other hand, where $\sigma_x > \sigma_z$, which is the case for columnar growing films, the observed shift on the detector $\Delta q_{z,D}$ is basically equal to Δq_z and the amplitude does not change significantly either. Figure 1 also illustrates that the discrepancies between $\Delta q_{z,D}$ and Δq_z become more pronounced with increasing diffraction angles, e.g., at higher diffraction orders.

B. Thermally induced strain measured with RSS

In this section, we evaluate the negative thermal expansion of the 75 nm thin NbO_2 layer on top of a TiO_2 substrate at the KMC-3 XPP beamline at the BESSY II synchrotron of the HZB,[16,17] using the reciprocal space slicing theory described in Sec. II.

The thin layer of NbO_2 exhibits a tetragonal crystal structure where the (100) direction, which coincides with the (110) direction of the rutile ordered TiO_2, is aligned out-of-plane, i.e., parallel to q_z. We scanned the full reciprocal space in proximity to the (200) and (220) Bragg reflections of NbO_2 and TiO_2, respectively, with 8 keV parallel x-rays and an area detector (*Pilatus 100 K* from DECTRIS). A projection onto the q_x/q_z-plane at a sample temperature of 100 K is displayed in Fig. 2(a). A projection of the intensity of both reflections onto the q_z-axis is displayed in (b), and the projection of the NbO_2 reflection onto the q_x-axis is displayed in (c). The black contour lines and graphs correspond to the RSM recorded at 100 K and the red lines to the RSM recorded at 300 K.

The Bragg reflections yield the following information about the crystalline structure of the sample. The reflection of the TiO_2 substrate

Structural Dynamics ARTICLE scitation.org/journal/sdy

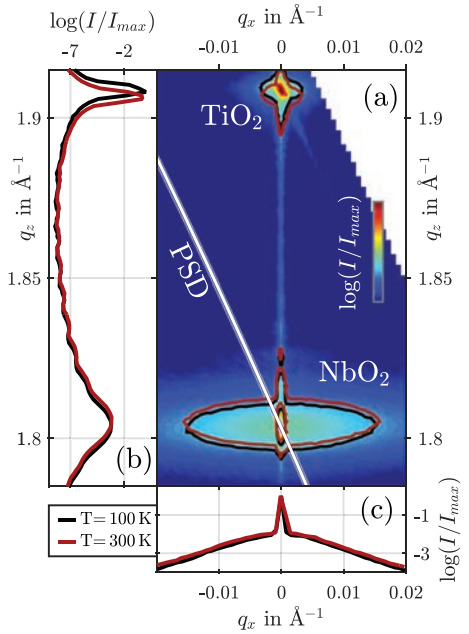

FIG. 2. (a) RSM of the sample recorded at 100 K at the KMC-3 XPP beamline in the vicinity of the (200) NbO_2-layer and (220) TiO_2-substrate Bragg reflections. The black and red lines are contour lines of the RSM at 100 K and at 300 K, respectively. (b) and (c) Projections of the RSM onto the q_z- and q_x-axis, respectively. The q_x-projection contains only the RSM in close proximity to the NbO_2 reflection ($1.78\,\text{Å}^{-1} < q_z < 1.83\,\text{Å}^{-1}$). The white line indicates the linear subset of the reciprocal space, which is measured simultaneously by the detector (PSD) and defined by Eq. (4). The intensity distribution on the detector is shown in Fig. 3.

is narrow in reciprocal space, only deformed and broadened by the crystal truncation rod, analyzer and monochromator streaks, and thermal diffuse scattering.[11] The NbO_2 reflection, on the other hand, reveals two contributions, indicated by the broad (b) horizontally elongated and narrow (n) vertically aligned ellipsoidal contour lines for two different intensities of the RSM, shown in Fig. 2(b). The projections onto the q_x and q_z axes allow the determination of the widths along the two directions by Gaussian fits and, consequently, the quantification of the coherence lengths parallel and perpendicular to the surface. We find a single width of $\sigma_z = 0.004$ Å^{-1} in the q_z direction and the widths of $\sigma_{x,b} = 0.009$ Å^{-1} for the broad part and an upper limit of $\sigma_{x,n} = 0.0003$ Å^{-1} for the narrow portion along q_x. This corresponds to an out-of-plane coherence length of $\xi_z = 66$ nm, which is close to the layer thickness of 75 nm. Parallel to the surface, the widths correspond to coherence lengths of $\xi_b = 30$ nm and at least $\xi_n = 900$ nm. The latter can be even larger, but we are limited by the scanning resolution. The occurrence of two coherence lengths parallel to the surface is associated with lattice mismatches of TiO_2 and NbO_2. The c-axes of both tetragonal materials are aligned with a small lattice mismatch of just 1%. This leads to a well-ordered crystalline structure of NbO_2 and a large coherence length parallel to this direction. Along the in-plane direction perpendicular to the c-axis, the lattice mismatch is considerably larger with over 5%. This leads to strong distortions in NbO_2 and a small coherence length. AFM measurements of the surface support this interpretation by revealing domains at the nanometer length scale.[20] Since the x-ray probe spot on the specimen measures tens to hundreds of micrometers in both directions, the signal of the diffracted intensity is a lateral average of the domains and thus, contains both contributions.

The change of the contour lines and graphs from black to red in Fig. 2 exemplify the lattice response of the TiO_2/NbO_2 heterostructure to static heating. A rise in temperature from 100 K to 300 K leads to the expected thermal expansion of TiO_2, which we measure directly by the shift of the (220) reflection of TiO_2 to lower q_z.[26] Simultaneously, both contributions of the NbO_2 (200) reflection shift to larger q_z with increasing temperature, which corresponds to the reported negative thermal expansion of NbO_2 along the a-axis of the tetragonal unit cell below room temperature.[27] The q_z shift due to the contraction can be quantified by the comparison of two RSMs and the projection onto the q_z axis [see Fig. 2(b)].

We now discuss reciprocal space slicing as a faster alternative for Δq_z assessments, which uses just one detector image of the RSM scan at 100 and 300 K. The two detector images for the two temperatures are displayed in Fig. 3 after integration of the intensity on the detector area perpendicular to the diffraction plane. The diffraction patterns on the detector exhibit the two contributions of the NbO_2 reflection, but only the broad part reveals a visible shift along the diffraction angle 2θ with increasing temperature. This finding agrees with the modeling in Sec. III A since the visible shift of the diffraction pattern on the detector line $\Delta 2\theta$ is proportional to the strain, but the proportionality factor S depends on the shape of the intensity distribution via Eq. (6). With the widths of the two contributions, we get $S_b = 1.01$ for the broad and $S_n = 11$ for the narrow component. Since the real thermally induced strain is expected to be identical for both contributions, $\Delta 2\theta$ must be more than ten times smaller for the narrow component of the

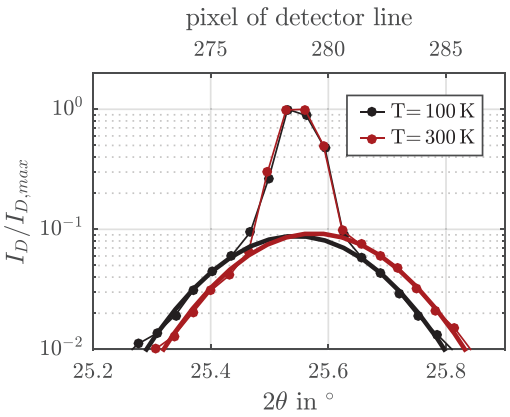

FIG. 3. Relative intensity distribution on the area detector after integration perpendicular to the diffraction plane for 100 and 300 K. The position of the detector pixels is transformed to 2θ, according to the diffraction geometry. The data are fitted by a broad Gaussian function to indicate the larger shift of the broad component of the NbO_2 (200) reflection in comparison to the narrow contribution that remains almost unchanged.

Structural Dynamics ARTICLE scitation.org/journal/sdy

NbO_2 reflection than for the broad component [see Eq. (3)]. This is consistent with the data in Fig. 3. Additionally, we crosschecked the quantitative agreement of the strain determined by conventional full reciprocal space mapping and slicing. Δq_z, determined with RSM data in Fig. 2, is, in fact, equal to $S_b \Delta q_{z,D}$.

This exemplifies that reciprocal space slicing can be a very effective way to determine out-of-plane strain if the intensity distribution in the vicinity of $\vec{G}$ is comparably broad along q_x compared to q_z, which is the limiting case depicted in Fig. 1(b). It also illustrates that shifts of $\vec{G}$ with a surrounding intensity distribution, which are very narrow along q_x compared to q_z, can be much better quantified with full reciprocal space mapping. Thus, slicing with highly parallel beams at synchrotrons is only effective for thin layers with in-plane coherence lengths comparable to the layer thickness, i.e., specimen with noticeable mosaicity or a domain structure.

IV. RECIPROCAL SPACE SLICING WITH A COMPLEX RESOLUTION AREA

A. The role of convergent and polychromatic x-rays in RSS

The resolution area can have a rather complex shape in many experimental setups. In this section, we illustrate the application of reciprocal space slicing for the plasma x-ray source (PXS) at the University of Potsdam, which is optimized for ultrafast x-ray diffraction (UXRD) with a pulse length on the order of 200 fs.[18] The probing x-ray pulses are composed of the $K_{\alpha 1}$ and $K_{\alpha 2}$ lines of copper and are focused onto the specimen by a Montel optic (Incoatec ELM45).[28] The diffracted signal is detected by an area detector (*Pilatus 100 K* from Dectris).[19] For static measurements, the PXS can be replaced by a microfocus x-ray tube (*UltraBright 96000* from Oxford instruments) with the focus positioned where the femtosecond x-rays emerge.

In both cases, the resolution area of this setup is described by the sum of two 2D Gaussian functions.[19] The Gaussian doublet is separated by 0.25% of the chosen scattering vector $\vec{Q}$ with respect to the q_z axis due to the energy difference of the $K_{\alpha 1}$ and $K_{\alpha 2}$ lines and is broadened along q_z by the natural linewidth of these characteristic lines. The major axis of the Gaussian doublet is determined by the convergence of 0.3° from the x-ray optic. The pixel size of the detector limits the resolution of the detected x-rays along the minor axis of the Gaussian doublet. This is associated with an uncertainty of the diffraction angle, which can reach from 0.1° to 0.005°, depending on the sample-detector distance of 0.1 to 2 m. In reciprocal space, the doublet is rotated by the diffraction angle of the incident x-rays ω [see Fig. 1(c)].[19]

As is shown in the Appendix, the intensity distribution I_D of an elongated $\vec{G}$ measured along the slice of the detector is again a Gaussian function and can be written as

$$I_D = A_{I_D} \exp\left(-\frac{\left(q_z - \frac{\Delta q_z}{S}\right)^2}{2\sigma_{I_D}^2}\right), \tag{7}$$

where A_{I_D} is the amplitude and σ_{I_D} is the width of the intensity distribution of the detector projected onto the q_z axis. The scaling factor S connects the measured q_z shift on the detector ($\Delta q_{z,D}$) with the real shift Δq_z of $\vec{G}$, similar to Eq. (6). In this case, S depends on the parameters of the resolution area as well. For symmetric diffraction geometries with $\omega = \theta_B$, S is given by Eq. (8) that contains two simple implications if we evaluate two opposite limiting cases.

On the one hand, we can assume very broad intensity distributions in the reciprocal space of the specimen in proximity to $\vec{G}$, i.e., $\sigma_x, \sigma_z \gg \sigma_{RA,x}, \sigma_{RA,z}$. This is the case for samples that exhibit small coherence lengths in- and out-of-plane, in particular, thin films with noticeable mosaicity. Then, Eq. (8) reduces to the definition of S in Eq. (6), which is expected, as the previously assumed δ-like resolution area is always narrower than any other feature in the reciprocal space of the specimen.

$$S := \frac{\sigma_{RA,x}^2 - \sigma_z^2 + \frac{\sigma_z^2}{\cos(\theta_B)^2} + \frac{\sigma_{RA,x}^2}{\cos(\theta_B)^2} - 4\sin(\theta_B)(\sigma_{RA,x}^2 - \sigma_{RA,z}^2)}{\sigma_x^2 + \sigma_z^2 - 2\sin(\theta_B)(\sigma_{RA,x}^2 - \sigma_{RA,z}^2)}. \tag{8}$$

On the other hand, we can assume a reciprocal space, which exhibits intensity distributions surrounding $\vec{G}$ that are far narrower than the resolution area of the PXS setup. This is the case for samples with large coherence lengths, i.e., substrates or films with high-quality crystallinity. In that case, the expression in Eq. (8) becomes

$$S = \frac{2\sin(\theta_B)^2(\sigma_{RA,x}^2 - \sigma_{RA,z}^2) - \frac{1}{2}\sigma_{RA,x}^2/\cos(\theta_B)^2}{\sin(\theta_B)^2(\sigma_{RA,x}^2 - \sigma_{RA,z}^2) - \sigma_{RA,x}^2/2}, \tag{9}$$

which converges to two for $\sigma_{RA,z} \gg \sigma_{RA,x}$, as it is the case for the PXS setup that has $\sigma_{RA,z} \approx 20 \times \sigma_{RA,x}$.[19] This limit of a factor of 2 can also be motivated via a geometrical reasoning shown in Fig. 1(c). A contour line of the measured intensity distribution from a substrate is sketched in red, neglecting the twofold nature of the resolution area at the PXS. The semi-major axis of this ellipse is related to $\sigma_{RA,z}$ and the semi-minor axis to $\sigma_{RA,x}$. The ellipse is tilted clockwise by the angle θ_B with respect to the q_z axis, whereas the detector line is inclined by the same angle, but counterclockwise. In this symmetric diffraction geometry, the semi-major axis of the ellipse, the detector line, and the q_z axis constitute an isosceles triangle (green). Therefore, the q_z projection of the intersection point F of the semi-major axis and the detector line always is exactly half of the true shift of $\vec{G}$.

B. Picosecond strain dynamics with RSS

In this section, we present a complete evaluation of picosecond strain dynamics of the sample in the context of reciprocal space slicing. To employ the slicing technique, we first record a full reciprocal space map (RSM) of the specimen without optical excitation to determine the shape of the resolution area and the reciprocal space in proximity to $\vec{G}$ of the thin NbO_2 layer. Ideally, the latter is determined at a synchrotron-based diffraction setup with very high angular resolution (see Fig. 2 for the RSM with a very small resolution area). Clearly, the TiO_2 substrate reflection is much sharper than the thin layer NbO_2 reflection, which is composed of two contributions with very different widths along q_x. Ultrafast diffraction experiments combining a time resolution of 100 fs with such a small resolution area can only be recorded at free-electron lasers or femto-slicing beamlines. At synchrotrons, the time resolution is typically limited to 100 ps. Here, we discuss a table top femtosecond x-ray diffraction setup driven by a PXS.

Structural Dynamics ARTICLE scitation.org/journal/sdy

The transient response of the sample is probed with a 200 fs x-ray pulse composed of the Cu K_α doublet in the convergent beam geometry described in Sec. IV A. For ultrafast x-ray diffraction experiments, we excite the sample with 100 fs pulses centered around 800 nm, at an incident pump-energy density of 10 mJ/cm^2. The time resolution of this setup approaches the state-of-the-art at free electron lasers, however, with many orders of magnitude less brilliance and with a much larger resolution area. We shall see in the following that the broad resolution area may be advantageous for the presented technique.

In Fig. 4(a), we display an RSM recorded at the PXS in proximity to the NbO_2 (200) and TiO_2 (220) Bragg reflections. The intensity distribution at $\vec{G}$ of the substrate TiO_2 illustrates the shape of the PXS's resolution area due to the high crystalline quality of the substrate. In principle, it can be approximated by two 2D-Gaussian functions that are elongated along q_z and rotated by the diffraction angle θ_B.[19] The scanning resolution of the RSM and the small diffraction angle, however, limit the clear separation of the K_α doublet. We fit the resolution area with a single 1D Gaussian function with $\sigma_{RA,x} = 6 \times 10^{-4}$ Å^{-1} and $\sigma_{RA,z} = 6 \times 10^{-3}$ Å^{-1}, which is rotated by $\theta_B - 3°$ to account for splitting.

The intensity distribution in proximity to the NbO_2 reflection consists of two components that are indicated by the black contour lines corresponding to different intensities in Fig. 4(a). The two components have been discussed in detail in Sec. III B, and here we see the instrumental broadening compared to synchrotron setups. Clearly, the narrow component is rotated, compared to the measurement at the synchrotron, see Fig. 2, exhibiting a similar shape as the substrate reflection, i.e., it is also limited by the resolution area of the setup.

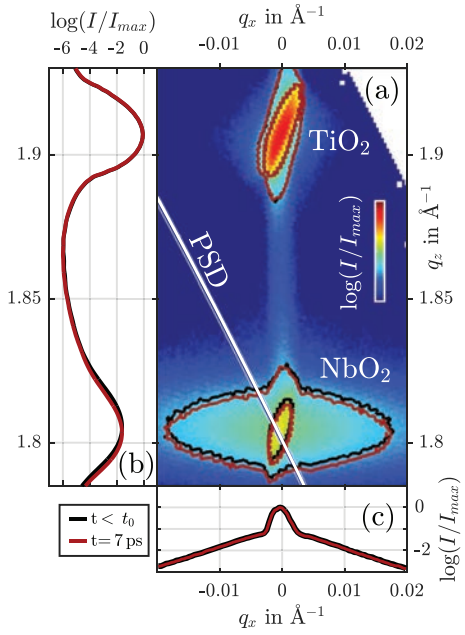

FIG. 4. RSM (a) of the sample with projections onto q_z- (b) and q_x-axes (c). The TiO_2 (110) substrate peak is visible at $q_z = 1.91$ Å^{-1} and the NbO_2 (100) layer peak at $q_z = 1.82$ Å^{-1}. The ellipses in (a) are contour lines of the RSM before (black) and 7 ps after excitation (red). Accordingly, the projections onto the axes in (b) and (c) are taken from the RSM before and after excitation. The white line indicates the linear subset of the reciprocal space, which is simultaneously measured by the area detector (PSD) and defined by Eq. (4).

Upon femtosecond laser excitation, the measured RSM changes, as phonons are coherently and incoherently excited, triggering a long-lasting thermal expansion and picosecond strain pulses.[29] Since the thermal expansion coefficient of NbO_2 perpendicular to the surface is positive above 300 K, the generated strain is positive, which leads to a shift of $\vec{G}$ to smaller q_z.[27] The red contour lines in Fig. 4 indicate the shift Δq_z after a pump–probe delay of 7 ps compared to the RSM before excitation (black contour lines). The projections onto the q_x and q_z axes confirm a shift exclusively along q_z. Also, the contour lines of the substrate reflection do not change since 7 ps is not enough time to transfer significant amounts of energy into the substrate by heat diffusion. Energy deposition inside the substrate by the initial excitation pulse is extremely unlikely as the bandgap of TiO_2 with over 3 eV exceeds the used pump photon energy of 1.55 eV.[30] The dynamics of both components from the twofold reflection of NbO_2 are the same since the pump and probe spots of the UXRD measurement with diameters of 1 and 0.3 mm, respectively, average over many of the small, equally strained domains with large and small coherence lengths, as described in the case of static heating.

To quantitatively determine the strain response of the thin NbO_2 layer after femtosecond laser excitation, we first recorded full reciprocal space maps and later slices of the reciprocal space as a function of the pump–probe delay under identical measurement conditions. The intensity distributions of the reciprocal space maps were projected onto the q_z axis, as shown in Fig. 4(b) to extract the shift Δq_z for each delay of pump and probe pulses. This is done with a single Gaussian fit since the twofold nature of the NbO_2 reflection manifests itself only in the q_x direction, not in q_z (see Fig. 4). Via the scaled derivative of Bragg's law, i.e., the right half of Eq. (3), the strain was calculated and is plotted in Fig. 5(b) as green circles (η_{RSM}). The error bars indicate the uncertainty of the strain assessment given by the standard deviation of the strain for negative delays.

In contrast to the full reciprocal space mapping approach, the diffraction geometry is not changed during the reciprocal space slicing. The detector measures the intensity of the reciprocal space slice along the 2θ-axis indicated by the white line in Fig. 4(a). The intensity distribution before excitation is displayed in Fig. 5(a). The sum of two Gaussian functions (black) fits the data.

According to Eq. (3), we calculate the strain $\eta(t)$ from the shifts of the two contributions to the intensity distribution on the detector $\Delta 2\theta(t)$ separately, where S is set to $S_n = 2.2$ and $S_b = 1.1$. The resulting strain transients η_{nG} and η_{bG} are displayed in Fig. 5(b) as magenta and blue lines, respectively. The scaling factors are calculated with Eq. (8) using the widths in the reciprocal space measured at the synchrotron and the widths of the resolution area of the PXS setup. To account for the Cu K_α doublet, we applied an angular offset of 3° to the diffraction angle. The transformation of the measured angles into reciprocal space is sensitive to experimental parameters such as the sample-detector distance, the relation between the 2θ and pixel axis, and the alignment of the sample to the rotation center of the goniometer.

Structural Dynamics ARTICLE scitation.org/journal/sdy

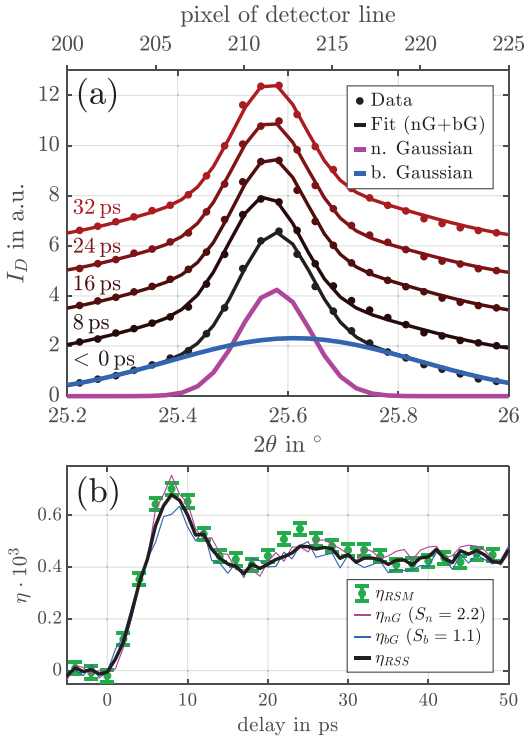

FIG. 5. (a) Intensity distribution on the detector line before excitation (black) and after several ps delays (black to red). The data are fitted with the sum of two Gaussian functions, a narrow Gaussian (nG, magenta) and a broad Gaussian (bG, blue). (b) Average strain inside the NbO_2 layer upon femtosecond laser excitation. The strain is determined with single Gaussian fits of the full reciprocal space map projection onto the q_z axis (green dots). A sum of two Gaussian functions is used to fit the reciprocal space slicing data (black). The latter is the average of the strain from the narrow Gaussian fit (magenta) and the broad Gaussian fit (blue), calculated via Eq. (3) with, respectively, different scaling factors $S_n = 2.2$ and $S_b = 1.1$.

We observe that the broad Gaussian part (blue) shifts significantly more on the detector after excitation than the narrow Gaussian part (magenta), i.e., $(\Delta 2\theta)_b > (\Delta 2\theta)_n$. Only the correct scaling of the shifts reveals a qualitative and quantitative agreement of the strain value deduced from the change in the diffraction pattern [thin blue and magenta lines in Fig. 5(b)]. The strain dynamics observed using the reciprocal space slicing technique also agree with the strain determined via conventional full reciprocal space mapping.

The presented strain response in NbO_2 upon femtosecond laser excitation corresponds well to the standard model of laser-excited thin film transducers probed by x-ray diffraction.[31] A bipolar strain wave is launched, which traverses and leaves the NbO_2 thin film within the first 20 ps. The average layer strain rises while the layer is expanding, and the compressive leading half of the bipolar wave is ejected into the substrate. When the trailing expansive half of the coherent phonon wavepacket exits the layer toward the substrate, the strain level decreases to 0.04%, which is 2/3 of the maximum strain as it is expected for a perfectly impedance matched layer. In this case, we observe an additional local maximum at 25 ps, which corresponds to the expansive strain of the partly reflected strain wave from the layer interface. The residual expansion beyond 35 ps originates solely from thermal expansion and decays on a nanosecond timescale via heat diffusion. The observed timings of the strain pulse in Fig. 5(b) are consistent with the thickness and the longitudinal sound velocity of the NbO_2 layer.

The presented example demonstrates that reciprocal space slicing yields the same quantitative and qualitative strain dynamics as conventional reciprocal space mapping does. The full reciprocal space mapping measurement took three times longer than the slicing while having only half of the delay steps scanned. Thus, the reciprocal space slicing can assess strain dynamics in thin films almost an order of magnitude faster. The slicing approach readily shows that the strain dynamics of both components of the (200) Bragg reflection in NbO_2 have the same amplitude. In general, different samples may exhibit nano-domains that exhibit disparate strain dynamics, and the slicing technique would be able to measure this difference as long as the dynamics are one-dimensional. This illustrates an advantage of the slicing performed at the PXS compared to the synchrotron evaluation presented in Sec. III. There, it is only practically possible to determine the strain from the broad component of the Bragg reflection since the resolution area was too small and not tilted in the reciprocal space. Paradoxically, the instrumental broadening by a convergence and energy spread is beneficial for the slicing scheme for samples of high crystalline quality.

It may be important to reanalyze experimental work in the field of ultrafast x-ray diffraction and strain assessment that uses some form of reduced reciprocal space analysis.[8–10,32–48] From the very early days of UXRD using plasma sources, the large convergence of the x-rays was used to speed up the measurements by area detectors. The correct scaling was often considered unimportant, maybe because experimental determination of the fluence introduces considerable uncertainties. In other cases, only scaled quantities were relevant. We would like to note, however, that some publications in this context use the phrase "rocking curve" for experimental conditions, where the sample is not "rocked," but instead the convergence of the source and the area detector are used to measure different angles simultaneously. We now think that it would be good to point out the precise experimental conditions in future publications. Several publications of our group were based on UXRD measurements applying the reciprocal space slicing approach.[8–10,42–48] We reviewed all of them and found that the claims and findings are still correct. In most cases, this is because the scaling factor is negligible due to large mosaicities of thin films and small diffraction angles. In some other cases, only the qualitative strain response is evaluated, rendering the scaling irrelevant.

V. CONCLUSIONS

Our analysis shows that the interpretation of ultrafast x-ray diffraction experiments using RSS instead of full RSM requires quantitative characterization of the natural Bragg peak widths in reciprocal space around the investigated reciprocal lattice point. We provide formulas to calculate the scaling factor S that is required to quantify the strain from the shift of a Bragg peak in a reciprocal space slice,

Structural Dynamics ARTICLE scitation.org/journal/sdy

which is recorded in experiments using position-sensitive detectors. The scaling factor depends on the width of the measured intensity distributions along q_x and q_z in reciprocal space. This is given by the instrumental resolution area, the structural properties of the crystal investigated, and the diffraction angle. Reciprocal space slicing is an excellent method for speeding up time-resolved x-ray diffraction experiments.

The formulas for the appropriate scaling factor indicate that the slicing is generally ineffective, when S is very large, due to a small signal-to-noise ratio. This is the case for large diffraction angles or reflections, which are much broader along q_z compared to q_x because the measurable shift on the detector $\Delta 2\theta$ then becomes very small. Our examples show that a broad resolution area may be advantageous for rapid slicing of the reciprocal space. In a typical synchrotron experiment with negligible instrumental broadening, reflections from crystals that have a much larger coherence length along q_x than along q_z exhibit scaling factor S that can be larger than 10, so that shifts along q_z yield only very small observable changes in a reciprocal space slicing experiment. For substrate-like reflections, which have large coherence lengths along both q_x and q_z, even tiny strains shift $\vec{G}$ along q_z such that the detector only intersects the wings of the associated Bragg reflection, with considerable intensity loss. Using a convergent x-ray beam with a consequently larger resolution area prevents this at the expense of angular resolution.

We conclude that reciprocal space slicing is a useful tool for strain assessment, from the static heating to femtosecond laser excitation. It works particularly well for small scaling factors S, i.e., small diffraction angles and small coherence lengths in-plane, for example, thin metal films with large mosaicities. The average strain of thin layers is correctly assessed even for inhomogeneous strain patterns, although details of the strain distribution are better characterized by full reciprocal space mapping, especially in the context of phase transitions. Even transient changes of the coherence lengths, due to strongly inhomogeneous strain patterns, and the resulting changes of the Bragg reflection widths can, in principle, be incorporated by a transient scaling factor and, thus, lead to a correct strain assessment. If strong structural changes in two or three dimensions, which change the coherence volume, are expected, full reciprocal space mapping is a better alternative. We hope that our analysis will help in designing and interpreting future UXRD experiments.

ACKNOWLEDGMENTS

We acknowledge the BMBF for the financial support via 05K16IPA. The synchrotron experiments were conducted at the XPP-KMC3 beamline D13.2 at the BESSY II electron storage ring operated by the Helmholtz-Zentrum Berlin.

DATA AVAILABILITY

The data that support the findings of this study are available from the corresponding authors upon reasonable request.

APPENDIX: CALCULATION OF THE SCALING FACTOR FOR THE PXS SETUP

With an ellipsoidal parameterization of the exponent of the Gaussian functions, the resolution area can be described by

$$\begin{aligned} RA(q_x, q_z) &= RA_1(q_x, q_z) + RA_2(q_x, q_z) \\ &= A_{\mathrm{RA},1} \exp\left(-aq_x^2 - 2bq_xq_z - cq_z^2\right) \\ &\quad + A_{\mathrm{RA},2} \exp\left(-aq_x^2 - 2bq_x\left(1 + \frac{\Delta k}{k_{\mathrm{in}}}\right)q_z \right. \\ &\quad \left. - c\left(1 + \frac{\Delta k}{k_{\mathrm{in}}}\right)^2 q_z^2\right), \end{aligned} \tag{A1}$$

where k_{in} is the wave vector of $K_{\alpha 1}$, Δk accounts for the separation, and $A_{\mathrm{RA},1}$ and $A_{\mathrm{RA},2}$ for the relative intensities of the K_α doublet. a, b, and c are parameters of the ellipsoid and are defined by

$$\begin{aligned} a &:= \frac{\cos(\omega)^2}{2\sigma_{\mathrm{RA},x}^2} + \frac{\sin(\omega)^2}{2\sigma_{\mathrm{RA},z}^2}, \\ b &:= -\frac{\sin(\omega)}{4\sigma_{\mathrm{RA},x}^2} + \frac{\sin(\omega)}{4\sigma_{\mathrm{RA},z}^2}, \\ c &:= \frac{\sin(\omega)^2}{2\sigma_{\mathrm{RA},x}^2} + \frac{\cos(\omega)^2}{2\sigma_{\mathrm{RA},z}^2}, \end{aligned} \tag{A2}$$

where $\sigma_{\mathrm{RA},x}$ and $\sigma_{\mathrm{RA},x}$ are the widths in q_x and q_z directions of the 2D Gaussian function before rotating by the angle ω.

The convolution of this resolution area with the reciprocal space of the specimen around $\vec{G}$ then equals the RSM measured at the PXS setup $I(q_x, q_z)$, as described by Eqs. (1) and (2) in Sec. II. Since convolutions are linear operations of functions, it is sufficient to evaluate the convolution integral of RS and the first addend RA_1. The convolution of the second part of RA with RS is identical after a coordinate transformation to account for the separation by $\Delta k/k_{\mathrm{in}}$. We find that the convolution $I_1(q_x, q_z) := (RS * RA_1)(q_x, q_z)$ is again a 2D Gaussian function. In order to derive the intensity distribution I_{D_1} of a shifted $\vec{G}$ measured along the slice of the detector, we again substitute q_x in $I_1(q_x, q_z)$ with its equivalent expression given in Eq. (4). The function is also Gaussian and can, therefore, be written as

$$\begin{aligned} I_{D_1} &= I_1(-(q_z - q_{z,0})\tan(\theta_{\mathrm{B}}), q_z) \\ &= A_{I_{D1}} \exp\left(-\frac{\left(q_z - \frac{\Delta q_z}{S}\right)^2}{2\sigma_{I_{D1}}^2}\right), \end{aligned} \tag{A3}$$

where $A_{I_{D1}}$ is the amplitude and $\sigma_{I_{D1}}$ is the width of the intensity distribution of the detector projected onto the q_z axis. The scaling factor S connects the measured q_z shift on the detector ($\Delta q_{z,D}$) with the real shift Δq_z of $\vec{G}$, similar to Eq. (6). In this case, S depends on the parameters of the resolution area as well.

REFERENCES

[1] A. Rousse, C. Rischel, and J.-C. Gauthier, "Femtosecond x-ray crystallography," Rev. Mod. Phys. **73**, 17–31 (2001).
[2] M. Bargheer, N. Zhavoronkov, M. Woerner, and T. Elsaesser, "Recent progress in ultrafast x-ray diffraction," Chemphyschem **7**, 783–792 (2006).
[3] M. Chergui and A. H. Zewail, "Electron and x-ray methods of ultrafast structural dynamics: Advances and applications," Chemphyschem **10**, 28–43 (2009).
[4] T. Elsaesser and M. Woerner, "Perspective: Structural dynamics in condensed matter mapped by femtosecond x-ray diffraction," J. Chem. Phys. **140**, 020901 (2014).

[5]M. Kozina, M. Fechner, P. Marsik, T. van Driel, J. M. Glownia, C. Bernhard, M. Radovic, D. Zhu, S. Bonetti, U. Staub, and M. C. Hoffmann, "Terahertz-driven phonon upconversion in $SrTiO_3$," Nat. Phys. **15**, 387–392 (2019).

[6]S. Pandey, R. Bean, T. Sato, I. Poudyal, J. Bielecki, J. C. Villarreal, O. Yefanov, V. Mariani, T. A. White, C. Kupitz, M. Hunter, M. H. Abdellatif, S. Bajt, V. Bondar, A. Echelmeier, D. Doppler, M. Emons, M. Frank, R. Fromme, Y. Gevorkov, G. Giovanetti, M. Jiang, D. Kim, Y. Kim, H. Kirkwood, A. Klimovskaia, J. Knoska, F. H. M. Koua, R. Letrun, S. Lisova, L. Maia, V. Mazalova, D. Meza, T. Michelat, A. Ourmazd, G. Palmer, M. Ramilli, R. Schubert, P. Schwander, A. Silenzi, J. Sztuk-Dambietz, A. Tolstikova, H. N. Chapman, A. Ros, A. Barty, P. Fromme, A. P. Mancuso, and M. Schmidt, "Time-resolved serial femtosecond crystallography at the european XFEL," Nat. Methods **17**, 73–76 (2020).

[7]G. J. Williams, S. Lee, D. A. Walko, M. A. Watson, W. Jo, D. R. Lee, and E. C. Landahl, "Direct measurements of multi-photon induced nonlinear lattice dynamics in semiconductors via time-resolved x-ray scattering," Sci. Rep. **6**, 39506 (2016).

[8]A. von Reppert, L. Willig, J.-E. Pudell, S. P. Zeuschner, G. Sellge, F. Ganss, O. Hellwig, J. A. Arregi, V. Uhl\v r, A. Crut, and M. Bargheer, "Spin stress contribution to the lattice dynamics of FePt," Sci. Adv. **6**, eaba1142 (2020).

[9]S. P. Zeuschner, J.-E. Pudell, A. von Reppert, M. Deb, E. Popova, N. Keller, M. Rössle, M. Herzog, and M. Bargheer, "Measurement of transient strain induced by two-photon excitation," Phys. Rev. Res. **2**, 022013 (2020).

[10]J. Pudell, A. A. Maznev, M. Herzog, M. Kronseder, C. H. Back, G. Malinowski, A. von Reppert, and M. Bargheer, "Layer specific observation of slow thermal equilibration in ultrathin metallic nanostructures by femtosecond x-ray diffraction," Nat. Commun. **9**, 3335 (2018).

[11]U. Pietsch, V. Holý, and T. Baumbach, *High-Resolution X-Ray Scattering: From Thin Films to Lateral Nanostructures*, Advanced Texts in Physics, 2nd ed. (Springer, New York, 2004).

[12]P. F. Fewster, "Reciprocal space mapping," Crit. Rev. Solid State Mater. Sci. **22**, 69–110 (1997).

[13]A. Kinne, M. Thoms, H. R. Ress, T. Gerhard, M. Ehinger, W. Faschinger, and G. Landwehr, "Image plates as one-dimensional detectors in high-resolution x-ray diffraction," J. Appl. Crystallogr. **31**, 446–452 (1998).

[14]O. Masson, A. Boulle, R. Guinebretière, A. Lecomte, and A. Dauger, "On the use of one-dimensional position sensitive detector for x-ray diffraction reciprocal space mapping: Data quality and limitations," Rev. Sci. Instrum. **76**, 063912 (2005).

[15]M. Kozina, T. Hu, J. S. Wittenberg, E. Szilagyi, M. Trigo, T. A. Miller, C. Uher, A. Damodaran, L. Martin, A. Mehta, J. Corbett, J. Safranek, D. A. Reis, and A. M. Lindenberg, "Measurement of transient atomic displacements in thin films with picosecond and femtometer resolution," Struct. Dyn. **1**, 034301 (2014).

[16]M. Reinhardt and W. Leitenberger, "Xpp: X-ray pump probe station at BESSY II," J. Large-Scale Res. Facil. **2**, 1–4 (2016).

[17]A. Koc, M. Reinhardt, A. von Reppert, M. Roessle, W. Leitenberger, K. Dumesnil, P. Gaal, F. Zamponi, and M. Bargheer, "Ultrafast x-ray diffraction thermometry measures the influence of spin excitations on the heat transport through nanolayers," Phys. Rev. B **96**, 014306 (2017).

[18]F. Zamponi, Z. Ansari, C. Korff Schmising, P. Rothhardt, N. Zhavoronkov, M. Woerner, T. Elsaesser, M. Bargheer, T. Trobitzsch-Ryll, and M. Haschke, "Femtosecond hard x-ray plasma sources with a kilohertz repetition rate," Appl. Phys. A **96**, 51–58 (2009).

[19]D. Schick, R. Shayduk, A. Bojahr, M. Herzog, C. von Korff Schmising, P. Gaal, and M. Bargheer, "Ultrafast reciprocal-space mapping with a convergent beam," J. Appl. Crystallogr. **46**, 1372–1377 (2013).

[20]J. Stoever, J. E. Boschker, S. Bin Anooz, M. Schmidbauer, P. Petrik, J. Schwarzkopf, M. Albrecht, and K. Irmscher, "Approaching the high intrinsic electrical resistivity of nbo 2 in epitaxially grown films," Appl. Phys. Lett. **116**, 182103 (2020).

[21]T. Sakata, K. Sakata, and I. Nishida, "Study of phase transition in NbO_2," Phys. Status Solidi B **20**, K155–K157 (1967).

[22]S. H. Shin, T. Halpern, and P. M. Raccah, "High–speed high–current field switching of NbO_2," J. Appl. Phys. **48**, 3150–3153 (1977).

[23]S. Kim, J. Park, J. Woo, C. Cho, W. Lee, J. Shin, G. Choi, S. Park, D. Lee, B. H. Lee, and H. Hwang, "Threshold-switching characteristics of a nanothin-NbO_2-layer-based Pt/NbO_2/Pt stack for use in cross-point-type resistive memories," Microelectron. Eng. **107**, 33–36 (2013).

[24]S. Slesazeck, H. Mähne, H. Wylezich, A. Wachowiak, J. Radhakrishnan, A. Ascoli, R. Tetzlaff, and T. Mikolajick, "Physical model of threshold switching in NbO_2 based memristors," RSC Adv. **5**, 102318–102322 (2015).

[25]M. R. Beebe, J. M. Klopf, Y. Wang, S. Kittiwatanakul, J. Lu, S. A. Wolf, and R. A. Lukaszew, "Time-resolved light-induced insulator-metal transition in niobium dioxide and vanadium dioxide thin films," Opt. Mater. Express **7**, 213 (2017).

[26]R. K. Kirby, "Thermal expansion of rutile from 100 to 700 °K," J. Res. Nat. Bur. Stand. Sect. A, Phys. Chem. **71A**, 363–369 (1967).

[27]J. Kaiser, D. S. Rimai, and R. J. Sladek, "Thermal expansivity in semiconducting NbO_2," Solid State Commun. **32**, 925–927 (1979).

[28]M. Bargheer, N. Zhavoronkov, R. Bruch, H. Legall, H. Stiel, M. Woerner, and T. Elsaesser, "Comparison of focusing optics for femtosecond x-ray diffraction," Appl. Phys. B **80**, 715–719 (2005).

[29]P. Ruello and V. E. Gusev, "Physical mechanisms of coherent acoustic phonons generation by ultrafast laser action," Ultrasonics **56**, 21–35 (2015).

[30]T. Guang-Lei, H. Hong-Bo, and S. Jian-Da, "Effect of microstructure of tio 2 thin films on optical band gap energy," Chin. Phys. Lett. **22**, 1787–1789 (2005).

[31]D. Schick, M. Herzog, A. Bojahr, W. Leitenberger, A. Hertwig, R. Shayduk, and M. Bargheer, "Ultrafast lattice response of photoexcited thin films studied by x-ray diffraction," Struct. Dyn. **1**, 064501 (2014).

[32]C. Rose-Petruck, R. Jimenez, T. Guo, A. Cavalleri, C. W. Siders, F. Rksi, J. A. Squier, B. C. Walker, K. R. Wilson, and C. P. J. Barty, "Picosecond–milliångström lattice dynamics measured by ultrafast x-ray diffraction," Nature **398**, 310–312 (1999).

[33]K. Sokolowski-Tinten, C. Blome, C. Dietrich, A. Tarasevitch, M. Horn von Hoegen, D. von der Linde, A. Cavalleri, J. Squier, and M. Kammler, "Femtosecond x-ray measurement of ultrafast melting and large acoustic transients," Phys. Rev. Lett. **87**, 225701 (2001).

[34]C. v. Korff Schmising, M. Bargheer, M. Kiel, N. Zhavoronkov, M. Woerner, T. Elsaesser, I. Vrejoiu, D. Hesse, and M. Alexe, "Strain propagation in nanolayered perovskites probed by ultrafast x-ray diffraction," Phys. Rev. B **73**, 212202 (2006).

[35]A. Morak, T. Kämpfer, I. Uschmann, A. Lübcke, E. Förster, and R. Sauerbrey, "Acoustic phonons in InSb probed by time-resolved x-ray diffraction," Phys. Status Solidi B **243**, 2728–2744 (2006).

[36]H. J. Lee, J. Workman, J. S. Wark, R. D. Averitt, A. J. Taylor, J. Roberts, Q. McCulloch, D. E. Hof, N. Hur, S.-W. Cheong, and D. J. Funk, "Optically induced lattice dynamics probed with ultrafast x-ray diffraction," Phys. Rev. B: Condens. Matter Mater. Phys. **77**, 132301 (2008).

[37]M. Nicoul, U. Shymanovich, A. Tarasevitch, D. von der Linde, and K. Sokolowski-Tinten, "Picosecond acoustic response of a laser-heated gold-film studied with time-resolved x-ray diffraction," Appl. Phys. Lett. **98**, 191902 (2011).

[38]F. Quirin, M. Vattilana, U. Shymanovich, A.-E. El-Kamhawy, A. Tarasevitch, J. Hohlfeld, D. von der Linde, and K. Sokolowski-Tinten, "Structural dynamics in FeRh during a laser-induced metamagnetic phase transition," Phys. Rev. B **85**, 020103(R) (2012).

[39]T. G. White, P. Mabey, D. O. Gericke, N. J. Hartley, H. W. Doyle, D. McGonegle, D. S. Rackstraw, A. Higginbotham, and G. Gregori, "Electron-phonon equilibration in laser-heated gold films," Phys. Rev. B: Condens. Matter Mater. Phys. **90**, 014305 (2014).

[40]R. Li, H. E. Elsayed-Ali, J. Chen, D. Dhankhar, A. Krishnamoorthi, and P. M. Rentzepis, "Ultrafast time-resolved structural changes of thin-film ferromagnetic metal heated with femtosecond optical pulses," J. Chem. Phys. **151**, 124702 (2019).

[41]M. Afshari, P. Krumey, D. Menn, M. Nicoul, F. Brinks, A. Tarasevitch, and K. Sokolowski-Tinten, "Time-resolved diffraction with an optimized short pulse laser plasma x-ray source," Struct. Dyn. **7**, 014301 (2020).

[42]M. Sander, A. Koc, C. T. Kwamen, H. Michaels, A. v. Reppert, J. Pudell, F. Zamponi, M. Bargheer, J. Sellmann, J. Schwarzkopf, and P. Gaal, "Characterization of an ultrafast bragg-switch for shortening hard x-ray pulses," J. Appl. Phys. **120**, 193101 (2016).

[43]A. von Reppert, J. Pudell, A. Koc, M. Reinhardt, W. Leitenberger, K. Dumesnil, F. Zamponi, and M. Bargheer, "Persistent nonequilibrium dynamics of the thermal energies in the spin and phonon systems of an antiferromagnet," Struct. Dyn. **3**, 054302 (2016).

Structural Dynamics ARTICLE scitation.org/journal/sdy

[44]A. von Reppert, R. M. Sarhan, F. Stete, J. Pudell, N. Del Fatti, A. Crut, J. Koetz, F. Liebig, C. Prietzel, and M. Bargheer, "Watching the vibration and cooling of ultrathin gold nanotriangles by ultrafast x-ray diffraction," J. Phys. Chem. C **120**, 28894–28899 (2016).
[45]A. von Reppert, L. Willig, J.-E. Pudell, M. Rössle, W. Leitenberger, M. Herzog, F. Ganss, O. Hellwig, and M. Bargheer, "Ultrafast laser generated strain in granular and continuous FePt thin films," Appl. Phys. Lett. **113**, 123101 (2018).
[46]S. P. Zeuschner, T. Parpiiev, T. Pezeril, A. Hillion, K. Dumesnil, A. Anane, J. Pudell, L. Willig, M. Rössle, M. Herzog, A. von Reppert, and M. Bargheer, "Tracking picosecond strain pulses in heterostructures that exhibit giant magnetostriction," Struct. Dyn. **6**, 024302 (2019).
[47]A. von Reppert, M. Mattern, J.-E. Pudell, S. P. Zeuschner, K. Dumesnil, and M. Bargheer, "Unconventional picosecond strain pulses resulting from the saturation of magnetic stress within a photoexcited rare earth layer," Struct. Dyn. **7**, 024303 (2020).
[48]J.-E. Pudell, M. Mattern, M. Hehn, G. Malinowski, M. Herzog, and M. Bargheer, "Heat transport without heating?—An ultrafast x-ray perspective into a metal heterostructure," Adv. Funct. Mater. **30**, 2004555 (2020).

VII Ultrafast control of lattice strain via magnetic circular dichroism

Marwan Deb, Elena Popova, Steffen Peer Zeuschner, Wolfram leitenberger, Niels Keller, Matthias Rössle and Matias Bargheer

Physical Review B 103, 064301 (2021)

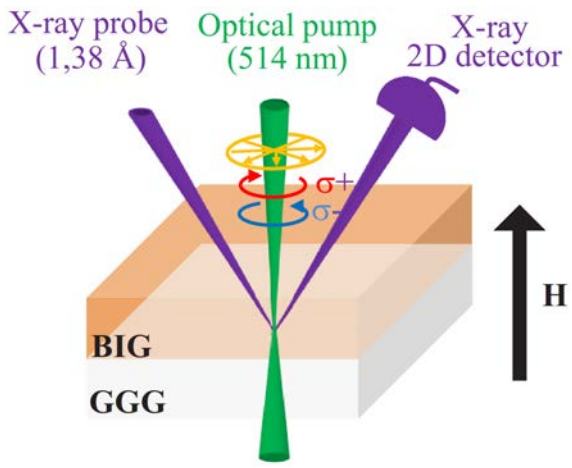

Abstract Using ultrafast x-ray diffraction, we directly monitor the lattice dynamics induced by femtosecond laser pulses in nanoscale thin films of bismuth iron garnet in external magnetic fields H_{ext}. We control the ultrafast laser-induced lattice strain amplitude by changing the laser pulse helicity. The strength of H_{ext} is used as an external parameter to switch the helicity dependence on and off, respectively. Based on magneto-optical spectroscopic measurements, we explain these phenomena by magnetic circular dichroism. Our findings highlight an important approach for ultrafast manipulation of lattice strain in magnetic materials, in particular insulators, and open exciting perspectives towards ultrafast control of lattice strain and heat-induced magnetization switching and spin waves in bismuth substituted iron garnets using the polarization of light.

Contributions to the work

I supported Marwan Deb in the design of the experiments with the previous ultrafast X-Ray diffraction experiments on Garnets and the discussions about the results. I commented on the manuscript. The samples were provided by Elena Popova and Nils Keller.

Comments

If parameters like temperature, external magnetic field or pump pulse characteristics change the response of a material significantly, it is more likely to be used in future technological applications. Consequently, physical research participates in the search of new systems which are efficiently manipulated and controlled by external stimuli to propel the technological advancement.

In this publication, we show that it is possible to change the amplitude of the ultrafast strain response of thin ferromagnetic Bi:YIG layers by changing the polarization state of the pump pulses. This provides a quick and easy way to manipulate the amplitude of the spin waves observed in Bi:YIG, which are triggered by the strain dynamics. In principle, the change of the polarization changes the amount of the absorbed energy in the film due to the magnetic circular dichroism of Bi:YIG. In article III, we are also able to change the amount of the absorbed energy via two-photon absorption by adjusting the pulse duration of the pump pulse and thus the peak intensity. However, to change the polarization is experimentally much easier to accomplish and to control with simple waveplates than setting a different pulse duration with the compressor of the used femtosecond laser system.

PHYSICAL REVIEW B **103**, 064301 (2021)

Ultrafast control of lattice strain via magnetic circular dichroism

Marwan Deb,[1,*] Elena Popova,[2] Steffen Peer Zeuschner,[1,3] Wolfram Leitenberger,[1] Niels Keller,[2] Matthias Rössle,[3] and Matias Bargheer[1,3]

[1]*Institut für Physik und Astronomie, Universität Potsdam, Karl-Liebknecht-Strasse 24–25, 14476 Potsdam, Germany*
[2]*Groupe d'Etude de la Matière Condensée (GEMaC), CNRS UMR 8635, Université Paris-Saclay, 78035 Versailles, France*
[3]*Helmholtz Zentrum Berlin für Materialien und Energie GmbH, Albert-Einstein-Strasse 15, 12489 Berlin, Germany*

(Received 8 September 2020; accepted 22 January 2021; published 1 February 2021)

Using ultrafast x-ray diffraction, we directly monitor the lattice dynamics induced by femtosecond laser pulses in nanoscale thin films of bismuth iron garnet in external magnetic fields H_{ext}. We control the ultrafast laser-induced lattice strain amplitude by changing the laser pulse helicity. The strength of H_{ext} is used as an external parameter to switch the helicity dependence on and off, respectively. Based on magneto-optical spectroscopic measurements, we explain these phenomena by magnetic circular dichroism. Our findings highlight an important approach for ultrafast manipulation of lattice strain in magnetic materials, in particular insulators, and open exciting perspectives towards ultrafast control of lattice strain and heat-induced magnetization switching and spin waves in bismuth substituted iron garnets using the polarization of light.

DOI: 10.1103/PhysRevB.103.064301

Controlling the properties of matter has always been a major issue in condensed-matter physics. From a fundamental point of view, it requires a deep understanding of the interactions among spins, charge, and lattice degrees of freedom and their response to external stimuli. Traditionally, such control has been realized by changing external conditions such as temperature, pressure, and electric or magnetic fields [1,2]. Recently, intense ultrashort laser pulses have been proven to be an efficient tool for manipulating magnetic [3–5], electric [6,7], optic [8], and crystallographic [9–11] properties of materials on ultrashort time scales. The coupled dynamics is measured in real time with high spatiotemporal resolution using time-resolved pump-probe techniques, which are selective for one of the subsystems [3–11]. This unique opportunity provided by ultrafast laser pulses has led to the discovery of important phenomena for both fundamental science and technological applications, such as laser-induced room temperature superconductivity [12], inverted strain pulses [13,14], control of the ferroelectric [15] and magnetic [3,4,16,17] order, and triggering coherent spin [4,18–20] and phonon [21,22] dynamics. Some of these phenomena are explained via processes involving the coupling and energy transfer between the degrees of freedom in solids [3–5,12,14,20,23] and others are triggered by nonlinear optical processes like impulsive simulated Raman scattering [4,5,16,18,19,21]. These nonlinear optical processes can offer the advantage of controlling physical properties using the light polarization [4,5,16,18,19]. For linear absorption such control has been reported in very few cases [24–28]. In particular, the effect of magnetic circular dichroism has mainly been discussed in the context of helicity-dependent all-optical switching in metallic magnets [25,28].

In magnetic materials, one of the most important approaches used for ultrafast control of their properties is based on the interaction between the lattice and the magnetization. So far, this approach has attracted attention in two different ways: The first is related to controlling the magnetization dynamics with picosecond strain pulses generated in metallic film by femtosecond laser pulses [29–33]. It was demonstrated that a strain pulse can trigger a coherent magnetization precession in metal [29–31], semiconductor [32], and dielectric [33,34] magnetic films. Because of its long propagation distance of several millimeters combined with low energy losses [35,36], strain pulses offer an important opportunity to excite magnetization precession in magnetic materials deeply embedded in opaque heterostructure devices [32–34]. The second way is related to control the lattice strain by the ultrafast modification of the magnetic order [14,23,37–41]. Most studies in this direction focus on measuring the lattice response upon the ultrafast demagnetization of a metallic magnet with femtosecond laser pulses [14,23,37–41]. The results of these investigations are explained by considering the transfer of angular momentum [37,40] and energy [14,23,38,39] from the spins to the lattice. By now, these efforts have yielded great progress in the fundamental understanding of lattice-spin interactions on ultrashort time scales. However, an important question remains: Is it possible to use the magnetization for ultrafast manipulation of the lattice strain via an external parameter of the laser pulse like the state of its polarization? If yes, what is the fundamental mechanism behind this phenomenon? In addition, what can be the impact of such control on the ultrafast magnetization dynamics, especially in magnetic insulators?

In this paper, we use ultrafast x-ray diffraction (UXRD) to directly monitor the lattice dynamics induced by a femtosecond laser excitation in nanoscale thin films of bismuth iron garnet under external magnetic fields, H_{ext}, applied

*Corresponding author: madeb@uni-potsdam.de

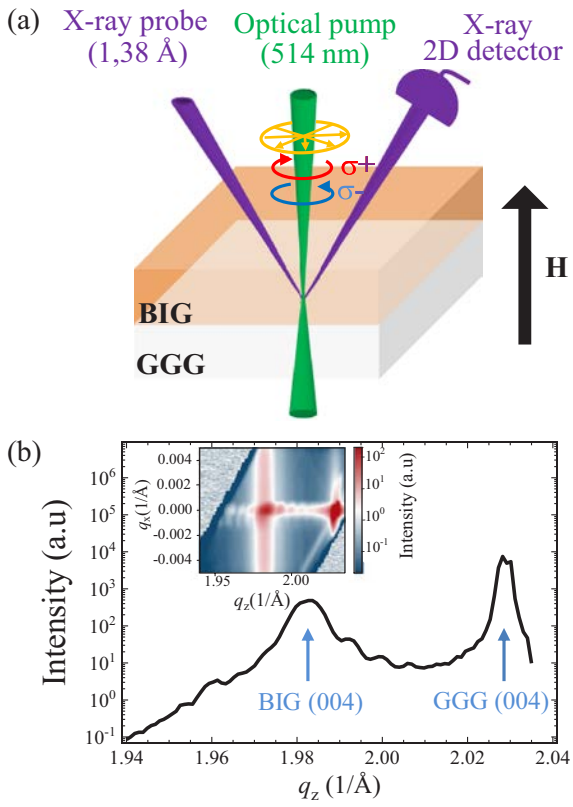

FIG. 1. Experimental configuration and static x-ray diffraction results. (a) Sketch of the UXRD configuration with pump pulses and external magnetic field perpendicular to the film. (b) X-ray diffraction line profile recorded along the q_z direction around the 004 Bragg reflections of the BIG layer and the GGG substrate. The arrows indicate the 004 Bragg reflection related to BIG and the GGG. The inset shows the reciprocal space map around the 004 Bragg reflections of BIG layer and GGG substrate.

perpendicular to the film plane [see Fig. 1(a)]. By changing the helicity of the laser pulse, we demonstrate ultrafast manipulation of the lattice strain: A huge 20% difference of the strain amplitude is controlled by the light helicities when the magnetization is saturated perpendicular to the film plane. In addition, we find that the lattice strain can be controlled by varying the strength of H_{ext}. Both effects rely on ultrafast but long lived stress and the concomitant strain dynamics are only limited by the sound velocity. Based on magneto-optical spectroscopic measurements, we demonstrate that these phenomena can be explained considering the circular magnetic dichroism.

Our study is based on a 90-nm thick bismuth iron garnet ($Bi_3Fe_5O_{12}$, BIG) film grown by pulsed laser disposition onto a (100) gadolinium gallium garnet ($Gd_3Ga_5O_{12}$, GGG) substrate. A detailed description of the growth conditions can be found in Ref. [42]. The BIG material is a ferrimagnetic insulator with a high Curie temperature ($T_C \sim 680$ K) [43], large optical band gap ($E_g \sim 2.4$ eV) [44,45] and giant magneto-optical Faraday rotation ($\sim$37 deg/μm at 2.3 eV) [46,47]. These combined properties make this material a promising candidate for nonreciprocal magneto-optical devices [48,49]. The UXRD measurements are performed at the XPP-KMC3 experimental station of the synchrotron radiation source BESSY II, Helmholtz-Zentrum Berlin (HZB), during the standard multibunch operation mode. In this operation mode, the bending magnet emits hard x-ray pulses with a duration of $\sim$100 ps. The sample is excited at normal incidence with a pump beam at the central wavelength of 514 nm, obtained by frequency doubling the output of a Yb:KGW laser system operating at 104 kHz repetition rate and with 600-fs pulse duration. At this pump wavelength, the BIG film absorbs about 38% of the incident energy. The pump pulse is focused onto the sample in a circular spot with a diameter of 560 μm, while the x-ray probe has a rectangular shape with dimensions of $460 \times 150\,\mu\text{m}^2$. The x-ray photon energy 9 keV ($\lambda = 1.38$ Å) was selected by a Si double crystal monochromator. The polarization of the pump beam is controlled using a quarter-wave plate (QWP). The external magnetic field H_{ext} is applied perpendicular to the plane of the film. All measurements are performed at room temperature.

Before the UXRD measurements, we investigated the static crystalline properties of the BIG/GGG sample using the same x-ray setup. Figure 1(b) shows the x-ray diffraction line profile recorded along the q_z direction under symmetric Bragg diffraction at $q_x = 0$, where q_z and q_x represent the scattering wave vector components along the out-of-plane and the in-plane directions of the sample. The corresponding reciprocal space map of diffracted intensity as a function of q_z and q_x is shown in the inset of Fig. 1(b). We observe two well-separated diffraction peaks at $q_z = 1.92$ Å^{-1} and $q_z = 2.03$ Å^{-1}, corresponding to the 004 Bragg diffraction of BIG and GGG, respectively. The absence of any other diffraction peaks indicates the single-crystalline and single-phase nature the BIG film. This is in agreement with transmission electron microscopy measurements in BIG samples obtained in identical growth conditions [50]. The width of the BIG Bragg reflection $\Delta q_z = 0.007$ Å^{-1} and the Laue oscillations indicate that the coherence length coincides with the film thickness. In the UXRD experiments, we measured the shift of this peak induced by laser excitation and we extracted via Bragg's law the corresponding lattice strain $\eta(t)$ as a function of the time delay t between the pump and the probe pulses.

Figure 2 shows the lattice strain induced by right (σ^+) and left (σ^-) circularly polarized laser pulses with a fluence of $F_{\text{pump}} = 3.5\,\text{mJ cm}^{-2}$ at an external magnetic field of $H_{\text{ext}} = 450$ mT. At this pump fluence, the static optical heating of the sample is about 50 K. This increases the global static temperature of the sample to 350 K, which is very small compared to T_C(BIG) $\sim$ 680 K. The lattice dynamics are governed by two distinct time scales. Within the first 150 ps an ultrafast lattice expansion by 0.02% is observed. The signal is limited by the x-ray pulse duration. The time of maximum expansion is given by $T = d/v = 17$ ps, where d is the thickness of the film and v is the sound velocity of BIG [51]. The long-lived expanded state exhibits very slow relaxation dynamics. In the measured time window of 5 ns, the strain amplitude decays only a little by heat transport to the substrate. The central observation depicted in Fig. 2 is the change of $\sim$20% in the

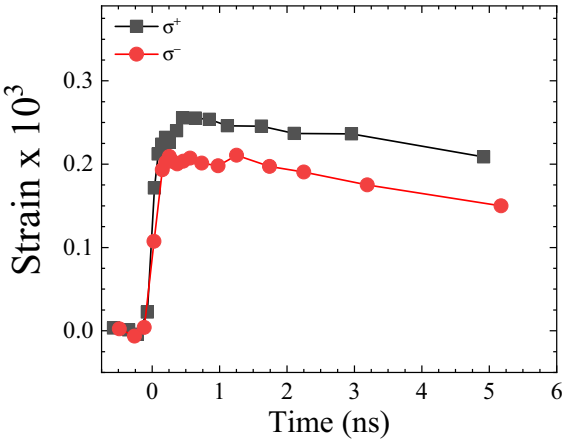

FIG. 2. Time-resolved lattice dynamics induced by right (σ^+, squares) and left (σ^-, solid circles) circular polarization pump beam with a pump fluence $F_{\text{pump}} = 3.5\,\text{mJ cm}^{-2}$ for $H_{\text{ext}} = 450\,\text{mT}$.

generated strain amplitude by reversing the helicity of the pump beam.

In order to study this phenomenon in more detail, we have measured the relative strain amplitude at different time delays of $t = 500\,\text{ps}$, $t = 1000\,\text{ps}$, and $t = 2000\,\text{ps}$ as a function of the angle θ between the fast axis of the QWP and the p-polarized beam [see Figs. 3(a), 3(b), and 3(c)]. For all time delays, the strain amplitude follows a clear sinusoidal form with a periodicity of 180°. The minimum strain is observed for the left circular polarization $\sigma^+(\theta = +45)$, while its minimum is observed for the right circular polarization $\sigma^-(\theta = -45)$. The p- or s- polarized pump beam π ($\theta = 0$ and ± 90) generate the same strain amplitude that is approximately the average of those induced by σ^+ and σ^- polarizations, i.e., $\eta(\pi) = (\eta(\sigma^+) + \eta(\sigma^-))/2$. In Fig. 3(d) we cross check this finding by comparing the helicity dependence of the photoinduced strain amplitude in BIG to the helicity dependence observed under the very same excitation conditions in a $SrRuO_3$ thin film that is nonmagnetic at room temperature and is used as a standard reference sample for finding the zero time delay in pump-probe experiments at the XPP-KMC3 beamline [52,53]. Clearly, the strain amplitude for the nonmagnetic reference sample [black in Fig. 3(d)] is independent of the pump polarization at 450 mT, where the strain in BIG shows a strong modulation. More importantly, we find that the helicity-dependent strain modulation generated in BIG can be nearly switched off by setting $H_{\text{ext}} = 0$. The black symbols in Fig. 3(e) show nearly the same strain for any rotation angle of the QWP.

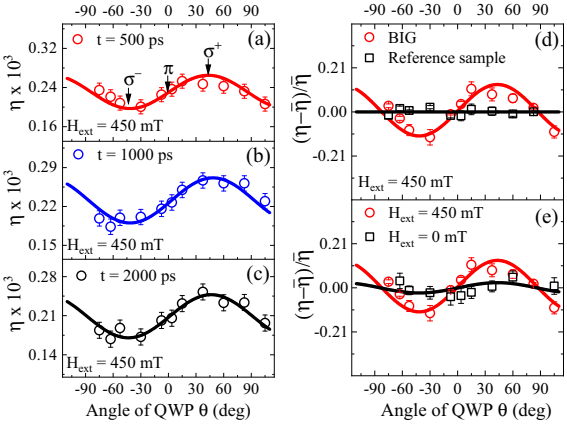

FIG. 3. Strain amplitude η measured as a function of orientation angle θ of the quarter wave plate for $F_{\text{pump}} = 3.5\,\text{mJ cm}^{-2}$. The absolute strain $\eta(\theta)$ obtained for BIG at three different time delays of (a) $t = 500\,\text{ps}$, (b) $t = 1000\,\text{ps}$, and (c) $t = 2000\,\text{ps}$ for $H_{\text{ext}} = 450\,\text{mT}$. (d) The relative strain $(\eta(\theta) - \bar{\eta})/\bar{\eta}$ obtained for BIG and the nonmagnetic reference sample at $t = 500\,\text{ps}$ for $H_{\text{ext}} = 450\,\text{mT}$. (e) The relative strain for BIG at $t = 500\,\text{ps}$ for $H_{\text{ext}} = 450\,\text{mT}$ and $H_{\text{ext}} = 0\,\text{mT}$. The arrows in (a) highlight the QWP angles corresponding to circular right ($\sigma+$), linear (π), and circular left ($\sigma+$) polarizations of the pump beam. The solid lines are guides to the eye. The error bars indicate the standard deviation of the time resolved data.

To give a comprehensive understanding of these phenomena, it is important to clarify first the mechanism of strain generation in BIG thin films by near-band-gap laser excitation. Qualitatively, such processes can be described in the following way. The light energy is absorbed in the BIG layer by electronic transitions related to the Fe^{3+} ions [46,54,55]. These electronic states are very short lived [51] and rapidly transfer the entire energy to vibrations of the lattice via electron-phonon coupling. This lattice temperature rise associated with this heat energy induces a lattice expansion, which is directly quantified by UXRD measurements. We note that the demagnetization dynamics in iron garnets is a very slow process that occurs on the nanosecond time scale [56]. Therefore, the magnetostrictive strain should have a very small or no contribution to the lattice dynamics measured in the first 50 ps, where the coherent and incoherent phonons are already generated. The heat in the BIG layer is mainly transported to the GGG substrate via phonon heat conduction. This process is characterized by an extremely long time scale (see Fig. 2), which is in good agreement with the low thermal conductivity in iron garnets [51,57].

From the above-described processes that lead to the lattice strain observed in Figs. 2 and 3, we can conclude that the origin of the polarization-dependent lattice dynamics should satisfy the following three fundamental criteria: (i) the absorption of light depends on the state of its polarization, (ii) occurs only in magnetic materials, and (iii) depends on the strength of H_{ext}, i.e., the amplitude of the magnetization. These criteria are fulfilled by the magnetic circular dichroism (MCD), which is manifested for a given direction of the magnetization by a variation in the light absorption when going over from right to left circular polarization [58].

In order to confirm the physical origin behind the helicity-dependent lattice strain dynamics, we investigated the wavelength- and magnetic-field dependence of the MCD, which corresponds to the difference in absorption between the right and left circular polarization [45,59]. The measurements are carried out using a magneto-optical spectrometer based on 90° polarization-modulation technique. A detailed description

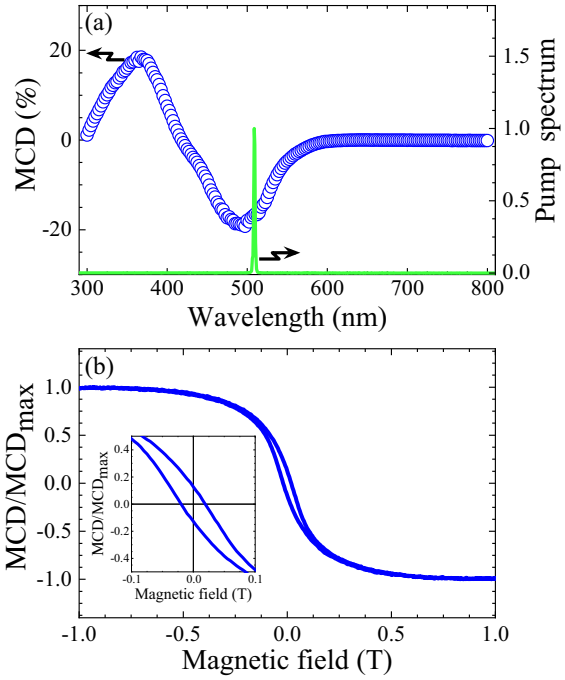

FIG. 4. Static magneto-optical and magnetic properties of the BIG film measured in polar configuration. (a) Magnetic circular dichroism spectrum of the BIG film, including the spectrum of the pump beam used in the UXRD measurements (green line). (b) Magnetic circular dichroism hysteresis loop. The inset shows a magnified view of the region round 0 T.

of the experimental setup has been given in Ref. [60]. Briefly, the white light emitted by a 150-W Xe arc lamp is polarized by a Rochon polarizer and modulated at a high frequency of 50 kHz by a photoelectric modulator (PEM). The modulated light is focused onto the sample at normal incidence. The transmitted light is collimated and analyzed with a Rochon analyzer, and focused into a spectrometer. The MCD is deduced from the signal measured by a photomultiplier detector signal that is analyzed by a lock-in amplifier referenced to the first harmonic of the PEM. Figure 4 shows the spectral dependence of MCD measured over a wide range of wavelength between 300 and 800 nm with a saturating H_{ext} applied perpendicular to the film plane. The MCD reaches a large value of $\sim -20\%$ at $\lambda = 514$ nm, which is the wavelength of the pump pulses used in UXRD experiments [see Fig. 4(a)]. This large difference of $\sim 20\%$ in the absorption between the opposite light helicities confirms the proposed origin behind the polarization dependent lattice strain. It also reveals that the one photon absorption process is the dominant mechanism at 514 nm, which is the expected result with a near-band-gap laser excitation. We note that the measured MCD is about 13 times higher than the one in GdFeCo [25], which is expected to be at the origin of the helicity-dependent all-optical switching in metallic magnets [25,28]. From a fundamental point of view, the large values of MCD in BIG can be explained by the large spin-orbit induced in Fe-3*d* orbitals due to their hybridization with the Bi-3*p* ones, which are characterized by a huge spin-orbit coupling [54,61]. This mechanism is supported by cluster molecular-orbital theory [62,63] and band-structure calculations [64]. On the other hand, to reveal the origin of the small signal modulation observed at zero external magnetic field [Fig. 3(e)], we measured the polar MCD hysteresis loop [see Fig. 4(b)]. It shows a clear remanent magnetization $M_r \sim 0.13\, M_s$ that is about 20% of the MCD signal for $H_{ext} = 450$ mT. This is in good agreement with the remaining strain modulation at $H_{ext} = 0$ mT reported in Fig. 3(e) compared to the modulation of the strain amplitude at $H_{ext} = 450$ mT. We note that this remnant magnetization corresponds to the average projection of the magnetic domains on the direction perpendicular to the film plane. These domains have a very small size ($\sim 0.2\, \mu m^2$) [42,65], which guarantees that hundreds of thousands of them are located within the x-ray probe. On the other hand, for $H_{ext} = 450$ mT, the magnetization of BIG is almost saturated perpendicular to the film plane and the difference in strain amplitude generated by the opposite helicity of light reaches a large value of $\sim 20\%$.

These findings should not be restricted to BIG, but occur in all magnetic materials with good magneto-optical properties. From a practical point of view, light polarization (helicity) can thus be used to control any ultrafast phenomena that are influenced by the lattice strain (or lattice heating). For example, in Bi-substituted iron garnets, it was recently demonstrated that an ultrafast heating of lattice can excite high frequency spin waves [20,66,67] and induce a full magnetization switching [68]. By choosing the appropriate pump wavelength to maximize the effect of MCD on lattice heating, it will be therefore possible to use the polarization of light in order to: (i) control the amplitude of the spin waves and (ii) obtain a helicity-dependent optical magnetization switching in magnetic insulators. Due to the low damping [49,69], large magneto-optical effect [46,47,49,70,71], and good transparency in the visible and infrared region [49,70,71] of bismuth substituted iron garnets, these phenomena are important for future data storage and processing technologies.

In summary, we demonstrated that femtosecond laser pulses can induce helicity-dependent ultrafast lattice dynamics in nanoscale thin films of BIG. We demonstrated a huge long-lived 20% difference in the lattice strain generated by the opposite light helicities when the magnetization is saturated perpendicular to the film plane. For both right and left circularly polarized light excitation, a variation of the external magnetic field strength can control the lattice strain amplitude. Based on magneto-optical spectroscopic measurements, we demonstrate that these phenomena can be explained by considering the MCD. Our findings open different perspectives on ultrafast manipulation of lattice strain and heat in magnetic materials, which allows for controlling magnetization switching and spin wave excitations in bismuth substituted iron garnets via the polarization of the laser pulse.

We acknowledge funding by the BMBF Project Grant No. 05K16IPA and M.D. acknowledges the Alexander von Humboldt Foundation for financial support.

[1] C. Kittel, *Introduction to Solid State Physics* (Wiley, New York, 1986).

[2] W. Martienssen and H. Warlimont, *Springer Handbook of Condensed Matter and Materials Data* (Springer Science & Business Media, Berlin,2006).

[3] E. Beaurepaire, J. C. Merle, A. Daunois, and J. Y. Bigot, Ultrafast Spin Dynamics in Ferromagnetic Nickel, Phys. Rev. Lett. **76**, 4250 (1996).

[4] J.-Y. Bigot, W. Hübner, T. Rasing, and R. Chantrell, *Ultrafast Magnetism I* (Springer, Berlin, 2016).

[5] A. Kirilyuk, A. V. Kimel, and T. Rasing, Ultrafast optical manipulation of magnetic order, Rev. Mod. Phys. **82**, 2731 (2010).

[6] R. Atanasov, A. Haché, J. L. P. Hughes, H. M. van Driel, and J. E. Sipe, Coherent Control of Photocurrent Generation in Bulk Semiconductors, Phys. Rev. Lett. **76**, 1703 (1996).

[7] A. Schiffrin, T. Paasch-Colberg, N. Karpowicz, V. Apalkov, D. Gerster, S. Mühlbrandt, M. Korbman, J. Reichert, M. Schultze, S. Holzner *et al.* Optical-field-induced current in dielectrics, Nature (London) **493**, 70 (2013).

[8] L. Le Guyader, A. Kirilyuk, T. Rasing, G. A. Wurtz, A. V. Zayats, P. F. A. Alkemade, and I. I. Smolyaninov, Coherent control of surface plasmon polariton mediated optical transmission, J. Phys. D **41**, 195102 (2008).

[9] M. Bargheer, N. Zhavoronkov, Y. Gritsai, J. C. Woo, D. S. Kim, M. Woerner, and T. Elsaesser, Coherent atomic motions in a nanostructure studied by femtosecond x-ray diffraction, Science **306**, 1771 (2004).

[10] C. V. Korff Schmising, M. Bargheer, M. Kiel, N. Zhavoronkov, M. Woerner, T. Elsaesser, I. Vrejoiu, D. Hesse, and M. Alexe, Coupled Ultrafast Lattice and Polarization Dynamics in Ferroelectric Nanolayers, Phys. Rev. Lett. **98**, 257601 (2007).

[11] M. Bargheer, N. Zhavoronkov, M. Woerner, and T. Elsaesser, Recent progress in ultrafast X-ray diffraction, Chem. Phys. Chem. **7**, 783 (2006).

[12] D. Fausti, R. I. Tobey, N. Dean, S. Kaiser, A. Dienst, M. C. Hoffmann, S. Pyon, T. Takayama, H. Takagi, and A. Cavalleri, Light-induced superconductivity in a stripe-ordered cuprate, Science **331**, 189 (2011).

[13] J. Pudell, A. von Reppert, D. Schick, F. Zamponi, M. Rössle, M. Herzog, H. Zabel, and M. Bargheer, Ultrafast negative thermal expansion driven by spin disorder, Phys. Rev. B **99**, 094304 (2019).

[14] A. V. Reppert, M. Mattern, J.-E. Pudell, S. P. Zeuschner, K. Dumesnil, and M. Bargheer, Unconventional picosecond strain pulses resulting from the saturation of magnetic stress within a photoexcited rare earth layer, Struct. Dyn. **7**, 024303 (2020).

[15] R. Mankowsky, A. von Hoegen, M. Först, and A. Cavalleri, Ultrafast Reversal of the Ferroelectric Polarization, Phys. Rev. Lett. **118**, 197601 (2017).

[16] C. D. Stanciu, F. Hansteen, A. V. Kimel, A. Kirilyuk, A. Tsukamoto, A. Itoh, and T. Rasing, All-Optical Magnetic Recording with Circularly Polarized Light, Phys. Rev. Lett. **99**, 047601 (2007).

[17] C.-H. Lambert, S. Mangin, B. S. D. C. S. Varaprasad, Y. K. Takahashi, M. Hehn, M. Cinchetti, G. Malinowski, K. Hono, Y. Fainman, M. Aeschlimann *et al.* All-optical control of ferromagnetic thin films and nanostructures, Science **345**, 1337 (2014).

[18] F. Hansteen, A. Kimel, A. Kirilyuk, and T. Rasing, Femtosecond Photomagnetic Switching of Spins in Ferrimagnetic Garnet Films, Phys. Rev. Lett. **95**, 047402 (2005).

[19] A. V. Kimel, A. Kirilyuk, P. A. Usachev, R. V. Pisarev, A. M. Balbashov, and T. Rasing, Ultrafast nonthermal control of magnetization by instantaneous photomagnetic pulses, Nature (London) **435**, 655 (2005).

[20] M. Deb, E. Popova, M. Hehn, N. Keller, S. Petit-Watelot, M. Bargheer, S. Mangin, and G. Malinowski, Femtosecond Laser-Excitation-Driven High Frequency Standing Spin Waves in Nanoscale Dielectric Thin Films of Iron Garnets, Phys. Rev. Lett. **123**, 027202 (2019).

[21] H. Katsuki, J. C. Delagnes, K. Hosaka, K. Ishioka, H. Chiba, E. S. Zijlstra, M. E. Garcia, H. Takahashi, K. Watanabe, M. Kitajima *et al.* All-optical control and visualization of ultrafast two-dimensional atomic motions in a single crystal of bismuth, Nat Commun. **4**, 2801 (2013).

[22] M. Lejman, G. Vaudel, I. C. Infante, P. Gemeiner, V. E. Gusev, B. Dkhil, and P. Ruello, Giant ultrafast photo-induced shear strain in ferroelectric BiFeO3, Nat. Commun. **5**, 4301 (2014).

[23] A. v. Reppert, J. Pudell, A. Koc, M. Reinhardt, W. Leitenberger, K. Dumesnil, F. Zamponi, and M. Bargheer, Persistent nonequilibrium dynamics of the thermal energies in the spin and phonon systems of an antiferromagnet, Struct. Dyn. **3**, 054302 (2016).

[24] F. Hansteen, A. Kimel, A. Kirilyuk, and T. Rasing, Nonthermal ultrafast optical control of the magnetization in garnet films, Phys. Rev. B **73**, 014421 (2006).

[25] A. R. Khorsand, M. Savoini, A. Kirilyuk, A. V. Kimel, A. Tsukamoto, A. Itoh, and T. Rasing, Role of Magnetic Circular Dichroism in All-Optical Magnetic Recording, Phys. Rev. Lett. **108**, 127205 (2012).

[26] A. Stupakiewicz, K. Szerenos, D. Afanasiev, A. Kirilyuk, and A. V. Kimel, Ultrafast nonthermal photomagnetic recording in a transparent medium, Nature (London) **542**, 71 (2017).

[27] A. Stupakiewicz, K. Szerenos, M. D. Davydova, K. A. Zvezdin, A. K. Zvezdin, A. Kirilyuk, and A. V. Kimel, Selection rules for all-optical magnetic recording in iron garnet, Nat. Commun. **10**, 612 (2019).

[28] Y. Quessab, M. Deb, J. Gorchon, M. Hehn, G. Malinowski, and S. Mangin, Resolving the role of magnetic circular dichroism in multishot helicity-dependent all-optical switching, Phys. Rev. B **100**, 024425 (2019).

[29] J.-W. Kim, M. Vomir, and J.-Y. Bigot, Ultrafast Magnetoacoustics in Nickel Films, Phys. Rev. Lett. **109**, 166601 (2012).

[30] J.-W. Kim, M. Vomir, and J.-Y. Bigot, Controlling the spins angular momentum in ferromagnets with sequences of picosecond acoustic pulses, Sci. Rep. **5**, 8511 (2015).

[31] T. L. Linnik, V. N. Kats, J. Jäger, A. S. Salasyuk, D. R. Yakovlev, A. W. Rushforth, A. V. Akimov, A. M. Kalashnikova, M. Bayer, and A. V. Scherbakov, The effect of dynamical compressive and shear strain on magnetic anisotropy in a low symmetry ferromagnetic film, Phys. Scripta **92**, 054006 (2017).

[32] A. V. Scherbakov, A. S. Salasyuk, A. V. Akimov, X. Liu, M. Bombeck, C. Brüggemann, D. R. Yakovlev, V. F. Sapega, J. K. Furdyna, and M. Bayer, Coherent Magnetization Precession in Ferromagnetic (Ga,Mn)As Induced by Picosecond Acoustic Pulses, Phys. Rev. Lett. **105**, 117204 (2010).

[33] M. Deb, E. Popova, M. Hehn, N. Keller, S. Mangin, and G. Malinowski, Picosecond acoustic-excitation-driven ultrafast

magnetization dynamics in dielectric Bi-substituted yttrium iron garnet, Phys. Rev. B **98**, 174407 (2018).

[34] M. Deb, E. Popova, S. P. Zeuschner, M. Hehn, N. Keller, S. Mangin, G. Malinowski, and M. Bargheer, Generation of spin waves via spin-phonon interaction in a buried dielectric thin film, Phys. Rev. B **103**, 024411 (2021).

[35] H. Y. Hao and H. J. Maris, Study of Phonon Dispersion in Silicon and Germanium at Long Wavelengths Using Picosecond Ultrasonics, Phys. Rev. Lett. **84**, 5556 (2000).

[36] O. L. Muskens and J. I. Dijkhuis, High Amplitude, Ultrashort, Longitudinal Strain Solitons in Sapphire, Phys. Rev. Lett. **89**, 285504 (2002).

[37] E. Jal, V. López-Flores, N. Pontius, T. Ferté, N. Bergeard, C. Boeglin, B. Vodungbo, J. Lüning, and N. Jaouen, Structural dynamics during laser-induced ultrafast demagnetization, Phys. Rev. B **95**, 184422 (2017).

[38] A. Koc, M. Reinhardt, A. von Reppert, M. Rössle, W. Leitenberger, M. Gleich, M. Weinelt, F. Zamponi, and M. Bargheer, Grueneisen-approach for the experimental determination of transient spin and phonon energies from ultrafast x-ray diffraction data: Gadolinium, J. Phys.: Condens. Matter **29**, 264001 (2017).

[39] A. H. Reid, X. Shen, P. Maldonado, T. Chase, E. Jal, P. W. Granitzka, K. Carva, R. K. Li, J. Li, L. Wu *et al.* Beyond a phenomenological description of magnetostriction, Nat. Commun. **9**, 388 (2018).

[40] C. Dornes, Y. Acremann, M. Savoini, M. Kubli, M. J. Neugebauer, E. Abreu, L. Huber, G. Lantz, C. A. F. Vaz, H. Lemke *et al.* The ultrafast Einstein–de Haas effect, Nature (London) **565**, 209 (2019).

[41] A. von Reppert, L. Willig, J.-E. Pudell, S. P. Zeuschner, G. Sellge, F. Ganss, O. Hellwig, J. A. Arregi, V. Uhlíř, A. Crut *et al.* Spin stress contribution to the lattice dynamics of FePt, Sci. Adv. **6**, eaba1142 (2020).

[42] E. Popova, L. Magdenko, H. Niedoba, M. Deb, B. Dagens, B. Berini, M. Vanwolleghem, C. Vilar, F. Gendron, A. Fouchet *et al.* Magnetic properties of the magnetophotonic crystal based on bismuth iron garnet, J. Appl. Phys. **112**, 093910 (2012).

[43] B. Vertruyen, R. Cloots, J. S. Abell, T. J. Jackson, R. C. da Silva, E. Popova, and N. Keller, Curie temperature, exchange integrals, and magneto-optical properties in off-stoichiometric bismuth iron garnet epitaxial films, Phys. Rev. B **78**, 094429 (2008).

[44] S. Kahl, V. Popov, and A. M. Grishin, Optical transmission and faraday rotation spectra of a bismuth iron garnet film, J. Appl. Phys. **94**, 5688 (2003).

[45] M. Deb, E. Popova, A. Fouchet, and N. Keller, Full spin polarization of complex ferrimagnetic bismuth iron garnet probed by magneto-optical Faraday spectroscopy, Phys. Rev. B **87**, 224408 (2013).

[46] M. Deb, E. Popova, A. Fouchet, and N. Keller, Magneto-optical faraday spectroscopy of completely bismuth-substituted $Bi_3Fe_5O_{12}$ garnet thin films, J. Phys. D **45**, 455001 (2012).

[47] M. Deb, E. Popova, and N. Keller, Different magneto-optical response of magnetic sublattices as a function of temperature in ferrimagnetic bismuth iron garnet films, Phys. Rev. B **100**, 224410 (2019).

[48] E. Popova, A. F. F. Galeano, M. Deb, B. Warot-Fonrose, H. Kachkachi, F. Gendron, F. Ott, B. Berini, and N. Keller, Magnetic anisotropies in ultrathin bismuth iron garnet films, J. Magn. Magn. Mater. **335**, 139 (2013).

[49] G. D. Winkler, *Magnetic Garnets* (Vieweg, Braunschweig, Germany, 1981).

[50] E. Popova, M. Deb, L. Bocher, A. Gloter, O. Stéphan, B. Warot-Fonrose, B. Berini, Y. Dumont, and N. Keller, Interplay between epitaxial strain and low dimensionality effects in a ferrimagnetic oxide, J. Appl. Phys. **121**, 115304 (2017).

[51] S. P. Zeuschner, J. E. Pudell, A. von Reppert, M. Deb, E. Popova, N. Keller, M. Rössle, M. Herzog, and M. Bargheer, Measurement of transient strain induced by two-photon excitation, Phys. Rev. Res. **2**, 022013(R) (2020).

[52] H. A. Navirian, D. Schick, P. Gaal, W. Leitenberger, R. Shayduk, and M. Bargheer, Thermoelastic study of nanolayered structures using time-resolved x-ray diffraction at high repetition rate, Appl. Phys. Lett. **104**, 021906 (2014).

[53] M. Reinhardt, A. Koc, W. Leitenberger, P. Gaal, and M. Bargheer, Optimized spatial overlap in optical pump-X-ray probe experiments with high repetition rate using laser-induced surface distortions, J. Synchrotron Radiat. **23**, 474 (2016).

[54] G. F. Dionne and G. A. Allen, Molecular-orbital analysis of magneto-optical Bi-O-Fe hybrid excited states, J. Appl. Phys. **75**, 6372 (1994).

[55] F. Iori, A. Teurtrie, L. Bocher, E. Popova, N. Keller, O. Stéphan, and A. Gloter, Bismuth iron garnet: Ab initio study of electronic properties, Phys. Rev. B **100**, 245150 (2019).

[56] L. A. Shelukhin, V. V. Pavlov, P. A. Usachev, P. Y. Shamray, R. V. Pisarev, and A. M. Kalashnikova, Ultrafast laser-induced changes of the magnetic anisotropy in a low-symmetry iron garnet film, Phys. Rev. B **97**, 014422 (2018).

[57] N. P. Padture and P. G. Klemens, Low thermal conductivity in garnets, J. Am. Ceram. Soc. **80**, 1018 (1997).

[58] D. Gignoux, M. Schlenker, and É. D. T. de Lacheisserie, *Magnetism: Fundamentals* (Springer, New York, 2005).

[59] M. Kucera, J. Bok, and K. Nitsch, Faraday rotation and MCD in Ce doped YIG, Solid State Commun. **69**, 1117 (1989).

[60] M. Deb, M. Vomir, J.-L. Rehspringer, and J.-Y. Bigot, Ultrafast optical control of magnetization dynamics in polycrystalline bismuth doped iron garnet thin films, Appl. Phys. Lett. **107**, 252404 (2015).

[61] S. Wittekoek and D. E. Lacklison, Investigation of the Origin of the Anomalous Faraday Rotation of $Bi_xCa_{3-x}Fe_{3.5+0.5x}V_{1.5-0.5x}O_{12}$ by Means of the Magneto-optical Kerr Effect, Phys. Rev. Lett. **28**, 740 (1972).

[62] A. V. Zenkov and A. S. Moskvin, Bismuth-induced increase of the magneto-optical effects in iron garnets: A theoretical analysis, J. Phys.: Condens. Matter **14**, 6957 (2002).

[63] S. Sugano and N. Kojima, *Magneto-optics* (Springer Science & Business Media, Berlin, 2013), Vol. 128.

[64] T. Oikawa, S. Suzuki, and K. Nakao, First-principles study of spin-orbit interactions in bismuth iron garnet, J. Phys. Soc. Jpn. **74**, 401 (2005).

[65] E. Popova, A. Shengelaya, D. Daraselia, D. Japaridze, S. Cherifi-Hertel, L. Bocher, A. Gloter, O. Stéphan, Y. Dumont, and N. Keller, Bismuth iron garnet Bi3Fe5O12: A room temperature magnetoelectric material, Appl. Phys. Lett. **110**, 142404 (2017).

[66] M. Deb, E. Popova, M. Hehn, N. Keller, S. Petit-Watelot, M. Bargheer, S. Mangin, and G. Malinowski, Damping of Standing Spin Waves in Bismuth-Substituted Yttrium Iron Garnet

as Seen via the Time-Resolved Magneto-Optical Kerr Effect, Phys. Rev. Appl. **12**, 044006 (2019).

[67] Y. Hashimoto, D. Bossini, T. H. Johansen, E. Saitoh, A. Kirilyuk, and T. Rasing, Frequency and wavenumber selective excitation of spin waves through coherent energy transfer from elastic waves, Phys. Rev. B **97**, 140404(R) (2018).

[68] C. S. Davies, K. H. Prabhakara, M. D. Davydova, K. A. Zvezdin, T. B. Shapaeva, S. Wang, A. K. Zvezdin, A. Kirilyuk, T. Rasing, and A. V. Kimel, Anomalously Damped Heat-Assisted Route for Precessional Magnetization Reversal in an Iron Garnet, Phys. Rev. Lett. **122**, 027202 (2019).

[69] L. Soumah, N. Beaulieu, L. Qassym, C. Carrétéro, E. Jacquet, R. Lebourgeois, J. Ben Youssef, P. Bortolotti, V. Cros, and A. Anane, Ultra-low damping insulating magnetic thin films get perpendicular, Nat. Commun. **9**, 3355 (2018).

[70] P. Hansen and J. P. Krumme, Magnetic and magneto-optical properties of garnet films, Thin Solid Films **114**, 69 (1984).

[71] G. F. Dionne, *Magnetic Oxides* (Springer, New York, 2009).

VIII Standing spin wave excitation in Bi:YIG films via temperature induced anisotropy changes and magnetoacoustic coupling

Steffen Peer Zeuschner, Xi-Guang Wang, Marwan Deb, Elena Popova, Michel Hehn, Niels Keller, Jamal Berakdar and Matias Bargheer

arXiv, 2203.07851 (2022)

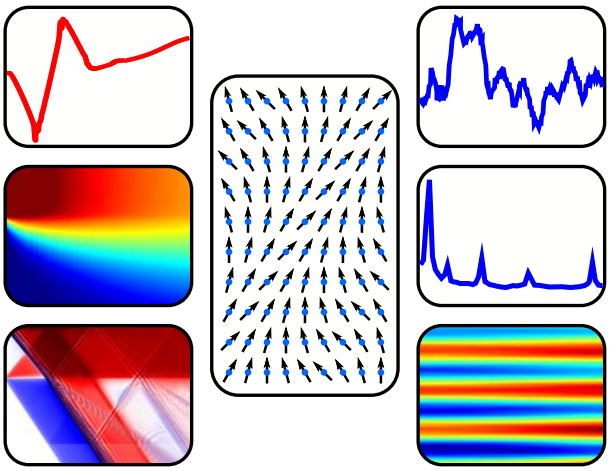

Abstract We connect experimental observations of the magnetization and lattice dynamics via numerical micromagnetic models based on the Landau-Lifshitz-Gilbert (LLG) equation. We compare direct optical excitation of the magnetic insulator Bi:YIG to indirect excitation via an optically opaque Pt/Cu double layer. In both cases the strain and temperature of the lattice are quantified via modeling ultrafast x-ray diffraction data. Measurements of the time-resolved magneto-optical Kerr effect agree well with the magnetization dynamics simulated according to the excitation via two mechanisms: magnetoacoustic coupling to the experimentally verified strain dynamics and ultrafast temperature-induced transient change of the anisotropy constant. The numerical modeling proves that both mechanisms drive the fundamental mode with opposite phase. The relative ratio of standing spin-wave amplitudes of higher order modes indicates that both mechanisms are substantially active.

Contributions to the work

I performed the ultrafast X-ray diffraction experiments together with Alexander von Reppert. I modeled the data numerically to extract the spatio-temporal temperature and strain distributions. Those were used as inputs for the micromagnetic modeling performed by Xi-Guang Wang and compared with the tr-MOKE measurements conducted by Marwan Deb. The samples were provided by Elena Popova, Michel Hehn and Niels Keller. I commented on the manuscript and created the figures.

Comments

This publication finalizes the investigation of the generation process of the standing spin waves observed in Bi:YIG by Marwan Deb [19, 29]. In the previous works, the generation of the high frequency SSWs were attributed to the coherent and incoherent phonons present in the thin films upon femtosecond laser excitation. With the help of our theoretically skilled colleagues, Jamal Berakdar and Xi-Guang Wang, we were able to model the spin dynamics generation process quantitatively [81]. The general idea is to characterize the strain and temperature of the thin film spatially and temporally with UXRD measurements, which probe the lattice dynamics. This information was used as an input for a spatio-temporal micromagnetic numerical modeling in which the strain acts via inverse magnetostriction and the temperature via thermal anisotropy change on the magnetization state. With this, it was possible to fit the frequency and the external field dependence as well as the relative amplitudes of the spin modes, observed in the tr-MOKE experiments, quantitatively. Our investigations show, that inhomogeneous anisotropy change and inverse magnetostriction alike generate SSWs but the phase of the ferromagnetic resonance mode is

inverted. Only a combination of both processes thus explains the large realtive amplitude of the higher order modes obeserved in the tr-MOKE experiments.

A comprehensive summary of this publication is given in Sec. 2.2.3 substantiated by the previous sections and the publications III, V and VII. In conclusion, this is an intriguing example to justify the combination of UXRD and tr-MOKE in the future, since this collaboration revealed the true nature of the excitation process of the higher order SSWs which was initially unclear, or at least not verified experimentally.

Standing spin wave excitation in Bi:YIG films via temperature induced anisotropy changes and magnetoacoustic coupling

Steffen Peer Zeuschner[1,2], Xi-Guang Wang[3,4], Marwan Deb[1], Elena Popova[5], Gregory Malinowski[6], Michel Hehn[6], Niels Keller[5], Jamal Berakdar[4] and Matias Bargheer[1,2,*]

[1]Institut für Physik und Astronomie, Universität Potsdam, Karl-Liebknecht-Str. 24-25, 14476 Potsdam, Germany

[2]Helmholtz Zentrum Berlin für Materialien und Energie GmbH, Albert-Einstein-Str. 15, 12489 Berlin, Germany

[3]School of Physics and Electronics, Central South University, Changsha 410083, China

[4]Institut für Physik, Martin-Luther Universität, Halle-Wittenberg, Halle/Saale D-06120, Germany

[5]Institut de Physique de Rennes (IPR), CNRS UMR6251 Univ Rennes, 35000 Rennes, France

[6]Institut Jean Lamour (IJL), CNRS UMR 7198, Université de Lorraine, 54506 Vandœuvre-lès-Nancy, France

*e-mail : bargheer@uni-potsdam.de

Based on micromagnetic simulations and experimental observations of the magnetization and lattice dynamics following the direct optical excitation of the magnetic insulator Bi:YIG or indirect excitation via an optically opaque Pt/Cu double layer, we disentangle the dynamical effects of magnetic anisotropy and magnetoelastic coupling. The strain and temperature of the lattice are quantified via modeling ultrafast x-ray diffraction data. Measurements of the time-resolved magneto-optical Kerr effect agree well with the magnetization dynamics simulated according to the excitation via two mechanisms: The magneto-acoustic coupling to the experimentally verified strain dynamics and the ultrafast temperature-induced transient change in the magnetic anisotropy. The numerical modeling proves that for direct excitation both mechanisms drive the fundamental mode with opposite phase. The relative ratio of standing spin-wave amplitudes of higher order modes indicates that both mechanisms are substantially active.

Introduction:

Information processing at GHz and THz frequencies entails a combination of photonic and magnetic channels, and hence the optical manipulation of collective spin excitations at high frequencies.(1, 2) Magnetic insulators are particularly suitable as the optical absorption is much lower than for metals and the damping of spin waves may be engineered to be very low. An example are Yttrium Iron Garnet (YIG) thin films which have become a test bed for the optical control of magnetization dynamics.(3, 4) Bismuth doping (resulting in Bi:YIG) enhances substantially the magneto-optical contrast while affecting only slightly the elastic parameters and the magnetic damping.(4–6) Recent experiments confirmed that the magnetization dynamics, in particular standing spin waves in thin films can be directly excited simultaneously by one- and two photon absorption in Bi:YIG.(7, 8) Under strong excitation conditions, the frequency of the fundamental mode is persistently changed by 20%.(9) Also indirect excitation of Bi:YIG via an adjacent opaque metal heterostructure can trigger standing spin waves.(10) Experimental evidence suggests that coherent or incoherent phonons entering Bi:YIG (propagating strain waves or diffusive phonon heat) are responsible for triggering the spin wave motion. Ultrafast x-ray diffraction experiments have been used to quantify the spatio-temporal profile of strain waves and phonon temperature changes under both excitation conditions.(11) While the two dominant mechanisms for exciting spin waves, namely the magnetoacoustic coupling and the temperature induced anisotropy changes, are surely active under the experimental conditions, it has never been quantitatively tested, how they individually affect the magnetization dynamics and what is their relative importance.

Here we analyze and contrast our experimental and simulation results to unveil quantitatively the relationship between the observed strain waves and/or the heat input and the standing spin waves in nanometric magnetic insulator films, which are directly or indirectly excited via ultrashort laser-pulses. Ultrafast x-ray diffraction (UXRD) data calibrate the spatio-temporal strain and the temperature profile in a Bi:YIG film after i) direct optical excitation of the insulating Bi:YIG, and ii) indirect excitation via an optically opaque Pt/Cu double layer. These experimentally verified spatio-temporal strain and heat profiles are adopted as source terms in the micromagnetic model based on the Landau-Lifshitz-Gilbert

(LLG) equation. The simulation results are compared to time-resolved magneto-optical Kerr effect (tr-MOKE) measurements of the spin-wave excitations in the same thin films. The relative ratio of the two mechanisms can be experimentally verified by the amplitude ratio of the excited higher order modes to the fundamental mode, because this mode is excited with opposite phase by the two mechanisms, which therefore partially cancel out. The strain is composed of propagating strain waves and quasi static thermal strain following the diffusion of heat. It couples to the magnetization via a linear magnetoacoustic coupling. In addition, the temperature induces local changes of the anisotropy constant. Consequently, both strain and temperature modulate the effective magnetic field on ultrafast timescales triggering standing spin waves.

The paper is structured as follows: First we discuss the micromagnetic model and an analytic solution of the LLG equation in section (A). In section (B) we show the experimental tr-MOKE signal for direct and indirect excitation. In section (C) we derive the spatiotemporal strain and temperature maps, $T(z,t)$ and $\eta(z,t)$ from the UXRD data. With these experimentally verified input data, the tr-MOKE signal is modeled numerically in section (D) according to the LLG equation. The model is compared to the experimental tr-MOKE data from section (B) for direct and indirect excitation of the magnetic layer. In both cases we separately model the influence of the two inputs, the spatio-temporal temperature, and the strain.

A) Micromagnetic model and analytical considerations

Before discussing the experimental observations and the results of full numerical modeling, we analyze a linearized analytical solution of the Landau-Lifshitz-Gilbert (LLG) equation(12) without damping and without dynamic dipole-dipole interaction. Here, only transversal spin dynamics that do not change the length of the magnetization vector is of interest. Hence, the magnetization field $\vec{M}$ can be described by a unit field vector $\vec{m}$ with $\vec{M} = M_s\vec{m}$ and M_s is the saturation magnetization. The time evolution of $\vec{m}$ is governed by $\partial_t\vec{m} = -\gamma\,\vec{m}\times\vec{H}_{eff}$, where the effective field $\vec{H}_{eff}$ follows from the functional derivative of the magnetization free-energy density with respect to $\vec{m}$ and is detailed below. For a small amplitude precession $\vec{m} = \vec{m}_0 + \delta\vec{m}_{sw}$ around the equilibrium $\vec{m}_0$ with $|\vec{m}_0| \gg |\delta\vec{m}_{SW}|$ one obtains to a linear order in $|\delta\vec{m}_{SW}|$ an analytical solution of the LLG:(13) In our case, the external field is perpendicular to the film and its field strength H_z can be set by an electromagnet. The effective field $\vec{H}_{eff}$(14) acting on the magnetization vector is a sum of the contributions(15) listed in Table 1. (the spatial and the time dependence of $\vec{m}$ are suppressed for brevity)

$$\vec{H}_{eff}(z,t) = H_z\vec{e}_z + \left[H_d + H_u(z,t) + H_{me}(z,t) + H_c(z,t)\left(m_x^2 + m_y^2\right)\right]m_z\vec{e}_z + H_c(z,t)\left[(m_y^2 + m_z^2)m_x\vec{e}_x + (m_x^2 + m_z^2)m_y\vec{e}_y\right] + D_{ex}\frac{\partial^2\vec{m}}{\partial z^2} \quad . \tag{1}$$

The magnetoelastic coupling $H_{me}(z,t) = -\frac{2b_1\eta_{zz}(z,t)}{\mu_0 M_s}$ depends on time and space via the spatio-temporal strain $\eta_{zz}(z,t)$.(10) The uniaxial and cubic anisotropy constants $K_x(T)$ are temperature dependent, and therefore the anisotropy fields $H_u(z,t) = -\frac{2}{\mu_0 M_s}K_x(T(z,t))$ depend on time and space via the spatiotemporal temperature profile $T(z,t)$.(16) The external field H_z along the $\vec{e}_z$ is partially compensated by the large uniaxial (H_u) anisotropy field and the demagnetization field $H_d = -N_z M_s$, where $N_z = 1$ is the demagnetization factor of the thin film geometry. The compensation is proportional to the z-component of the unit magnetization vector m_z. Since m_z grows with H_z as the magnetization tilts out of plane, the effective field would be zero without the cubic anisotropy as long as $H_z < H_s$ (see Fig. 1(a) for illustration). Thus, the small cubic (H_c) essentially determines the direction of the magnetization at low external fields. When H_z reaches the saturation field (critical field) H_s, above which the magnetization is aligned along $\vec{e}_z$, the effective field grows linearly with the external field (Kittel mode). This field H_s is determined by the minimum of the free energy, including cubic anisotropy.

	constants at RT	Effective field	Effective Field (in mT/μ_0)
Cubic Anisotropy	$K_c = 400$ J/m^3	$H_c = \frac{2K_c(T(z,t))}{\mu_0 M_s}$	$H_c = 5.9$
Uniaxial Anisotropy	$K_u = 5750$ J/m^3	$H_u = -\frac{2K_u(T(z,t))}{\mu_0 M_s}$	$H_u = -85$
Demagnetization field / saturation magnetization	$M_s = 170$ mT	$H_d = -N_z M_s$	$H_d = -170$
Saturation Field		$H_s = -(H_u + H_d)$	$H_s = 260$
Magnetoelastic field(17)	$b_1 = 3.5 \cdot 10^5$ J/m^3	$H_{me} = -\frac{2b_1\eta_{zz}(z,t)}{\mu_0 M_s}$	$H_{me} = 62$ per 1% strain $H_{me} = 8$ per $\Delta T = 100K$
Change of uniaxial anisotropy with T(18)			$\Delta H_u = 31$ per $\Delta T = 100$K
Exchange constant	$A_{ex} = 3.5 \cdot 10^{-12}$ J/m	$D_{ex}k_z^2 = \frac{2A_{ex}}{\mu_0 M_s}k_z^2$	
Gyromagnetic ratio	$\frac{\gamma}{2\pi} =$ 28 GHz/T		

Table1: Magnetic properties of the Bi:YIG film according to the simultaneous fit of the lower branches for the modes n = 0, … 4. The second column collects formulas converting magnetic constants to effective fields which enter the LLG equation. The third column compares the values of the time-dependent effective fields ΔH_u (per strain) and H_{me} (per strain and per ΔT) to the magnitude of the static effective fields. Note that the largest contributions $H_d m_z$ and $H_u m_z$ are canceled by the external filed H_z in the perpendicular geometry chosen here.

Before excitation, i.e., in the stationary state with $\frac{\partial m}{dt} = 0$, the state $\vec{m}_0 = (0,0,1)$ is stable, if $H_z > -H_d - H_u + H_c = H_s$ (upper branch or Kittel mode – see Fig. 1(c). In wavevector space, the exchange term $D_{ex}\frac{\partial^2 \vec{m}}{\partial z^2}$ transforms to $D_{ex}k_z^2$ for a mode with a wavevector k_z. Submitting $\vec{m} = \vec{m}_0 + \delta\vec{m}_{sw}$ into the LLG equation, we obtain to linear order in $|\delta\vec{m}_{sw}|$ the frequency on the external field.

$$\omega_u(H_z) = \gamma(D_{ex}k_z^2 + H_z + H_d + H_u - H_c). \qquad (2)$$

If $H_z < H_s$ (lower branch) the stable magnetization is at an angle θ_M with respect to the surface normal $\vec{m}_0 = (sin\theta_M \cos\varphi_M, sin\theta_M \sin\varphi_M, cos\theta_M)$, and φ_M describes the in-plane rotation of $\vec{m}$. Here, $H_z + \left(H_d + H_u + \frac{H_c}{2}\right)\cos\theta_M - \frac{3H_c}{2}\cos^3\theta_M = 0$ and $\varphi_M = \frac{\pi}{4}$. In this case the frequency is

$$\omega_l(H_z) = \gamma\sqrt{(D_{ex}k_z^2 + H_c sin^2\theta_M)\left(D_{ex}k_z^2 - \left(H_d + H_u - 4H_c\cos^2\theta_M + \frac{1}{2}H_c\sin^2\theta_M\right)\sin^2\theta_M\right)} \qquad (3)$$

For the fundamental mode ($k_z = 0$), the frequency $\omega_l(H_z)$ of the lower branch would be strictly zero without cubic anisotropy (see first factor of the radicand), if the external field H_{ext} has no in-plane components ($H_{ext} = H_z$). H_z would then be perfectly cancelled out by $(H_d + H_u)cos\theta_M$. Thus, the cubic anisotropy is crucial for obtaining a finite frequency. Eq. (3) exhibits only an implicit dependence of the frequency on the external field which determines the direction of the magnetization parametrized by θ_M. See Fig. 1(a) for an illustration of the complete cancellation of the out-of plane components of the effective field at the saturation field. For $H_z \geq H_s$, the cubic anisotropy contributions to the effective field disappears [Fig. 1(b)] according to Eq. (1), because m_x and m_y vanish.

Thus, there are two branches of the spin wave frequency [Fig. 1(c)] as a function of the external field, which both depend on the wavevector component along the external field. For the thin film, the out-of plane wavevector component is quantized: $k_z = \frac{n\pi}{d}$. This spatial quantization of the spin waves essentially enters their frequency via the exchange term $D_{ex}k_z^2$ in Eq. (2) and (3). In Fig. 1(c) we fit equation Eq. (3) to the lower branch of the experimental data from Deb et al.(7) We obtain a convincing agreement for the lower branches for $n = 0, \ldots, 4$ under the assumption of the parameters given in Table

1, which agree reasonably well with the literature. For the upper branch, the magnetization points perfectly out of plane. Hence, the spin wave amplitude is exceedingly small for a perfect alignment of the external field, because the excitation is forbidden by symmetry. This and a tiny experimental in-plane field may explain the deviations.

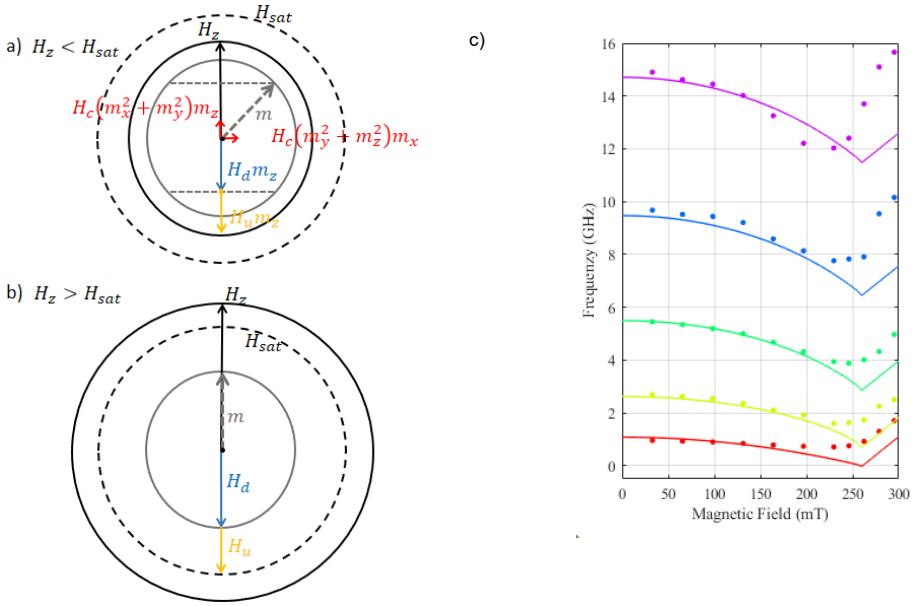

Fig. 1: a) Vector diagram of the contributions to the effective field for $H_z < H_s$. The cubic anisotropy H_c determines the effective field and hence the stable direction of the magnetization vector (see the contributions to the effective field in Eq. (1), because $H_d m_z + H_u m_z$ nearly cancel H_z. b) For $H_z \geq H_s$ the magnetization points along $\overrightarrow{e_z}$. At the saturation field ($H_z = H_s$), all effective field contributions cancel to zero. c) Spin wave frequencies according to Eq. (2) and (3) for the first five standing spin wave modes (n=0,…,4). All branches fit well simultaneously to the tr-MOKE data from Deb et al., i.e. they fit the quadratic dependence on the mode number.(7)

B) Experimental spin wave spectrum for direct and indirect excitation

In this paper we study a pair of $Bi_1Y_2Fe_5O_{12}$ (Bi:YIG) single crystalline thin films with a thickness of 135 nm grown by pulsed laser deposition on a gadolinium gallium garnet (GGG) (100) substrate.(19, 20) One of the two films is covered by a Pt (5 nm)/Cu (100 nm) bilayer on top of the Bi:YIG film using direct current magnetron sputtering. During this procedure the thickness of the Bi:YIG is reduced by few nanometers. The top Pt layer absorbs nearly all photons from the optical excitation pulses and the 100 nm Cu layer ensures that no photons reach the Bi:YIG layer. However, the metallic bilayer is known to efficiently conduct the absorbed photon energy by efficient heat transport via hot electrons to the magnetic film. For metallic ferromagnets, the hot electron pulse would directly funnel energy into its electronic system.(21) However, the electrons are stopped at the interface to the ferromagnetic insulator Bi:YIG, and energy is transported in the ferromagnet via coherent and incoherent phonons.
In the following we compare the magnetization dynamics triggered in the Bi:YIG film by energy directly deposited in the bulk of the uncovered Bi:YIG film to the scenario, where the energy is transported to the Bi:YIG interface via the Cu film, excluding direct optical excitation. Fig. 1(c) we reproduce the measurement of the standing spin wave modes upon laser-excitation using tr-MOKE.(7) The standard setup has been described previously.(22) In the left column of Fig. 2 we show the direct absorption of 800 nm pulses in the Bi:YIG film (by one and two photon absorption) and the right column of Fig. 2 shows the results for indirect excitation, where the 800 nm light pulses are fully absorbed in the Pt/Cu layers with 5nm/100nm thickness. Figs. 2(a) and 2(b) show schematics for direct and indirect excitation of the Bi:YIG film by pump pulses with a wavelength of the 800 nm. The Kerr rotation of a 400 nm probe pulse detects the magnetization dynamics Fig. 2(c) and 2(d) show exemplary tr-MOKE traces

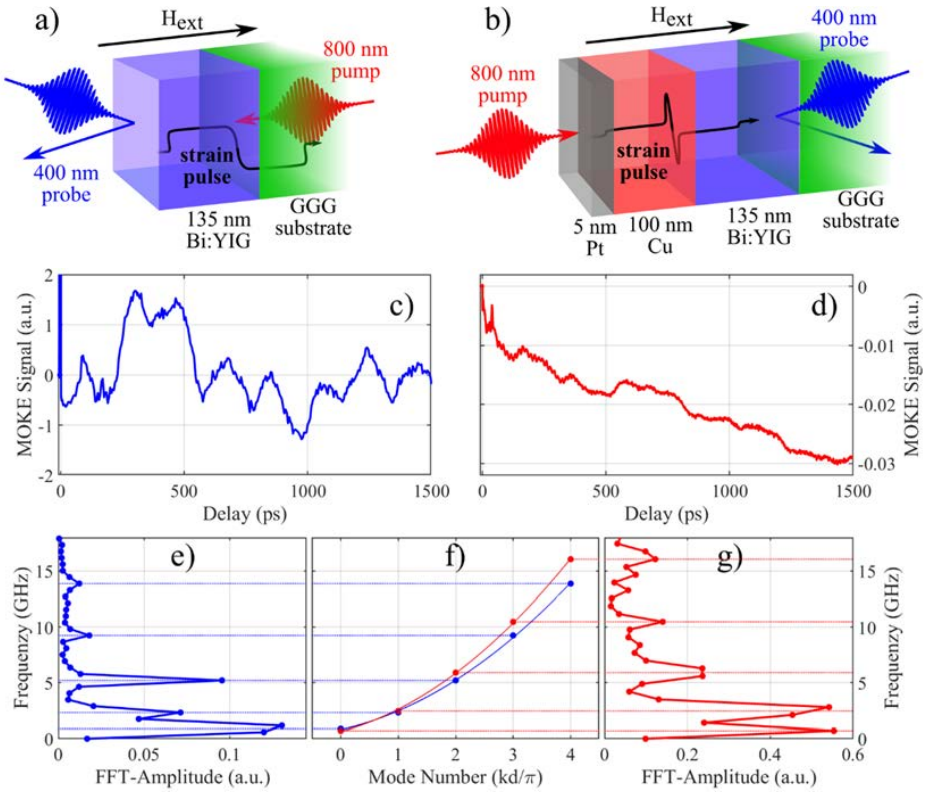

Fig. 2) Measurement of standing spin waves by MOKE a) Schematic of the direct excitation geometry, where 800 nm pump pulses at 10 mJ/cm^2 incident fluence are absorbed in Bi:YIG. b) Schematic of the indirect excitation geometry. c) Tr-MOKE for an external field of $\mu_0 H_z = 98$ mT perpendicular to the sample for direct excitation. d) Time resolved MOKE at $\mu_0 H_z = 88$ mT for indirect excitation. Fourier-transforms of the spectra exhibiting five resonance frequencies shown for the direct e) and indirect g) excitation. f) Measured spin wave frequencies for direct (blue) and indirect (red) excitation extracted from the maxima in panels e) and g). The quadratic dependence of the mode number is given by the exchange energy [cf. Eq. (3)], and is slightly steeper for the indirect excitation, where the Bi:YIG film is thinner and the external field is smaller (higher frequencies in the lower branch of Fig. 1(c).

under the two excitation conditions. The Fourier-transforms of these spectra are shown in2(e) and 2(g), which clearly show the same higher order spin wave modes at slightly different frequencies, because of the different thickness of the two Bi:YIG films. We link these exemplary spectra to the full experimental determination of the dependence of the frequency spectrum on the external field in f), which shows the quadratic dependence of the frequency on the mode number. The solid lines show fits through the data in f) using Eq. (3), which contains a linear and quadratic contribution in $n = \frac{k_z d}{\pi}$ because we fit the lower branch [Eq. (3)].

C) Experimental quantification of the strain and temperature by UXRD

The standing spin waves reported in Fig. 2 are excited by laser-induced coherent and incoherent phonons, meaning by strain waves and phonon heating. The transient strain $\eta_{zz}(z,t)$ including the quasi-static strain due to thermal expansion couples to the spins via the magnetoacoustic coupling term $H_{me}(z,t)$. The temperature rise $T(z,t)$ induces changes of the magnetocrystalline anisotropy ($H_u(z,t)$ and $H_c(z,t)$), triggering spin precession, too. Fig. 3 summarizes the characterization of strain waves and heat transport by UXRD as reported by Zeuschner et al.(11) We probe the strain in the Bi:YIG layer by the shift of the Bragg peak via reciprocal space slicing(23) at our laser-driven x-ray plasma source.(24) In analogy to Fig. 2, the left column of Fig. 3 shows direct excitation and the right column shows indirect excitation which is identical to the conditions for the tr-MOKE experiments in Fig.2, i.e. in the indirect excitation all light is absorbed in the metal layers. The x-ray probe pulses penetrate the entire

heterostructure and we can determine the average transient strain $\bar{\eta} = \frac{\Delta c}{c}$ by following the angular shift of the Bragg peak [dots in Fig. 3 (a) and 3(d)]. The average transient strain $\bar{\eta}(t)$ is the direct observable in our experiments. On the other hand, for time-delays beyond 100 ps the propagating strain waves have left the Bi:YIG layer and the remaining quasi-static strain $\bar{\eta}$ is a direct measure of the average temperature change in the Bi:YIG layer. A thorough modeling of the transient strain (solid lines) gives access to the spatio-temporal temperature gradient $T(z,t)$ and transient strain $\eta(z,t)$.(11, 21) We calculate the energy deposited in the Bi:YIG layer and in the heterostructure from the incident fluence. The diffusive two temperature model is required to correctly account for the non-equilibrium heat transport in the Pt/Cu bilayer.(11, 21) We use the thermo-elastic parameters given in Table 2.

The spatio-temporal strain [Fig. 3(b) and 3(e)] and heat [Fig. 3(c) and 3(f)] maps serve as input parameters for the simulation of the magnetization dynamics. Since we recorded the MOKE and UXRD data in different setups, with different focusing conditions and laser pulse parameters, we scale the strain in the UXRD data according to the absorbed fluence. For the indirect excitation the absorption of light in the metals and the heat flow are nearly linear in the excitation fluence. The direct excitation was shown to have linear and quadratic contributions.(7, 11) We scaled the absorbed fluence to match the absorption of the light pulses observed in the MOKE setup. The modeling confirms that the observed strain and heat do not significantly depend on the relative weight of the linear and quadratic absorption contributions.

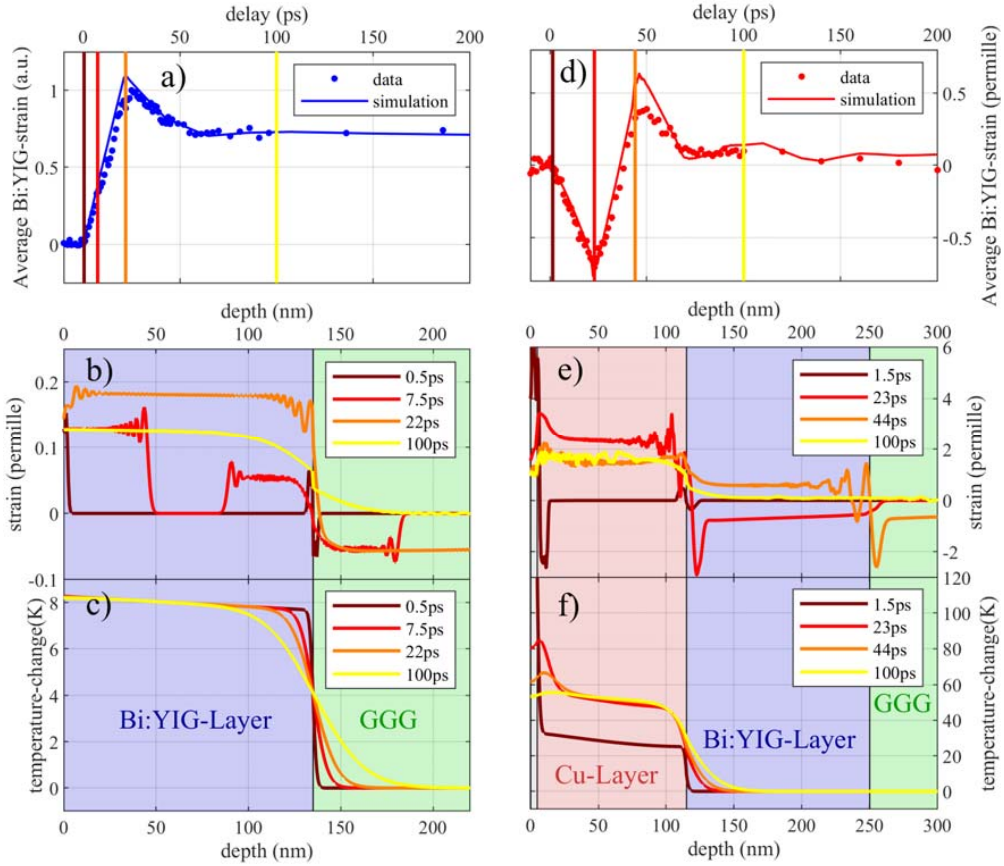

Fig. 3 Calibration of strain and heat by UXRD

a) Transient strain in Bi:YIG following direct excitation at 800 nm extracted from Zeuschner et al.(11) and scaled to the fluence 10 mJ/cm^2 used in the tr-MOKE experiment. The blue line is a fit according to the model. The spatial dependence of the calculated strain b) and temperature c) is shown for the selected times indicated by the color code in a). The right panels d),e) and f) show the same for indirect excitation, where the data are reproduced from Deb et al.(8) Note the larger temperature rise (f) in the metal films and the strong gradient in the Bi:YIG layer. The average temperature in Bi:YIG is smaller for the indirect excitation, but the standing spin wave modes are efficiently excited by the gradient. The simulations of the magnetization dynamics in Fig. 4 use only the spatiotemporal strain and temperature in the blue shaded areas, which symbolize the Bi:YIG layers.

In the following we comment briefly on the main observations for strain and heat. Fig. 3(b) illustrates, that upon direct excitation the Bi:YIG layer expands via two counter-propagating strain fronts starting at the surface and the interface. At 22 ps both strain fronts have reached the opposite side of the film, the maximum average strain is reached and the Bi:YIG layer is nearly homogeneously expanded. In the next 22 ps, the expansive strain front that started at the GGG interface is converted to a contraction wave at the surface. Then, the acoustic dynamics cease as both strain fronts have propagated into the substrate. In the Bi:YIG layer, the quasi-static expansion given by the thermal load in the film remains and very slowly relaxes via thermal transport to the substrate. Fig. 3(c) illustrates, that already on short timescales the heat flow yields a temperature gradient at the interface, which is already considerable after about 100 ps.

For the indirect excitation, Fig 3(d) illustrates that the strain in Bi:YIG film is essentially driven by a bipolar strain pulse, which results from an expansion of the Cu layer. Unlike one may have expected, the short bipolar strain pulse with high amplitude generated in Pt does not considerably alter the average strain in Bi:YIG. The simulation clearly shows that the very localized bipolar pulse from Pt, which has three times larger an amplitude than the compression launched by Cu, travels through Bi:YIG (see e.g. the snapshot at 23 ps in Fig. 3(e). However, the Bi:YIG strain is essentially determined by the Cu transducer. We emphasize that electrons transport energy to the Cu/Bi:YIG interface quasi instantaneously (see 1.5 ps snapshot in Fig. 3(f) and hence start the relevant acoustic compression of Bi:YIG immediately, as indicated by the experiment [Fig. 3(d)]. After the dominant passage of the bipolar strain in the first 75 ps, only a small expansion of Bi:YIG is observed due to the slow phononic heat transport into the Bi:YIG layer, which is quantified in Fig. 3(f). Again, at 100 ps, a considerable temperature gradient is built, however in this case, it is located at the interface to Cu and not towards the substrate.

Property at 300K	**GGG**	**Bi:YIG**
Sound velocity (nm/ps)	**6.34** (25)	**6.3** (26)
Density (g/cm^3)	**7.085** (27)	**5.9** (26)
Linear thermal expansion (10^{-5}/K)	**1.65** (28)	1
Heat Capacity (J/kg/K)	**381.2** (29)	560
Poisson-Correction $(1 + 2C_{12}/C_{11})$(30)		1.8
Thermal conductivity (W/m K)	7.05	7.4

Table. 2 Thermoelastic parameters of Bi_1Y_2IG and the substrate GGG: The bold parameters can be found for Bi:YIG in the given references. The other parameters are assumed reported for YIG and assumed to be similar for Bi:YIG. Parameters for Pt and Cu are identical to the ones used in the publication from Pudell et al.(21)

D) Numerical micromagnetic modeling that uses strain and temperature from UXRD

Fig. 4) summarizes the results of the micromagnetic simulations according to the model introduced in section A). The full LLG equation is solved numerically based on the parameters given in Table 1 and the explicit spatiotemporal dependence of the strain $\eta_{zz}(z,t)$ and the temperature $T(z,t)$, which were derived in section C) by modeling the lattice strain calibrated by the UXRD data. In analogy to Fig. 2 and 3 the left column of Fig. 4 collects simulation results for the direct excitation of Bi:YIG and the right column for indirect excitation. The only difference in the simulations stems from the different UXRD calibrated input values for strain $\eta_{zz}(z,t)$ and temperature $T(z,t)$.

The upper row displays results, where the magnetoacoustic coupling constant b_1 is set to zero and only the temperature driven anisotropy change $\Delta H_u(z,t) \propto \Delta H_c(z,t) \propto T(z,t)$ are at work (we use the linearized dependence $\Delta H_u(T)$ from Table 1 for parametrization.(5, 18) In the second row only the magnetoacoustic coupling launches spin waves, because we set the anisotropy to be temperature independent, i.e. constant. While all calculated spectra show the expected frequency spectrum, we clearly see the excitation of the fundamental mode upon direct excitation to be much stronger than in the experiment. The calculated magnetization dynamics (insets in Figs 4(a) and 4(c) display $m_z(z,t)$) show that the fundamental mode is triggered with opposite phase for the two mechanisms. In order to achieve at least a qualitative agreement with tr-MOKE data, both mechanisms must be active. Both mechanisms individually trigger a much larger fundamental mode amplitude compared to the higher order modes. Because the precise values for magnetoacoustic coupling coefficients and anisotropy

changes of our samples may differ from the literature values,(5, 18) we scale the relative magnitude of the magnetoacoustic coupling with respect to the anisotropy mechanism $\mathrm{H}_{me}/\Delta\mathrm{H}_u = c\,\mathrm{H}_{me}^{\mathrm{lit}}/\Delta\mathrm{H}_{\mathrm{u}}^{\mathrm{lit}}$ by a coefficient c.

For the literature value ($c = 1$) the fundamental mode has much too large amplitude. We obtain reasonable agreement with the experimentally observed spectra in Fig. 2(c) for direct excitation, by using $c \approx 3$. The modeling of the indirect excitation depends much less on the parameter c. The experiments rely on the same Bi:YIG film and are only different in terms of excitation. The main difference between the direct and indirect excitation is that for the indirect excitation the strain essentially travels through the Bi:YIG film quickly. The temperature change in Bi:YIG induced by the heat flow from the metal to the film has a very strong spatial gradient, which imposes a strong spatial gradient not only on $\Delta\mathrm{H}_u$, but also on the effective field change, $\mathrm{H}_{me}^{\mathrm{qs}}$ due to the quasistatic change of the strain by thermal heating.

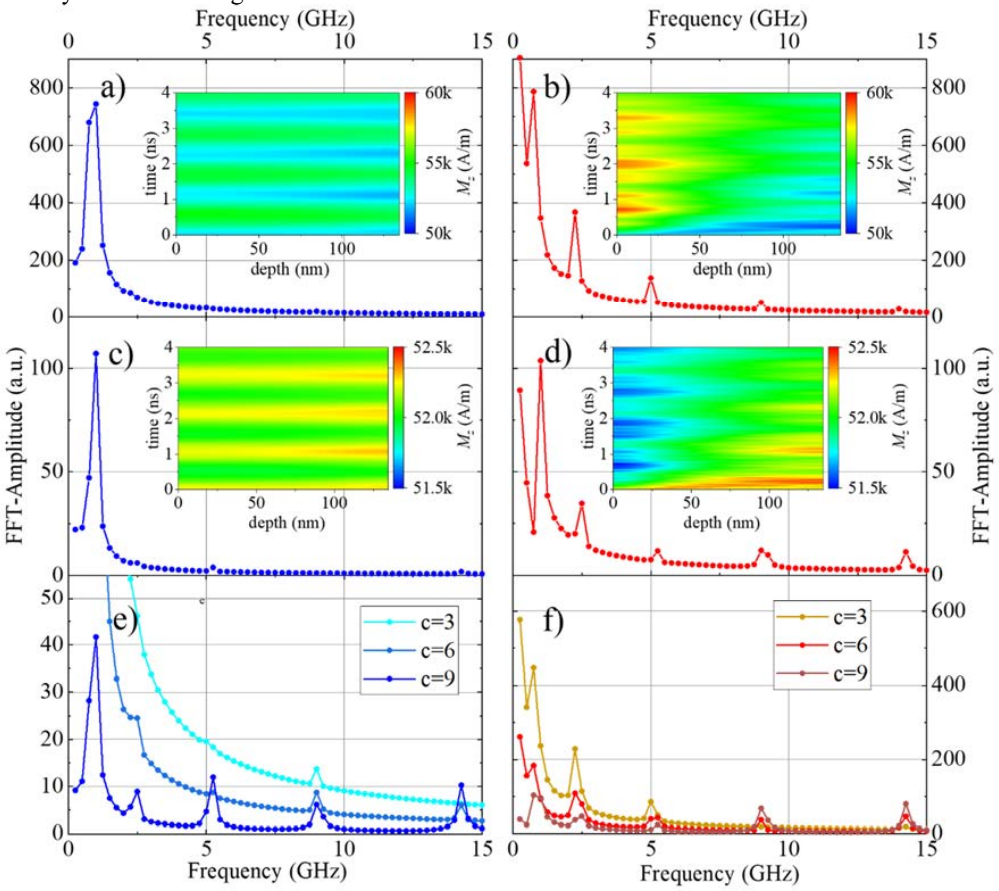

Fig. 4 Numerical micromagnetic modeling based on the input of $\boldsymbol{\eta_{zz}(z,t)}$ and $\boldsymbol{T(z,t)}$ from experimental UXRD data Spin-wave spectra resulting from the Fourier-analysis of the calculated $m_z(z,t)$ shown in the respective inset. The first row shows the result, were the magnetoacoustic coupling is zero ($H_{me} = 0$) and only the temperature induced anisotropy change is active ($H_u = -\frac{2K_u(T(z,t))}{\mu_0 M_s}$). a) direct excitation b) indirect excitation. For the second row only the magnetoacoustic term $H_{me} = -\frac{2b_1\eta_{zz}(z,t)}{\mu_0 M_s}$ is on, whereas the anisotropy is constant ($H_u = -\frac{2K_u}{\mu_0 M_s}$). c) direct excitation d) indirect excitation. From the insets, which show $m_z(z,t)$ we see that the two mechanisms drive the fundamental mode with opposite phase (see panels a) and c). In the last row both mechanisms are active and the parameter c quantifies the relative strength of the magnetoacoustic coupling. e) for the direct excitation and $c \approx 3$ the fundamental mode is considerably lowered, and the calculated spectrum resembles the experimental observation in Fig. 2(f). For the indirect excitation (f) the suppression of the fundamental mode does not exceed the suppression of the higher modes. For the choice of the same $c \approx 3$ the calculated spectra are again in reasonable agreement with experiment [Fig. 2(g)].

Discussion

The modeling of UXRD data strictly determines the connection of the transient strain profile $\eta(z,t)$ and the transient temperature $T(z,t)$. For direct excitation, the temperature change leads to a nearly homogeneous quasi-static $\eta_{QS} = \alpha\Delta T$ determined by the temperature rise, where $\alpha = 10^{-5}1/K$ is the thermal expansion coefficient. The effective magneto-elastic coupling field $H_{me}^{qs} = 8$ mT due to the quasi-static strain η_{QS}(100K) is about four times smaller than $\Delta \mathrm{H}_u = 31$ mT for $\Delta T = 100$ K. This temperature-induced quasi static strain necessarily enters the effective field, and hence the temperature changes ΔT act on the effective field in two ways. The anisotropy route is about four times more efficient, however. We note that in addition to the quasi-static strain, the ultrafast optical excitation generates strain waves which may dominate the spin wave excitation if the acoustic wave timescale is resonant with the spinwave. For the indirect excitation the strain wave is launched in the Pt/Cu structure, and hence the contribution of the magneto-elastic coupling can be relatively larger, because the related temperature change is high in the metal but less pronounced in Bi:YIG. Hence the temperature induced changes in Bi:YIG contribute less, the thicker the Cu film is. The magnetoacoustic strain wave has two bipolar components, which are given by the Pt and Cu thickness [Fig. 3(e)]. Both transients enter the LLG equation via the effective field given in Eq. (1). The numerical modeling has essentially only two tuning parameters: The change of the anisotropy constant with temperature $\Delta \mathrm{H}_u(T)$ and the magnetoelastic coupling $\mathrm{H}_{me}(\eta)$. The change of the magnetocrystalline anisotropy due to magnetostriction(31) is negligible in the case of YIG and therefore Bi:YIG which leads to independent excitation routes of SSWs in Bi:YIG: Thermally induced anisotropy change via ultrafast heating on the one hand and picosecond strain waves and thermal expansion paired with inverse magnetostriction on the other hand.

In our modeling of the spin-wave spectrum we tune the relative magnitude of the magnetoacoustic coupling coefficient. We have tested that the magnetic response to both excitations is still in the linear regime. We find that the experimental spin wave spectrum for direct excitation of Bi:YIG in Fig. 2(c) can only be reproduced for a relatively strong magnetoacoustic coupling. The key is that the zero order mode (ferromagnetic resonance (FMR) mode) is excited with opposite phase for the two mechanisms. If we neglect either the magneto-acoustic coupling [Fig. 4(a)] or the temperature-induced anisotropy change [Fig. 4 (c)] the higher order modes have a much too small amplitude compared to the FMR mode. For an appropriately increased magnitude of the magneto-elastic coupling ($c \approx 3$), or alternatively a reduced $\Delta \mathrm{H}_u(T)$, we arrive at a simulated spin-wave spectrum that approximately reproduces the measured one.

Conclusion

We have set up a micromagnetic model to quantitatively test the relative importance of strain waves and temperature changes for the excitation of spin waves. We find that the two mechanisms counteract each other for the FMR mode, but may have a different phase relationship for higher order modes. We can quantitatively test our model by calibrating the input parameters of transient strain and transient phonon temperature via UXRD and comparing the simulated spin wave spectrum with experimental result obtained in MOKE experiments under the same excitation conditions. We have verified the model for both cases, the indirect excitation of Bi:YIG via a metal bilayer on the one hand, as well as by one and two-photon absorption on the other hand. We believe that this analysis of the two coupled routes of generating magnetization dynamics via coherent and incoherent phonons is widely applicable for other ferromagnetic, ferrimagnetic and antiferromagnetic materials and may help to design new devices.

Acknowledgement:

This work was funded by the Deutsche Forschungsgemeinschaft (DFG, German Research Foundation) – Project-ID 328545488 – TRR 227, projects A10 and B06. X.-G.W. thanks the National Natural Science Foundation of China (Nos. 12174452, 12074437, 11704415), and the Natural Science Foundation of Hunan Province of China (No. 2021JJ30784) for support. M.D. acknowledges the Alexander von Humboldt Foundation for financial support.

References:

References

1. M. van Kampen, C. Jozsa, J. T. Kohlhepp, P. LeClair, L. Lagae, W. J. M. de Jonge, B. Koopmans, All-optical probe of coherent spin waves. *Physical review letters* **88**, 227201 (2002).
2. A. V. Kimel, A. Kirilyuk, P. A. Usachev, R. V. Pisarev, A. M. Balbashov, T. Rasing, Ultrafast non-thermal control of magnetization by instantaneous photomagnetic pulses. *Nature* **435**, 655–657 (2005).
3. A. A. Serga, A. V. Chumak, B. Hillebrands, YIG magnonics. *J. Phys. D: Appl. Phys.* **43**, 264002 (2010).
4. L. Soumah, N. Beaulieu, L. Qassym, C. Carrétéro, E. Jacquet, R. Lebourgeois, J. Ben Youssef, P. Bortolotti, V. Cros, A. Anane, Ultra-low damping insulating magnetic thin films get perpendicular. *Nat Commun* **9**, 3355 (2018).
5. P. Hansen, J.-P. Krumme, Magnetic and magneto-optical properties of garnet films. *Thin Solid Films* **114**, 69–107 (1984).
6. M. Deb, E. Popova, M. Hehn, N. Keller, S. Petit-Watelot, M. Bargheer, S. Mangin, G. Malinowski, Damping of Standing Spin Waves in Bismuth-Substituted Yttrium Iron Garnet as Seen via the Time-Resolved Magneto-Optical Kerr Effect. *Phys. Rev. Applied* **12**, 677 (2019).
7. M. Deb, E. Popova, M. Hehn, N. Keller, S. Petit-Watelot, M. Bargheer, S. Mangin, G. Malinowski, Femtosecond Laser-Excitation-Driven High Frequency Standing Spin Waves in Nanoscale Dielectric Thin Films of Iron Garnets. *Physical review letters* **123**, 27202 (2019).
8. M. Deb, E. Popova, S. P. Zeuschner, M. Hehn, N. Keller, S. Mangin, G. Malinowski, M. Bargheer, Generation of spin waves via spin-phonon interaction in a buried dielectric thin film. *Phys. Rev. B* **103**, 24411 (2021).
9. L. Soumah, D. Bossini, A. Anane, S. Bonetti, Optical Frequency Up-Conversion of the Ferromagnetic Resonance in an Ultrathin Garnet Mediated by Magnetoelastic Coupling. *Phys. Rev. Lett.* **127 (**2021).
10. M. Deb, E. Popova, M. Hehn, N. Keller, S. Mangin, G. Malinowski, Picosecond acoustic-excitation-driven ultrafast magnetization dynamics in dielectric Bi-substituted yttrium iron garnet. *Phys. Rev. B* **98**, 444 (2018).
11. S. P. Zeuschner, J.-E. Pudell, A. von Reppert, M. Deb, E. Popova, N. Keller, M. Rössle, M. Herzog, M. Bargheer, Measurement of transient strain induced by two-photon excitation. *Phys. Rev. Research* **2**, 22013 (2020).
12. J.-W. Kim, M. Vomir, J.-Y. Bigot, Ultrafast magnetoacoustics in nickel films. *Physical review letters* **109**, 166601 (2012).
13. S. A. Manuilov, A. M. Grishin, Pulsed laser deposited Y3Fe5O12 films: Nature of magnetic anisotropy II. *Journal of Applied Physics* **108**, 13902 (2010).
14. O. Kovalenko, T. Pezeril, V. V. Temnov, New concept for magnetization switching by ultrafast acoustic pulses. *Physical review letters* **110**, 266602 (2013).
15. L. Chotorlishvili, X.-G. Wang, Z. Toklikishvili, J. Berakdar, Thermoelastic enhancement of the magnonic spin Seebeck effect in thin films and bulk samples. *Phys. Rev. B* **97 (**2018).
16. C. Zener, Classical Theory of the Temperature Dependence of Magnetic Anisotropy Energy. *Phys. Rev.* **96**, 1335–1337 (1954).
17. W. Strauss, "Magnetoelastic Properties of Yttrium-Iron Garnet" in *Applications to Quantum and Solid State Physics* (Elsevier, 1968), pp. 211–268.
18. P. Hansen, K. Witter, W. Tolksdorf, Magnetic and magneto-optic properties of lead- and bismuth-substituted yttrium iron garnet films. *Phys. Rev. B* **27**, 6608–6625 (1983).

19. M. Deb, E. Popova, A. Fouchet, N. Keller, Magneto-optical Faraday spectroscopy of completely bismuth-substituted Bi 3 Fe 5 O 12 garnet thin films. *J. Phys. D: Appl. Phys.* **45**, 455001 (2012).
20. E. Popova, L. Magdenko, H. Niedoba, M. Deb, B. Dagens, B. Berini, M. Vanwolleghem, C. Vilar, F. Gendron, A. Fouchet, J. Scola, Y. Dumont, M. Guyot, N. Keller, Magnetic properties of the magnetophotonic crystal based on bismuth iron garnet. *Journal of Applied Physics* **112**, 93910 (2012).
21. J.-E. Pudell, M. Mattern, M. Hehn, G. Malinowski, M. Herzog, M. Bargheer, Heat Transport without Heating?—An Ultrafast X-Ray Perspective into a Metal Heterostructure. *Advanced Functional Materials* **30**, 2004555 (2020).
22. Y. Xu, M. Deb, G. Malinowski, M. Hehn, W. Zhao, S. Mangin, Ultrafast Magnetization Manipulation Using Single Femtosecond Light and Hot-Electron Pulses. *Adv. Mater.* **29 (**2017).
23. S. P. Zeuschner, M. Mattern, J.-E. Pudell, A. von Reppert, M. Rössle, W. Leitenberger, J. Schwarzkopf, J. E. Boschker, M. Herzog, M. Bargheer, Reciprocal space slicing: A time-efficient approach to femtosecond x-ray diffraction. *Structural dynamics (Melville, N.Y.)* **8**, 14302 (2021).
24. D. Schick, A. Bojahr, M. Herzog, C. von Korff Schmising, R. Shayduk, W. Leitenberger, P. Gaal, M. Bargheer, Normalization schemes for ultrafast x-ray diffraction using a table-top laser-driven plasma source. *The Review of scientific instruments* **83**, 25104 (2012).
25. V. F. Kitaeva, E. V. Zharikov, I. L. Chistyi, The properties of crystals with garnet structure. *physica status solidi (a)* **92**, 475–488 (1985).
26. G. G. Siu, C. M. Lee, Y. Liu, Magnons and acoustic phonons in Y3-xBixFe5O12. *Physical review. B, Condensed matter* **64**, 94421 (2001).
27. L. J. Graham, R. Chang, Elastic Moduli of Single-Crystal Gadolinium Gallium Garnet. *Journal of Applied Physics* **41**, 2247–2248 (1970).
28. R. Liang, F. Liu, Measurement of thermal expansion coefficient of substrate GGG and its epitaxial layer YIG. *Powder Diffr.* **14**, 2–4 (1999).
29. H. Shen, J. Xu, A. Wu, J. Zhao, M. Shi, Magnetic and thermal properties of perovskite YFeO3 single crystals. *Materials Science and Engineering B: Solid-State Materials for Advanced Technology* **157**, 77–80 (2009).
30. D. Royer, E. Dieulesaint, *Elastic waves in solids: Including nonlinear dynamics* (Springer, 2000).
31. C. Kittel, Physical Theory of Ferromagnetic Domains. *Rev. Mod. Phys.* **21**, 541–583 (1949).

Chapter 4

Conclusion

This cumulative doctoral thesis summarizes my work in the research field of ultrafast lattice dynamics and magnetoacoustics and my contributions to the further development of ultrafast X-ray diffraction on the basis of 8 publications. My work thus covers the two fundamental parts of experimental physics research: the experimental results and findings as well as their interpretation, conception and modeling on the one side, the design and development of the experiment itself to be optimized for the respective research theme on the other side.

With the conception of reciprocal space slicing in article VI, I introduced a time saving alternative approach for strain assessment on an ultrafast time scale with femtosecond X-ray diffraction. This technique utilizes the capability of area detectors to measure the diffracted intensity for multiple diffraction angles simultaneously and thus for multiple scattering vectors, the so called slice of the reciprocal space. A movement of the diffraction peak in reciprocal space due to strain can thus be monitored without scanning the diffraction angles of the goniometer. RSS is employed in the majority of publications of the UDKM group at the Universtiy of Potsdam in the recent past, which utilize UXRD, and is particularly useful at large scale facilities because of the limited and sparse measurement time.

The second experimental development I contributed to, was the implementation of UXRD measurements into the research field of ultrafast magnetism. In publication I, IV, V and VIII we directly compared UXRD data with tr-MOKE data under similar excitation conditions and in article II the strain dynamics are rationalized by the ultrafast response of the spin system. This development peaked in the design and commissioning of the actual implementation of a tr-MOKE setup into the UXRD setup with a laser-driven plasma X-ray source at the UDKM group. This is, to my knowledge, the first setup of its kind and will be used in the future simultaneous quantifaction of magnetization and lattice dynamics.

Combining the experimental findings of UXRD and tr-MOKE measurements, my colleagues and I were able to develop a comprehensive model based on the excitation of standing spin waves in the ferromagnetic insulator $Bi_1Y_2Fe_5O_{12}$ by coherent and incoherent phonons. I provided the measurement and modeling of the lattice dynamics of directly photoexcited Bi:YIG in article III, revealing a two-photon absorption process which induces an ultrafast heating and thermal expansion as well as picosecond strain pulses. In article V, I found that a biploar strain waves is immediately injected into a buried Bi:YIG thin film as the capping Copper layer, in which hot electrons equilibrate faster than a picosecond, acts as a transducer. Additionally, phonon heat is quickly flowing from the Cu into the Bi:YIG, heating up the latter on a timescale of a few hundred picoseconds. In article VIII, those information are fed into a spatio-temporally resolved micromagnetic modelling to fit the observation of excited standing spin waves in the direct and indirect exctiation scheme. We found that sound and heat, i.e. coherent and incoherent phonons alike, generate higher order standing spin waves. The SSWs are generated via the thermally induced ultrafast changes of the anisotropy and via inverse magnetostriction. Interestingly, the phase of the ferromagnetic resonance mode is reversed for the two processes, which explains the relatively low

amplitude of the FMR mode compared to the higher order modes observed in the tr-MOKE experiments.

Chapter 5

Outlook

Based on the results of this thesis, there are several possibilities to carry on the work in ultrafast X-ray diffraction and magnetoacoustics. Our future investigations have the potential to further cement UXRD as a substantial part of ultrafast magnetism and picosecond ultrasonic research fields. This is based on the fact that UXRD offers the direct quantification of lattice dynamics which are a sensor for all kinds of ultrafast phenomena, as discussed in this thesis.

On the one hand, UXRD itself can be further optimized as I have shown with the conception of reciprocal space slicing. This technique can not only be transferred in principle to other diffraction techniques, i.e. neutron or electron diffraction. The modeling can also be expanded to be even more general and comprehensive. For now, the RSS described in this thesis assumes a fixed RSS scaling factor S, which is only viable for diffraction peaks which do not change drastically in width and especially do not exhibit a change of the width ratio along q_z and q_x. With that being the case, for example during phase transitions, S needs to be treated as a time dependent variable. Fortunately, an area detector is capable of measuring the width of diffraction peaks along two dimensions in the reciprocal space simultaneously, supporting a practical route to implement this addition. Another extension to the presented RSS technique can be the application for time resolved intensity measurements of Bragg peaks. This is in particular important for ultrafast investigations of the structure factor which can be a measure of coherent optical phonon modes, for example in Bismuth [94]. The problem for intensity measurements with the fixed angle detection scheme of RSS is, that the intensity on the detector is not only modulated by the structure factor but also by the strain which results in a peak shift in reciprocal space and moves the peak out of the detection window. This however can be corrected by monitoring the RSS factor time resolved and relate the measured peak shift with the decrease of intensity.

On the other hand, I have shown that the combination of UXRD and time resolved magneto-optical Kerr effect measurement is a powerful tool to unravel the intricacies of the ultrafast magnetoelastic and thermomagnetic coupling mechanisms on the example of Bi:YIG. UXRD can not only determine whether or not the excitation process of magnetization dynamics with tr-MOKE is thermally induced. This is important, since a non-thermal mechanism, like inverse Faraday and Cotton-Mouton effects or photoinduced magnetic anisotropy, are thought to be the main excitation process in some cases [84, 85]. It is also possible to monitor the thermal and coherent strain dynamics, if the absorption of the pump light is significant, as shown in this thesis. Besides the thermal aspects it has been shown, that picosecond strain pulses change the optical parameters of a specimen in a way tr-MOKE is sensitive to. With that, a tr-MOKE signal can suggest a magnetization change, without actually being present [95]. In the case of the strain pulse echoes of article I, this can be ruled out, when repeating the measurement in a manner where $TbFe_2$ is fully demagnetized, so that the tr-MOKE trace is saturated by the magnetization change. Then, inverse magnetostriction is not possible anymore and if the echoes are still detectable with tr-MOKE, their origin is not magnetically. With that, UXRD can be employed in future investigations where a thermal or non-thermal excitation processes or inverse magnetostriction is assumed or expected

to experimentally confirm or disprove the modeling conceptions. Moreover, the combination of UXRD and tr-MOKE at the same experimental setup introduces the possibility to measure strain and magnetization dynamics under the same exact excitation conditions, which drastically reduces the margin of error in the quantification.

Bibliography

[1] Antoine Rousse, Christian Rischel, and Jean-Claude Gauthier. Femtosecond x-ray crystallography. *Reviews of Modern Physics*, 73(1):17–31, 2001. ISSN: 0034-6861. DOI: 10.1103/RevModPhys.73.17.

[2] M. Bargheer, N. Zhavoronkov, M. Woerner, and T. Elsaesser. Recent progress in ultrafast x-ray diffraction. *Chemphyschem: a European journal of chemical physics and physical chemistry*, 7(4):783–792, 2006. ISSN: 1439-4235. DOI: 10.1002/cphc.200500591.

[3] Majed Chergui and Ahmed H. Zewail. Electron and x-ray methods of ultrafast structural dynamics: advances and applications. *Chemphyschem: a European journal of chemical physics and physical chemistry*, 10(1):28–43, 2009. ISSN: 1439-4235. DOI: 10.1002/cphc.200800667.

[4] T. Elsaesser and M. Woerner. Perspective: structural dynamics in condensed matter mapped by femtosecond x-ray diffraction. *The Journal of Chemical Physics*, 140(2):020901, 2014. ISSN: 0253-2964. DOI: 10.1063/1.4855115.

[5] Neil W. Ashcroft and N. David Mermin. *Solid state physics*. Brooks/Cole Thomson Learning, South Melbourne, repr edition, 2012. ISBN: 9780030839931.

[6] J. Hohlfeld, S.-S. Wellershoff, J. Güdde, U. Conrad, V. Jähnke, and E. Matthias. Electron and lattice dynamics following optical excitation of metals. *Chemical Physics*, 251(1-3):237–258, 2000. ISSN: 03010104. DOI: 10.1016/S0301-0104(99)00330-4.

[7] J. P. Joule. On the effects of magnetism upon the dimensions of iron and steel bars. *The London, Edinburgh, and Dublin Philosophical Magazine and Journal of Science*, 3, 1847. ISSN: 1941-5966. DOI: 10.1080/14786444708645656.

[8] J. Bardeen and W. Shockley. Deformation potentials and mobilities in non-polar crystals. *Physical Review*, 80(1):72–80, 1950. ISSN: 0031-899X. DOI: 10.1103/PhysRev.80.72.

[9] S. I. Anisimov, B. L. Kapeliovich, and T. L. Perel'man. Electron emission from metal surfaces exposed to ultrashort laser pulses. *Sov. Phys. JETP*, 39:375, 1974. URL: http://www.jetp.ras.ru/cgi-bin/dn/e_039_02_0375.pdf.

[10] Philip B. Allen. Theory of thermal relaxation of electrons in metals. *Physical review letters*, 59(13):1460–1463, 1987. DOI: 10.1103/PhysRevLett.59.1460.

[11] E. Beaurepaire, J.-C. Merle, A. Daunois, and J.-Y. Bigot. Ultrafast spin dynamics in ferromagnetic nickel. *Physical review letters*, 76(22):4250–4253, 1996. DOI: 10.1103/physrevlett.76.4250.

[12] E. Grüneisen. Theorie des festen Zustandes einatomiger Elemente. *Annalen der Physik*, 344(12):257–306, 1912. ISSN: 00033804. DOI: 10.1002/andp.19123441202.

[13] Jan-Etienne Pudell, Maximilian Mattern, Michel Hehn, Grégory Malinowski, Marc Herzog, and Matias Bargheer. Heat Transport without Heating? - An Ultrafast X–Ray Perspective into a Metal Heterostructure. *Advanced Functional Materials*, 30(46):2004555, 2020. ISSN: 1616-3028. DOI: 10.1002/adfm.202004555.

[14] Antoine Rousse, Christian Rischel, S. Fourmaux, Ingo Uschmann, Stéphane Sebban, G. Grillon, Ph. Balcou, Eckhart Förster, Jean-Paul Geindre, Patrick Audebert, et al. Non-thermal melting in semiconductors measured at femtosecond resolution. *Nature*, 410(6824):65–68, 2001. DOI: 10.1038/35065045.

[15] Nevill F. Mott. Metal-insulator transition. *Reviews of Modern Physics*, 40(4):677, 1968. DOI: 10.1103/RevModPhys.40.677.

[16] C. Thomsen, J. Strait, Z. Vardeny, H. J. Maris, J. Tauc, and J. J. Hauser. Coherent phonon generation and detection by picosecond light pulses. *Physical Review Letters*, 53(10):989–992, 1984. ISSN: 0031-9007. DOI: 10.1103/PhysRevLett.53.989.

[17] C. Thomsen, H. T. Grahn, H. J. Maris, and J. Tauc. Surface generation and detection of phonons by picosecond light pulses. *Physical review. B, Condensed matter*, 34(6):4129–4138, 1986. ISSN: 0163-1829. DOI: 10.1103/physrevb.34.4129.

[18] A. von Reppert, R. M. Sarhan, F. Stete, J. Pudell, N. Del Fatti, A. Crut, J. Koetz, F. Liebig, C. Prietzel, and M. Bargheer. Watching the vibration and cooling of ultrathin gold nanotriangles by ultrafast x-ray diffraction. *The Journal of Physical Chemistry C*, 120(50):28894–28899, 2016. ISSN: 1932-7447. DOI: 10.1021/acs.jpcc.6b11651.

[19] Marwan Deb, Elena Popova, Michel Hehn, Niels Keller, Sébastien Petit-Watelot, Matias Bargheer, Stéphane Mangin, and Gregory Malinowski. Femtosecond laser-excitation-driven high frequency standing spin waves in nanoscale dielectric thin films of iron garnets. *Physical review letters*, 123(2):027202, 2019. DOI: 10.1103/PhysRevLett.123.027202.

[20] L. Willig, A. von Reppert, M. Deb, F. Ganss, O. Hellwig, and M. Bargheer. Finite-size effects in ultrafast remagnetization dynamics of fept. *Physical Review B*, 100(22), 2019. ISSN: 2469-9950. DOI: 10.1103/PhysRevB.100.224408.

[21] Charles Kittel. Physical theory of ferromagnetic domains. *Reviews of Modern Physics*, 21(4):541–583, 1949. ISSN: 0034-6861. DOI: 10.1103/RevModPhys.21.541.

[22] A. V. Scherbakov, A. S. Salasyuk, A. V. Akimov, X. Liu, M. Bombeck, C. Brüggemann, D. R. Yakovlev, V. F. Sapega, J. K. Furdyna, and M. Bayer. Coherent magnetization precession in ferromagnetic (Ga,Mn)As induced by picosecond acoustic pulses. *Physical Review Letters*, 105(11):117204, 2010. DOI: 10.1103/PhysRevLett.105.117204.

[23] S. N. Piramanayagam and Chong Tow Chong. *Developments in data storage: Materials perspective*. Wiley IEEE Press and IEEE Xplore, Hoboken, New Jersey and Piscataway, New Jersey, 2011. ISBN: 9780470501009. DOI: 10.1002/9781118096833.

[24] D. Weller and A. Moser. Thermal effect limits in ultrahigh-density magnetic recording. *IEEE Transactions on Magnetics*, 35(6):4423–4439, 1999. ISSN: 00189464. DOI: 10.1109/20.809134.

[25] Seagate Technology LLC. Heat Assisted Magnetic Recording (HAMR). https://www.seagate.com/de/de/innovation/hamr/, 2022. [Online; accessed 12-02-2022].

[26] M. H. Kryder, E. C. Gage, T. W. McDaniel, W. A. Challener, R. E. Rottmayer, Ganping Ju, Yiao-Tee Hsia, and M. F. Erden. Heat assisted magnetic recording. *Proceedings of the IEEE*, 96(11):1810–1835, 2008. ISSN: 0018-9219. DOI: 10.1109/JPROC.2008.2004315.

[27] Dieter Weller, Gregory Parker, Oleksandr Mosendz, Andreas Lyberatos, Dmitriy Mitin, Nataliia Y. Safonova, and Manfred Albrecht. Review Article: FePt heat assisted magnetic recording media. *Journal of Vacuum Science & Technology B, Nanotechnology and Microelectronics: Materials, Processing, Measurement, and Phenomena*, 34(6):060801, 2016. ISSN: 2166-2746. DOI: 10.1116/1.4965980.

[28] A. V. Kimel, A. M. Kalashnikova, A. Pogrebna, and A. K. Zvezdin. Fundamentals and perspectives of ultrafast photoferroic recording. *Physics Reports*, 852:1–46, 2020. ISSN: 03701573. DOI: 10.1016/j.physrep.2020.01.004.

[29] Marwan Deb, Elena Popova, Michel Hehn, Niels Keller, Stéphane Mangin, and Gregory Malinowski. Picosecond acoustic-excitation-driven ultrafast magnetization dynamics in dielectric Bi-substituted yttrium iron garnet. *Physical Review B*, 98(17):444, 2018. ISSN: 2469-9950. DOI: 10.1103/PhysRevB.98.174407.

[30] Amal El-Ghazaly, Jon Gorchon, Richard B. Wilson, Akshay Pattabi, and Jeffrey Bokor. Progress towards ultrafast spintronics applications. *Journal of Magnetism and Magnetic Materials*, 502:166478, 2020. ISSN: 03048853. DOI: 10.1016/j.jmmm.2020.166478.

[31] K. Uchida, S. Takahashi, K. Harii, J. Ieda, W. Koshibae, Kazuya Ando, S. Maekawa, and E. Saitoh. Observation of the spin Seebeck effect. *Nature*, 455(7214):778–781, 2008. DOI: 10.1038/nature07321.

[32] Johannes Kimling, Gyung Min Choi, Jack T. Brangham, Tristan Matalla-Wagner, Torsten Huebner, Timo Kuschel, Fengyuan Yang, and D. G. Cahill. Picosecond Spin Seebeck Effect. *Physical Review Letters*, 118(5), 2017. ISSN: 0031-9007. DOI: 10.1103/PhysRevLett.118.057201.

[33] Osamu Matsuda, Maria Cristina Larciprete, Roberto Li Voti, and Oliver B. Wright. Fundamentals of picosecond laser ultrasonics. *Ultrasonics*, 56:3–20, 2015. DOI: 10.1016/J.ULTRAS.2014.06.005.

[34] Pascal Ruello and Vitalyi E. Gusev. Physical mechanisms of coherent acoustic phonons generation by ultrafast laser action. *Ultrasonics*, 56:21–35, 2015. DOI: 10.1016/J.ULTRAS.2014.06.004.

[35] Bragg W. H., Bragg W. L. The reflection of x-rays by crystals. *Proceedings of the Royal Society of London A: Mathematical, Physical and Engineering Sciences*, 88(605):428–438, 1913. DOI: 10.1098/rspa.1913.0040.

[36] Jens Als-Nielsen and Des McMorrow. *Elements of modern X-ray physics*. Wiley, Chichester, second edition edition, 2011. ISBN: 978-0-470-97394-3.

[37] M. Herzog, A. Bojahr, J. Goldshteyn, W. Leitenberger, I. Vrejoiu, D. Khakhulin, M. Wulff, R. Shayduk, P. Gaal, and M. Bargheer. Detecting optically synthesized quasi-monochromatic subterahertz phonon wavepackets by ultrafast x-ray diffraction. *Applied Physics Letters*, 100(9):094101, 2012. ISSN: 0003-6951. DOI: 10.1063/1.3688492.

[38] Jean-Claude Diels and Wolfgang Rudolph. *Ultrashort laser pulse phenomena: Fundamentals, techniques, and applications on a femtosecond time scale*. Optics and photonics. Acad. Press/Elsevier, Amsterdam, 2. ed. Edition, 2006. ISBN: 9780122154935.

[39] D. Schick, A. Bojahr, M. Herzog, R. Shayduk, C. von Korff Schmising, and M. Bargheer. udkm1Dsim—A simulation toolkit for 1D ultrafast dynamics in condensed matter. *Computer Physics Communications*, 185(2):651–660, 2014. ISSN: 00104655. DOI: 10.1016/j.cpc.2013.10.009.

[40] Daniel Schick. udkm1Dsim - A Python Simulation Toolkit for 1D Ultrafast Dynamics in Condensed Matter. https://github.com/dschick/udkm1Dsim, 2022. [Online; accessed 12-02-2022].

[41] Ullrich Pietsch, Václav Holý, and Tilo Baumbach. *High-Resolution X-Ray Scattering: From Thin Films to Lateral Nanostructures*. Advanced texts in physics. Springer, New York, NY, second edition edition, 2004. ISBN: 978-1-4419-2307-3. DOI: 10.1007/978-1-4757-4050-9.

[42] Paul F. Fewster. Reciprocal space mapping. *Critical Reviews in Solid State and Materials Sciences*, 22(2):69–110, 1997. DOI: 10.1080/10408439708241259.

[43] A. Kinne, M. Thoms, H. R. Ress, T. Gerhard, M. Ehinger, W. Faschinger, and G. Landwehr. Image plates as one-dimensional detectors in high-resolution x-ray diffraction. *Journal of Applied Crystallography*, 31(3):446–452, 1998. ISSN: 0021-8898. DOI: 10.1107/S002188989701947X.

[44] Olivier Masson, Alexandre Boulle, René Guinebretière, André Lecomte, and Alain Dauger. On the use of one-dimensional position sensitive detector for x-ray diffraction reciprocal space mapping: Data quality and limitations. *Review of Scientific Instruments*, 76(6):063912, 2005. ISSN: 0272-9172. DOI: 10.1063/1.1938850.

[45] Daniel Schick, Roman Shayduk, André Bojahr, Marc Herzog, Clemens von Korff Schmising, Peter Gaal, and Matias Bargheer. Ultrafast reciprocal-space mapping with a convergent beam. *Journal of Applied Crystallography*, 46(5):1372–1377, 2013. ISSN: 0021-8898. DOI: 10.1107/S0021889813020013.

[46] M. Mattern, J.-E. Pudell, G. Laskin, A. von Reppert, and M. Bargheer. Analysis of the temperature- and fluence-dependent magnetic stress in laser-excited srruo 3. *Structural Dynamics*, 8(2):024302, 2021. ISSN: 2329-7778. DOI: 10.1063/4.0000072.

[47] John Kerr LL.D. On rotation of the plane of polarization by reflection from the pole of a magnet. *The London, Edinburgh, and Dublin Philosophical Magazine and Journal of Science*, 3(19):321–343, 1877. DOI: 10.1080/14786447708639245.

[48] P. S. Pershan. Magneto–optical effects. *Journal of Applied Physics*, 38(3):1482–1490, 1967. ISSN: 0021-8979. DOI: 10.1063/1.1709678.

[49] A. E. Clark and H. S. Belson. Giant Room-Temperature Magnetostrictions in TbFe2 and DyFe2. *Physical Review B*, 5(9):3642–3644, 1972. ISSN: 2469-9950. DOI: 10.1103/PhysRevB.5.3642.

[50] Tymur Parpiiev. *Ultrafast magnetoacoustics in magnetostrictive materials*. PhD thesis, Le Mans Université, 2017. URL: https://tel.archives-ouvertes.fr/tel-01798696.

[51] Alexander von Reppert. *Ultrafast Magnetostriction in Dysprosium studied by Femtosecond X-Ray diffraction*. MSc thesis, Universität Potsdam, Potsdam, 2015. URL: https://www.uni-potsdam.de/fileadmin/projects/udkm/Documents/BaMa_theses/repp2015msc.pdf.

[52] A. von Reppert, J. Pudell, A. Koc, M. Reinhardt, W. Leitenberger, K. Dumesnil, F. Zamponi, and M. Bargheer. Persistent nonequilibrium dynamics of the thermal energies in the spin and phonon systems of an antiferromagnet. *Structural Dynamics*, 3(5):054302, 2016. ISSN: 2329-7778. DOI: 10.1063/1.4961253.

[53] Alexander von Reppert. *Magnetic strain contributions in laser-excited metals studied by time-resolved X-ray diffraction*. PhD Thesis, Universität Potsdam, 2021. DOI: 10.25932/publishup-53558.

[54] A. von Reppert, L. Willig, J.-E. Pudell, M. Rössle, W. Leitenberger, M. Herzog, F. Ganss, O. Hellwig, and M. Bargheer. Ultrafast laser generated strain in granular and continuous FePt thin films. *Applied Physics Letters*, 113(12):123101, 2018. ISSN: 0003-6951. DOI: 10.1063/1.5050234.

[55] Marwan Deb, Mircea Vomir, Jean-Luc Rehspringer, and Jean-Yves Bigot. Ultrafast optical control of magnetization dynamics in polycrystalline bismuth doped iron garnet thin films. *Applied Physics Letters*, 107(25):252404, 2015. ISSN: 0003-6951. DOI: 10.1063/1.4938538.

[56] Jan-Etienne Pudell. *Lattice dynamics*. PhD thesis, Universität Potsdam, 2020. DOI: 10.25932/publishup-48445.

[57] N. Zhavoronkov, Y. Gritsai, M. Bargheer, M. Woerner, and T. Elsaesser. Generation of ultrashort k_α radiation from quasipoint interaction area of femtosecond pulses with thin foils. *Applied Physics Letters*, 86(24):244107, 2005. ISSN: 0003-6951. DOI: 10.1063/1.1946915.

[58] M. Bargheer, N. Zhavoronkov, R. Bruch, H. Legall, H. Stiel, M. Woerner, and T. Elsaesser. Comparison of focusing optics for femtosecond x-ray diffraction. *Applied Physics B*, 80(6):715–719, 2005. ISSN: 0946-2171. DOI: 10.1007/s00340-005-1792-7.

[59] M. Bargheer, N. Zhavoronkov, Y. Gritsai, J. C. Woo, D. S. Kim, M. Woerner, and T. Elsaesser. Coherent atomic motions in a nanostructure studied by femtosecond x-ray diffraction. *Science*, 306(5702):1771–1773, 2004. DOI: 10.1126/science.1104739.

[60] F. Zamponi, Z. Ansari, C. Korff Schmising, P. Rothhardt, N. Zhavoronkov, M. Woerner, T. Elsaesser, M. Bargheer, T. Trobitzsch-Ryll, and M. Haschke. Femtosecond hard x-ray plasma sources with a kilohertz repetition rate. *Applied Physics A*, 96(1):51–58, 2009. ISSN: 0947-8396. DOI: 10.1007/s00339-009-5171-9.

[61] D. Schick, A. Bojahr, M. Herzog, C. von Korff Schmising, R. Shayduk, W. Leitenberger, P. Gaal, and M. Bargheer. Normalization schemes for ultrafast x-ray diffraction using a table-top laser-driven plasma source. *The Review of scientific instruments*, 83(2):025104, 2012. DOI: 10.1063/1.3681254.

[62] Lisa Willig. *Ultrafast Magneto-Optical Studies of Remagnetisation Dynamics in Transition Metals*. PhD thesis, Universität Potsdam, 2019. URL: https://www.uni-potsdam.de/fileadmin/projects/udkm/Documents/PhD_theses/will2019phd.pdf.

[63] A. B. Chizhik, I. I. Davidenko, A. Maziewski, and A. Stupakiewicz. High-temperature photomagnetism in Co-doped yttrium iron garnet films. *Phys. Rev. B*, 57:14366–14369, 22, 1998. DOI: 10.1103/PhysRevB.57.14366.

[64] Fredrik Hansteen, Alexey Kimel, Andrei Kirilyuk, and Theo Rasing. Femtosecond photomagnetic switching of spins in ferrimagnetic garnet films. *Physical Review Letters*, 95(4):047402, 2005. ISSN: 0031-9007. DOI: 10.1103/PhysRevLett.95.047402.

[65] Fredrik Hansteen, Alexey Kimel, Andrei Kirilyuk, and Theo Rasing. Nonthermal ultrafast optical control of the magnetization in garnet films. *Physical Review B*, 73(1):1376, 2006. ISSN: 2469-9950. DOI: 10.1103/PhysRevB.73.014421.

[66] Marwan Deb, Pierre Molho, Bernard Barbara, and Jean-Yves Bigot. Temperature and magnetic field dependence of rare−earth↔ iron exchange resonance mode in a magnetic oxide studied with femtosecond magneto-optical kerr effect. *Physical Review B*, 94(5):153, 2016. ISSN: 2469-9950. DOI: 10.1103/PhysRevB.94.054422.

[67] A. Stupakiewicz, K. Szerenos, D. Afanasiev, A. Kirilyuk, and A. V. Kimel. Ultrafast nonthermal photo-magnetic recording in a transparent medium. *Nature*, 542(7639):71–74, 2017. DOI: 10.1038/nature20807.

[68] Yusuke Hashimoto, Davide Bossini, Tom H. Johansen, Eiji Saitoh, Andrei Kirilyuk, and Theo Rasing. Frequency and wavenumber selective excitation of spin waves through coherent energy transfer from elastic waves. *Physical Review B*, 97(14):140404, 2018. ISSN: 2469-9950. DOI: 10.1103/PhysRevB.97.140404.

[69] Marwan Deb, Pierre Molho, Bernard Barbara, and Jean-Yves Bigot. Controlling laser-induced magnetization reversal dynamics in a rare-earth iron garnet across the magnetization compensation point. *Physical Review B*, 97(13):134419, 2018. ISSN: 2469-9950. DOI: 10.1103/PhysRevB.97.134419.

[70] A. A. Serga, A. V. Chumak, and B. Hillebrands. YIG magnonics. *Journal of Physics D: Applied Physics*, 43(26):264002, 2010. ISSN: 0022-3727. DOI: 10.1088/0022-3727/43/26/264002.

[71] Daniel Schick, Marc Herzog, André Bojahr, Wolfram Leitenberger, Andreas Hertwig, Roman Shayduk, and Matias Bargheer. Ultrafast lattice response of photoexcited thin films studied by x-ray diffraction. *Structural Dynamics*, 1(6):064501, 2014. ISSN: 2329-7778. DOI: 10.1063/1.4901228.

[72] David G. Cahill, Wayne K. Ford, Kenneth E. Goodson, Gerald D. Mahan, Arun Majumdar, Humphrey J. Maris, Roberto Merlin, and Simon R. Phillpot. Nanoscale thermal transport. *Journal of Applied Physics*, 93(2):793–818, 2003. ISSN: 0021-8979. DOI: 10.1063/1.1524305.

[73] G. G. Siu, C. M. Lee, and Yulong Liu. Magnons and acoustic phonons in Y(3-x)Bi(x)Fe5O12. *Physical review. B, Condensed matter*, 64(9):094421, 2001. ISSN: 0163-1829. DOI: 10.1103/PhysRevB.64.094421.

[74] V. F. Kitaeva, E. V. Zharikov, and I. L. Chistyi. The properties of crystals with garnet structure. *physica status solidi (a)*, 92(2):475–488, 1985. ISSN: 00318965. DOI: 10.1002/pssa.2210920217.

[75] Molecular Technology MolTech GmbH. Single Crystalline Substrates. http://www.mt-berlin.com/frames_cryst/descriptions/substrates.htm, 2022. [Online; accessed 12-02-2022].

[76] Rui-sheng Liang and Feng-chao Liu. Measurement of thermal expansion coefficient of substrate GGG and its epitaxial layer YIG. *Powder Diffraction*, 14(1):2–4, 1999. ISSN: 0885-7156. DOI: 10.1017/S0885715600010216.

[77] A. E. Clark and R. E. Strakna. Elastic Constants of Single-Crystal YIG. *Journal of Applied Physics*, 32(6):1172–1173, 1961. DOI: 10.1063/1.1736184.

[78] Daniel Royer and Eugène Dieulesaint. *Elastic waves in solids: Including nonlinear dynamics*. Advanced texts in physics. Springer, Berlin, 3., rev. and enl. ed. Edition, 2000. ISBN: 3-540-65931-5.

[79] Hui Shen, Jiayue Xu, Anhua Wu, Jingtai Zhao, and Minli Shi. Magnetic and thermal properties of perovskite YFeO3 single crystals. *Materials Science and Engineering: B*, 157(1-3):77–80, 2009. DOI: 10.1016/j.mseb.2008.12.020.

[80] G. A. Saunders, S. C. Parker, N. Benbattouche, and H. L. Alberts. Elastic and nonlinear acoustic properties of the Terbium Iron garnet Tb3Fe5O12 in relation to those of other garnets. *Physical review. B, Condensed matter*, 46(14):8756–8767, 1992. ISSN: 0163-1829. DOI: 10.1103/PhysRevB.46.8756.

[81] Jamal Berakdar. Nonequilibrium Many-Body Systems Group at the Martin-Luther-University Halle-Wittenberg. http://qft0.physik.uni-halle.de/, 2022. [Online; accessed 12-02-2022].

[82] Yooleemi Shin, Mircea Vomir, Dong-Hyun Kim, Phuoc Cao Van, Jong-Ryul Jeong, and Jiwan Kim. Quasi-static strain governing ultrafast spin dynamics. *ArXiv*, 2021. DOI: 10.21203/rs.3.rs-773488/v1.

[83] F. J. Darnell and E. P. Moore. Crystal structure of dysprosium at low temperatures. *Journal of Applied Physics*, 34(4):1337–1338, 1963. ISSN: 0021-8979. DOI: 10.1063/1.1729497.

[84] A. V. Kimel, A. Kirilyuk, P. A. Usachev, R. V. Pisarev, A. M. Balbashov, and Th Rasing. Ultrafast non-thermal control of magnetization by instantaneous photomagnetic pulses. *Nature*, 435(7042):655–657, 2005. DOI: 10.1038/nature03564.

[85] Christian Tzschaschel, Kensuke Otani, Ryugo Iida, Tsutomu Shimura, Hiroaki Ueda, Stefan Günther, Manfred Fiebig, and Takuya Satoh. Ultrafast optical excitation of coherent magnons in antiferromagnetic NiO. *Physical Review B*, 95(17):1–11, 2017. ISSN: 2469-9950. DOI: 10.1103/PhysRevB.95.174407.

[86] D. Afanasiev, B. A. Ivanov, A. Kirilyuk, Th. Rasing, R. V. Pisarev, and A. V. Kimel. Control of the ultrafast photoinduced magnetization across the Morin transition in DyFeO3. *Physical Review Letters*, 116(9):097401, 2016. URL: 10.1103/PhysRevLett.116.097401.

[87] C. S. Davies, K. H. Prabhakara, M. D. Davydova, K. A. Zvezdin, T. B. Shapaeva, S. Wang, A. K. Zvezdin, A. Kirilyuk, Th Rasing, and A. V. Kimel. Anomalously Damped Heat-Assisted Route for Precessional Magnetization Reversal in an Iron Garnet. *Physical review letters*, 122(2):027202, 2019. DOI: 10.1103/PhysRevLett.122.027202.

[88] Benny Koene, Marwan Deb, Elena Popova, Niels Keller, Theo Rasing, and Andrei Kirilyuk. Spectrally resolved optical probing of laser induced magnetization dynamics in bismuth iron garnet. *Journal of Physics: Condensed Matter*, 28(27):276002, 2016. ISSN: 0281-1847. DOI: 10.1088/0953-8984/28/27/276002.

[89] F. Atoneche, A. M. Kalashnikova, A. V. Kimel, A. Stupakiewicz, A. Maziewski, A. Kirilyuk, and Th. Rasing. Large ultrafast photoinduced magnetic anisotropy in a cobalt-substituted yttrium iron garnet. *Physical Review B*, 81(21), 2010. ISSN: 2469-9950. DOI: 10.1103/PhysRevB.81.214440.

[90] D. Afanasiev, I. Razdolski, K. M. Skibinsky, D. Bolotin, S. V. Yagupov, M. B. Strugatsky, A. Kirilyuk, Th. Rasing, and A. V. Kimel. Laser excitation of lattice-driven anharmonic magnetization dynamics in dielectric febo3. *Physical Review Letters*, 112(14):147403, 2014. DOI: 10.1103/PhysRevLett.112.147403.

[91] A. M. Kalashnikova, A. V. Kimel, R. V. Pisarev, V. N. Gridnev, P. A. Usachev, Andrei Kirilyuk, and Th. Rasing. Impulsive excitation of coherent magnons and phonons by subpicosecond laser pulses in the weak ferromagnet FeBO3. *Physical Review B*, 78(10):104301, 2008. DOI: 10.1103/PhysRevB.78.104301.

[92] G. D. Barrera, J. A. O. Bruno, T. H. K. Barron, and N. L. Allan. Negative thermal expansion. *Journal of Physics: Condensed Matter*, 17(4):R217–R252, 2005. ISSN: 0281-1847. DOI: 10.1088/0953-8984/17/4/R03.

[93] J. Pudell, A. A. Maznev, M. Herzog, M. Kronseder, C. H. Back, G. Malinowski, A. von Reppert, and M. Bargheer. Layer specific observation of slow thermal equilibration in ultrathin metallic nanostructures by femtosecond x-ray diffraction. *Nature Communications*, 9(1):3335, 2018. ISSN: 2041-1723. DOI: 10.1038/s41467-018-05693-5.

[94] Klaus Sokolowski-Tinten, Christian Blome, Juris Blums, Andrea Cavalleri, Clemens Dietrich, Alexander Tarasevitch, Ingo Uschmann, Eckhard Förster, Martin Kammler, Michael Horn-von Hoegen, and Dietrich von der Linde. Femtosecond x-ray measurement of coherent lattice vibrations near the lindemann stability limit. *Nature*, 422(6929):287–289, 2003. DOI: 10.1038/nature01490.

[95] L. Thevenard, E. Peronne, C. Gourdon, C. Testelin, M. Cubukcu, E. Charron, S. Vincent, A. Lemaître, and B. Perrin. Effect of picosecond strain pulses on thin layers of the ferromagnetic semiconductor (Ga,Mn)(As,P). *Physical Review B*, 82(10):444, 2010. ISSN: 2469-9950. DOI: 10.1103/PhysRevB.82.104422.

Statement of Authorship - Selbstständigkeitserklärung

I hereby confirm that I drew up this submitted dissertation independently, used no other than the specified aids whereas the parts of the thesis which are equivalent or verbatim to provided sources are precisely marked as references.

Hiermit erkläre ich, dass ich die vorliegende Dissertation selbstständig angefertigt, keine anderen als die angegebenen Hilfsmittel benutzt und die Stellen der Arbeit, die im Wortlaut oder im wesentlichen Inhalt aus anderen Werken entnommen wurden, mit genauer Quellenangabe kenntlich gemacht habe.

Ort, Datum	Steffen Peer Zeuschner

Acknowledgements

This thesis, my work, my contributions would not have been possible without the wonderful community that is the UDKM joint research group at the University of Potsdam and the Helmholtz Zentrum Berlin. First and foremost, this is true for Matias Bargheer from whom I learned a lot about how to work, how to write and how to talk as a scientist. I am greatful that i was employed, supported and and encouraged all the time with his endless hunger for knowledge and enthusiasm during my Bachelors, Masters and now PhD studies. The same is true for Alexander von Reppert, Jan-Etienne Pudell and Marc Herzog with which I worked endless hours in the lab, shared lunch or offices and went on journeys to synchrotrons or conferences. I did not have the luck to work as closely with the rest of the group but for the countless nice talks, helping hands and great times, I am very thankful aswell.

Many of the experiments would not have been possible without the right samples to work on. I am thanking Karine Dumesnil and her group, Niels Keller and Elena Popova, Jutta Schwarzkopf and Jos Boschker as well as the group of Olav Hellwig for providing the samples I used during my research. I would also like to thank the Helmholtz Zentrum Berlin for providing a enjoyable and productive workspace for me as their employee and the University of Potsdam for now more than ten flourishing years of learning and teaching.

Last but not least, I want to thank the most important people in my life, my friends and family, my loved ones. I am blessed to have such loyal, reliable and from-the-bottom-of-their-hearts good people in my life. I am thankful for the hours, days and weeks I had and will have with my friends playing games, watching movies, cooking, talking, laughing, crying, living. All of this and more is true for my family; my forgiving, successful and hard working love Charlott, my strong, sensitive and persistent big brother René, my brave, adventurous and sensible little sister Leya, my selfless, caring and loving mother Birgit and my wise, fun-loving and dutiful old man, Markus. To you, I dedicate this work.

Er... yeah and to the cat.